

See discussions, stats, and author profiles for this publication at: <https://www.researchgate.net/publication/225789595>

A Biphasic Continuum Approach for Viscoelastic High-Porosity Foams: Comprehensive Theory, Numerics, and Application

Article in Archives of Computational Methods in Engineering · December 2008

DOI: 10.1007/s11831-008-9023-0

CITATIONS

48

READS

494

1 author:



Bernd Markert

RWTH Aachen University

331 PUBLICATIONS 2,600 CITATIONS

SEE PROFILE

Some of the authors of this publication are also working on these related projects:



Phase-field modelling applications in damage and fracture [View project](#)



Monte Carlo Simulations in nonlinear structural dynamics [View project](#)

A Biphasic Continuum Approach for Viscoelastic High-Porosity Foams: Comprehensive Theory, Numerics, and Application

Bernd Markert

Received: 30 October 2007 / Accepted: 30 October 2007 / Published online: 13 August 2008
© CIMNE, Barcelona, Spain 2008

Abstract This work aims to present a valuable and predictive model for the description of polymeric soft foams which are widely exploited as packaging, padding, or cushioning materials. Belonging to the class of cellular solids, polymeric foams and synthetic sponges can be regarded as permeable or impermeable fluid-saturated porous materials depending on whether their microstructure is open-celled or closed-celled. The pore space formed by the cellular polymer skeleton is filled with a pore fluid (e.g., liquid or gas) which can significantly affect the transient compressive and impact response making particularly air-filled foamed plastics a light-weight and shock-absorbing material par excellence.

In view of their practical application, it is the intention to model the macroscopic bulk response of high-porosity foams without getting lost in the description of the deformation habits of a distinct cell on the microstructure. It is rather the goal to phenomenologically capture the coupled dissipative phenomena stemming from the viscoelasticity of the polymer matrix and the usually underestimated or even neglected influence of the viscous pore-fluid motion which essentially constitute the favorable characteristics of these materials. Therefore, a general framework is derived by merging the advances in porous media theories and the state of the art in finite solid viscoelasticity. Against a thermodynamically consistent background, a constitutive setting is presented where, based on the internal variable concept, an extended Ogden-type viscoelasticity law is embedded into the macroscopic Theory of Porous Media (TPM). By regarding foamed polymers as immiscible binary solid-fluid

aggregates, essential nonlinearities are modularly included in the formulation. In detail, the developed biphasic continuum approach accounts for the relevant physical properties emanating from the cellular microstructure, such as the densification behavior under finite compression, the trapped or potentially moving and interacting viscous pore fluid (compressible or incompressible), and the superimposed intrinsic viscoelasticity of the polymeric skeleton itself.

The numerical treatment of this strongly coupled solid-fluid problem is carried out through the Finite Element Method (FEM) where the governing equations are formulated in the primary variables solid displacement and pore-fluid pressure. The two-field variational problem is then efficiently solved by recourse to stable mixed finite element formulations and an appropriate implicit time-stepping scheme in combination with a two-stage solution strategy for the discrete nonlinear equation system.

Finally, in order to demonstrate its capabilities, the presented model is calibrated to the energy-absorbing response of an open-celled polyurethane (PUR) foam as it shows all conceivable nonlinearities under absolute finite viscoelastic deformations. The FE simulations of a real impact experiment on fragmented PUR foam blocks and the fast compressive loading of a whole car seat cushion excellently mimic the flow-dependent size effect and the pneumatic damping behavior of the material. Moreover, the overall performance of the numerical implementation is shown by convergence studies for different mixed FE discretizations.

In summary, the presented details convincingly demonstrate that for a quantitative simulation particularly of permeable soft foams under compression, the consideration of an independent pore-fluid phase is indispensable. It becomes moreover apparent that only a multiphasic continuum approach which accounts for the essential nonlinearities and

B. Markert (✉)
Institute of Applied Mechanics (CE), Universität Stuttgart,
Pfaffenwaldring 7, 70569 Stuttgart, Germany
e-mail: markert@mechbau.uni-stuttgart.de

rate-dependent solid and fluid properties is appropriate for the realistic description of viscoelastic low-density foams.

1 Introduction

1.1 Motivation

It is quite obvious that the volumetric deformation of a permeable fluid-saturated porous solid will always cause viscous pore-fluid motion thereby initiating the well-known consolidation process under drained conditions [132]. This time-dependent effect is overlaid by another dissipative phenomenon if the porous solid skeleton itself exhibits relaxation and creep behavior, i.e., behaves viscoelastic. This actually applies to most low-density polymer foams. In general, the flow-dependent and the flow-independent (intrinsic) viscoelastic properties are strongly coupled and must be treated within the framework of the nonlinear thermodynamics of multi-phase materials. In this context, all investigations must be carried out in the large strain regime since foamed plastics or synthetic sponges are generally intended to undergo finite viscoelastic deformations during their practical application. Focusing on the microscale of these materials, depending on the polymeric ground substance and the foaming agent, a variety of skeletal or cellular structures built by a conglomerate of open and/or closed fluid-filled cells can be found [60, 78, 140]. Subjected to external loads, these microstructures undergo complex deformation mechanisms typically resulting in a highly nonlinear stress-strain response of the macroscopic foam, cf. [62, 139, 145].

Nowadays, sophisticated imaging techniques, such as the Micro Computer Tomography (Micro CT) or the Magnetic Resonance Imaging (MRI), allow the three-dimensional (3-d) reconstruction of many porous microstructures with resolutions up to a few microns [19, 53, 110]. However, even through increased computer power, the numerical simulation of real applications on the microscale using reconstructed geometries is currently not reasonable. Alternatively, the cellular microstructure can be idealized by discrete beam or shell elements, instead of dealing with the real pore geometry, see, e.g., [94, 123, 143]. Even then, the computer resources required to solve problems of practical relevance are out of scale. Furthermore, in these discrete approaches, the description of a free-moving pore fluid and, as a consequence, the frictional drag on the microstructural skeleton, as well as the inner contact in collapsing pores, are more than problematic.

A further possibility to analyze the stress response of porous materials is to apply homogenization techniques to idealized models of the microstructure. In the case of foamed solids, an average pore can be approximated by a simple beam or shell model of a volume-filling polyhedron, such as the widely-used Kelvin cell [133], where

the effective (macroscopic) moduli and critical stress values can be determined from scaling laws [60]. This leads to a good description concerning materials with a more or less regular and well-defined pore structure, such as honeycombs. The same applies to unit cell approaches where the foam microstructure is treated as a periodic cell structure [80] or as a composite structure with periodic hollow inclusions [11]. However, albeit the simplified representation of the microstructure often entails empirical corrections, particularly when inelasticity comes into play, these models definitely reach their limits in describing the considerable influence of a moving and interacting pore fluid during finite compression.

Thus, it can be concluded that for general real-scale problems with cellular polymers where the pore-fluid flow can have a distinct influence on the transient response of the entire foam (cf. [71]), a macroscopic mixture approach provides the convenient solution strategy. Following this, an independent fluid constituent can be easily considered even if there exists no detailed geometry information about the cellular microstructure. To this end, a statistical, multiphase continuum mechanical model will be derived to successfully represent the fully coupled behavior of viscoelastic high-porosity foams under external loads. Surprisingly, besides some own previous works [48, 49, 91], as far as the author is aware, only Schraad and Harlow [120] apply a multi-field approach to capture the influence of a percolating fluid in cellular solids.

1.2 State of the Art

In the present contribution, the macroscopic description of viscoelastic high-porosity foams is considered in the framework of the well-founded Theory of Porous Media (TPM). The TPM as a multiphase continuum theory combines the Theory of Mixtures (TM) with the concept of volume fractions yielding an excellent tool for the macroscopic description of general immiscible solid-fluid aggregates. In particular, according to the TM, all constituents are assumed to be statistically distributed over the regarded domain in the sense of superimposed and interacting continua where the microstructural information is only considered by local volumetric ratios following the concept of volume fractions. For a detailed discussion of the TPM approach, see, e.g., [14, 15, 30, 31, 39, 42] and the quotations therein.

Here, focusing on the applicability of the standard TPM approach to biphasic porous materials excluding thermal effects and any mass exchanges where one solid skeleton is saturated by a single pore fluid, a broad field of engineering problems can still be addressed. This is because arbitrary, thermodynamically admissible constitutive relations for the effective solid stress and the effective fluid momentum production can be consistently added to the macroscopic formu-

lation according to the effective stress principle [32]. However, the traditional application of the TPM, as well as any other mixture theory, to geomechanical problems, primarily led to the development of sophisticated elastoplastic and elasto-viscoplastic constitutive models that are capable of describing localization phenomena in saturated and unsaturated soils [35, 39, 40, 50]. More recently, proceeding from works on finite porous media elasticity [43, 51], the elastoplastic models are extended towards geometrical nonlinearities applying simple neo-Hookean-type elasticity formulations and are adapted for the description of hard polymer and metal foams which suffer immense plastic deformations [36, 89].

For the purpose of this work, an appropriate finite viscoelasticity law accounting for the highly nonlinear behavior of the cellular polymer matrix must be developed and has to be added to the biphasic formulation. Certainly, the combination of porous media theories with viscoelastic constitutive equations for the solid skeleton is not a new idea, see [9, 90]. Particularly, the linear biphasic poroviscoelastic (BPVE) theory proposed by Mak [90] which applies the linear integral-type viscoelasticity model by Fung [58] has been established for the description of cartilaginous tissues [122]. However, the numerical treatment of such integral-type formulations where the external state variables expressed as functionals of the process history capture the idea of materials with fading memory by a continuous relaxation spectrum [22, 24, 65], turns out to be very inefficient because of the intensive computational burden associated with the time integration of the convolution integrals [130].

A more convenient approach to solid viscoelasticity, especially from a numerical point of view, is provided by the model rheology in combination with the thermodynamics with internal state variables [23, 87, 137]. Proceeding from a rheological model that covers the response of viscoelastic solids by an appropriate assembly of elastic springs and viscous dashpots, such as the generalized Maxwell model, strain-equivalent internal variables can be introduced which can directly be associated with the dashpot deformations. This phenomenological procedure yields a differential representation of viscoelasticity where a discrete relaxation spectrum allows for an efficient numerical treatment. The internal variables can then be treated as history variables depending on the time discretization of the constitutive differential evolution equations. For the simple geometrically linear case, the discrete spectrum algorithm has already been successfully applied within the TPM for the 3-d simulation of soft hydrated biological tissues [46, 47].

In terms of finite deformations where the introduction of internal variables and the choice of evolution laws is not so evident nor unique, one can adopt the state of the art in finite viscoelasticity of non-porous solids and extend it to porous media applications. Following the related literature [73, 81,

85, 116], it is convenient to proceed from the aforementioned internal variable concept where the phenomenological introduction of strain-equivalent internal variables is accomplished by multiplicative decompositions of the deformation gradient into elastic and inelastic parts as it is well-established in finite plasticity theories according to Lee [82]. In principle, the formal similarities in multiplicative inelasticity allow the exploitation of the sophisticated solution strategies that were developed over the years in the field of finite elastoplasticity. For further particulars on multiplicative viscoelasticity and possible micromechanical motivations, see [88, 115, 125].

Alternatively, also stress-equivalent internal variables can be introduced representing the rate-dependent over stresses which relax towards the thermodynamical equilibrium. The current stress state can then be computed from a recursive formula which is derived from a time discretization of the convolution integrals covering the categorical linear differential evolution equations of the over stresses. Therefore, this procedure can be regarded as an intermediate approach applying the internal variable concept in combination with an integral-type representation of the evolution equations [72, 75, 127, 131]. However, the required linearity of the evolution laws actually restricts the theoretical applicability of this procedure to problems with moderate deformation rates. Instead, following the multiplicative concept, consistent evolution equations for the introduced strain-equivalent internal variables can be found by evaluation of the entropy principle without being restricted to small perturbations away from the thermodynamic equilibrium.

Regarding the constitutive relations used for the stress and the over stress computation in finite viscoelasticity of single-phase materials, mostly isotropic strain-energy functions are concerned with the description of dense rubber-like or polymeric materials. In order to reproduce the nonlinear stress-strain behavior of these materials, Ogden-type formulations [101, 104, 105] are extensively used because of their mathematical validity [6, 21, 103] and their good, although challenging, adaptability to experimental observations. However, due to the supposed incompressibility of the considered materials, the formulations are usually restricted to isochoric deformations. In contrast, in the case of porous media viscoelasticity applied to foams, compressible formulations are required since, due to pore-space deformations and possible pore-fluid outflows, the macroscopic material is volumetrically deformable even if both the skeleton material and the pore fluid itself are materially incompressible. Therefore, special volumetric extensions must be developed which guarantee the volumetric stiffening of the porous medium towards the point of compaction [51], i.e., the deformation state with zero void ratio where all pores are closed. This concept of the compaction point directly implies the characteristic property of structural densification of

porous materials under finite compression which can be very well observed experimentally for foamed solids [19, 60]. In this context, it is also referred to the constitutive strain energies suggested by Blatz and Ko [12] and Ogden [102] for the description of foam-like elastomers as compressible singlephasic materials.

Now, focusing on the description of the pore-fluid constituent, the flow of incompressible liquids, compressible gases, as well as inseparable mixture phases of liquid and gas, through saturated porous media is a common issue addressed in various publications. However, two main categories can be distinguished. On the one hand, investigating deformable porous materials, continuum theories like the TPM are applied to primarily recover the macroscopic deformation behavior. However, the included flow equations are usually based on a simple, although consistent, linear ansatz for the effective fluid momentum production, i.e., the interaction or drag force in biphasic solid-fluid mixtures, yielding a Darcy-type filter law [26, 42]. This linear relation between lingering seepage flow and hydraulic gradient, firstly obtained by Darcy [28], indeed, cannot always be met in real applications. In order to account for flow changes due to skeleton deformations, some authors introduce the permeability as a function of the deformation state, e.g., governed by the volume dilatation using an exponential ansatz [97] or governed by the current porosity following a power law [51]. On the other hand, particularly in the disciplines of chemical, environmental and petroleum engineering, and hydrology, investigators proceed from undeformable porous media and are therefore primarily concerned with the detailed description of the percolation process through the rigid skeleton. In this context, turbulence as well as microscopic inertia and drag forces, apparently responsible for the deviations from a laminar Darcy flow, are experimentally and theoretically discussed where usually empirical observations lead to slight variations of the classical 1-d Forchheimer flow rule [57], see also [7, 37, 99]. More recent works apply averaging and homogenization methods to derive physical sound Forchheimer terms [83] but also involve numerical simulations of microscopic Navier-Stokes flow, e.g., by use of the Lattice Boltzmann Method (LBM), in order to predict effective permeabilities and to study the transition from laminar to non-Darcy flows within porous structures, cf. [1, 107, 138]. Mills [95] uses Computational Fluid Dynamics (CFD) to predict the permeability for laminar air flow through a Kelvin model of open-celled polyurethane foams. However, the objective of the present study lies in the combination of both finite skeleton deformations and a 3-d non-linear filter law. In this regard, experimental evidence reveals the considerable dependence of the permeability on the skeleton deformation where, in general, also initial and deformation-induced anisotropic flow properties are of practical importance, and thus, must be taken into consideration.

Concerning the numerical treatment of coupled solid-fluid problems, the Finite Element Method (FEM) is a convenient technique for the solution of arbitrary initial boundary-value problems, see [84] for references. As far as the author is aware, the first results of finite element simulations of a fluid-saturated deformable porous medium are published by Sandhu and Wilson [119]. It is noteworthy that their principle approach, particularly the choice of the skeleton displacement and the pore-fluid pressure as primary field variables in combination with the approximation by quadratic and linear interpolations in mixed finite elements, defines the standard of porous media FE discretizations. Alternative approaches, which are especially designed for dynamical porous media problems in the field of geotechnical earthquake engineering, proceed from so-called splitting (operator split) or fractional algorithms which are adopted from CFD [146, 148]. These iterative semi-implicit-explicit schemes allow for an equal-order interpolation of the coupled fields without loss of stability [109, 147]. However, the procedure has other drawbacks, such as the somehow tricky treatment of the boundary conditions. Here, the numerical treatment of the presented TPM model is carried out through the Finite Element Method proceeding from a displacement-pressure formulation of the governing field equations with respect to the whole mixture. Due to material incompressibility and/or quasi-static considerations, the spatial semi-discretization by stable mixed finite elements [3, 18] leads to a system of differential-algebraic equations (DAE) in the time domain. The numerical integration of this semi-discrete system can be efficiently performed by suitable time integration schemes, such as diagonally implicit Runge-Kutta (DIRK) methods [35, 52] where an embedded error estimator and a time step control can be added. Moreover, Diebels et al. [35] successfully used the sophisticated global time integration schemes also for the local time discretization of plastic evolution equations. This idea can directly be adopted for the time integration of viscoelastic evolution laws including an adaptive time step control which is crucial in the case of creep or relaxation dominated processes, cf. [67].

For the practical application, the mathematical model has to be adjusted to real material behavior, i.e., the constitutively introduced material parameters have to be determined. Due to the complexity of the macroscopic material formulation, not all of the included material parameters can be associated with a distinct physical meaning, which is the price to pay in continuum approaches. Moreover, the superposed dissipative phenomena of the viscous pore-fluid flow and the viscoelastic skeleton usually cannot be separately addressed in large strain experiments. Thus, based on suitable material tests that can be reproduced by coupled FE simulations, the application of numerical optimization techniques is inevitable. The challenge is to find a set of admissible mate-

rial parameters such that the function of the squared deviations of simulation from experimental data becomes least. For this purpose, a constraint minimization strategy has to be applied, see, e.g., [56, 100]. Here, following the works of Powell [111, 112], a derivative-free, direct search algorithm is used for the minimization of the least-squares functional, where a hierarchical simulation strategy keeps the computational overhead under an acceptable limit. In particular, Powell's *constrained optimization by linear approximations* (COBYLA) algorithm is used to adapt the viscoelastic model to a highly porous, open-celled polyurethane (PUR) foam.

In summary, to reach the goal of the present contribution, an interacting biphasic solid-fluid mixture is considered in the framework of the Theory of Porous Media. For simplicity, the presentation is restricted to isothermal conditions, and mass exchanges between the constituents, e.g., due to phase transitions or chemical reactions, are excluded. The macroscopic behavior of the materially incompressible, isotropic polymer matrix is described by a multiplicative finite viscoelasticity formulation based on extended Ogden-type strain energies. The interaction with the materially compressible or incompressible pore fluid is taken into account by a nonlinear viscous drag force, where a 3-d Forchheimer-type filter law with deformation-dependent permeability coefficients is finally used to govern the non-Darcy pore-gas or -liquid flow. Moreover, initial and deformation induced anisotropic permeability effects are included in the macroscopic formulation. All this is carried out against the background of a thermodynamically consistent theory where the admissibility of the introduced constitutive relations is throughout guaranteed by the entropy principle. The numerical treatment is carried out through the FEM where the solid displacement and the pore-fluid pressure as primary unknowns are approximated by stable mixed finite element formulations. The usage of Runge-Kutta time integration schemes for the global as well as for the local time discretization in combination with a two-stage Newton procedure allows for an efficient time-adaptive computation of large coupled viscoelastic systems. Finally, to show the overall applicability and the practical relevance of the presented macroscopic approach, the model is numerically adapted to the behavior of a soft cellular polymer foam, subsequently followed by two illustrative numerical examples. Thus, the present work delivers several new aspects to porous media theories concerning consistent modeling, efficient numerical treatment, and model adaption, where the overall combination defines the new state of the art in porous media viscoelasticity with special focus on cellular polymers.

1.3 Overview

To begin with, in Sect. 2, the theoretical fundamentals of the TPM approach are briefly reviewed including the concept of volume fractions and the kinematics, the governing balance laws, and the entropy principle for mixtures. In this context, the particular focus is on a comprehensible introduction of the finite inelastic solid kinematics based on the multiplicative geometric concept in the framework of the natural basis representation.

The objective of Sect. 3 is to present a convenient constitutive setting on the basis of a general biphasic solid-fluid mixture which accounts for the coupled dissipative phenomena caused by the interplay of a viscous pore fluid streaming through a viscoelastic polymer skeleton. Therefore, a thermodynamically consistent biphasic TPM model is introduced and admissible constitutive equations for the description of the finite viscoelastic deformation habits of the cellular solid as well as the nonlinear percolation process of a general pore fluid are derived.

The numerical treatment of the viscoelastic two-phase model within the mixed Finite Element Method is shown in Sect. 4. To this end, the required weak formulations of the governing balance relations and their linearizations are presented, followed by appropriate techniques for the discretization in the space and the time domain including a convenient strategy for the treatment of the inelastic evolution equations. Finally, the algorithm for the nonlinear viscoelastic solid stress computation is described.

In Sect. 5, in order to demonstrate its practical applicability, the presented model is adapted for the description of a soft open-celled polyurethane (PUR) foam. Therefore, the model is correlated with experimental data by identifying the constitutively introduced material parameters with the help of the derivative-free optimization algorithm COBYLA. Finally, two numerical simulations are carried out to reveal the efficiency of the numerical implementation, the considerable influence of the pore fluid on the material response, and the overall applicability of the model to real engineering problems.

A final conclusion and discussion is given in the *last Section* including some statements on conceivable further developments and the future potential of the presented model in other disciplines, such as soft tissue biomechanics.

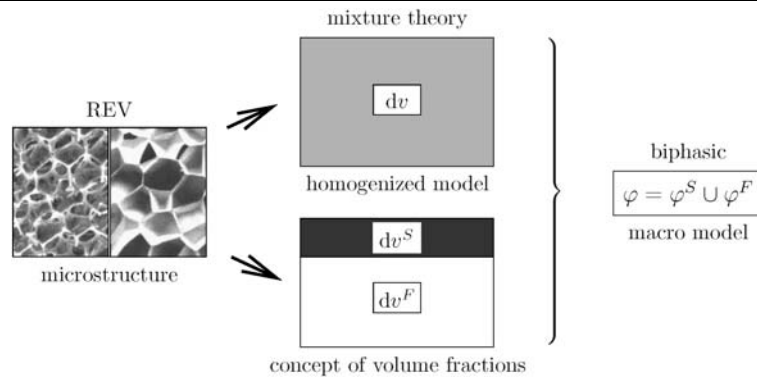
2 Theoretical Fundamentals

2.1 Theory of Porous Media

2.1.1 Macroscopic Mixture Approach

In the framework of the Theory of Porous Media, a fluid-saturated porous medium can be treated as an immiscible

Fig. 1 REV with exemplary microstructures of open (*left*) and closed-celled (*right*) polymer foams and the biphasic TPM macro model



binary mixture of constituents φ^α ($\alpha = S$: solid skeleton; $\alpha = F$: pore fluid) which are assumed to be in a state of ideal disarrangement. Following this, the prescription of a real or a virtual averaging process over a representative elementary volume (REV) leads to a macroscopic model $\varphi = \bigcup_\alpha \varphi^\alpha = \varphi^S \cup \varphi^F$ of superimposed and interacting continua (Fig. 1) where the incorporated physical quantities are then understood as the local averages of their microscopic representatives [42].

Regarding the notation, the constituent identifier $\alpha = \{S, F\}$ is used as subscript in case of kinematical and as superscript in case of non-kinematical quantities.

2.1.2 Volume Fractions and Density Functions

In order to account for the local composition of the mixture, local volumetric ratios are introduced according to the concept of volume fractions. The volume V of the overall medium \mathcal{B} results from the sum of the partial volumes V^α of the constituent bodies \mathcal{B}^α :

$$V = \int_{\mathcal{B}} dv = \sum_{\alpha} V^\alpha \quad \text{with} \quad V^\alpha = \int_{\mathcal{B}^\alpha} dv = \int_{\mathcal{B}} dv^\alpha =: \int_{\mathcal{B}} n^\alpha dv. \quad (1)$$

Following this, the volume fractions n^α of φ^α are defined as the local ratios of the partial volume elements dv^α with respect to the volume element dv of the whole mixture φ :

$$n^\alpha := \frac{dv^\alpha}{dv}, \quad \text{where} \quad \begin{cases} n^S : \text{solidity,} \\ n^F : \text{porosity.} \end{cases} \quad (2)$$

As a further consequence of (1), assuming fully saturated conditions, i.e., avoiding any vacant space within the porous medium, the saturation constraint yields

$$\sum_{\alpha} n^\alpha = n^S + n^F = 1. \quad (3)$$

Note that for some specific applications, where the pore fluid does not affect the mechanical properties of the porous

medium, such as a pore gas in a stiff metal foam, an empty (non-saturated) solid matrix can be assumed, i.e., $\varphi = \varphi^S$ yielding $\sum_{\alpha} n^\alpha = n^S < 1$.

Proceeding from the definition of the volume fractions (2), associated with each constituent φ^α is a material (realistic or effective) density $\rho^{\alpha R}$ defined as the local mass dm^α of φ^α per unit of dv^α and a partial density ρ^α where the local mass element dm^α is related to the bulk volume element dv . Moreover, the so-called mixture density can be introduced as the sum of the partial densities ρ^α . Thus, the density functions read

material density	partial density	mixture density
$\rho^{\alpha R} := \frac{dm^\alpha}{dv^\alpha}$	$\rho^\alpha := \frac{dm^\alpha}{dv}$	$\rho = \sum_{\alpha} \rho^\alpha \quad (4)$
$\begin{array}{ccc} \hookrightarrow & \rho^\alpha = n^\alpha \rho^{\alpha R} & \leftarrow \end{array}$		

By virtue of (4), it is obvious that the property of material incompressibility of a constituent φ^α (defined by $\rho^{\alpha R} = \text{const.}$) does not lead to macroscopic incompressibility as the partial density ρ^α and thus ρ can still change through changes in the volume fractions n^α .

Remark The fact that porous materials under drained conditions are in general macroscopically compressible even if the single constituents are materially (intrinsically) incompressible is one important issue that must be taken into account for the development of an appropriate material law for the solid skeleton. Moreover, it is convenient to proceed from a materially incompressible solid constituent in regard to the large bulk compressibility of the porous medium. However, in the finite strain regime proceeding from $\rho^{SR} = \text{const.}$, the macroscopic material formulation for the solid skeleton must restrict the maximum volumetric contraction to the compaction point given by $n^F = 0$ or $n^S = 1$, respectively, thereby describing the stiffening in the course of the densification of the material.

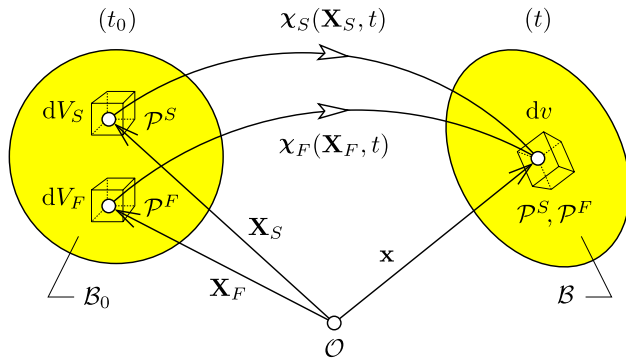


Fig. 2 Motion of a biphasic mixture. $dV_\alpha := dv_{0\alpha}$ is the reference bulk volume element w.r.t. an arbitrary initial state of the motion of φ^α at time t_0

2.2 Kinematical Relations

2.2.1 Mixture Kinematics

Concerning the kinematics of mixtures, the idea of superimposed and interacting continua implies that, starting from different reference positions $\mathbf{X}_\alpha := \mathbf{x}_{0\alpha}$ at time t_0 , each constituent follows its individual Lagrangean (material) motion function and has its own velocity and acceleration fields, viz.:

$$\mathbf{x} = \chi_\alpha(\mathbf{X}_\alpha, t), \quad \dot{\mathbf{x}}_\alpha = \frac{d\chi_\alpha(\mathbf{X}_\alpha, t)}{dt}, \quad \ddot{\mathbf{x}}_\alpha = \frac{d^2\chi_\alpha(\mathbf{X}_\alpha, t)}{dt^2}. \quad (5)$$

Following this, each spatial point \mathbf{x} of the current configuration at time t is simultaneously occupied by material points \mathcal{P}^α of both constituents (Fig 2). Unique individual motions χ_α of the material points \mathcal{P}^α require the existence of unique inverse motion functions based on non-singular functional determinants (Jacobians) J_α :

$$\mathbf{X}_\alpha = \chi_\alpha^{-1}(\mathbf{x}, t), \quad \text{if } J_\alpha := \det \frac{\partial \chi_\alpha(\mathbf{X}_\alpha, t)}{\partial \mathbf{X}_\alpha} \neq 0. \quad (6)$$

Thus, supposing that χ_α is a local diffeomorphism, χ_α^{-1} represents the inverse motion functions yielding the Eulerian (spatial) description of the velocity and acceleration fields as

$$\dot{\mathbf{x}}_\alpha = \dot{\mathbf{x}}_\alpha(\mathbf{x}, t), \quad \ddot{\mathbf{x}}_\alpha = \ddot{\mathbf{x}}_\alpha(\mathbf{x}, t). \quad (7)$$

Furthermore, by use of the mixture density ρ from (4), the so-called mixture velocity $\dot{\mathbf{x}}$ describing the barycentric velocity of the overall medium and the diffusion velocity \mathbf{d}_α describing the relative velocity of φ^α with respect to φ can be introduced as

$$\dot{\mathbf{x}} = \frac{1}{\rho} \sum_\alpha \rho^\alpha \dot{\mathbf{x}}_\alpha, \quad \mathbf{d}_\alpha = \dot{\mathbf{x}}_\alpha - \dot{\mathbf{x}} \quad \text{with} \quad \sum_\alpha \rho^\alpha \mathbf{d}_\alpha = \mathbf{0}. \quad (8)$$

In the above relations, $(\cdot)'_\alpha$ indicates the material time derivative following the motion of φ_α and $(\cdot)^*$ denotes the material time derivative following the barycentric motion of the whole mixture φ (mixture derivative). Suppose that Ψ and $\boldsymbol{\Psi}$ are arbitrary, steady and sufficiently steadily differentiable scalar- and vector-valued field functions. Then, the respective derivatives are computed as follows:

$$\begin{aligned} \dot{\Psi}_\alpha &= \frac{d_\alpha \Psi}{dt} = \frac{\partial \Psi}{\partial t} + \text{grad } \Psi \cdot \dot{\mathbf{x}}_\alpha, \\ \dot{\boldsymbol{\Psi}}_\alpha &= \frac{d_\alpha \boldsymbol{\Psi}}{dt} = \frac{\partial \boldsymbol{\Psi}}{\partial t} + (\text{grad } \boldsymbol{\Psi}) \dot{\mathbf{x}}_\alpha, \\ \dot{\Psi} &= \frac{d\Psi}{dt} = \frac{\partial \Psi}{\partial t} + \text{grad } \Psi \cdot \dot{\mathbf{x}}, \\ \dot{\boldsymbol{\Psi}} &= \frac{d\boldsymbol{\Psi}}{dt} = \frac{\partial \boldsymbol{\Psi}}{\partial t} + (\text{grad } \boldsymbol{\Psi}) \dot{\mathbf{x}}. \end{aligned} \quad (9)$$

Therein, the differential operator $\text{grad}(\cdot) := \partial(\cdot)/\partial \mathbf{x}$ denotes the partial derivative with respect to the actual position vector \mathbf{x} .

In porous media theories, it is generally convenient to proceed from a Lagrangean description of the solid matrix via the solid displacement vector \mathbf{u}_S as the primary kinematical variable. In contrast, according to Gibson et al. [61], the pore-fluid flow is better expressed in a modified Eulerian setting via the seepage velocity \mathbf{w}_{FR} describing the fluid motion relative to the deforming skeleton. Moreover, relating \mathbf{w}_{FR} only to the fluid part of the mixture, the so-called filter or superficial velocity \mathbf{w}_F can be introduced. Thus,

$$\mathbf{u}_S = \mathbf{x} - \mathbf{X}_S, \quad \mathbf{w}_{FR} = \mathbf{v}_F - \mathbf{v}_S \quad \text{with } \mathbf{v}_\alpha := \dot{\mathbf{x}}_\alpha, \quad \mathbf{w}_F = n^F \mathbf{w}_{FR}. \quad (10)$$

Given (5)₁ and (6)₁, the material deformation gradients and their inverses are defined by

$$\mathbf{F}_\alpha = \frac{\partial \mathbf{x}}{\partial \mathbf{X}_\alpha} =: \text{Grad}_\alpha \mathbf{x}, \quad \mathbf{F}_\alpha^{-1} = \frac{\partial \mathbf{X}_\alpha}{\partial \mathbf{x}} = \text{grad } \mathbf{X}_\alpha, \quad (11)$$

where the gradient operator $\text{Grad}_\alpha(\cdot) := \partial(\cdot)/\partial \mathbf{X}_\alpha$ denotes the partial derivative with respect to the reference position vector \mathbf{X}_α . Particularly, the solid deformation gradient \mathbf{F}_S as a basic kinematical quantity of the large strain regime can be expressed in terms of the solid displacement using (10)₁:

$$\mathbf{F}_S = \frac{\partial \mathbf{x}}{\partial \mathbf{X}_S} = \text{Grad}_S \mathbf{x} = \mathbf{I} + \text{Grad}_S \mathbf{u}_S. \quad (12)$$

According to (6), the existence of uniquely invertible motions requires non-zero Jacobians J_α . Starting the deformation process from an undeformed (natural) state at time t_0 , the initial condition $\mathbf{F}_\alpha(t_0) = \mathbf{I}$ restricts the domain of $\det \mathbf{F}_\alpha$ to positive values

$$\det \mathbf{F}_\alpha = J_\alpha > 0 \quad \text{with } \det \mathbf{F}_\alpha(t_0) = 1. \quad (13)$$

Moreover, following the remark on page 376, the assumption of solid incompressibility ($\rho^{SR} = \text{const.}$) implies that volumetric compression is only possible until the pore space is completely closed ($n^F = 0$). Therefore, the lower limit of the finite volume dilatation e_{VS} of the solid matrix is predefined by the initial porosity n_{0S}^F , i.e.,

$$e_{VS} = \frac{dv - dV_S}{dV_S} = \det \mathbf{F}_S - 1 > -n_{0S}^F, \quad (14)$$

thus, directly yielding the stronger restriction

$$\det \mathbf{F}_S = J_S > n_{0S}^S \quad \text{with } n_{0S}^S = 1 - n_{0S}^F. \quad (15)$$

Therein, the transport property, $dv = (\det \mathbf{F}_S) dV_S$, of $\det \mathbf{F}_S$ is used (cf. (24)) describing the finite volume change of the reference volume element $dV_S = dv_{0S}$ to the volume element dv of the current configuration (Fig. 2). Furthermore, $(\cdot)_{0S}$ indicates initial values with respect to an undeformed solid state at time t_0 . In particular, $n_{0S}^S = dV_S^S/dV_S$ and $n_{0S}^F = dV_S^F/dV_S$ are the initial solidity and porosity consistent with (3).

2.2.2 Inelastic Solid Kinematics

For the description of the intrinsic relaxation and creep behavior, at first, the basic frame for the inelastic kinematics of the solid skeleton must be provided. As mentioned in the introduction, benefiting from finite viscoelasticity of single-phase materials, the fundamental approach is principally based on the rheological structure of the generalized Maxwell model ($1+2N$ element viscoelastic solid) depicted in Fig. 3. This parallel assembly of one Hooke element (elastic spring) and N Maxwell elements (spring and dashpot in series) directly implies the internal variable concept with the dashpot deformations as the independently developing strain-equivalent internal variables.

Proceeding from initially unitary lengths and cross-sections of the massless rheological elements, such that stresses and strains can be treated like forces and displacements, the $n = 1, \dots, N$ parallel Maxwell branches meet the following kinematics:

$$\begin{aligned} \varepsilon_S &= (\varepsilon_{Se})_n + (\varepsilon_{Si})_n \\ (\varepsilon_S)'_S &= [(\varepsilon_{Se})'_S]_n + [(\varepsilon_{Si})'_S]_n \\ \xrightarrow{\text{3-d}} \quad \begin{cases} \boldsymbol{\varepsilon}_S = (\boldsymbol{\varepsilon}_{Se})_n + (\boldsymbol{\varepsilon}_{Si})_n, \\ (\boldsymbol{\varepsilon}_S)'_S = [(\boldsymbol{\varepsilon}_{Se})'_S]_n + [(\boldsymbol{\varepsilon}_{Si})'_S]_n. \end{cases} \end{aligned} \quad (16)$$

These additive decompositions of the total solid strain ε_S as well as the total solid strain rate $(\varepsilon_S)'_S$ into elastic parts $(\varepsilon_{Se})_n$ and $[(\varepsilon_{Se})'_S]_n$ and inelastic parts $(\varepsilon_{Si})_n$ and $[(\varepsilon_{Si})'_S]_n$, respectively, can be straightforwardly transferred to the 3-d infinitesimal theory. Therefore, the scalar quantities must be

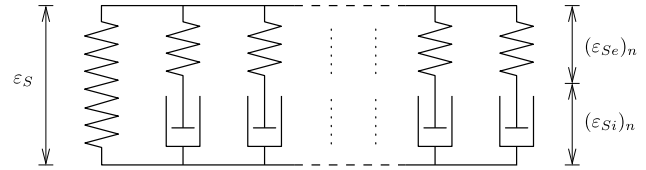


Fig. 3 Kinematics of the generalized Maxwell model

replaced with their corresponding tensorial counterparts. In particular, the geometric linear total strain and total strain rate tensors of φ^S read

$$\begin{aligned} \boldsymbol{\varepsilon}_S &= \frac{1}{2} (\text{Grad}_S \mathbf{u}_S + \text{Grad}_S^T \mathbf{u}_S), \\ (\boldsymbol{\varepsilon}_S)'_S &= \frac{1}{2} (\text{Grad}_S \mathbf{v}_S + \text{Grad}_S^T \mathbf{v}_S) \end{aligned} \quad (17)$$

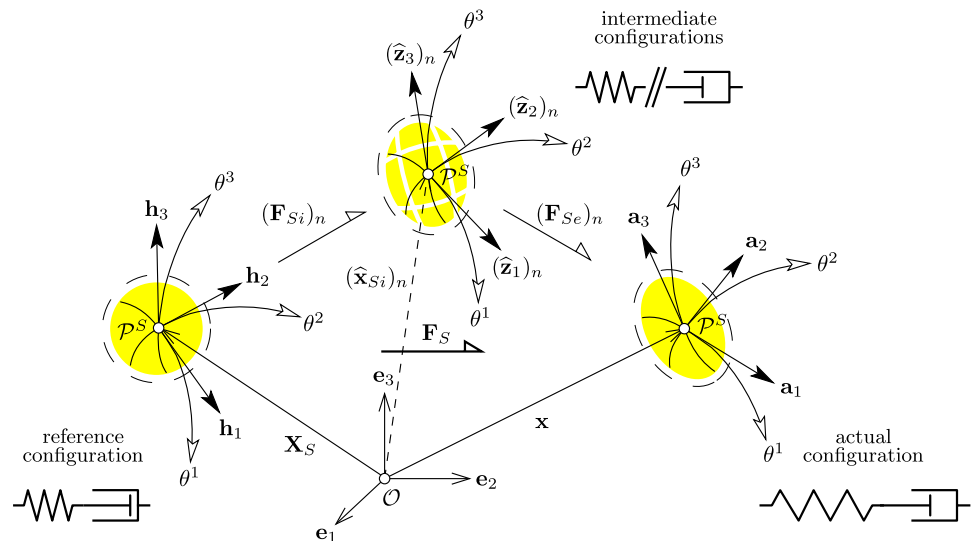
with $\mathbf{v}_S = (\mathbf{u}_S)'_S = \dot{\mathbf{x}}_S$ representing the solid velocity vector (see also (134)).

In the framework of a finite deformation theory of porous materials with elastic and inelastic behavior, it is convenient to proceed from a local multiplicative split of the solid deformation gradient

$$\mathbf{F}_S = (\mathbf{F}_{Se})_n (\mathbf{F}_{Si})_n, \quad n = 1, \dots, N \quad (18)$$

into elastic parts $(\mathbf{F}_{Se})_n$ and inelastic parts $(\mathbf{F}_{Si})_n$. From elastoplasticity, it is commonly known that the concept of the multiplicative decomposition of deformation gradients is connected with the notion of a locally unloaded, stress-free intermediate configuration where the purely inelastic state of deformation is frozen into the memory of the material [77]. In viscoelasticity, from a rheological point of view, in the intermediate states, the springs in the Maxwell models are assumed to be completely relaxed (i.e., stress-free), e.g., due to a virtual cut of the model, while the dashpot deformations remain (Fig. 4). Due to the independent local unloading (elastic release via $(\mathbf{F}_{Se}^{-1})_n$) of the usually non-uniformly strained solid skeleton at adjacent material points \mathcal{P}^S , the intermediate configurations are geometrically incompatible unless in the special case of homogeneous deformations. Thus, $(\mathbf{F}_{Se})_n$ and $(\mathbf{F}_{Si})_n$ generally do not have the character of gradient field functions; however, they are commonly termed elastic and inelastic deformation gradients, which will, for convenience, also be retained in this contribution. Moreover, note that the multiplicative decompositions (18) are not unique but can only be determined up to superposed rigid-body rotations. Therefore, $(\mathbf{F}_{Se})_n$ and $(\mathbf{F}_{Si})_n$, respectively, must be regarded as representatives of the class of admissible decompositions, see, e.g., [124]. However, in this contribution, the multiplicative decompositions of the solid deformation gradient (18) are phenomenologically introduced without insisting on somehow abstract and somewhat controversial interpretations. Instead, they are understood as constitutive definitions that will consequently

Fig. 4 Solid configurations with covariant local basis systems



yield the additive decompositions of finite strain measures into elastic and inelastic parts, and thus, directly reflect the structure of the underlying rheological model in Fig. 3.

In preparation for a comprehensible introduction of the finite inelastic deformation and strain measures and their spatiotemporal derivatives, it is an elegant alternative to describe the solid configurations within a local curvilinear frame (natural basis representation) with respect to a globally fixed Cartesian basis system $\{O; \mathbf{e}_k\}$, see Fig. 4. The curvilinear coordinates $\theta^k = \theta^k(\mathbf{x}, t)$ are assumed to continuously follow the deforming material lines at each ma-

terial point \mathcal{P}^S of the solid skeleton body \mathcal{B}^S in the sense of *convective coordinates*, cf. [70]. Consequently, together with the position vectors of the reference, intermediate, and actual configurations

$$\begin{aligned} \mathbf{X}_S &= X_S^l(\theta^k, t_0) \mathbf{e}_l, & (\hat{\mathbf{x}}_{Si})_n &= (\hat{x}_{Si}^l)_n(\theta^k, t) \mathbf{e}_l, \\ \mathbf{x} &= x^l(\theta^k, t) \mathbf{e}_l, \end{aligned} \quad (19)$$

the following tangential covariant and dual (reciprocal) contravariant local basis vectors can be defined:

covariant bases	configurations	contravariant bases
$\mathbf{h}_k := \frac{\partial \mathbf{X}_S}{\partial \theta^k} = \frac{\partial X_S^l}{\partial \theta^k} \mathbf{e}_l$	reference	$\mathbf{h}^k := \frac{\partial \theta^k}{\partial \mathbf{X}_S} = \frac{\partial \theta^k}{\partial X_S^l} \mathbf{e}_l$
$(\hat{\mathbf{z}}_k)_n := \frac{\partial (\hat{\mathbf{x}}_{Si})_n}{\partial \theta^k} = \frac{\partial (\hat{x}_{Si}^l)_n}{\partial \theta^k} \mathbf{e}_l$	intermediate	$(\hat{\mathbf{z}}^k)_n := \frac{\partial \theta^k}{\partial (\hat{\mathbf{x}}_{Si})_n} = \frac{\partial \theta^k}{\partial (\hat{x}_{Si}^l)_n} \mathbf{e}_l$
$\mathbf{a}_k := \frac{\partial \mathbf{x}}{\partial \theta^k} = \frac{\partial x^l}{\partial \theta^k} \mathbf{e}_l$	actual	$\mathbf{a}^k := \frac{\partial \theta^k}{\partial \mathbf{x}} = \frac{\partial \theta^k}{\partial x^l} \mathbf{e}_l$

Herein, (\cdot) indicates the belonging to the inelastic intermediate configurations. For the sake of clarity, the solid constituent identifier $(\cdot)_S$ is omitted in connection with the natural bases. In the sequel, tensorial objects are called co- or contravariant depending on the variant type of the basis vectors included in their components (cf. [29, 63, 108]).

Now, the introduced material deformation gradients and their inverses can be expressed in terms of the natural basis vectors (20), viz.:

$$\begin{aligned} \mathbf{F}_S &= \text{Grad}_S \mathbf{x} = \frac{\partial \mathbf{x}}{\partial \mathbf{X}_S} = \frac{\partial \mathbf{x}}{\partial \theta^k} \otimes \frac{\partial \theta^k}{\partial \mathbf{X}_S} = \mathbf{a}_k \otimes \mathbf{h}^k, \\ \mathbf{F}_S^{-1} &= \text{grad} \mathbf{X}_S = \frac{\partial \mathbf{X}_S}{\partial \mathbf{x}} = \frac{\partial \mathbf{X}_S}{\partial \theta^k} \otimes \frac{\partial \theta^k}{\partial \mathbf{x}} = \mathbf{h}_k \otimes \mathbf{a}^k, \\ (\mathbf{F}_{Se})_n &= (\text{grad}_{Si} \mathbf{x})_n = \frac{\partial \mathbf{x}}{\partial (\hat{\mathbf{x}}_{Si})_n} = \frac{\partial \mathbf{x}}{\partial \theta^k} \otimes \frac{\partial \theta^k}{\partial (\hat{\mathbf{x}}_{Si})_n} \\ &= \mathbf{a}_k \otimes (\hat{\mathbf{z}}^k)_n, \end{aligned}$$

$$\begin{aligned}
(\mathbf{F}_{Se}^{-1})_n &= \text{grad}(\widehat{\mathbf{x}}_{Si})_n = \frac{\partial(\widehat{\mathbf{x}}_{Si})_n}{\partial \mathbf{x}} = \frac{\partial(\widehat{\mathbf{x}}_{Si})_n}{\partial \theta^k} \otimes \frac{\partial \theta^k}{\partial \mathbf{x}} \\
&= (\widehat{\mathbf{z}}_k)_n \otimes \mathbf{a}^k, \\
(\mathbf{F}_{Si})_n &= \text{Grad}_S(\widehat{\mathbf{x}}_{Si})_n = \frac{\partial(\widehat{\mathbf{x}}_{Si})_n}{\partial \mathbf{X}_S} = \frac{\partial(\widehat{\mathbf{x}}_{Si})_n}{\partial \theta^k} \otimes \frac{\partial \theta^k}{\partial \mathbf{X}_S} \\
&= (\widehat{\mathbf{z}}_k)_n \otimes \mathbf{h}^k, \\
(\mathbf{F}_{Si}^{-1})_n &= (\text{grad}_{Si} \mathbf{X}_S)_n = \frac{\partial \mathbf{X}_S}{\partial(\widehat{\mathbf{x}}_{Si})_n} = \frac{\partial \mathbf{X}_S}{\partial \theta^k} \otimes \frac{\partial \theta^k}{\partial(\widehat{\mathbf{x}}_{Si})_n} \\
&= \mathbf{h}_k \otimes (\widehat{\mathbf{z}}^k)_n. \quad (21)
\end{aligned}$$

Therein, $(\text{grad}_{Si}(\cdot))_n := \partial(\cdot)/\partial(\widehat{\mathbf{x}}_{Si})_n$ represent *fictitious* gradient operators with respect to the position vectors of the intermediate configurations. The term *fictitious* should emphasize that, in the inhomogeneous case, the $(\widehat{\mathbf{z}}_k)_n$ and $(\widehat{\mathbf{z}}^k)_n$, respectively, are not necessarily defined by some gradient-type equations since gradients with respect to $(\widehat{\mathbf{x}}_{Si})_n$ as well as the inverse relations, in general, do not exist. More precisely, from a geometrical perspective, the intermediate configurations represent a 3-d proper Riemannian manifold of material points \mathcal{P}^S [124] with the intermediate metric coefficients $(\widehat{z}_{kl})_n = (\widehat{\mathbf{z}}_k)_n \cdot (\widehat{\mathbf{z}}_l)_n$ as the carrier of the geometric characteristics violating certain compatibility or integrability conditions [70, 108]. However, every Riemannian structure is locally flat (no curvature), i.e., Euclidean. Accordingly, the introduction of local tangent (covariant) and cotangent (contravariant) Euclidean bases in \mathcal{P}^S almost promotes the presented approach to the inelastic intermediate configurations.

From (21), it is easy to recognize that, in terms of natural bases, the deformation gradients are mixed-variant, two-field or two-point tensors with identity metric, which directly implies their special property of acting as transport mechanisms between configurations, cf. [54, Sect. III]. This becomes clearer by applying \mathbf{F}_S and \mathbf{F}_S^{-1} as linear mappings to the covariant basis vectors \mathbf{h}_l and \mathbf{a}_l of the reference and the actual configuration, respectively. Thus, from the mutual reciprocity of co- and contravariant bases, it follows

$$\begin{aligned}
\mathbf{F}_S \mathbf{h}_l &= (\mathbf{a}_k \otimes \mathbf{h}^k) \mathbf{h}_l = \mathbf{a}_k \delta_l^k = \mathbf{a}_l, \\
\mathbf{F}_S^{-1} \mathbf{a}_l &= (\mathbf{h}_k \otimes \mathbf{a}^k) \mathbf{a}_l = \mathbf{h}_k \delta_l^k = \mathbf{h}_l, \quad (22)
\end{aligned}$$

where δ_l^k is the Kronecker symbol. The transformations $(22)_1$ and $(22)_2$ are commonly known as covariant *push-forward* (reference \rightarrow actual) and *pull-back* (actual \rightarrow reference) operations. The respective contravariant transport mechanisms are simply given by applying the transposes of \mathbf{F}_S^{-1} and \mathbf{F}_S to the contravariant basis vectors \mathbf{h}^l and \mathbf{a}^l :

$$\begin{aligned}
\mathbf{F}_S^{T-1} \mathbf{h}^l &= (\mathbf{h}_k \otimes \mathbf{a}^k)^T \mathbf{h}^l = (\mathbf{a}^k \otimes \mathbf{h}_k) \mathbf{h}^l = \mathbf{a}^k \delta_k^l = \mathbf{a}^l, \\
\mathbf{F}_S^T \mathbf{a}^l &= (\mathbf{a}_k \otimes \mathbf{h}^k)^T \mathbf{a}^l = (\mathbf{h}^k \otimes \mathbf{a}_k) \mathbf{a}^l = \mathbf{h}^k \delta_k^l = \mathbf{h}^l. \quad (23)
\end{aligned}$$

Following this, the transport mechanisms of material line, oriented area, and scalar volume elements of φ^S can be formulated:

$$\begin{aligned}
d\mathbf{x}_{(k)} &= \mathbf{a}_k d\theta^k = \mathbf{F}_S \mathbf{h}_k d\theta^k = \mathbf{F}_S d\mathbf{X}_{S(k)}, \\
d\mathbf{a}_{(k)} &= d\mathbf{x}_{(l)} \times d\mathbf{x}_{(m)} = \text{cof} \mathbf{F}_S (d\mathbf{X}_{S(l)} \times d\mathbf{X}_{S(m)}) \\
&= \text{cof} \mathbf{F}_S d\mathbf{A}_{S(k)}, \quad (24) \\
dv &= (d\mathbf{x}_{(k)} \times d\mathbf{x}_{(l)}) \cdot d\mathbf{x}_{(m)} \\
&= \det \mathbf{F}_S (d\mathbf{X}_{S(k)} \times d\mathbf{X}_{S(l)}) \cdot d\mathbf{X}_{S(m)} = \det \mathbf{F}_S dV_S.
\end{aligned}$$

Herein, $d\mathbf{X}_{S(k)} := d\mathbf{x}_{0S(k)}$, $d\mathbf{x}_{(k)}$ and $d\mathbf{A}_{S(k)} = \mathbf{n}_{0S(k)} dA_{S(k)}$, $d\mathbf{a}_{(k)} = \mathbf{n}_{(k)} da_{(k)}$ denote the covariant line and the contravariant area elements of the reference and the actual configuration with $dA_{S(k)} := da_{0S(k)}$ and $da_{(k)}$ as the scalar area elements, and $\mathbf{n}_{0S(k)}$ and $\mathbf{n}_{(k)}$ as the corresponding reference and actual outward oriented unit surface normals.

Next, the transport properties of the gradient operator are discussed. Proceeding from the natural basis representations of the material deformation gradients (21), depending on the type of the differentiable field function, the following contravariant transport mechanisms are apparent:

$$\begin{aligned}
\text{Grad}_S \Psi &= \frac{\partial \Psi}{\partial \mathbf{X}_S} = \frac{\partial \Psi}{\partial \theta^k} \mathbf{h}^k \\
&\xrightarrow[\mathbf{F}_S^T]{\mathbf{F}_S^{T-1}} \frac{\partial \Psi}{\partial \theta^k} \mathbf{a}^k = \frac{\partial \Psi}{\partial \mathbf{x}} = \text{grad} \Psi, \\
\text{Grad}_S \Psi &= \frac{\partial \Psi}{\partial \mathbf{X}_S} = \frac{\partial \Psi}{\partial \theta^k} \otimes \mathbf{h}^k \quad (25) \\
&\xrightarrow[\mathbf{F}_S^T]{(\mathbf{I} \otimes \mathbf{F}_S^{T-1})^T} \frac{\partial \Psi}{\partial \theta^k} \otimes \mathbf{a}^k = \frac{\partial \Psi}{\partial \mathbf{x}} = \text{grad} \Psi.
\end{aligned}$$

Herein, $(\cdot)^{kl}$ indicates an exchange of the k th and the l th basis vector included in the polyadic components of higher-order tensors. Following this, with the common rules of tensor calculus, transport mechanisms for tensors of arbitrary order can be defined including the inelastic and elastic transformations in the framework of the multiplicative geometric concept. A summary of the required co- and contravariant push-forward and pull-back operations is given in Appendix A.1.

To continue, based on the multiplicative decomposition of \mathbf{F}_S (18) with restriction to $N = 1$, the following right and

left Cauchy-Green deformation tensors can be defined:

$$\begin{aligned}\mathbf{C}_S &= \mathbf{F}_S^T \mathbf{F}_S = a_{kl} \mathbf{h}^k \otimes \mathbf{h}^l, \\ \mathbf{B}_S &= \mathbf{F}_S \mathbf{F}_S^T = h^{kl} \mathbf{a}_k \otimes \mathbf{a}_l, \\ \widehat{\mathbf{C}}_{Se} &= \mathbf{F}_{Se}^T \mathbf{F}_{Se} = a_{kl} \widehat{\mathbf{z}}^k \otimes \widehat{\mathbf{z}}^l, \\ \mathbf{B}_{Se} &= \mathbf{F}_{Se} \mathbf{F}_{Se}^T = \widehat{z}^{kl} \mathbf{a}_k \otimes \mathbf{a}_l, \\ \mathbf{C}_{Si} &= \mathbf{F}_{Si}^T \mathbf{F}_{Si} = \widehat{z}_{kl} \mathbf{h}^k \otimes \mathbf{h}^l, \\ \widehat{\mathbf{B}}_{Si} &= \mathbf{F}_{Si} \mathbf{F}_{Si}^T = h^{kl} \widehat{\mathbf{z}}_k \otimes \widehat{\mathbf{z}}_l.\end{aligned}\quad (26)$$

The corresponding inverse relations read:

$$\begin{aligned}\mathbf{C}_S^{-1} &= \mathbf{F}_S^{-1} \mathbf{F}_S^{T-1} = a^{kl} \mathbf{h}_k \otimes \mathbf{h}_l, \\ \mathbf{B}_S^{-1} &= \mathbf{F}_S^{T-1} \mathbf{F}_S^{-1} = h_{kl} \mathbf{a}^k \otimes \mathbf{a}^l, \\ \widehat{\mathbf{C}}_{Se}^{-1} &= \mathbf{F}_{Se}^{-1} \mathbf{F}_{Se}^{T-1} = a^{kl} \widehat{\mathbf{z}}_k \otimes \widehat{\mathbf{z}}_l, \\ \mathbf{B}_{Se}^{-1} &= \mathbf{F}_{Se}^{T-1} \mathbf{F}_{Se}^{-1} = \widehat{z}_{kl} \mathbf{a}^k \otimes \mathbf{a}^l, \\ \mathbf{C}_{Si}^{-1} &= \mathbf{F}_{Si}^{-1} \mathbf{F}_{Si}^{T-1} = \widehat{z}^{kl} \mathbf{h}_k \otimes \mathbf{h}_l, \\ \widehat{\mathbf{B}}_{Si}^{-1} &= \mathbf{F}_{Si}^{T-1} \mathbf{F}_{Si}^{-1} = h_{kl} \widehat{\mathbf{z}}^k \otimes \widehat{\mathbf{z}}^l.\end{aligned}\quad (27)$$

Then, by formally introducing the contravariant Green-Lagrange and Almansi strain tensors, the following additive relations hold:

$$\begin{aligned}\mathbf{E}_S &= \mathbf{E}_{Se} + \mathbf{E}_{Si} = \frac{1}{2} (\mathbf{C}_S - \mathbf{I}) = \frac{1}{2} (a_{kl} - h_{kl}) \mathbf{h}^k \otimes \mathbf{h}^l, \\ \widehat{\mathbf{\Gamma}}_S &= \widehat{\mathbf{\Gamma}}_{Se} + \widehat{\mathbf{\Gamma}}_{Si} = \frac{1}{2} (\widehat{\mathbf{C}}_{Se} - \widehat{\mathbf{B}}_{Si}^{-1}) = \frac{1}{2} (a_{kl} - h_{kl}) \widehat{\mathbf{z}}^k \otimes \widehat{\mathbf{z}}^l, \\ \mathbf{A}_S &= \mathbf{A}_{Se} + \mathbf{A}_{Si} = \frac{1}{2} (\mathbf{I} - \mathbf{B}_S^{-1}) = \frac{1}{2} (a_{kl} - h_{kl}) \mathbf{a}^k \otimes \mathbf{a}^l.\end{aligned}\quad (28)$$

Analogously, the class of covariant Kani-Reiner strain tensors is introduced:

$$\begin{aligned}\mathbf{K}_S^R &= \mathbf{K}_{Se}^R + \mathbf{K}_{Si}^R = \frac{1}{2} (\mathbf{I} - \mathbf{C}_S^{-1}) = \frac{1}{2} (h^{kl} - a^{kl}) \mathbf{h}_k \otimes \mathbf{h}_l, \\ \widehat{\mathbf{K}}_S &= \widehat{\mathbf{K}}_{Se} + \widehat{\mathbf{K}}_{Si} = \frac{1}{2} (\widehat{\mathbf{B}}_{Si} - \widehat{\mathbf{C}}_{Se}^{-1}) = \frac{1}{2} (h^{kl} - a^{kl}) \widehat{\mathbf{z}}_k \otimes \widehat{\mathbf{z}}_l, \\ \mathbf{K}_S &= \mathbf{K}_{Se} + \mathbf{K}_{Si} = \frac{1}{2} (\mathbf{B}_S - \mathbf{I}) = \frac{1}{2} (h^{kl} - a^{kl}) \mathbf{a}_k \otimes \mathbf{a}_l.\end{aligned}\quad (29)$$

Note that in this representation only the tensorial bases account for the difference of related strain measures while the metric coefficients are identical. A summary of the co- and contravariant strain tensors and their transport mechanisms is given in Appendix A.2.

In order to formulate rate equations, time derivatives of the introduced deformation and strain measures are re-

quired. Proceeding from the material solid velocity gradient

$$\begin{aligned}(\mathbf{F}_S)'_S &= \frac{d_S}{dt} \left(\frac{\partial \mathbf{x}}{\partial \mathbf{X}_S} \right) = \frac{\partial \dot{\mathbf{x}}_S}{\partial \mathbf{X}_S} = \frac{\partial \dot{\mathbf{x}}_S}{\partial \theta^k} \otimes \frac{\partial \theta^k}{\partial \mathbf{X}_S} = (\mathbf{a}_k)'_S \otimes \mathbf{h}^k \\ &= \text{Grad}_S \dot{\mathbf{x}}_S = \frac{\partial \dot{\mathbf{x}}_S}{\partial \mathbf{x}} \frac{\partial \mathbf{x}}{\partial \mathbf{X}_S} =: \mathbf{L}_S \mathbf{F}_S,\end{aligned}\quad (30)$$

the spatial solid velocity gradient is given by

$$\begin{aligned}\mathbf{L}_S &:= \text{grad} \dot{\mathbf{x}}_S = \frac{\partial \dot{\mathbf{x}}_S}{\partial \mathbf{x}} = \frac{\partial \dot{\mathbf{x}}_S}{\partial \mathbf{X}_S} \frac{\partial \mathbf{X}_S}{\partial \mathbf{x}} = (\mathbf{F}_S)'_S \mathbf{F}_S^{-1} \\ &= [(\mathbf{a}_k)'_S \otimes \mathbf{h}^k] \mathbf{F}_S^{-1} = (\mathbf{a}_k)'_S \otimes \mathbf{F}_S^{T-1} \mathbf{h}^k \\ &= (\mathbf{a}_k)'_S \otimes \mathbf{a}^k.\end{aligned}\quad (31)$$

Additionally, following the multiplicative geometric concept (18), local inelastic material and spatial solid velocity gradients, can be introduced:

$$\begin{aligned}(\mathbf{F}_{Si})'_S &= \frac{d_S}{dt} \left(\frac{\partial \widehat{\mathbf{x}}_{Si}}{\partial \mathbf{X}_S} \right) = \frac{\partial (\widehat{\mathbf{x}}_{Si})'_S}{\partial \mathbf{X}_S} \\ &= \frac{\partial (\widehat{\mathbf{x}}_{Si})'_S}{\partial \theta^k} \otimes \frac{\partial \theta^k}{\partial \mathbf{X}_S} = (\widehat{\mathbf{z}}_k)'_S \otimes \mathbf{h}^k \\ &= \text{Grad}_S (\widehat{\mathbf{x}}_{Si})'_S \\ &= \frac{\partial (\widehat{\mathbf{x}}_{Si})'_S}{\partial \widehat{\mathbf{x}}_{Si}} \frac{\partial \widehat{\mathbf{x}}_{Si}}{\partial \mathbf{X}_S} =: \widehat{\mathbf{L}}_{Si} \mathbf{F}_{Si},\end{aligned}\quad (32)$$

$$\begin{aligned}\widehat{\mathbf{L}}_{Si} &:= \text{grad}_{Si} (\widehat{\mathbf{x}}_{Si})'_S = \frac{\partial (\widehat{\mathbf{x}}_{Si})'_S}{\partial \widehat{\mathbf{x}}_{Si}} \\ &= \frac{\partial (\widehat{\mathbf{x}}_{Si})'_S}{\partial \mathbf{X}_S} \frac{\partial \mathbf{X}_S}{\partial \widehat{\mathbf{x}}_{Si}} = (\mathbf{F}_{Si})'_S \mathbf{F}_{Si}^{-1} \\ &= [(\widehat{\mathbf{z}}_k)'_S \otimes \mathbf{h}^k] \mathbf{F}_{Si}^{-1} = (\widehat{\mathbf{z}}_k)'_S \otimes \mathbf{F}_{Si}^{T-1} \mathbf{h}^k \\ &= (\widehat{\mathbf{z}}_k)'_S \otimes \widehat{\mathbf{z}}^k.\end{aligned}\quad (33)$$

From the above together with the identities

$$\left. \begin{aligned}(\mathbf{F}_S \mathbf{F}_S^{-1})'_S &= \mathbf{0} \\ (\mathbf{F}_{Si} \mathbf{F}_{Si}^{-1})'_S &= \mathbf{0}\end{aligned} \right\} \longrightarrow \left\{ \begin{aligned}\mathbf{L}_S &= -\mathbf{L}_S^{-1} = -\mathbf{a}_k \otimes (\mathbf{a}^k)'_S, \\ \widehat{\mathbf{L}}_{Si} &= -\widehat{\mathbf{L}}_{Si}^{-1} = -\widehat{\mathbf{z}}_k \otimes (\widehat{\mathbf{z}}^k)'_S,\end{aligned} \right.\quad (34)$$

provided that the inverses $[(\mathbf{F}_S)'_S]^{-1}$ and $[(\mathbf{F}_{Si})'_S]^{-1}$ exist, it is directly concluded that

$$\begin{aligned}(\mathbf{a}_k)'_S &= \mathbf{L}_S \mathbf{a}_k = (\mathbf{F}_S)'_S \mathbf{h}_k, \\ (\mathbf{a}^k)'_S &= -\mathbf{L}_S^T \mathbf{a}^k = (\mathbf{F}_S^{T-1})'_S \mathbf{h}^k, \\ (\widehat{\mathbf{z}}_k)'_S &= \widehat{\mathbf{L}}_{Si} \widehat{\mathbf{z}}_k = (\mathbf{F}_{Si})'_S \mathbf{h}_k, \\ (\widehat{\mathbf{z}}^k)'_S &= -\widehat{\mathbf{L}}_{Si}^T \widehat{\mathbf{z}}^k = (\mathbf{F}_{Si}^{T-1})'_S \mathbf{h}^k.\end{aligned}\quad (35)$$

In this context, note that the introduction of an elastic spatial solid velocity gradient \mathbf{L}_{Se} is somehow artificial as it cannot be associated with a reasonable physical meaning comparable to the relations (35) (see also [39]). Moreover, following the above, the material time derivatives of the infinitesimal material elements (24) can be expressed as

$$\begin{aligned} (d\mathbf{x})'_S &= \mathbf{L}_S d\mathbf{x}, & (d\mathbf{a})'_S &= (\mathbf{L}_S \otimes \mathbf{I}) d\mathbf{a}, \\ (d\mathbf{v})'_S &= (\mathbf{L}_S \cdot \mathbf{I}) d\mathbf{v} \end{aligned} \quad (36)$$

with “ \otimes ” denoting the outer (double cross) tensor product of tensors, cf. [29]. The symmetric and skew-symmetric parts of \mathbf{L}_S and $\widehat{\mathbf{L}}_{Si}$, commonly termed total and inelastic solid stretching or deformation rate and solid spin or vorticity tensors, read:

$$\begin{aligned} \mathbf{D}_S &= \frac{1}{2} (\mathbf{L}_S + \mathbf{L}_S^T) = \mathbf{D}_S^T, \\ \widehat{\mathbf{D}}_{Si} &= \frac{1}{2} (\widehat{\mathbf{L}}_{Si} + \widehat{\mathbf{L}}_{Si}^T) = \widehat{\mathbf{D}}_{Si}^T, \\ \mathbf{W}_S &= \frac{1}{2} (\mathbf{L}_S - \mathbf{L}_S^T) = -\mathbf{W}_S^T, \\ \widehat{\mathbf{W}}_{Si} &= \frac{1}{2} (\widehat{\mathbf{L}}_{Si} - \widehat{\mathbf{L}}_{Si}^T) = -\widehat{\mathbf{W}}_{Si}^T. \end{aligned} \quad (37)$$

In terms of natural bases, a special property of the deformation rates \mathbf{D}_S and $\widehat{\mathbf{D}}_{Si}$ emerges. Apparently, they admit a co- and a contravariant form in the frame of convected coordinates with the material time derivative acting only on the time-dependent metric coefficients:

$$\begin{aligned} \mathbf{D}_S &= -\frac{1}{2} (a^{kl})'_S \mathbf{a}_k \otimes \mathbf{a}_l = \frac{1}{2} (a_{kl})'_S \mathbf{a}^k \otimes \mathbf{a}^l, \\ \widehat{\mathbf{D}}_{Si} &= -\frac{1}{2} (\widehat{z}^{kl})'_S \widehat{\mathbf{z}}_k \otimes \widehat{\mathbf{z}}_l = \frac{1}{2} (\widehat{z}_{kl})'_S \widehat{\mathbf{z}}^k \otimes \widehat{\mathbf{z}}^l. \end{aligned} \quad (38)$$

Moreover, one finds

$$\begin{aligned} \mathbf{D}_S &= -\frac{1}{2} \mathbf{F}_S (\mathbf{C}_S^{-1})'_S \mathbf{F}_S^T = \frac{1}{2} \mathbf{F}_S^{T-1} (\mathbf{C}_S)'_S \mathbf{F}_S^{-1}, \\ \widehat{\mathbf{D}}_{Si} &= -\frac{1}{2} \mathbf{F}_{Si} (\mathbf{C}_{Si}^{-1})'_{Si} \mathbf{F}_{Si}^T = \frac{1}{2} \mathbf{F}_{Si}^{T-1} (\mathbf{C}_{Si})'_S \mathbf{F}_{Si}^{-1} \end{aligned} \quad (39)$$

with

$$\begin{aligned} (\mathbf{C}_S^{-1})'_S &= (a^{kl})'_S \mathbf{h}_k \otimes \mathbf{h}_l, & (\mathbf{C}_S)'_S &= (a_{kl})'_S \mathbf{h}^k \otimes \mathbf{h}^l, \\ (\mathbf{C}_{Si}^{-1})'_S &= (\widehat{z}^{kl})'_S \mathbf{h}_k \otimes \mathbf{h}_l, & (\mathbf{C}_{Si})'_S &= (\widehat{z}_{kl})'_S \mathbf{h}^k \otimes \mathbf{h}^l \end{aligned} \quad (40)$$

recalling that the reference basis vectors \mathbf{h}_k and \mathbf{h}^k are independent of time.

The above motivates the introduction of a special class of *objective* time derivatives. In continuum mechanics, the most familiar is the *convective* or Oldroyd derivative [106] which applied to a tensor field is essentially its Lie derivative

along the velocity vector, cf. [74, 142]. The procedure is to compute a pull-back to the reference configuration, take the material time derivative, and push-forward the result back to the actual configuration. Thus, the *lower* (covariant) and the *upper* (contravariant) Lie or Oldroyd derivatives read

$$\begin{aligned} (\cdot)_S^\nabla &:= \mathcal{L}_{\mathbf{v}_S}(\cdot)^\sharp = \mathbf{F}_S \left(\frac{d_S}{dt} [\mathbf{F}_S^{-1}(\cdot) \mathbf{F}_S^{T-1}] \right) \mathbf{F}_S^T \\ &= (\cdot)'_S - \mathbf{L}_S(\cdot) - (\cdot) \mathbf{L}_S^T, \\ (\cdot)_S^\Delta &:= \mathcal{L}_{\mathbf{v}_S}(\cdot)^b = \mathbf{F}_S^{T-1} \left(\frac{d_S}{dt} [\mathbf{F}_S^T(\cdot) \mathbf{F}_S] \right) \mathbf{F}_S^{-1} \\ &= (\cdot)'_S + \mathbf{L}_S^T(\cdot) + (\cdot) \mathbf{L}_S. \end{aligned} \quad (41)$$

In analogy, convective inelastic time derivatives can be defined [39]:

$$\begin{aligned} (\widehat{\cdot})_{Si}^\nabla &:= (\widehat{\cdot})'_S - \widehat{\mathbf{L}}_{Si}(\widehat{\cdot}) - (\widehat{\cdot}) \widehat{\mathbf{L}}_{Si}^T, \\ (\widehat{\cdot})_{Si}^\Delta &:= (\widehat{\cdot})'_S + \widehat{\mathbf{L}}_{Si}^T(\widehat{\cdot}) + (\widehat{\cdot}) \widehat{\mathbf{L}}_{Si}. \end{aligned} \quad (42)$$

In summary, the lower and upper Lie time derivatives are material time derivatives of the tensorial components while keeping the co- and contravariant tensorial bases fixed. Following this, it is easily concluded that

$$\begin{aligned} (\mathbf{K}_S)_S^\nabla &= \mathbf{D}_S = -\frac{1}{2} (a^{kl})'_S \mathbf{a}_k \otimes \mathbf{a}_l, \\ (\mathbf{A}_S)_S^\Delta &= \mathbf{D}_S = \frac{1}{2} (a_{kl})'_S \mathbf{a}^k \otimes \mathbf{a}^l, \\ (\widehat{\mathbf{K}}_{Si})_{Si}^\nabla &= \widehat{\mathbf{D}}_{Si} = -\frac{1}{2} (\widehat{z}^{kl})'_S \widehat{\mathbf{z}}_k \otimes \widehat{\mathbf{z}}_l, \\ (\widehat{\mathbf{F}}_{Si})_{Si}^\Delta &= \widehat{\mathbf{D}}_{Si} = \frac{1}{2} (\widehat{z}_{kl})'_S \widehat{\mathbf{z}}^k \otimes \widehat{\mathbf{z}}^l. \end{aligned} \quad (43)$$

Now, convenient co- and contravariant strain rates can be introduced, which admit the same transport properties as the underlying strain measures. Moreover, the additive concept is kept consistent with the serial structure of the inelastic Maxwell branches. Thus, the respective co- and contravariant strain rates read (see also Appendix A.3):

$$\begin{aligned} (\mathbf{K}_S)_S^R &= (\mathbf{K}_{Se})'_S + (\mathbf{K}_{Si})'_S = -\frac{1}{2} (\mathbf{C}_S^{-1})'_S \\ &= -\frac{1}{2} (a^{kl})'_S \mathbf{h}_k \otimes \mathbf{h}_l, \\ (\widehat{\mathbf{K}}_{Si})_{Si}^\nabla &= (\widehat{\mathbf{K}}_{Se})_{Si}^\nabla + (\widehat{\mathbf{K}}_{Si})_{Si}^\nabla = -\frac{1}{2} (\widehat{z}^{kl})'_S \widehat{\mathbf{z}}_k \otimes \widehat{\mathbf{z}}_l, \\ (\mathbf{K}_S)_S^\nabla &= (\mathbf{K}_{Se})_S^\nabla + (\mathbf{K}_{Si})_S^\nabla = \mathbf{D}_S = -\frac{1}{2} (a^{kl})'_S \mathbf{a}_k \otimes \mathbf{a}_l, \\ (\mathbf{E}_S)'_S &= (\mathbf{E}_{Se})'_S + (\mathbf{E}_{Si})'_S = \frac{1}{2} (\mathbf{C}_S)'_S = \frac{1}{2} (a_{kl})'_S \mathbf{h}^k \otimes \mathbf{h}^l, \\ (\widehat{\mathbf{F}}_{Si})_{Si}^\Delta &= (\widehat{\mathbf{F}}_{Se})_{Si}^\Delta + (\widehat{\mathbf{F}}_{Si})_{Si}^\Delta = \frac{1}{2} (\widehat{z}_{kl})'_S \widehat{\mathbf{z}}^k \otimes \widehat{\mathbf{z}}^l, \\ (\mathbf{A}_S)_S^\Delta &= (\mathbf{A}_{Se})_S^\Delta + (\mathbf{A}_{Si})_S^\Delta = \mathbf{D}_S = \frac{1}{2} (a_{kl})'_S \mathbf{a}^k \otimes \mathbf{a}^l. \end{aligned} \quad (44)$$

2.2.3 Polar Decomposition and Spectral Representation

For a concise formulation of the subsequent constitutive material equations, it is, for some applications, of considerable assistance to express the deformation tensors by means of their eigenvalues and -vectors or -tensors, respectively. Proceeding from the fundamental theorem of polar decomposition, the solid deformation gradient can be multiplicatively split into a rotation tensor of the special (proper) orthogonal group $\mathbf{R}_S \in \mathcal{SO}_3$ and a symmetric, positive definite right (material) or left (spatial) stretch tensor \mathbf{U}_S or \mathbf{V}_S , respectively:

$$\mathbf{F}_S = \mathbf{R}_S \mathbf{U}_S = \mathbf{V}_S \mathbf{R}_S$$

$$\text{with } \mathbf{R}_S^T = \mathbf{R}_S^{-1}, \mathbf{U}_S^T = \mathbf{U}_S, \mathbf{V}_S^T = \mathbf{V}_S. \quad (45)$$

Following this, the solid deformation tensors and their inverses can be expressed as

$$\begin{aligned} \mathbf{C}_S &= \mathbf{F}_S^T \mathbf{F}_S = \mathbf{U}_S \mathbf{U}_S = \mathbf{U}_S^2, \\ \mathbf{B}_S &= \mathbf{F}_S \mathbf{F}_S^T = \mathbf{V}_S \mathbf{V}_S = \mathbf{V}_S^2, \\ \mathbf{C}_S^{-1} &= (\mathbf{U}_S^{-1})^2 = (\mathbf{U}_S^2)^{-1}, \\ \mathbf{B}_S^{-1} &= (\mathbf{V}_S^{-1})^2 = (\mathbf{V}_S^2)^{-1}. \end{aligned} \quad (46)$$

Moreover, with the rotation tensor, one finds the relationships

$$\begin{aligned} \mathbf{V}_S &= \mathbf{R}_S \mathbf{U}_S \mathbf{R}_S^T, & \mathbf{U}_S &= \mathbf{R}_S^T \mathbf{V}_S \mathbf{R}_S, \\ \mathbf{B}_S &= \mathbf{R}_S \mathbf{C}_S \mathbf{R}_S^T, & \mathbf{C}_S &= \mathbf{R}_S^T \mathbf{B}_S \mathbf{R}_S, \\ \mathbf{V}_S^{-1} &= \mathbf{R}_S \mathbf{U}_S^{-1} \mathbf{R}_S^T, & \mathbf{U}_S^{-1} &= \mathbf{R}_S^T \mathbf{V}_S^{-1} \mathbf{R}_S, \\ \mathbf{B}_S^{-1} &= \mathbf{R}_S \mathbf{C}_S^{-1} \mathbf{R}_S^T, & \mathbf{C}_S^{-1} &= \mathbf{R}_S^T \mathbf{B}_S^{-1} \mathbf{R}_S, \end{aligned} \quad (47)$$

and thus, a transformation rule between the co- and contravariant strain tensors

$$\begin{aligned} \mathbf{K}_S &= \mathbf{R}_S \mathbf{E}_S \mathbf{R}_S^T, & \mathbf{E}_S &= \mathbf{R}_S^T \mathbf{K}_S \mathbf{R}_S, \\ \mathbf{A}_S &= \mathbf{R}_S \mathbf{K}_S \mathbf{R}_S^T, & \mathbf{K}_S &= \mathbf{R}_S^T \mathbf{A}_S \mathbf{R}_S. \end{aligned} \quad (48)$$

In this connection, $\mathbf{R}_S(\cdot) \mathbf{R}_S^T$ and $\mathbf{R}_S^T(\cdot) \mathbf{R}_S$ denote so-called push-forward and pull-back rotations which are special transport mechanisms that simultaneously alter the variant type of the argument due to the orthogonality property $\mathbf{R}_S = \mathbf{R}_S^{T-1}$. From this, it also becomes clear that the two-field character of \mathbf{F}_S is included in the rotation tensor \mathbf{R}_S rather than in the stretch tensors \mathbf{U}_S or \mathbf{V}_S , respectively.

It is now easily concluded that \mathbf{C}_S and \mathbf{B}_S obey the same eigenvalues which are the squares of the principal stretches, i.e., the eigenvalues of \mathbf{U}_S or \mathbf{V}_S , respectively. Moreover, the principal directions, i.e., the eigenvectors, of \mathbf{C}_S and \mathbf{U}_S as well as of \mathbf{B}_S and \mathbf{V}_S coincide. For the purpose of this

contribution, it is sufficient to consider the eigenvalue problems of the Cauchy-Green deformation tensors only. They read:

$$\left\{ \begin{array}{l} (\mathbf{C}_S - \lambda_S \mathbf{I}) \mathbf{m}_S = \mathbf{0} \\ (\mathbf{B}_S - \lambda_S \mathbf{I}) \mathbf{n}_S = \mathbf{0} \end{array} \right\} \longleftrightarrow \left\{ \begin{array}{l} \mathbf{C}_S \mathbf{m}_{S(k)} = \lambda_{S(k)} \mathbf{m}_{S(k)}, \\ \mathbf{B}_S \mathbf{n}_{S(k)} = \lambda_{S(k)} \mathbf{n}_{S(k)} \end{array} \right. \quad (49)$$

with $\lambda_{S(k)} := \lambda_{\mathbf{C}_S(k)} = \lambda_{\mathbf{B}_S(k)} = (\lambda_{\mathbf{U}_S(k)})^2 = (\lambda_{\mathbf{V}_S(k)})^2 \in \mathbb{R}^+$ ($k = 1, 2, 3$) as the three real, positive eigenvalues of the symmetric and positive definite deformation tensors \mathbf{C}_S or \mathbf{B}_S , respectively, and $\mathbf{m}_{S(k)}$ and $\mathbf{n}_{S(k)}$ as the corresponding orthonormal eigenvectors of the reference and the actual configuration with the property $\mathbf{m}_{S(k)} \cdot \mathbf{m}_{S(l)} = \mathbf{n}_{S(k)} \cdot \mathbf{n}_{S(l)} = \delta_{kl}$. The non-trivial solution of (49) requires the characteristic polynomial to be zero, i.e.,

$$\begin{aligned} \det(\mathbf{C}_S - \lambda_S \mathbf{I}) &= \det(\mathbf{B}_S - \lambda_S \mathbf{I}) \\ &= \lambda_S^3 - I_S \lambda_S^2 + II_S \lambda_S - III_S = 0 \end{aligned} \quad (50)$$

with the principal invariants of the solid deformation tensors given as

$$\begin{aligned} I_S &:= I_{\mathbf{C}_S} = I_{\mathbf{B}_S} = \frac{1}{2} (\mathbf{C}_S \otimes \mathbf{I}) \cdot \mathbf{I} = \text{tr } \mathbf{C}_S = \mathbf{C}_S \cdot \mathbf{I} \\ &= \mathbf{F}_S \cdot \mathbf{F}_S, \\ II_S &:= II_{\mathbf{C}_S} = II_{\mathbf{B}_S} = \frac{1}{2} (\mathbf{C}_S \otimes \mathbf{C}_S) \cdot \mathbf{I} = \text{cof } \mathbf{C}_S \cdot \mathbf{I} \\ &= \text{cof } \mathbf{F}_S \cdot \text{cof } \mathbf{F}_S, \\ III_S &:= III_{\mathbf{C}_S} = III_{\mathbf{B}_S} = \frac{1}{6} (\mathbf{C}_S \otimes \mathbf{C}_S) \cdot \mathbf{C}_S \\ &= \det \mathbf{C}_S = (\det \mathbf{F}_S)^2. \end{aligned} \quad (51)$$

Note that the representation of the principal invariants by means of \mathbf{F}_S , $\text{cof } \mathbf{F}_S$, and $\det \mathbf{F}_S$ is of special interest in regard to certain stability requirements of the to-be defined constitutive functions (see Sect. 3.2.2). In this context, recall that the transport mechanisms of the material line, area, and volume elements of φ^S (24) are defined by exactly these terms.

If the eigenvalues $\lambda_{S(k)}$ are known, the principal invariants can also be obtained from

$$\begin{aligned} I_S &= \sum_{k=1}^3 \lambda_{S(k)} = \lambda_{S(1)} + \lambda_{S(2)} + \lambda_{S(3)}, \\ II_S &= \frac{1}{2} \sum_{\substack{k,l=1 \\ l \neq k}}^3 \lambda_{S(k)} \lambda_{S(l)} = \lambda_{S(1)} \lambda_{S(2)} + \lambda_{S(2)} \lambda_{S(3)} \\ &\quad + \lambda_{S(3)} \lambda_{S(1)}, \\ III_S &= \prod_{k=1}^3 \lambda_{S(k)} = \lambda_{S(1)} \lambda_{S(2)} \lambda_{S(3)} \end{aligned} \quad (52)$$

with the products $\lambda_{S(1)} \lambda_{S(2)}$, $\lambda_{S(2)} \lambda_{S(3)}$, and $\lambda_{S(3)} \lambda_{S(1)}$ precisely representing the eigenvalues of $\text{cof } \mathbf{C}_S$ or $\text{cof } \mathbf{B}_S$, respectively. Moreover, knowing the eigenvectors, the symmetric eigentensors or eigenbases of the reference and the actual configuration are introduced via

$$\mathbf{M}_{S(k)} := \mathbf{m}_{S(k)} \otimes \mathbf{m}_{S(k)} \quad \text{and} \quad \mathbf{N}_{S(k)} := \mathbf{n}_{S(k)} \otimes \mathbf{n}_{S(k)} \quad (53)$$

which accordingly obey the following properties:

$$\begin{aligned} \sum_{k=1}^3 \mathbf{M}_{S(k)} &= \mathbf{I}, & \sum_{k=1}^3 \mathbf{N}_{S(k)} &= \mathbf{I}, \\ \mathbf{M}_{S(k)} \cdot \mathbf{M}_{S(l)} &= \delta_{kl}, & \mathbf{N}_{S(k)} \cdot \mathbf{N}_{S(l)} &= \delta_{kl}, \\ \mathbf{M}_{S(k)} \mathbf{M}_{S(l)} &= \mathbf{0} \quad \forall k \neq l, & \mathbf{N}_{S(k)} \mathbf{N}_{S(l)} &= \mathbf{0} \quad \forall k \neq l, \\ (\mathbf{M}_{S(k)})^m &= \mathbf{M}_{S(k)} \quad \forall m \in \mathbb{R}^+, & & \\ (\mathbf{N}_{S(k)})^m &= \mathbf{N}_{S(k)} \quad \forall m \in \mathbb{R}^+, & & \\ \mathbf{C}_S \mathbf{M}_{S(k)} &= \mathbf{M}_{S(k)} \mathbf{C}_S = \lambda_{S(k)} \mathbf{M}_{S(k)}, & & \\ \mathbf{B}_S \mathbf{N}_{S(k)} &= \mathbf{N}_{S(k)} \mathbf{B}_S = \lambda_{S(k)} \mathbf{N}_{S(k)}. \end{aligned} \quad (54)$$

Thus, the spectral representations of arbitrary real-valued powers $m \in \mathbb{R}$ of the solid deformation tensors are given by

$$\begin{aligned} (\mathbf{C}_S)^m &= \sum_{k=1}^3 (\lambda_{S(k)})^m \mathbf{M}_{S(k)}, \\ (\mathbf{B}_S)^m &= \sum_{k=1}^3 (\lambda_{S(k)})^m \mathbf{N}_{S(k)}. \end{aligned} \quad (55)$$

Following this, the right and left solid stretch tensors take the form

$$\begin{aligned} \mathbf{U}_S &= (\mathbf{C}_S)^{1/2} = \sum_{k=1}^3 \sqrt{\lambda_{S(k)}} \mathbf{M}_{S(k)}, \\ \mathbf{V}_S &= (\mathbf{B}_S)^{1/2} = \sum_{k=1}^3 \sqrt{\lambda_{S(k)}} \mathbf{N}_{S(k)}, \end{aligned} \quad (56)$$

and it can be directly deduced that

$$\begin{aligned} \mathbf{R}_S &= \sum_{k=1}^3 \mathbf{n}_{S(k)} \otimes \mathbf{m}_{S(k)} \\ \longrightarrow \quad \mathbf{F}_S &= \sum_{k=1}^3 \sqrt{\lambda_{S(k)}} \mathbf{n}_{S(k)} \otimes \mathbf{m}_{S(k)}. \end{aligned} \quad (57)$$

In particular, \mathbf{R}_S and $\mathbf{R}_S^T = \mathbf{R}_S^{-1}$ act as transport mechanisms (cf. (47) and (48)) by rotating the principal directions of the reference (i.e., of \mathbf{C}_S or \mathbf{U}_S) into those of the actual config-

uration (i.e., of \mathbf{B}_S or \mathbf{V}_S) and *vice versa*, viz.,

$$\begin{aligned} \mathbf{m}_{S(k)} &\xrightarrow[\mathbf{R}_S^T]{\mathbf{R}_S} \mathbf{n}_{S(k)}, \\ \mathbf{M}_{S(k)} &\xrightarrow[\mathbf{R}_S^T(\cdot)\mathbf{R}_S]{\mathbf{R}_S(\cdot)\mathbf{R}_S^T} \mathbf{N}_{S(k)}. \end{aligned} \quad (58)$$

Note that due to the orthogonality of the principal axes, in spectral representation no distinction between co- and contravariant is necessary comparable to the self-reciprocal Cartesian basis vectors \mathbf{e}_k . However, regarding the transport property of eigenvectors and -tensors including both rotation and stretch, it turns out as a kinematical consequence of

$$\begin{aligned} \mathbf{B}_S &= \mathbf{F}_S \mathbf{F}_S^T = \mathbf{F}_S \mathbf{I} \mathbf{F}_S^T = \mathbf{F}_S \left(\sum_{k=1}^3 \mathbf{M}_{S(k)} \right) \mathbf{F}_S^T \\ &= \sum_{k=1}^3 \mathbf{F}_S \mathbf{M}_{S(k)} \mathbf{F}_S^T = \sum_{k=1}^3 \lambda_{S(k)} \mathbf{N}_{S(k)} \end{aligned} \quad (59)$$

that they accordingly obey a covariant transformation behavior. Thus,

$$\begin{aligned} \mathbf{m}_{S(k)} &\xrightarrow[\mathbf{F}_S^{-1}]{\mathbf{F}_S} \sqrt{\lambda_{S(k)}} \mathbf{n}_{S(k)}, \\ \mathbf{M}_{S(k)} &\xrightarrow[\mathbf{F}_S^{-1}(\cdot)\mathbf{F}_S^{T-1}]{\mathbf{F}_S(\cdot)\mathbf{F}_S^T} \lambda_{S(k)} \mathbf{N}_{S(k)}. \end{aligned} \quad (60)$$

Remark In the context of multiplicative finite inelasticity associated with $\mathbf{F}_S = \mathbf{F}_{Se} \mathbf{F}_{Si}$ (cf. Sect. 2.2.2), the presented polar and spectral decompositions can be applied straightforwardly to both the elastic and the inelastic parts of \mathbf{F}_S . Following this, respective elastic and inelastic stretch and rotation tensors can be directly introduced via

$$\mathbf{F}_{Se} = \mathbf{R}_{Se} \hat{\mathbf{U}}_{Se} = \mathbf{V}_{Se} \mathbf{R}_{Se}, \quad \mathbf{F}_{Si} = \mathbf{R}_{Si} \mathbf{U}_{Si} = \hat{\mathbf{V}}_{Si} \mathbf{R}_{Si} \quad (61)$$

which obviously obey properties equivalent to (45)–(47). Furthermore, the eigenvalue problems of $\hat{\mathbf{C}}_{Se} = \hat{\mathbf{U}}_{Se}^2$ and $\mathbf{B}_{Se} = \mathbf{V}_{Se}^2$ as well as of $\mathbf{C}_{Si} = \mathbf{U}_{Si}^2$ and $\hat{\mathbf{B}}_{Si} = \hat{\mathbf{V}}_{Si}^2$ are treated analogously to those of \mathbf{C}_S and \mathbf{B}_S yielding the corresponding spectral representations. Here, the spectral forms of the elastic deformation tensors are of particular interest

for the formulation of the inelastic constitutive material law. Accordingly, they read

$$\widehat{\mathbf{C}}_{Se} = \sum_{k=1}^3 \lambda_{Se(k)} \widehat{\mathbf{M}}_{Se(k)}, \quad \mathbf{B}_{Se} = \sum_{k=1}^3 \lambda_{Se(k)} \mathbf{N}_{Se(k)} \quad (62)$$

with $\lambda_{Se(k)}$ representing the eigenvalues of the elastic deformation tensors $\widehat{\mathbf{C}}_{Se}$ or \mathbf{B}_{Se} , respectively, and $\widehat{\mathbf{M}}_{Se(k)} = \widehat{\mathbf{m}}_{Se(k)} \otimes \widehat{\mathbf{m}}_{Se(k)}$ and $\mathbf{N}_{Se(k)} = \mathbf{n}_{Se(k)} \otimes \mathbf{n}_{Se(k)}$ as the elastic eigentensors built by the dyadic products of the elastic intermediate eigenvectors $\widehat{\mathbf{m}}_{Se(k)}$ and the elastic principal axes of the actual frame $\mathbf{n}_{Se(k)}$.

To continue, additionally, the partial derivatives of the eigenvalues, -vectors, and -tensors with respect to the corresponding deformation tensors are required. For their derivation, one initially proceeds from the general case of three distinct eigenvalues $\lambda_{S(1)} \neq \lambda_{S(2)} \neq \lambda_{S(3)} \neq \lambda_{S(1)}$. Necessary modifications for the special cases of equal values of the $\lambda_{S(k)}$ will be discussed later. At first, to find those derivatives of the reference frame with respect to \mathbf{C}_S , it is assumed that the principal referential directions $\mathbf{m}_{S(k)}$ can be determined from a time-dependent rotation $\mathbf{Q}_S = \mathbf{Q}_S(t) \in \mathcal{SO}_3$ of the spatially fixed orthonormal basis vectors \mathbf{e}_k , i.e., $\mathbf{m}_{S(k)} = \mathbf{Q}_S \mathbf{e}_k$. Taking the material time derivative, it follows that

$$\begin{aligned} (\mathbf{m}_{S(k)})'_S &= (\mathbf{Q}_S)'_S \mathbf{e}_k = \boldsymbol{\Omega}_S \mathbf{m}_{S(k)}, \\ (\mathbf{C}_S)'_S &= \boldsymbol{\Omega}_S \mathbf{C}_S - \mathbf{C}_S \boldsymbol{\Omega}_S \end{aligned} \quad (63)$$

with $\boldsymbol{\Omega}_S := (\mathbf{Q}_S)'_S \mathbf{Q}_S^T = -\boldsymbol{\Omega}_S^T$ representing the skew-symmetric gyration tensor of the principal directions of \mathbf{C}_S or \mathbf{U}_S , respectively. Then, the respective partial derivatives can be deduced from the following rate equations:

$$(\lambda_{S(k)})'_S = \frac{\partial \lambda_{S(k)}}{\partial \mathbf{C}_S} \cdot (\mathbf{C}_S)'_S, \quad (\mathbf{m}_{S(k)})'_S = \frac{\partial \mathbf{m}_{S(k)}}{\partial \mathbf{C}_S} (\mathbf{C}_S)'_S. \quad (64)$$

In particular, after some algebraic manipulations, one finds

$$\begin{aligned} \frac{\partial \lambda_{S(k)}}{\partial \mathbf{C}_S} &= \mathbf{m}_{S(k)} \otimes \mathbf{m}_{S(k)} = \mathbf{M}_{S(k)}, \\ \frac{\partial \mathbf{m}_{S(k)}}{\partial \mathbf{C}_S} &= \frac{1}{2} \sum_{\substack{l=1 \\ l \neq k}}^3 \frac{1}{\lambda_{S(k)} - \lambda_{S(l)}} \mathbf{M}_{S[lk]} =: \mathbf{M}_{S(k)}^3, \\ \frac{\partial \mathbf{M}_{S(k)}}{\partial \mathbf{C}_S} &= \frac{\partial (\mathbf{m}_{S(k)} \otimes \mathbf{m}_{S(k)})}{\partial \mathbf{C}_S} \\ &= \frac{1}{2} \sum_{\substack{l=1 \\ l \neq k}}^3 \frac{1}{\lambda_{S(k)} - \lambda_{S(l)}} (\mathbf{M}_{S[kl]}^4 + \mathbf{M}_{S[lk]}^4) =: \mathbf{M}_{S(k)}^4 \end{aligned} \quad (65)$$

with the abbreviations

$$\begin{aligned} \mathbf{M}_{S[lk]}^3 &= (\mathbf{M}_{S(l)} \otimes \mathbf{m}_{S(k)})^{23} + \mathbf{M}_{S(l)} \otimes \mathbf{m}_{S(k)}, \\ \mathbf{M}_{S[kl]}^4 &= (\mathbf{M}_{S(k)} \otimes \mathbf{M}_{S(l)})^{23} + (\mathbf{M}_{S(k)} \otimes \mathbf{M}_{S(l)})^{24}. \end{aligned} \quad (66)$$

In analogy, the corresponding derivatives of the actual frame are introduced

$$\begin{aligned} \frac{\partial \lambda_{S(k)}}{\partial \mathbf{B}_S} &= \mathbf{n}_{S(k)} \otimes \mathbf{n}_{S(k)} = \mathbf{N}_{S(k)}, \\ \frac{\partial \mathbf{n}_{S(k)}}{\partial \mathbf{B}_S} &= \frac{1}{2} \sum_{\substack{l=1 \\ l \neq k}}^3 \frac{1}{\lambda_{S(k)} - \lambda_{S(l)}} \mathbf{N}_{S[lk]}^3 =: \mathbf{N}_{S(k)}^3, \\ \frac{\partial \mathbf{N}_{S(k)}}{\partial \mathbf{B}_S} &= \frac{1}{2} \sum_{\substack{l=1 \\ l \neq k}}^3 \frac{1}{\lambda_{S(k)} - \lambda_{S(l)}} (\mathbf{N}_{S[kl]}^4 + \mathbf{N}_{S[lk]}^4) =: \mathbf{N}_{S(k)}^4 \end{aligned} \quad (67)$$

with the abbreviations

$$\begin{aligned} \mathbf{N}_{S[lk]}^3 &= (\mathbf{N}_{S(l)} \otimes \mathbf{n}_{S(k)})^{23} + \mathbf{N}_{S(l)} \otimes \mathbf{n}_{S(k)}, \\ \mathbf{N}_{S[kl]}^4 &= (\mathbf{N}_{S(k)} \otimes \mathbf{N}_{S(l)})^{23} + (\mathbf{N}_{S(k)} \otimes \mathbf{N}_{S(l)})^{24}. \end{aligned} \quad (68)$$

According to (60) and the relations in Appendix A.1, it holds

$$\begin{aligned} (\mathbf{F}_S \otimes \mathbf{F}_S)^T \mathbf{M}_{S[lk]}^3 \mathbf{F}_S^T &= \lambda_{S(l)} \sqrt{\lambda_{S(k)}} \mathbf{N}_{S[lk]}^3, \\ (\mathbf{F}_S \otimes \mathbf{F}_S)^T \mathbf{M}_{S[kl]}^4 (\mathbf{F}_S^T \otimes \mathbf{F}_S^T)^T &= \lambda_{S(k)} \lambda_{S(l)} \mathbf{N}_{S[kl]}^4. \end{aligned} \quad (69)$$

As an important application of the preceding, regard a scalar-valued, isotropic tensor function of the solid deformation tensors which in spectral representation takes the form

$$\begin{aligned} \Psi &= \Psi(\mathbf{C}_S) = \Psi(\mathbf{B}_S) = \Psi(I_S, II_S, III_S) \\ &\longrightarrow \Psi = \Psi(\lambda_{S(1)}, \lambda_{S(2)}, \lambda_{S(3)}). \end{aligned} \quad (70)$$

Then, the first and second derivatives with respect to \mathbf{C}_S read:

$$\begin{aligned} \frac{\partial \Psi}{\partial \mathbf{C}_S} &= \sum_{k=1}^3 \frac{\partial \Psi}{\partial \lambda_{S(k)}} \frac{\partial \lambda_{S(k)}}{\partial \mathbf{C}_S} = \sum_{k=1}^3 \frac{\partial \Psi}{\partial \lambda_{S(k)}} \mathbf{M}_{S(k)}, \\ \frac{\partial^2 \Psi}{\partial \mathbf{C}_S \otimes \partial \mathbf{C}_S} &= \sum_{k,l=1}^3 \frac{\partial^2 \Psi}{\partial \lambda_{S(k)} \partial \lambda_{S(l)}} \frac{\partial \lambda_{S(k)}}{\partial \mathbf{C}_S} \otimes \frac{\partial \lambda_{S(l)}}{\partial \mathbf{C}_S} \\ &\quad + \sum_{k=1}^3 \frac{\partial \Psi}{\partial \lambda_{S(k)}} \frac{\partial \mathbf{M}_{S(k)}}{\partial \mathbf{C}_S} \\ &= \sum_{k,l=1}^3 \frac{\partial^2 \Psi}{\partial \lambda_{S(k)} \partial \lambda_{S(l)}} \mathbf{M}_{S(k)} \otimes \mathbf{M}_{S(l)} \end{aligned}$$

$$\begin{aligned}
& + \sum_{k=1}^3 \frac{\partial \Psi}{\partial \lambda_{S(k)}} \mathbf{M}_{S(k)}^4 \\
& = \sum_{k,l=1}^3 \frac{\partial^2 \Psi}{\partial \lambda_{S(k)} \partial \lambda_{S(l)}} \mathbf{M}_{S(k)} \otimes \mathbf{M}_{S(l)} \\
& + \frac{1}{2} \sum_{\substack{k,l=1 \\ l \neq k}}^3 \frac{\frac{\partial \Psi}{\partial \lambda_{S(k)}} - \frac{\partial \Psi}{\partial \lambda_{S(l)}}}{\lambda_{S(k)} - \lambda_{S(l)}} \mathbf{M}_{S[kl]}^4. \quad (71)
\end{aligned}$$

The corresponding relations in the actual configuration result from a covariant push-forward of the previous results, but may also be obtained from (67), i.e.,

$$\begin{aligned}
\mathbf{F}_S \frac{\partial \Psi}{\partial \mathbf{C}_S} \mathbf{F}_S^T &= \frac{\partial \Psi}{\partial \mathbf{B}_S} \mathbf{B}_S = \mathbf{B}_S \frac{\partial \Psi}{\partial \mathbf{B}_S} \\
&= \sum_{k=1}^3 \frac{\partial \Psi}{\partial \lambda_{S(k)}} \lambda_{S(k)} \mathbf{N}_{S(k)}, \\
(\mathbf{F}_S \otimes \mathbf{F}_S)^T \frac{\partial^2 \Psi}{\partial \mathbf{C}_S \otimes \partial \mathbf{C}_S} (\mathbf{F}_S^T \otimes \mathbf{F}_S^T)^T & \\
&= \left[\mathbf{B}_S \frac{\partial^2 \Psi}{\partial \mathbf{B}_S \otimes \partial \mathbf{B}_S} \mathbf{B}_S \right]^4 \\
&= \sum_{k,l=1}^3 \frac{\partial^2 \Psi}{\partial \lambda_{S(k)} \partial \lambda_{S(l)}} \lambda_{S(k)} \lambda_{S(l)} \mathbf{N}_{S(k)} \otimes \mathbf{N}_{S(l)} \\
&+ \frac{1}{2} \sum_{\substack{k,l=1 \\ l \neq k}}^3 \frac{\frac{\partial \Psi}{\partial \lambda_{S(k)}} - \frac{\partial \Psi}{\partial \lambda_{S(l)}}}{\lambda_{S(k)} - \lambda_{S(l)}} \lambda_{S(k)} \lambda_{S(l)} \mathbf{N}_{S[kl]}^4. \quad (72)
\end{aligned}$$

Herein, $(\cdot)^n$ indicates that the tensor product in the argument has to be carried out so that it yields a tensor of n th order. Note that the representation by means of \mathbf{B}_S can be achieved by some algebraic transformations and usage of (45)–(47).

Since the above relations are developed for the case of distinct roots, special modifications must be provided for the case of multiple eigenvalues. It is easily observed that if $\lambda_{S(k)} = \lambda_{S(l)}$, the fractions in the second sums of (71)₂ and (72)₂ yield undetermined expressions. However, the limits of the rational expressions can be computed by exploiting l'Hôpital's rule. Hence, the fraction of the reference frame yields

$$\lim_{\lambda_{S(k)} \rightarrow \lambda_{S(l)}} \frac{\frac{\partial \Psi}{\partial \lambda_{S(k)}} - \frac{\partial \Psi}{\partial \lambda_{S(l)}}}{\lambda_{S(k)} - \lambda_{S(l)}} = \frac{\partial^2 \Psi}{\partial \lambda_{S(k)}^2} - \frac{\partial^2 \Psi}{\partial \lambda_{S(l)} \partial \lambda_{S(k)}} \quad (73)$$

and the limit of the rational expression of the actual frame results in

$$\lim_{\lambda_{S(k)} \rightarrow \lambda_{S(l)}} \frac{\left(\frac{\partial \Psi}{\partial \lambda_{S(k)}} - \frac{\partial \Psi}{\partial \lambda_{S(l)}} \right) \lambda_{S(k)} \lambda_{S(l)}}{\lambda_{S(k)} - \lambda_{S(l)}}$$

$$\begin{aligned}
&= \left(\frac{\partial \Psi}{\partial \lambda_{S(k)}} - \frac{\partial \Psi}{\partial \lambda_{S(l)}} \right) \lambda_{S(l)} \\
&+ \left(\frac{\partial^2 \Psi}{\partial \lambda_{S(k)}^2} - \frac{\partial^2 \Psi}{\partial \lambda_{S(l)} \partial \lambda_{S(k)}} \right) \lambda_{S(k)} \lambda_{S(l)}. \quad (74)
\end{aligned}$$

Note that the above limits are valid for the case of double roots $\lambda_{S(k)} = \lambda_{S(l)} \neq \lambda_{S(m)}$ ($k \neq l \neq m \neq k$) as well as for the case of three identical eigenvalues $\lambda_{S(1)} = \lambda_{S(2)} = \lambda_{S(3)}$.

2.3 Balance Relations

2.3.1 Stress Concept and Dual Variables

According to the intersection (free-body) principle, each partial body $\mathcal{B}^\alpha \subset \mathcal{B}$ of φ is subjected to an external mass-specific body (volume) force $\mathbf{b}^\alpha = \mathbf{b}^\alpha(\mathbf{x}, t)$ and an external traction (contact) force $\mathbf{t}^\alpha = \mathbf{t}^\alpha(\mathbf{x}, t, \mathbf{n})$ acting on parts or the whole of the boundary surface $\mathcal{S}^\alpha \subset \mathcal{S}$ with orientation \mathbf{n} . Then, the whole mixture body $\mathcal{B} = \bigcup_\alpha \mathcal{B}^\alpha$ is exposed to the total body force $\rho \mathbf{b} = \sum_\alpha \rho^\alpha \mathbf{b}^\alpha$ and the total surface traction $\mathbf{t} = \sum_\alpha \mathbf{t}^\alpha$ on the entire surface $\mathcal{S} = \bigcup_\alpha \mathcal{S}^\alpha$. In conclusion, one finds the resultant force vectors \mathbf{f} and \mathbf{f}^α acting on the overall medium φ and on the constituents φ^α to

$$\mathbf{f} = \underbrace{\int_{\mathcal{B}} \rho \mathbf{b} dv}_{\mathbf{f}_v} + \underbrace{\int_{\mathcal{S}} \mathbf{t} da}_{\mathbf{f}_a}, \quad \mathbf{f}^\alpha = \underbrace{\int_{\mathcal{B}} \rho^\alpha \mathbf{b}^\alpha dv^\alpha}_{\mathbf{f}_v^\alpha} + \underbrace{\int_{\mathcal{S}} \mathbf{t}^\alpha da^\alpha}_{\mathbf{f}_a^\alpha}. \quad (75)$$

Applying Cauchy's theorem, one recovers the Cauchy stress tensor of the mixture $\mathbf{T} = \mathbf{T}(\mathbf{x}, t)$ and the partial Cauchy stress tensor $\mathbf{T}^\alpha = \mathbf{T}^\alpha(\mathbf{x}, t)$ of φ^α from

$$\mathbf{t}(\mathbf{x}, t, \mathbf{n}) = \mathbf{T}(\mathbf{x}, t) \mathbf{n}, \quad \mathbf{t}^\alpha(\mathbf{x}, t, \mathbf{n}) = \mathbf{T}^\alpha(\mathbf{x}, t) \mathbf{n}. \quad (76)$$

The total Cauchy stress may also be expressed by means of partial quantities, viz.,

$$\mathbf{T} = \sum_\alpha (\mathbf{T}^\alpha - \rho^\alpha \mathbf{d}_\alpha \otimes \mathbf{d}_\alpha), \quad (77)$$

where $\rho^\alpha \mathbf{d}_\alpha \otimes \mathbf{d}_\alpha$ represents an apparent stress comparable to the Reynolds stress in turbulent flows which is caused by fluctuations of the entire velocity field due to the diffusion velocities \mathbf{d}_α superimposed on the averaged velocity of the whole mixture $\dot{\mathbf{x}}$ given in (8).

Following the above, the Cauchy stresses as the true stresses represent the current stress state at material points by describing the surface force acting on an area element in the actual configuration. Proceeding from the incremental surface force on \mathcal{S}^S , additional solid stress tensors are introduced via

$$\begin{aligned} d\mathbf{f}_a^S &= \mathbf{t}^S da^S = \mathbf{T}^S d\mathbf{a}^S \\ &= \mathbf{T}^S \text{cof} \mathbf{F}_S d\mathbf{A}_S^S = \underbrace{\mathbf{T}^S (\det \mathbf{F}_S) \mathbf{F}_S^{T-1}}_{\mathbf{P}^S} d\mathbf{A}_S^S, \end{aligned} \quad (78)$$

where in terms of natural basis vectors

$$\begin{aligned} \mathbf{T}^S &= t^{kl} \mathbf{a}_k \otimes \mathbf{a}_l \quad : \\ &\text{Cauchy stress (true stress),} \\ \boldsymbol{\tau}^S &= (\det \mathbf{F}_S) \mathbf{T}^S = \tau^{kl} \mathbf{a}_k \otimes \mathbf{a}_l \quad : \\ &\text{Kirchhoff stress (weighted Cauchy stress),} \\ \mathbf{P}^S &= \boldsymbol{\tau}^S \mathbf{F}_S^{T-1} = \tau^{kl} \mathbf{a}_k \otimes \mathbf{h}_l \quad : \\ &\text{1st Piola-Kirchhoff stress (nominal stress).} \end{aligned} \quad (79)$$

Moreover, it is of considerable assistance to formally introduce two further stress tensors which operate on the ref-

erence and the inelastic intermediate configuration, respectively:

$$\begin{aligned} \mathbf{S}^S &= \mathbf{F}_S^{-1} \mathbf{P}^S = \mathbf{F}_S^{-1} \boldsymbol{\tau}^S \mathbf{F}_S^{T-1} = \tau^{kl} \mathbf{h}_k \otimes \mathbf{h}_l \quad : \\ &\text{2nd Piola-Kirchhoff stress,} \\ \hat{\boldsymbol{\tau}}^S &= \mathbf{F}_{Si} \mathbf{S}^S \mathbf{F}_{Si}^T = \mathbf{F}_{Se}^{-1} \boldsymbol{\tau}^S \mathbf{F}_{Se}^{T-1} = \tau^{kl} \hat{\mathbf{z}}_k \otimes \hat{\mathbf{z}}_l \quad : \\ &\text{intermediate stress.} \end{aligned} \quad (80)$$

Note that the covariant representation of the introduced stress measures is a direct consequence of the contravariant nature of the oriented area elements and the corresponding surface normals (recall (24)).

In analogy to the covariant strain rates given in (44)_{1,2,3}, by use of the lower Oldroyd derivatives (41)₁ and (42)₁, convenient stress rates which obey the same transport mechanisms as the corresponding stresses can be introduced (see (81)).

Solid stress tensors and solid stress rates

$$\begin{aligned} \mathbf{S}^S &\xrightarrow{\mathbf{F}_S(\cdot) \mathbf{F}_S^T} \hat{\boldsymbol{\tau}}^S \xrightarrow{\mathbf{F}_{Se}(\hat{\cdot}) \mathbf{F}_{Se}^T} \boldsymbol{\tau}^S \\ (\mathbf{S}^S)'_S &\xrightarrow{\mathbf{F}_{Si}^{-1}(\hat{\cdot}) \mathbf{F}_{Si}^{T-1}} (\hat{\boldsymbol{\tau}}^S)'_{Si} \xrightarrow{\mathbf{F}_{Se}^{-1}(\cdot) \mathbf{F}_{Se}^{T-1}} (\boldsymbol{\tau}^S)'_S \\ &\quad \xrightarrow{\mathbf{F}_S^{-1}(\cdot) \mathbf{F}_S^{T-1}} \end{aligned} \quad (81)$$

The natural bond between certain stresses and strains is best described by the concept of *dual variables* stating that physically relevant scalar products between associated (conjugate) stress-strain pairs, such as the rate of internal mechanical work (stress power), stay invariant due to any transport operation between configurations. One finds,

$$\begin{aligned} \mathbf{S}^S \cdot \mathbf{E}_S &= \hat{\boldsymbol{\tau}}^S \cdot \hat{\mathbf{\Gamma}}_S = \boldsymbol{\tau}^S \cdot \mathbf{A}_S = \frac{1}{2} \tau^{kl} (a_{kl} - h_{kl}), \\ \mathbf{S}^S \cdot (\mathbf{E}_S)'_S &= \hat{\boldsymbol{\tau}}^S \cdot (\hat{\mathbf{\Gamma}}_S)'_{Si} = \boldsymbol{\tau}^S \cdot (\mathbf{A}_S)'_S = \frac{1}{2} \tau^{kl} (a_{kl})'_S, \\ (\mathbf{S}^S)'_S \cdot \mathbf{E}_S &= (\hat{\boldsymbol{\tau}}^S)'_{Si} \cdot \hat{\mathbf{\Gamma}}_S = (\boldsymbol{\tau}^S)'_S \cdot \mathbf{A}_S \\ &= \frac{1}{2} (\tau^{kl})'_S (a_{kl} - h_{kl}), \\ (\mathbf{S}^S)'_S \cdot (\mathbf{E}_S)'_S &= (\hat{\boldsymbol{\tau}}^S)'_{Si} \cdot (\hat{\mathbf{\Gamma}}_S)'_{Si} = (\boldsymbol{\tau}^S)'_S \cdot (\mathbf{A}_S)'_S \\ &= \frac{1}{2} (\tau^{kl})'_S (a_{kl})'_S. \end{aligned} \quad (82)$$

2.3.2 Master Balance Principle for Mixtures

According to Truesdell's *metaphysical principles* for mixtures [135, p. 221], each constituent φ^α can be described by individual balance equations accounting for interactions between them by additional production terms. The balance equations of the whole mixture are obtained as the sum of the balance equations of the constituents and must have the same form as the respective balance equations of a single-phase material. Due to the fact that the mathematical structure of the fundamental balance relations, namely of mass, linear momentum, moment of momentum (m.o.m.), energy, and entropy, is in principle identical, they can be formulated within the concise shape of a master balance, cf. [41, 42].

To begin with, let Ψ and $\boldsymbol{\Psi}$ be volume-specific scalar- and vector-valued densities of a physical quantity to be balanced. Then, proceeding from classical continuum mechanics of single-phase materials, the general balance relations of a multiphasic mixture $\varphi = \sum_\alpha \varphi^\alpha$ take the global (integral) form:

$$\begin{aligned} \frac{d}{dt} \int_B \Psi \, dv &= \int_S (\boldsymbol{\phi} \cdot \mathbf{n}) \, da + \int_B \sigma \, dv + \int_B \hat{\Psi} \, dv, \\ \frac{d}{dt} \int_B \Psi \, dv &= \int_S (\boldsymbol{\Phi} \cdot \mathbf{n}) \, da + \int_B \sigma \, dv + \int_B \hat{\Psi} \, dv. \end{aligned} \quad (83)$$

Herein, $\boldsymbol{\phi} \cdot \mathbf{n}$ and $\boldsymbol{\Phi} \cdot \mathbf{n}$ are the surface densities defined per unit current area representing the efflux of the physical quantity over the surface S of B , σ and σ are the volume densities describing the supply (external source) of the physical quantity, and $\hat{\Psi}$ and $\hat{\Psi}$ represent the productions of the physical quantity due to couplings of φ with its environment. Supposing adequate continuity properties for all occurring fields, the equivalent local (differential) form of the master balance equations (83) results from differentiation of the left-hand sides and transformation of the surface integrals into volume integrals on the right-hand sides:

$$\begin{aligned} \dot{\Psi} + \Psi \operatorname{div} \dot{\mathbf{x}} &= \operatorname{div} \boldsymbol{\phi} + \sigma + \hat{\Psi}, \\ \dot{\Psi} + \Psi \operatorname{div} \dot{\mathbf{x}} &= \operatorname{div} \boldsymbol{\Phi} + \sigma + \hat{\Psi}. \end{aligned} \quad (84)$$

Proceeding from the axiomatically introduced balance principles, namely of mass, linear momentum, moment of momentum (m.o.m.), energy, and entropy, one identifies the quantities in (83) and (84) according to the following table:

	Ψ, Ψ	$\boldsymbol{\phi}, \boldsymbol{\Phi}$	σ, σ	$\hat{\Psi}, \hat{\Psi}$
mass	ρ	$\mathbf{0}$	0	0
momentum	$\rho \dot{\mathbf{x}}$	\mathbf{T}	$\rho \mathbf{b}$	$\mathbf{0}$
m.o.m.	$\mathbf{x} \times (\rho \dot{\mathbf{x}})$	$\mathbf{x} \times \mathbf{T}$	$\mathbf{x} \times (\rho \mathbf{b})$	$\mathbf{0}$
energy	$\rho \varepsilon + \frac{1}{2} \dot{\mathbf{x}} \cdot (\rho \dot{\mathbf{x}})$	$\mathbf{T}^T \dot{\mathbf{x}} - \mathbf{q}$	$\dot{\mathbf{x}} \cdot (\rho \mathbf{b}) + \rho r$	0
entropy	$\rho \eta$	$\boldsymbol{\phi}_\eta$	σ_η	$\hat{\eta}$

(85)

Herein, $\rho \dot{\mathbf{x}}$ is the momentum of the entire mixture and $\mathbf{x} \times (\rho \dot{\mathbf{x}})$ is the corresponding moment of momentum. Concerning the energy and the entropy balances, ε is the internal energy, \mathbf{q} is the heat influx vector, and r is the external heat supply. Moreover, η is the entropy, $\boldsymbol{\phi}_\eta$ and σ_η are the efflux of entropy and the external entropy supply, and $\hat{\eta} \geq 0$ is the non-negative entropy production which considers the irreversibility of the overall thermodynamical process. Furthermore, regarding the mixture as a closed system, all remaining production terms are equal to zero. By inserting the respective quantities of (85) into the local master balances (84), one recovers the specific balance relations known from classical continuum mechanics of single-phase materials:

Mixture balance relations

$$\begin{aligned} \text{mass:} \quad & \dot{\rho} + \rho \operatorname{div} \dot{\mathbf{x}} = 0 \\ \text{momentum:} \quad & \rho \ddot{\mathbf{x}} = \operatorname{div} \mathbf{T} + \rho \mathbf{b} \\ \text{m. o. m.:} \quad & \mathbf{0} = \mathbf{I} \times \mathbf{T} \longrightarrow \mathbf{T} = \mathbf{T}^T \quad (86) \\ \text{energy:} \quad & \rho \dot{\varepsilon} = \mathbf{T} \cdot \mathbf{L} - \operatorname{div} \mathbf{q} + \rho r \\ & \text{with } \mathbf{L} = \operatorname{grad} \dot{\mathbf{x}} \\ \text{entropy:} \quad & \rho \dot{\eta} \geq \operatorname{div} \boldsymbol{\phi}_\eta + \sigma_\eta \end{aligned}$$

Furthermore, following Truesdell's principles, the general balances of the individual constituents yield, in analogy to (83), the global form

$$\begin{aligned} \frac{d_\alpha}{dt} \int_B \Psi^\alpha \, dv &= \int_S (\boldsymbol{\phi}^\alpha \cdot \mathbf{n}) \, da + \int_B \sigma^\alpha \, dv + \int_B \hat{\Psi}^\alpha \, dv, \\ \frac{d_\alpha}{dt} \int_B \Psi^\alpha \, dv &= \int_S (\boldsymbol{\Phi}^\alpha \cdot \mathbf{n}) \, da + \int_B \sigma^\alpha \, dv + \int_B \hat{\Psi}^\alpha \, dv \end{aligned} \quad (87)$$

and according to (84) the local form

$$\begin{aligned} (\Psi^\alpha)'_\alpha + \Psi^\alpha \operatorname{div} \dot{\mathbf{x}}_\alpha &= \operatorname{div} \boldsymbol{\phi}^\alpha + \sigma^\alpha + \hat{\Psi}^\alpha, \\ (\Psi^\alpha)'_\alpha + \Psi^\alpha \operatorname{div} \dot{\mathbf{x}}_\alpha &= \operatorname{div} \boldsymbol{\Phi}^\alpha + \sigma^\alpha + \hat{\Psi}^\alpha. \end{aligned} \quad (88)$$

In the above equations, the partial quantities $(\cdot)^\alpha$ have the same physical meaning as the quantities included in the master balances of the overall mixture. However, they have to satisfy additional conservation conditions such that summation of a partial balance of all φ^α yields the respective fields of the multiphasic continuum φ :

$$\begin{aligned} \Psi &= \sum_\alpha \Psi^\alpha, & \boldsymbol{\phi} \cdot \mathbf{n} &= \sum_\alpha (\boldsymbol{\phi}^\alpha - \Psi^\alpha \mathbf{d}_\alpha) \cdot \mathbf{n}, \\ \sigma &= \sum_\alpha \sigma^\alpha, & \hat{\Psi} &= \sum_\alpha \hat{\Psi}^\alpha, \\ \Psi &= \sum_\alpha \Psi^\alpha, & \boldsymbol{\Phi} \cdot \mathbf{n} &= \sum_\alpha (\boldsymbol{\Phi}^\alpha - \Psi^\alpha \otimes \mathbf{d}_\alpha) \cdot \mathbf{n}, \\ \sigma &= \sum_\alpha \sigma^\alpha, & \hat{\Psi} &= \sum_\alpha \hat{\Psi}^\alpha. \end{aligned} \quad (89)$$

The specific balance equations of the constituents are then derived in analogy to those of single-phase materials accounting for the interaction mechanisms by additional production terms. Actually, the local partial continua can be regarded as open systems staying in thermodynamical exchange with each other. In particular, one identifies the partial physical quantities according to the following table:

	ψ^α, Ψ^α	ϕ^α, Φ^α	$\sigma^\alpha, \sigma^\alpha$	$\hat{\psi}^\alpha, \hat{\Psi}^\alpha$
mass	ρ^α	$\mathbf{0}$	0	$\hat{\rho}^\alpha$
momentum	$\rho^\alpha \dot{\mathbf{x}}_\alpha$	\mathbf{T}^α	$\rho^\alpha \mathbf{b}^\alpha$	$\hat{\mathbf{s}}^\alpha$
m.o.m.	$\mathbf{x} \times (\rho^\alpha \dot{\mathbf{x}}_\alpha)$	$\mathbf{x} \times \mathbf{T}^\alpha$	$\mathbf{x} \times (\rho^\alpha \mathbf{b}^\alpha)$	$\hat{\mathbf{h}}^\alpha$
energy	$\rho^\alpha \varepsilon^\alpha + \frac{1}{2} \dot{\mathbf{x}}_\alpha \cdot (\rho^\alpha \dot{\mathbf{x}}_\alpha)$	$(\mathbf{T}^\alpha)^T \dot{\mathbf{x}}_\alpha - \mathbf{q}^\alpha$	$\dot{\mathbf{x}}_\alpha \cdot (\rho^\alpha \mathbf{b}^\alpha) + \rho^\alpha r^\alpha$	$\hat{\varepsilon}^\alpha$
entropy	$\rho^\alpha \eta^\alpha$	ϕ_η^α	σ_η^α	$\hat{\eta}^\alpha$

Herein, $\hat{\rho}^\alpha$ is the mass production describing mass exchanges or phase transitions between the constituents, $\hat{\mathbf{s}}^\alpha$ is the total momentum production of φ^α , and $\hat{\mathbf{h}}^\alpha$ is the total production of angular momentum. Moreover, $\hat{\varepsilon}^\alpha$ and $\hat{\eta}^\alpha$ are the total energy and entropy productions of φ^α . In mixture theories, it is convenient to split the total production terms into direct parts and parts including productions of the preceding (lower) balances:

$$\begin{aligned}\hat{\mathbf{s}}^\alpha &= \hat{\mathbf{p}}^\alpha + \hat{\rho}^\alpha \dot{\mathbf{x}}_\alpha, & \hat{\mathbf{h}}^\alpha &= \hat{\mathbf{m}}^\alpha + \mathbf{x} \times (\hat{\mathbf{p}}^\alpha + \hat{\rho}^\alpha \dot{\mathbf{x}}_\alpha), \\ \hat{\varepsilon}^\alpha &= \hat{\varepsilon}^\alpha + \hat{\mathbf{p}}^\alpha \cdot \dot{\mathbf{x}}_\alpha + \hat{\rho}^\alpha \left(\varepsilon^\alpha + \frac{1}{2} \dot{\mathbf{x}}_\alpha \cdot \dot{\mathbf{x}}_\alpha \right), \\ \hat{\eta}^\alpha &= \hat{\zeta}^\alpha + \hat{\rho}^\alpha \eta^\alpha.\end{aligned}\quad (91)$$

In (91), $\hat{\mathbf{p}}^\alpha$ denotes the direct momentum production which can be interpreted as the volume-specific local interaction force between φ^α and the other constituents of φ , and $\hat{\mathbf{m}}^\alpha$ represents the direct moment of momentum production describing the angular momentum couplings between the constituents. Moreover, $\hat{\varepsilon}^\alpha$ and $\hat{\zeta}^\alpha$ are the direct terms of the energy and the entropy productions. As is usual in the framework of single-phase continua, one proceeds from an *a priori* constitutive assumption for the partial entropy efflux and the external entropy supply, viz.,

$$\phi_\eta^\alpha = -\frac{1}{\Theta^\alpha} \mathbf{q}^\alpha, \quad \sigma_\eta^\alpha = \frac{1}{\Theta^\alpha} \rho^\alpha r^\alpha, \quad (92)$$

where different absolute Kelvin's temperatures $\Theta^\alpha > 0$ allow for an individual temperature field for each constituent. Following this, the final form of the specific partial balance relations is obtained in analogy to those of the whole mixture (86):

Constituent balance relations

mass:	$(\rho^\alpha)'_\alpha + \rho^\alpha \operatorname{div} \dot{\mathbf{x}}_\alpha = \hat{\rho}^\alpha$
momentum:	$\rho^\alpha \ddot{\mathbf{x}}_\alpha = \operatorname{div} \mathbf{T}^\alpha + \rho^\alpha \mathbf{b}^\alpha + \hat{\mathbf{p}}^\alpha$
m.o.m.:	$\mathbf{0} = \mathbf{I} \times \mathbf{T}^\alpha + \hat{\mathbf{m}}^\alpha$
energy:	$\rho^\alpha (\varepsilon^\alpha)'_\alpha = \mathbf{T}^\alpha \cdot \mathbf{L}_\alpha - \operatorname{div} \mathbf{q}^\alpha + \rho^\alpha r^\alpha + \hat{\varepsilon}^\alpha$
entropy:	$\rho^\alpha (\eta^\alpha)'_\alpha = \operatorname{div} \left(-\frac{1}{\Theta^\alpha} \mathbf{q}^\alpha \right) + \frac{1}{\Theta^\alpha} \rho^\alpha r^\alpha + \hat{\zeta}^\alpha$

(93)

According to the sum relations (89), the physical quantities of the mixture can be expressed by means of the respective partial quantities extended by a diffusion term in the case of the surface densities. As an example, recall the previously introduced total Cauchy stress tensor \mathbf{T} in (77). Moreover, one finds the following restrictions for the partial production terms:

$$\begin{aligned}\sum_\alpha \hat{\rho}^\alpha &= 0, & \sum_\alpha \hat{\mathbf{s}}^\alpha &= \mathbf{0}, & \sum_\alpha \hat{\mathbf{h}}^\alpha &= \mathbf{0}, \\ \sum_\alpha \hat{\varepsilon}^\alpha &= 0, & \sum_\alpha \hat{\eta}^\alpha &\geq 0.\end{aligned}\quad (94)$$

Remark In this contribution, only non-polar materials (Boltzmann continua) are considered. Thus, proceeding from non-polar mixtures, evaluation of the mixture balance of angular momentum yields the symmetry of the total Cauchy stress tensor, $\mathbf{T} = \mathbf{T}^T$, as depicted in (86)₃. However, regarding the partial m. o. m. balances of the non-polar φ^α (93)₃, direct angular momentum couplings $\hat{\mathbf{m}}^\alpha$ must be considered yielding non-symmetric partial Cauchy stresses, $\mathbf{T}^\alpha \neq (\mathbf{T}^\alpha)^T$. Nevertheless, proceeding from intrinsically non-polar materials associated with symmetric Cauchy stresses on the microscale, it can be shown by homogenization that the macroscopic stresses must also be symmetric [68]. Thus,

$$\mathbf{T}^\alpha = (\mathbf{T}^\alpha)^T \quad \longrightarrow \quad \hat{\mathbf{m}}^\alpha \equiv \mathbf{0}. \quad (95)$$

Accordingly, the partial Kirchhoff and 2nd Piola-Kirchhoff stresses $\boldsymbol{\tau}^\alpha$ and \mathbf{S}^α are also symmetric, while the 1st Piola-Kirchhoff stress \mathbf{P}^α is generally not. For specific extensions to micropolar materials (Cosserat continua), see, e.g., [33, 34, 42].

2.3.3 Entropy Principle for Mixtures

In order to formulate admissible constitutive relations for the description of specific material behavior, evaluation of the entropy principle for mixtures provides the thermodynamical restrictions. According to inequality (94)₅ together with (91)₄ and the partial entropy balance (93)₅, the entropy

principle for mixtures takes the form

$$\sum_{\alpha} \left[\rho^{\alpha} (\eta^{\alpha})'_{\alpha} + \hat{\rho}^{\alpha} \eta^{\alpha} + \operatorname{div} \left(\frac{1}{\Theta^{\alpha}} \mathbf{q}^{\alpha} \right) - \frac{1}{\Theta^{\alpha}} \rho^{\alpha} r^{\alpha} \right] \geq 0. \quad (96)$$

Next, by formal introduction of the Helmholtz free-energy density

$$\psi^{\alpha} := \varepsilon^{\alpha} - \Theta^{\alpha} \eta^{\alpha} \quad (97)$$

and by use of the partial energy balance (93)₄, the entropy principle can be rephrased in the most common Clausius-Duhem representation

$$\sum_{\alpha} \frac{1}{\Theta^{\alpha}} \left\{ \mathbf{T}^{\alpha} \cdot \mathbf{L}_{\alpha} - \rho^{\alpha} [(\psi^{\alpha})'_{\alpha} + (\Theta^{\alpha})'_{\alpha} \eta^{\alpha}] - \hat{\mathbf{p}}^{\alpha} \cdot \dot{\mathbf{x}}_{\alpha} - \hat{\rho}^{\alpha} \left(\psi^{\alpha} + \frac{1}{2} \dot{\mathbf{x}}_{\alpha} \cdot \dot{\mathbf{x}}_{\alpha} \right) - \frac{1}{\Theta^{\alpha}} \mathbf{q}^{\alpha} \cdot \operatorname{grad} \Theta^{\alpha} + \hat{e}^{\alpha} \right\} \geq 0. \quad (98)$$

Assuming that all constituents have the same constant Kelvin's temperature $\Theta^{\alpha} \equiv \Theta = \text{const.}$, the above inequality reduces to the so-called Clausius-Planck inequality

$$\mathcal{D}_{\text{int}} = \sum_{\alpha} \left[\mathbf{T}^{\alpha} \cdot \mathbf{L}_{\alpha} - \rho^{\alpha} (\psi^{\alpha})'_{\alpha} - \hat{\mathbf{p}}^{\alpha} \cdot \dot{\mathbf{x}}_{\alpha} - \hat{\rho}^{\alpha} \left(\psi^{\alpha} + \frac{1}{2} \dot{\mathbf{x}}_{\alpha} \cdot \dot{\mathbf{x}}_{\alpha} \right) \right] \geq 0 \quad (99)$$

which actually represents the non-negative internal dissipation $\mathcal{D}_{\text{int}} \geq 0$ of the overall isothermal process. Furthermore, if the constituents undergo neither an exchange of matter nor phase transitions due to any biological, chemical, or physical process, the mass production terms can be excluded, i.e., $\hat{\rho}^{\alpha} \equiv 0$. Thus, proceeding from non-polar φ^{α} yielding $\mathbf{T}^{\alpha} = (\mathbf{T}^{\alpha})^T$ and a purely mechanical process, (99) simplifies to

$$\mathcal{D}_{\text{int}} = \sum_{\alpha} [\mathbf{T}^{\alpha} \cdot \mathbf{D}_{\alpha} - \rho^{\alpha} (\psi^{\alpha})'_{\alpha} - \hat{\mathbf{p}}^{\alpha} \cdot \dot{\mathbf{x}}_{\alpha}] \geq 0, \quad (100)$$

where the interaction mechanisms are solely considered by the momentum productions $\hat{\mathbf{p}}^{\alpha}$. As examples of conceivable processes with $\hat{\rho}^{\alpha} \neq 0$, think of the growing of cells governed by metabolism or the melting of ice where solid ice transforms into liquid water.

3 Constitutive Modeling

3.1 The General Biphasic TPM Model

In this section, the entropy principle for mixtures is evaluated for a general binary porous medium and prepared for

the formulation of specific constitutive material equations. In particular, the general biphasic model incorporates the standard incompressible model which proceeds from materially incompressible constituents as well as the so-called hybrid model which additionally considers the compressibility of the fluid phase. Thus, the general biphasic model is capable of describing liquid and gas flows through deformable porous solids, such as they particularly occur in open-celled polymer foams.

3.1.1 Preliminaries

With regard to a comprehensible thermodynamical treatment, the biphasic model excludes thermal effects as well as any mass exchanges. In particular, the arising purely mechanical binary model is subject to the following assumptions:

- saturated solid-fluid mixture:

$$n^S + n^F = 1,$$

- materially incompressible solid:

$$\rho^{SR} = \text{const.},$$

- materially compressible or incompressible pore fluid,

- inert constituents:

$$\hat{\rho}^{\alpha} \equiv 0,$$

- dissipative solid material,
- non-polar materials:

$$\mathbf{T}^{\alpha} = (\mathbf{T}^{\alpha})^T,$$

- uniform body force:

$$\mathbf{b}^{\alpha} = \mathbf{b},$$

- quasi-static conditions:

$$\ddot{\mathbf{x}}_{\alpha} \equiv \mathbf{0}, \quad \ddot{\mathbf{x}} \equiv \mathbf{0},$$

- isothermal process:

$$\Theta^{\alpha} \equiv \Theta = \text{const.},$$

- viscous pore-fluid flow.

(101)

Following this, according to Sect. 2.3, the governing partial balance relations and the entropy principle for the biphasic mixture read:

- Solid mass balance \rightarrow solid volume balance:

$$\begin{aligned} (\rho^S)'_S + \rho^S \operatorname{div} \dot{\mathbf{x}}_S &= 0 \\ \rightarrow (n^S)'_S + n^S \operatorname{div} \dot{\mathbf{x}}_S &= 0, \end{aligned} \quad (102)$$

- Fluid mass balance:

$$(\rho^F)'_F + \rho^F \operatorname{div} \dot{\mathbf{x}}_F = 0, \quad (103)$$

- Partial momentum balances:

$$\begin{aligned} \mathbf{0} &= \operatorname{div} \mathbf{T}^S + \rho^S \mathbf{b} - \hat{\mathbf{p}}^F, \\ \mathbf{0} &= \operatorname{div} \mathbf{T}^F + \rho^F \mathbf{b} + \hat{\mathbf{p}}^F, \end{aligned} \quad (104)$$

- Clausius-Planck inequality:

$$\begin{aligned} \mathbf{T}^S \cdot \mathbf{D}_S + \mathbf{T}^F \cdot \mathbf{D}_F - \rho^S (\psi^S)'_S - \rho^F (\psi^F)'_F \\ - \hat{\mathbf{p}}^F \cdot \mathbf{w}_{FR} \geq 0. \end{aligned} \quad (105)$$

Herein, proceeding from the convenient assumption of a materially incompressible solid skeleton, the solid mass balance degenerates to a volume balance as $(n^S \rho^{SR})'_S = (n^S)'_S \rho^{SR}$ due to $(\rho^{SR})'_S \equiv 0$. Thus, one finds for the solidity n^S by analytical integration:

$$(n^S)'_S = -n^S \operatorname{div}' \mathbf{x}_S \quad \longrightarrow \quad n^S = n^S_{0S} \det \mathbf{F}_S^{-1}. \quad (106)$$

Furthermore, according to (91)₁ and (94)₂ together with the assumption $\hat{\rho}^\alpha \equiv 0$, $\hat{\mathbf{p}}^S = -\hat{\mathbf{p}}^F$ must hold due to the overall conservation of momentum. Moreover, proceeding from an overall isothermal, purely mechanical process, the energy balances are not considered.

3.1.2 Saturation Constraint and Effective Stress Principle

Throughout the thermodynamical process, the saturation constraint (3) must be fulfilled. This is guaranteed by adding the derivation of the saturation condition weighted by a Lagrangean multiplier \mathcal{P} to the entropy inequality of the biphasic model (105):

$$\begin{aligned} \mathbf{T}^S \cdot \mathbf{D}_S + \mathbf{T}^F \cdot \mathbf{D}_F - \rho^S (\psi^S)'_S - \rho^F (\psi^F)'_F \\ - \hat{\mathbf{p}}^F \cdot \mathbf{w}_{FR} - \mathcal{P} (n^S + n^F)'_S \geq 0. \end{aligned} \quad (107)$$

Therein, the additional constraint has the nature of a volume balance, and thus, \mathcal{P} will be easily identified as the excess pore-fluid pressure. For further investigations, the volumetric constraint is rewritten by replacing the derivatives $(n^\alpha)'_S$ with respective evolution equations. Since the volume fractions represent additional independent variables describing the local composition of the porous microstructure, there generally exist no distinct balance relations for the determination. However, due to the assumed solid incompressibility, $(n^S)'_S$ can be directly substituted by the solid volume balance (106)₁. Concerning the evolution of n^F , the concurrent consideration of compressible as well as incompressible pore-fluid behavior demands for a particular treatment. Therefore, the rate of change of the effective fluid density $(\rho^{FR})'_F$ is regarded as a free variable of the overall thermodynamical process. Then, after applying the product rule to

$(\rho^F)'_F = (n^F \rho^{FR})'_F$, the fluid balance of mass (103) yields a conditional equation for the porosity evolution, viz.:

$$(n^F)'_F = -\frac{n^F}{\rho^{FR}} (\rho^{FR})'_F - n^F \operatorname{div}' \mathbf{x}_F \quad \text{with } \rho^{FR} > 0. \quad (108)$$

Note that the treatment of $(\rho^{FR})'_F$ as a free variable is not a precarious assumption. Actually, it is a direct consequence of exploiting the fluid mass balance as an evolution equation for n^F since obviously no further balance exists for the determination of $(\rho^{FR})'_F$. Thus, with (106)₁, (108), and the relations

$$\begin{aligned} \operatorname{div}' \mathbf{x}_\alpha &= \mathbf{L}_\alpha \cdot \mathbf{I} = \mathbf{D}_\alpha \cdot \mathbf{I}, \\ (n^F)'_S &= (n^F)'_F - \operatorname{grad} n^F \cdot \mathbf{w}_{FR}, \end{aligned} \quad (109)$$

the additional constraint can be rewritten as

$$\begin{aligned} -\mathcal{P} (n^S + n^F)'_S &= \mathcal{P} \left[n^S \mathbf{D}_S \cdot \mathbf{I} + n^F \mathbf{D}_F \cdot \mathbf{I} + \frac{n^F}{\rho^{FR}} (\rho^{FR})'_F \right. \\ &\quad \left. + \operatorname{grad} n^F \cdot \mathbf{w}_{FR} \right]. \end{aligned} \quad (110)$$

Note that in the case of an incompressible pore fluid, i.e., $\rho^{FR} = \text{const.}$ yielding $(\rho^{FR})'_F \equiv 0$, the expression $(n^S + n^F)'_S$ naturally reduces to a continuity-like equation, viz., the volume balance of the standard incompressible biphasic model:

$$-(n^S + n^F)'_S = \operatorname{div} [(\mathbf{u}_S)'_S + n^F \mathbf{w}_{FR}] = 0. \quad (111)$$

Finally, inserting (110) into the dissipation inequality (107) yields

$$\begin{aligned} \overbrace{(\mathbf{T}^S + \mathcal{P} n^S \mathbf{I}) \cdot \mathbf{D}_S}^{\mathbf{T}_E^S} + \overbrace{(\mathbf{T}^F + \mathcal{P} n^F \mathbf{I}) \cdot \mathbf{D}_F}^{\mathbf{T}_E^F} - \rho^S (\psi^S)'_S \\ - \rho^F (\psi^F)'_F + \mathcal{P} \frac{n^F}{\rho^{FR}} (\rho^{FR})'_F \\ - \underbrace{(\hat{\mathbf{p}}^F - \mathcal{P} \operatorname{grad} n^F) \cdot \mathbf{w}_{FR}}_{\hat{\mathbf{p}}_E^F} \geq 0, \end{aligned} \quad (112)$$

where \mathbf{T}_E^S , \mathbf{T}_E^F , and $\hat{\mathbf{p}}_E^F$ are the so-called extra quantities which act as substitutes for the respective over- and under-braced terms. This is in full agreement with the classical concept of effective stresses which originally presumes that the effective soil stress in a geotechnical consolidation problem is determined by the total stress minus the excess pore pressure, cf. [32]. Accordingly, the extra terms

$$\begin{aligned} \mathbf{T}_E^S &= \mathbf{T}^S + \mathcal{P} n^S \mathbf{I}, & \mathbf{T}_E^F &= \mathbf{T}^F + \mathcal{P} n^F \mathbf{I}, \\ \hat{\mathbf{p}}_E^F &= \hat{\mathbf{p}}^F - \mathcal{P} \operatorname{grad} n^F \end{aligned} \quad (113)$$

represent effective field quantities for which suitable constitutive equations must be found. Thus, the effective stress principle enables the modular treatment of specific solid skeleton, pore-fluid, and interaction properties.

3.1.3 Constitutive Variables

To close the general biphasic model under study, a convenient set of constitutive relations must be found for the energy functions and the extra quantities satisfying the entropy principle in form of (112). Thus, based on the fundamental principles of constitutive modeling, namely *determinism*, *local action*, *equipresence*, *frame indifference*, and *dissipation*, the following set of response functions must be determined:

$$\mathcal{R} = \{\psi^S, \psi^F, \mathbf{T}_E^S, \mathbf{T}_E^F, \hat{\mathbf{p}}_E^F\}. \quad (114)$$

According to the principle of equipresence, each of these response functions may depend on a common set \mathcal{V} of independent constitutive or process variables, i.e.,

$$\mathcal{R} := \mathcal{R}(\mathcal{V}) \quad \text{with } \mathcal{V} = \mathcal{V}^S \cup \mathcal{V}^F \quad (115)$$

as the union of sets of independent state variables of the solid and the fluid constituent. Following the arguments of Ehlers [42], proceeding from assumptions (101) and initially homogeneous constituents φ^α , the partial set of process variables describing the behavior of a potentially inelastic solid skeleton with dissipative properties is found as

$$\mathcal{V}^S = \{\mathbf{F}_S, \text{Grad}_S \mathbf{F}_S, \mathbf{Q}_n^S, \text{Grad}_S \mathbf{Q}_n^S\}. \quad (116)$$

Therein, based on the thermodynamics with internal state variables [23, 137], \mathbf{Q}_n^S represents a finite number of independent internal state or history variables which have to be implicitly defined via respective evolution equations:

$$(\mathbf{Q}_n^S)' = \mathcal{F}_n(\mathcal{V}^S), \quad n = 1, \dots, N. \quad (117)$$

Hence, the internal variables are assumed to govern the inelastic state of the solid matrix, i.e., they represent the memory of φ^S depending on the process history (cf. [87]). Here, they are introduced as tensor-valued fields, but, in general, also scalar or vector-valued functions can be introduced. Moreover, the set of objective (frame-indifferent) constitutive variables for a possibly compressible pore fluid reads

$$\mathcal{V}^F = \{\mathbf{w}_{FR}, \mathbf{D}_F, n^F, \text{grad } n^F, \rho^{FR}, \text{grad } \rho^{FR}\}. \quad (118)$$

Thus, the overall set of independent process variables is found as

$$\mathcal{V} = \{\mathbf{F}_S, \text{Grad}_S \mathbf{F}_S, \mathbf{Q}_n^S, \text{Grad}_S \mathbf{Q}_n^S, \mathbf{w}_{FR}, \mathbf{D}_F, \rho^{FR}, \text{grad } \rho^{FR}\}, \quad (119)$$

where n^F and $\text{grad } n^F$ are removed from the list as they are directly coupled to the skeleton deformation via (3). In particular, with the aid of (106)₂, it can be shown that

$$\begin{aligned} n^F &= 1 - n^S = 1 - n_{0S}^S \det \mathbf{F}_S^{-1}, \\ \text{grad } n^F &= -\text{grad } n^S \\ &= n_{0S}^S (\det \mathbf{F}_S^{-1}) \mathbf{F}_S^{T-1} (\mathbf{F}_S^{T-1} \text{Grad}_S \mathbf{F}_S)^{\perp}. \end{aligned} \quad (120)$$

Moreover, it is easily concluded that in the case of a materially incompressible pore fluid, additionally, ρ^{FR} and $\text{grad } \rho^{FR}$ can be removed from \mathcal{V}^F and \mathcal{V} , respectively. In this context, note that \mathcal{V}^S , \mathcal{V}^F , and, as a consequence, \mathcal{V} only represent specific subsets of the fundamental constitutive variables for general mixtures. However, the second-grade character of multiphase materials remains by inclusion of the gradients of the considered basic variables. For further particulars, see the more comprehensive works of Ehlers [38, 39, 42].

To continue, regarding the constituent free energies, further *a priori* constitutive assumptions can be made. Proceeding from the *principle of phase separation* [38], the energy potential ψ^α of φ^α only depends on the non-dissipative variables included into the process by the respective constituent itself without circumventing the principle of equipresence. Moreover, according to Bowen [14, 15], the second-grade character of multiphase mixtures is only associated with the involved production terms. Thus, it is supposed that

$$\begin{aligned} \left. \begin{aligned} \psi^S &= \psi^S(\mathcal{V}^S) \\ \psi^F &= \psi^F(\mathcal{V}^F) \end{aligned} \right\} \\ \longrightarrow \quad \left\{ \begin{aligned} \psi^S &= \psi^S(\mathbf{F}_S, \mathbf{Q}_n^S) \quad \text{with } n = 1, \dots, N, \\ \psi^F &= \psi^F(n^F, \rho^{FR}) \end{aligned} \right. \longrightarrow \psi^F = \psi^F(\rho^{FR}), \end{aligned} \quad (121)$$

where, additionally, the dependence of ψ^F on the porosity n^F is constitutively neglected because of the assumption that the energy potential of a fluid does not recognize the domain on which the fluid exists [42]. Note that a general evaluation of the mixture entropy principle with $\psi^\alpha = \psi^\alpha(\mathcal{V})$ would recover assumptions (121) as a natural result of the binary model.

3.1.4 Evaluation of the Entropy Inequality

In the preceding, a convenient reduction of the set of process variables is achieved by *a priori* constitutive assumptions based on logical deduction and experience. Hence, the effort to evaluate the entropy principle is kept to a minimum. It is now the goal of the evaluation procedure to derive logical consequences from the mixture entropy inequality in order to find constitutive equations which restrict the admissible

processes in the mixture body $\mathcal{B} = \mathcal{B}^S \cup \mathcal{B}^F$ consisting of the supposed constituent materials. Here, in order to satisfy the dissipation inequality in form of (112), the approved evaluation procedure of Coleman and Noll [25] is applied (see also [13, 33, 38]).

To begin with, proceeding from the assumed functional dependencies of the constituent free energy densities (121), the corresponding material time derivatives read

$$\begin{aligned} (\psi^S)'_S &= \frac{\partial \psi^S}{\partial \mathbf{F}_S} \cdot (\mathbf{F}_S)'_S + \sum_{n=1}^N \frac{\partial \psi^S}{\partial \mathbf{Q}_n^S} \cdot (\mathbf{Q}_n^S)'_S, \\ (\psi^F)'_F &= \frac{\partial \psi^F}{\partial \rho^{FR}} (\rho^{FR})'_F. \end{aligned} \quad (122)$$

By inserting the above derivatives into the dissipation inequality (112) together with the definition of the spatial velocity gradient (31), one obtains

$$\begin{aligned} & \left(\mathbf{T}_E^S - \rho^S \frac{\partial \psi^S}{\partial \mathbf{F}_S} \mathbf{F}_S^T \right) \cdot \mathbf{L}_S - \rho^S \sum_{n=1}^N \frac{\partial \psi^S}{\partial \mathbf{Q}_n^S} \cdot (\mathbf{Q}_n^S)'_S \\ & + \mathbf{T}_E^F \cdot \mathbf{D}_F + \left(\mathcal{P} \frac{n^F}{\rho^{FR}} - \rho^F \frac{\partial \psi^F}{\partial \rho^{FR}} \right) (\rho^{FR})'_F \\ & - \hat{\mathbf{p}}_E^F \cdot \mathbf{w}_{FR} \geq 0. \end{aligned} \quad (123)$$

The validity of this inequality can now be guaranteed following the standard arguments. Accordingly, at a particular time, the included constitutive variables are locally determined, but their temporal derivatives as free variables can be assigned arbitrarily depending on the ongoing process. Thus, the factors belonging to the free variables $\mathbf{L}_S = (\mathbf{F}_S)'_S \mathbf{F}_S^{-1}$ and $(\rho^{FR})'_F$ must vanish in order to satisfy the equality condition which holds in the state of thermodynamic equilibrium. Note that the rates of the internal variables $(\mathbf{Q}_n^S)'_S$ are not to be considered as free variables of the process since they have to be defined by evolution equations associated with the intrinsic dissipation mechanisms of φ^S . However, according to Coleman and Gurtin [23], each dissipative system tends towards thermodynamic equilibrium ($\mathcal{D}_{\text{int}} = 0$) implying that also the internal state variables reach equilibrium, i.e.,

$$\lim_{t \rightarrow \infty} \mathbf{Q}_n^S = \mathbf{Q}_n^{*S}, \quad n = 1, \dots, N. \quad (124)$$

Thus, the considered biphase mixture is in an equilibrium state, whenever

$$\begin{aligned} (\mathbf{Q}_n^S)'_S &= \mathcal{F}_n(\mathbf{F}_S, \mathbf{Q}_n^{*S}) = \mathbf{0}, \\ \hat{\mathbf{D}}_F &= \mathbf{0}, \quad \mathbf{w}_{FR} = \mathbf{0} \end{aligned} \quad (125)$$

where $(\cdot)^*$ indicates the equilibrium quantities. Then, from [23]'s *equation of internal equilibrium* [23, p. 602], it can be consequently deduced that

$$\left. \frac{\partial \psi^S(\mathbf{F}_S, \mathbf{Q}_n^S)}{\partial \mathbf{Q}_n^S} \right|_{\mathbf{Q}_n^S = \mathbf{Q}_n^{*S}} = \mathbf{0} \quad \longrightarrow \quad \psi^{*S} = \psi^S(\mathbf{F}_S), \quad (126)$$

which means that for a sufficiently slow process or as $t \rightarrow \infty$, the dissipative solid skeleton actually behaves perfectly elastic.

Following the above, by claiming the terms in parentheses to vanish, the solid extra stress tensor is equivalently determined by

$$\begin{aligned} \mathbf{T}_E^S &= \rho^S \frac{\partial \psi^S}{\partial \mathbf{F}_S} \mathbf{F}_S^T, \quad \boldsymbol{\tau}_E^S = \rho_{0S}^S \frac{\partial \psi^S}{\partial \mathbf{F}_S} \mathbf{F}_S^T, \\ \mathbf{P}_E^S &= \rho_{0S}^S \frac{\partial \psi^S}{\partial \mathbf{F}_S}, \quad \mathbf{S}_E^S = \rho_{0S}^S \mathbf{F}_S^{-1} \frac{\partial \psi^S}{\partial \mathbf{F}_S}, \end{aligned} \quad (127)$$

where $\rho_{0S}^S = n_{0S}^S \rho^{SR}$ is the partial solid density with respect to the solid reference configuration. In this context, one commonly proceeds from a scalar-valued strain-energy function $\mathcal{W}^S := \rho_{0S}^S \psi^S$ which represents the elastic potential or the stored elastic energy in *hyperelasticity* and is defined per unit reference volume rather than per unit mass.

To continue, from the second term in parentheses of (123) the Lagrangean multiplier \mathcal{P} is easily identified as the effective pore-fluid pressure p^{FR} or simply p :

$$p = p^{FR} := \mathcal{P} = (\rho^{FR})^2 \frac{\partial \psi^F}{\partial \rho^{FR}}. \quad (128)$$

In the case of an incompressible pore fluid, it is easily deduced that $p = p^{FR}$ degenerates to an unspecified pore-fluid pressure in the sense of a constraining force which has to be determined from the boundary conditions of the boundary-value problem under study.

The remainder of the Clausius-Planck inequality (123), the so-called *residual inequality*,

$$-\rho^S \sum_{n=1}^N \frac{\partial \psi^S}{\partial \mathbf{Q}_n^S} \cdot (\mathbf{Q}_n^S)'_S + \mathbf{T}_E^F \cdot \mathbf{D}_F - \hat{\mathbf{p}}_E^F \cdot \mathbf{w}_{FR} \geq 0, \quad (129)$$

represents the irreversible or dissipative parts responsible for the non-equilibrium states ($\mathcal{D}_{\text{int}} > 0$) of the binary model. The residual inequality essentially serves as a restrictive condition for the formulation of admissible constitutive laws for $(\mathbf{Q}_n^S)'_S$, \mathbf{T}_E^F , and $\hat{\mathbf{p}}_E^F$. Moreover, it reveals the overlay of the dissipative solid and fluid properties during general deformation processes which gives rise to a challenging model adaption when applied to real material behavior. For the subsequent treatment, it is convenient to proceed from the sufficient condition that each expression of the residual inequality (129) satisfies the inequality itself. This is guaranteed

if each expression yields a positive definite quadratic form which can be accomplished by assuming the following natural proportionalities:

$$(\mathcal{Q}_n^S)' \propto -\rho^S \frac{\partial \psi^S}{\partial \mathcal{Q}_n^S}, \quad (130)$$

$$\mathbf{T}_E^F \propto \mathbf{D}_F, \quad \hat{\mathbf{p}}_E^F \propto -\mathbf{w}_{FR}.$$

However, further investigations require detailed information about the constituent materials, particularly concerning the type of solid inelasticity, the pore-fluid behavior, and the solid-fluid interaction mechanisms.

3.2 Viscoelastic Solid Constituent

3.2.1 Introduction to Solid Viscoelasticity

A solid material is said to be viscoelastic if it exhibits a rate-dependent material response without showing an equilibrium hysteresis. Accordingly, viscoelastic solids show distinct relaxation and creep behavior as well as frequency-dependent stiffness and damping effects which makes them indispensable for applications where continual energy absorption is demanded. Particularly, the relaxation and creep response originally led to the description as *materials with fading memory* with the fading memory represented by means of rate-dependent functionals implying that the current state of stress (or strain) depends on the whole strain (or stress) history [24]. Following this, to formally establish the 1-d effective stress response $\sigma_E^S(t)$ of a linear viscoelastic solid skeleton to a strain-driven uniaxial process, the current stress can be expressed as a functional of the whole solid strain history

$$\sigma_E^S(t) = \mathcal{F}[\varepsilon_S(\tau)] \quad \text{with } -\infty < \tau \leq t. \quad (131)$$

Excluding aging effects and assuming that the functional is linear and the strain history is represented by a series of

steps, application of the Boltzmann superposition principle yields the known integral representation of linear solid viscoelasticity [20]:

$$\begin{aligned} \sigma_E^S(t) &:= \mathcal{G}^S(t - \tau) * d\sigma_E^S(\tau) \\ &= \int_{-\infty}^t \mathcal{G}^S(t - \tau) \frac{d\varepsilon_S(\tau)}{d\tau} d\tau. \end{aligned} \quad (132)$$

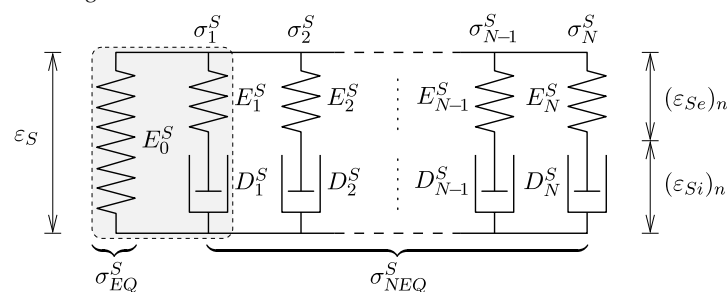
Therein, \mathcal{G}^S represents a constitutive relaxation function which essentially serves as a weighting function for the past deformation process, and thus, represents the memory of the material. Moreover, the symbol “*” denotes a convolution product (cf. [65]). By analogous considerations, one finds the dual formulation for seeking the linear solid strain response $\varepsilon_S(t)$ to a subjected effective stress on the solid skeleton as

$$\begin{aligned} \varepsilon_S(t) &:= \mathcal{J}^S(t - \tau) * d\varepsilon_S(\tau) \\ &= \int_{-\infty}^t \mathcal{J}^S(t - \tau) \frac{d\sigma_E^S(\tau)}{d\tau} d\tau \end{aligned} \quad (133)$$

with \mathcal{J}^S representing the so-called creep or retardation function. However, in order to render the fading memory property more precisely, the relaxation and creep functions \mathcal{G}^S and \mathcal{J}^S , respectively, have to be specified. In principle, any form of the relaxation or creep function is conceivable if it fits the observed material behavior. Accordingly, many different empirical formulations have been suggested ranging from error functions of probability theory [10] over fractional power forms [141] to finite uniform relaxation spectra [59]. However, a more physically-based selection of \mathcal{G}^S and \mathcal{J}^S can be motivated by reverting to rheological models where, in this contribution, the generalized Maxwell model as depicted in (134) is the convenient choice. The usage of rheological models to phenomenologically display viscoelastic material behavior is directly connected with the differential representation of the material equations which is given preference for the following considerations.

1- and 3-d linear solid viscoelasticity

Rheological model:



- generalized Maxwell model ($1+2N$ element linear viscoelastic solid)
- $N = 1$: Poynting-Thomson model (standard linear viscoelastic solid)

Equilibrium:

$$\begin{aligned}\sigma_E^S &= \sigma_{EQ}^S + \sigma_{NEQ}^S & \sigma_E^S &= \sigma_{EQ}^S + \sigma_{NEQ}^S \\ \sigma_{NEQ}^S &= \sum_{n=1}^N \sigma_n^S & \sigma_{NEQ}^S &= \sum_{n=1}^N \sigma_n^S \\ \sigma_n^S &= (\sigma_{Se}^S)_n = (\sigma_{Si}^S)_n & \sigma_n^S &= (\sigma_{Se}^S)_n = (\sigma_{Si}^S)_n\end{aligned}$$

Kinematics:

$$\varepsilon_S = (\varepsilon_{Se})_n + (\varepsilon_{Si})_n \quad \mathbf{e}_S = (\mathbf{e}_{Se})_n + (\mathbf{e}_{Si})_n$$

Constitutive laws^a:

$$\begin{aligned}\sigma_{EQ}^S &= E_0^S \varepsilon_S & \sigma_{EQ}^S &= \mathbf{E}_0^S \mathbf{e}_S, \quad \mathbf{E}_0^S = 2\mu_0^S \mathbf{I} + \Lambda_0^S \mathbf{I}_{tr} \\ (\sigma_{Se}^S)_n &= E_n^S (\varepsilon_{Se})_n & (\sigma_{Se}^S)_n &= \mathbf{E}_n^S (\mathbf{e}_{Se})_n, \quad \mathbf{E}_n^S = 2\mu_n^S \mathbf{I} + \Lambda_n^S \mathbf{I}_{tr} \\ (\sigma_{Si}^S)_n &= D_n^S [(\varepsilon_{Si})_n]'_S & (\sigma_{Si}^S)_n &= \mathbf{D}_n^S [(\mathbf{e}_{Si})_n]'_S, \quad \mathbf{D}_n^S = 2\eta_n^S \mathbf{I} + \zeta_n^S \mathbf{I}_{tr}\end{aligned}$$

Evolution equations:

$$\begin{aligned}[(\varepsilon_{Si})_n]'_S &= (\tau_n^S)^{-1} [\varepsilon_S - (\varepsilon_{Si})_n] & [(\mathbf{e}_{Si})_n]'_S &= (\boldsymbol{\tau}_n^S)^{-1} [\mathbf{e}_S - (\mathbf{e}_{Si})_n] \\ \tau_n^S &:= D_n^S / E_n^S : \text{relaxation times} & \boldsymbol{\tau}_n^S &:= (\mathbf{E}_n^S)^{-1} \mathbf{D}_n^S : \text{relaxation tensors}\end{aligned}$$

^aWith the 4th-order fundamental tensors $\mathbf{I} := (\mathbf{I} \otimes \mathbf{I})^T$ and $\mathbf{I}_{tr} := (\mathbf{I} \otimes \mathbf{I})$

Proceeding from the notions and the governing equations on the left hand side in (134), it is seen that in addition to the additive kinematics in the Maxwell elements, the parallel structure yields an additive composition of the stresses. In particular, the linear solid extra stress is composed of the elastic stress response σ_{EQ}^S of the single spring and the sum of the transient viscoelastic overstresses σ_n^S ($n = 1, \dots, N$) collected in σ_{NEQ}^S . Usually, σ_{EQ}^S is referred to as equilibrium (EQ) stress associated with the time infinity property of the single spring, whereas σ_{NEQ}^S represents the non-equilibrium (NEQ) part describing the perturbation away from thermodynamic equilibrium. Following this, the linear viscoelastic material response can be easily visualized. For example, taking only one Maxwell element into consideration ($N = 1$), i.e., restricting the presentation to the so-called Poynting-Thomson model (cf. (134)), the descriptive differential equation is found by rephrasing the time derivative of the equilibrium condition for the solid extra stress by use of the compatibility and constitutive relations such that only the external state variables σ_E^S and ε_S as well as their rates remain. Thus, assuming constant spring elasticities $E_0^S, E_1^S > 0$ and a constant dashpot viscosity $D_1^S > 0$, after some algebraic manipulations, one finally obtains the first-order ordinary differential equation (ODE)

$$\sigma_E^S + \tau_1^S (\sigma_E^S)'_S = E_0^S \varepsilon_S + \tau_1^S (E_0^S + E_1^S) (\varepsilon_S)'_S \quad (135)$$

with $\tau_1^S = D_1^S / E_1^S > 0$ representing the relaxation time constant of the single Maxwell element. The characteristic behavior of the standard linear viscoelastic model described by the above differential equation is best displayed by regarding its response to subjected step loads in the strain or the stress variable. The readily determined solution of the ODE (135) due to a strain step $\varepsilon_S(t) = \varepsilon_{S0} H(t)$ takes the form

$$\sigma_E^S(t) = \underbrace{(E_0^S + E_1^S e^{-t/\tau_1^S})}_{\mathcal{G}^S(t)} \varepsilon_{S0} H(t) \quad (136)$$

and for a prescribed stress step $\sigma_E^S(t) = \sigma_{E0}^S H(t)$, it follows

$$\begin{aligned}\varepsilon_S(t) &= \underbrace{\left(\frac{1}{E_0^S + E_1^S} + \frac{E_1^S}{E_0^S (E_0^S + E_1^S)} (1 - e^{-t/\tau_1^S}) \right)}_{\mathcal{J}^S(t)} \sigma_{E0}^S H(t).\end{aligned} \quad (137)$$

Herein, $H(t)$ is the Heaviside step function with the properties $H(t) = 0$ if $t < 0$ and $H(t) = 1$ if $t \geq 0$, ε_{S0} and σ_{E0}^S are the respective strain and stress amplitudes, and $\bar{\tau}_1^S = \tau_1^S (E_0^S + E_1^S) / E_0^S > 0$ denotes the retardation time constant. In (136) and (137), the constitutive relaxation and retardation functions $\mathcal{G}^S(t)$ and $\mathcal{J}^S(t)$ are now easily identified. It is directly seen that they describe an instantaneous

elastic response followed by a time-delayed monotonic relaxation or creep behavior with the decaying exponential function representing the fading memory. The general behavior of the Poynting-Thomson model is depicted in Fig. 5. The subfigures (a) and (b) show the distinct relaxation and retardation (creep) responses to subjected step loads as given in (136) and (137) where the relaxation and retardation times can directly be identified. Moreover, subfigure (c) shows the hysteretic stress response due to a cyclic loading at a constant strain rate. The area enclosed by the hysteresis curve is a measure of the dissipated energy during the deformation process. Subfigure (d) finally displays the frequency dependent stiffness and damping effects of viscoelastic solid materials. It is seen that the hysteresis loop expands when the strain rate is increased, thereby increasing the energy absorption and the transient stiffness.

Remark Note that the consideration of more Maxwell elements ($N > 1$) does not change the principle shape of the relaxation and creep curves in Fig. 5. Actually, the order of the ODE (135) is increased by one with each additional Maxwell branch but relaxation functions \mathcal{G}^S always decrease monotonously to an asymptotic end value $\mathcal{G}_{EQ}^S(t \rightarrow \infty)$, i.e., $(\mathcal{G}^S)'_S \leq 0$, whereas retardation functions \mathcal{J}^S are monotone increasing functions with an asymptotic end value $\mathcal{J}_{EQ}^S(t \rightarrow \infty)$, i.e., $(\mathcal{J}^S)'_S \geq 0$. Typically, the number of Maxwell elements is chosen according to the considered frequency range; as a rule of thumb, approximately one

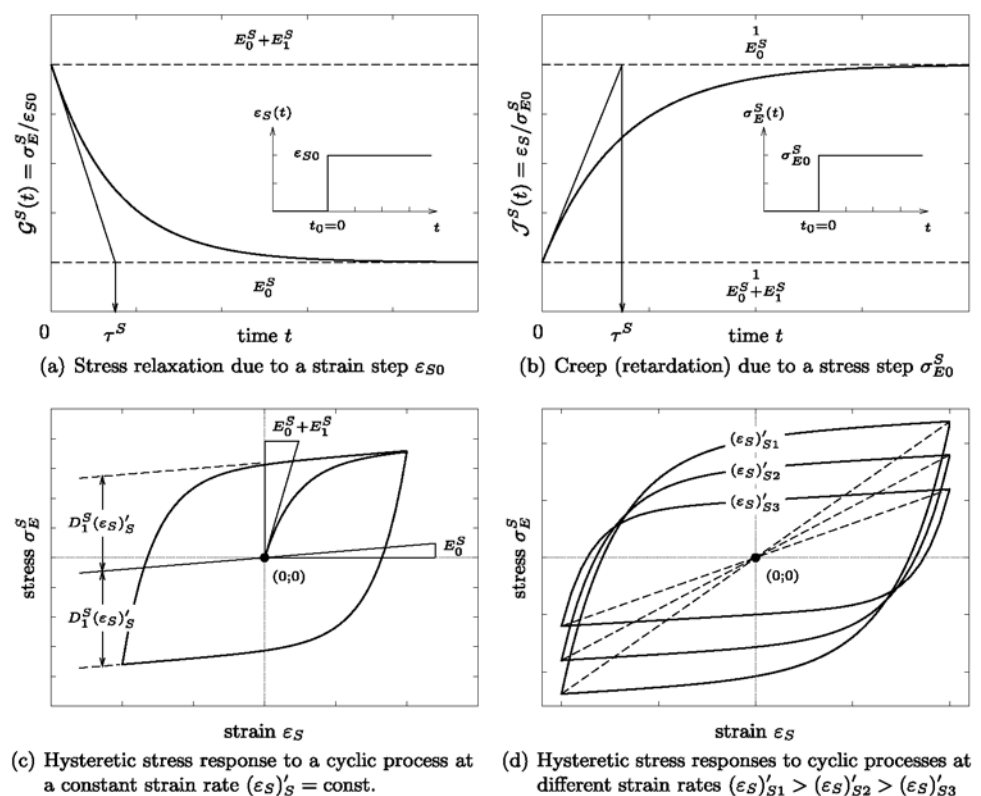
Maxwell element per decade in frequency (cf. [86]). However, one has to be aware of the identification problem of the included material parameters, which is the major drawback compared to the integral formulations with continuous relaxation spectra.

Recalling Sect. 3.1.3 on constitutive variables, the simple linear 1-d model can further be used to find additional assumptions for the solid free energy. Particularly, from the additive composition of the solid extra stress, it is easily deduced that

$$\begin{aligned}\sigma_E^S &= \sigma_{EQ}^S + \sigma_{NEQ}^S = E_0^S \varepsilon_S + E_1^S \varepsilon_{Se} \\ &= \underbrace{\frac{\partial}{\partial \varepsilon_S} \left(\frac{1}{2} E_0^S \varepsilon_S^2 \right)}_{\psi_{EQ}^S(\varepsilon_S)} + \underbrace{\frac{\partial}{\partial \varepsilon_{Se}} \left(\frac{1}{2} E_1^S \varepsilon_{Se}^2 \right)}_{\psi_{NEQ}^S(\varepsilon_{Se})}.\end{aligned}\quad (138)$$

Thus, in view of the fact that energy can only be stored in the elastic springs, the constitutive split of the solid energy potential in analogy to the stresses into an equilibrium part $\psi_{EQ}^S(\varepsilon_S)$ and a non-equilibrium part $\psi_{NEQ}^S(\varepsilon_{Se})$ is a natural choice. However, based on the internal variable concept, the reasonably reduced dependencies of the solid free energy given in (121) must be brought into accordance with the above findings. This can be accomplished by formal decomposition of the infinitesimal 1-d representation of ψ^S into an equilibrium part and a *pseudo potential* depending on the

Fig. 5 Characteristic behavior of the standard linear viscoelastic solid model: (a) and (b) are the plots of the solution functions (136) and (137), (c) and (d) are achieved through numerical integration of (135)



internal variables:

$$\begin{aligned}\psi^S &= \psi^S(\mathbf{F}_S, \mathbf{Q}_n^S) \\ \longrightarrow \psi^S(\varepsilon_S, \mathbf{Q}_n^S) &= \psi_{EQ}^S(\varepsilon_S) + \psi^S(\mathbf{Q}_n^S).\end{aligned}\quad (139)$$

Then, identifying the dashpot deformation as the scalar-valued, strain-equivalent internal variable of the Poynting-Thomson model, i.e., $\mathbf{Q}_1^S = \varepsilon_{Si}$, the dependency of the pseudo potential $\psi(\mathbf{Q}_1^S) = \psi(\varepsilon_{Si})$ is rewritten by use of the additive kinematics yielding

$$\psi^S(\varepsilon_{Si}) \longrightarrow \psi^S(\varepsilon_S, \varepsilon_{Se}) \longrightarrow \psi_{NEQ}^S(\varepsilon_{Se}), \quad (140)$$

where it is assumed that the dependency on the total solid strain ε_S is completely included in the equilibrium part $\psi_{EQ}^S(\varepsilon_S)$. This is in full agreement with Coleman and Gurtin's equation of internal equilibrium (126) as in the state of thermodynamic equilibrium with $\tau_1^S > 0$ the following relations hold:

$$\begin{aligned}(\varepsilon_{Si}^*)'_S &= (\tau_1^S)^{-1} (\varepsilon_S^* - \varepsilon_{Si}^*) = 0 \\ \longrightarrow \varepsilon_{Si}^* &\equiv \varepsilon_S^* = \text{const.} \longrightarrow \varepsilon_{Se}^* \equiv 0, \\ \psi^S &= \psi^S(\varepsilon_S^*, \varepsilon_{Se}^*) = \psi^S(\varepsilon_S^*) \equiv \psi_{EQ}^S(\varepsilon_S^*), \\ \psi_{NEQ}^S &(\varepsilon_{Se}^*) \equiv 0.\end{aligned}\quad (141)$$

Note that a theoretical relaxation time $\tau_1^S = 0$ due to $D_1^S = 0$ would imply instantaneous relaxation meaning that the Maxwell element does not contribute to the response of the model. Thus, the model would behave purely elastic governed by the single spring, and hence, is always in equilibrium. In conclusion, it is convenient to proceed from the following form of the free energy for the $1+2N$ element linear viscoelastic solid model:

$$\begin{aligned}\psi^S[\varepsilon_S, \mathbf{Q}_n^S] &= (\varepsilon_{Si})_n \\ \longrightarrow \psi^S[\varepsilon_S, (\varepsilon_{Se})_n] &= \psi_{EQ}^S(\varepsilon_S) + \psi_{NEQ}^S[(\varepsilon_{Se})_n].\end{aligned}\quad (142)$$

Moreover, based on the 1-d rheological structure of the generalized Maxwell model, 3-d linear viscoelastic material behavior can be described by formal extension of the governing scalar equations to three dimensions. As depicted on the right hand side in (134), the 3-d extension of the infinitesimal theory is straightforward by simply replacing the scalar quantities with their tensorial counterparts. In addition to the already defined infinitesimal strain tensors given in (16) and (17), $\boldsymbol{\sigma}_E^S \approx \mathbf{T}_E^S$ denotes the linear solid extra stress tensor of the infinitesimal theory with $\boldsymbol{\sigma}_{EQ}^S$ and $\boldsymbol{\sigma}_{NEQ}^S = \sum_n \boldsymbol{\sigma}_n^S$ as the equilibrium and non-equilibrium parts. The elastic stresses are determined by linear Hooke-type elasticity laws with the positive definite 4th-order elasticity tensors $(\mathbf{E}_0^S)^4$ and $(\mathbf{E}_n^S)^4$, wherein μ_0^S, Λ_0^S and μ_n^S, Λ_n^S

are the respective Lamé constants. As isotropic tensor functions, the positive definite viscosity tensors $(\mathbf{D}_n^S)^4$ are given analogously to the elasticity tensors with η_n^S and ζ_n^S representing the viscosity parameters. Thus, the porous solid matrix is allowed to be linear viscoelastic in both shear and bulk deformation with independent relaxation and retardation properties. This motivates the introduction of 4th-order relaxation tensors $(\boldsymbol{\tau}_n^S)^4$ to control the rate of the 3-d inelastic strain evolution instead of using scalar relaxation constants such as in the 1-d case. In this context, it should be noted that by decomposition of the solid extra stress tensor into *deviatoric* and *spheric* parts, it is possible to uncouple the governing viscoelastic equations in order to handle them separately in analogy to the 1-d formulation. A more detailed discussion of the procedure, its numerical treatment and application within the TPM approach, e.g., for the description of soft biological tissues, can be found in [46, 47]. For further particulars, see also [20, 55, 65, 136].

3.2.2 Aspects of Finite Solid Viscoelasticity

For the description of the intrinsic dissipative phenomena of the porous solid skeleton, an appropriate finite viscoelastic material formulation is required. Therefore, the solid strain energy \mathcal{W}^S as the response function that governs the hyperelastic solid material behavior must be specified accounting for all essential large strain properties of φ^S . Proceeding from the generalized Maxwell model as the convenient phenomenological basis, one can directly follow the arguments of the 1-d linear viscoelasticity theory given in (139)–(142). Accordingly, the dependencies of the solid free-energy function of the finite theory are rewritten by use of the multiplicative geometric concept (18) with the inelastic deformation gradients $(\mathbf{F}_{Si})_n$ identified as the internal variables associated with the dashpot deformations:

$$\begin{aligned}\psi^S(\mathbf{F}_S, \mathbf{Q}_n^S) &\longrightarrow \psi^S[\mathbf{F}_S, (\mathbf{F}_{Si})_n] \\ &\longrightarrow \psi^S[\mathbf{F}_S, (\mathbf{F}_{Se})_n].\end{aligned}\quad (143)$$

Moreover, adopting the constitutive split of ψ^S of the 1-d infinitesimal case (142), one assumes a solid strain-energy function of the form

$$\mathcal{W}^S[\mathbf{F}_S, (\mathbf{F}_{Se})_n] = \mathcal{W}_{EQ}^S(\mathbf{F}_S) + \mathcal{W}_{NEQ}^S[(\mathbf{F}_{Se})_n]. \quad (144)$$

Before proceeding, it should be noted that the specific choice of \mathcal{W}_{EQ}^S and \mathcal{W}_{NEQ}^S is constrained by certain important properties which are not to be sacrificed for obtaining rigorous results. In particular, the strain-energy function must ensure *polyconvexity*, certain *growth conditions*, and *objectivity*. These conditions and the resulting restrictions on the constitutive shape of \mathcal{W}^S are briefly discussed in the following paragraphs.

Polyconvexity The solution of boundary-value problems (BVP) using the presented model will be based on the solution of some *variational problem* by searching a deformed configuration in which the energy of the system is a minimum under prescribed boundary conditions. Therefore, the stored energy must be chosen in such a way that the existence of minimizers of the energy functional is guaranteed. A necessary and sufficient condition is *quasiconvexity* introduced by Morrey [96] claiming isothermal stability of an all-round fixed homogeneous body of hyperelastic material by ensuring the energy functional to be weakly lower semicontinuous. However, quasiconvexity as an integral inequality is complicated to handle and disallows singularities which cannot be reconciled with finite material behavior. In this regard, Ball [6] established the more practical notion of *polyconvexity* which is a sufficient condition for quasiconvex functions that can be evaluated locally and allows infinite function values. In particular, a scalar-valued tensor function $\Psi(\mathbf{F}_S)$ is said to be polyconvex if it can be expressed as a convex function of subdeterminants of its tensorial variables, viz.,

$$\Psi(\mathbf{F}_S) = \Psi(\mathbf{F}_S, \text{cof } \mathbf{F}_S, \det \mathbf{F}_S) \\ \text{or } \Psi(\mathbf{F}_S) = \Psi_I(\mathbf{F}_S) + \Psi_a(\text{cof } \mathbf{F}_S) + \Psi_v(\det \mathbf{F}_S), \quad (145)$$

where the second equality denotes an additive polyconvex function with each part convex in the associated variable. Assuming Ψ to be twice differentiable, the convexity is easily verified by showing that the second derivative with respect to each variable is positive semidefinite. Following this, \mathcal{W}^S is polyconvex by choosing its parts of the form

$$\mathcal{W}_{EQ}^S(\mathbf{F}_S) = \mathcal{W}_{EQ}^S(\mathbf{F}_S, \text{cof } \mathbf{F}_S, \det \mathbf{F}_S), \\ \mathcal{W}_{NEQ}^S[(\mathbf{F}_{Se})_n] = \mathcal{W}_{NEQ}^S[(\mathbf{F}_{Se})_n, \text{cof } (\mathbf{F}_{Se})_n, \det (\mathbf{F}_{Se})_n] \quad (146)$$

with the properties that $\forall \mathbf{H} \neq \mathbf{0}$

$$\begin{aligned} \frac{\partial^2 \mathcal{W}_{EQ}^S}{\partial \mathbf{F}_S \otimes \partial \mathbf{F}_S} \cdot (\mathbf{H} \otimes \mathbf{H}) &\geq 0, \\ \frac{\partial^2 \mathcal{W}_{NEQ}^S}{\partial (\mathbf{F}_{Se})_n \otimes \partial (\mathbf{F}_{Se})_n} \cdot (\mathbf{H} \otimes \mathbf{H}) &\geq 0, \\ \frac{\partial^2 \mathcal{W}_{EQ}^S}{\partial \text{cof } \mathbf{F}_S \otimes \partial \text{cof } \mathbf{F}_S} \cdot (\mathbf{H} \otimes \mathbf{H}) &\geq 0, \\ \frac{\partial^2 \mathcal{W}_{NEQ}^S}{\partial \text{cof } (\mathbf{F}_{Se})_n \otimes \partial \text{cof } (\mathbf{F}_{Se})_n} \cdot (\mathbf{H} \otimes \mathbf{H}) &\geq 0, \\ \frac{\partial^2 \mathcal{W}_{EQ}^S}{\partial (\det \mathbf{F}_S)^2} \geq 0, \quad \frac{\partial^2 \mathcal{W}_{NEQ}^S}{\partial [(\det \mathbf{F}_{Se})_n]^2} &\geq 0. \end{aligned} \quad (147)$$

From a continuum mechanical perspective, polyconvexity claims local material stability with regard to perturbations in length, area, and volume as \mathbf{F}_S , $\text{cof } \mathbf{F}_S$, and $\det \mathbf{F}_S$ as well as the elastic counterparts, respectively, govern the changes

of the corresponding material elements (cf. (24)). However, it should be noted that polyconvexity as a guarantor for the existence of solutions in connection with finite inelasticity is not mathematically proven. That is because investigations must also account for the numerical treatment of the inelastic rate equations within the variational problem. However, proceeding from (locally) iterated evolution equations associated with updated internal variables which are constant for the subsequent (global) solution step of the BVP, conditions (147) induce at least a physically meaningful material tangent. For a more comprehensive discussion of convexity conditions and constitutive inequalities, see, e.g., [5, 6, 21, 27, 93, 121, 126].

Growth Conditions It is quite an obvious physical fact that extreme values in stress are accompanied by extreme values in strain. In the case of a hyperelastic solid material this corresponds to the requirement that total compression and infinite distortion or expansion must yield infinite values of the strain energy. Thus, for the equilibrium part it follows

$$\mathcal{W}_{EQ}^S \rightarrow +\infty \quad \text{as} \quad \begin{cases} \det \mathbf{F}_S \rightarrow n_{0S}^S, \\ (\|\mathbf{F}_S\| + \|\text{cof } \mathbf{F}_S\| + \det \mathbf{F}_S) \rightarrow +\infty, \end{cases} \quad (148)$$

where $\|(\cdot)\|$ indicates the norm of a tensor, e.g., $\|\mathbf{F}_S\| = \sqrt{\mathbf{F}_S \cdot \mathbf{F}_S}$. The first condition differs from the one of singlephasic materials ($\det \mathbf{F} \rightarrow 0^+$) insofar as the volumetric compression of the materially incompressible solid skeleton is limited to the point of compaction, i.e., the transition point to a dense solid material associated with $n^S = 1$. In this context recall the remark on page 8 and the relations (14) and (15). Following Ciarlet [21, Sect. 4.6], the second condition can be expressed in the sharper form of a *coerciveness inequality* describing the rate of growth of the strain-energy function:

$$\mathcal{W}_{EQ}^S \geq \alpha [\|\mathbf{F}_S\|^p + \|\text{cof } \mathbf{F}_S\|^q + (\det \mathbf{F}_S)^r] + \beta \\ \exists \{\alpha, p, q, r > 0, \beta\} \in \mathbb{R}. \quad (149)$$

In particular, the inequality guarantees that the strain energy grows sufficiently rapid with its variables such that equilibrium solutions exist even under extreme loading conditions, see, e.g., [2]. For the non-equilibrium part analogous considerations yield

$$\mathcal{W}_{NEQ}^S \rightarrow +\infty \quad \text{as} \quad \begin{cases} \det (\mathbf{F}_{Se})_n \rightarrow (n_{Si}^S)_n, \\ [\|(\mathbf{F}_{Se})_n\| + \|\text{cof } (\mathbf{F}_{Se})_n\| + \det (\mathbf{F}_{Se})_n] \rightarrow +\infty. \end{cases} \quad (150)$$

Herein, the finite elastic volume compressions in the associated Maxwell elements are limited by the inelastic solid

volume fractions $(n_{Si}^S)_n$ resulting from preceding inelastic volume contractions. In fact, the inelastic intermediate configurations act as reference configurations for the subsequent elastic deformation processes (cf. Fig. 4). Thus, the $(n_{Si}^S)_n$ can be regarded as referential solidities for the elastic volume contractions in the same way as n_{0S}^S represents the initial value for the total volume deformation of φ^S . Proceeding from the multiplicative split of \mathbf{F}_S (18), elastic and inelastic solid Jacobians can be introduced:

$$\begin{aligned} J_S &= \det \mathbf{F}_S = \det[(\mathbf{F}_{Se})_n (\mathbf{F}_{Si})_n] = \det[(\mathbf{F}_{Se})_n] \det[(\mathbf{F}_{Si})_n] \\ &= (J_{Se})_n (J_{Si})_n \quad \text{with } (J_{Se})_n := \det[(\mathbf{F}_{Se})_n], \\ & \quad (J_{Si})_n := \det[(\mathbf{F}_{Si})_n]. \end{aligned} \quad (151)$$

Then, the conditional equation for the intermediate solid volume fractions is found by inserting the above result into the conditional equation of n^S (106)₂ yielding

$$\begin{aligned} n^S &= n_{0S}^S J_S^{-1} = n_{0S}^S [(J_{Se}^{-1})_n (J_{Si}^{-1})_n] = (n_{Si}^S)_n (J_{Se}^{-1})_n \\ & \quad \text{with } (n_{Si}^S)_n := n_{0S}^S (J_{Si}^{-1})_n. \end{aligned} \quad (152)$$

In analogy, elastic volume fractions can be defined as $(n_{Se}^S)_n := n_{0S}^S (J_{Se}^{-1})_n$, so that a relation between the current solidity and its elastic and inelastic parts can be formulated:

$$\begin{aligned} \frac{n^S}{n_{0S}^S} &= \frac{(n_{Se}^S)_n}{n_{0S}^S} \frac{(n_{Si}^S)_n}{n_{0S}^S} \\ &\Leftrightarrow n^S n_{0S}^S = (n_{Se}^S)_n (n_{Si}^S)_n. \end{aligned} \quad (153)$$

Objectivity Material objectivity or material frame indifference postulates that the constitutive material equations are independent of the current frame of reference. In other words, the described material properties remain unaltered due to changes of the observer (observer invariance). Following this, in the case of hyperelastic material behavior, the strain-energy function is assumed to be invariant with respect to any superimposed rigid-body motions on the current configuration. Accordingly, the invariance conditions for the equilibrium and non-equilibrium energies can be expressed as

$$\begin{aligned} \star \mathcal{W}_{EQ}^S(\mathbf{F}_S) &= \mathcal{W}_{EQ}^S(\star \mathbf{F}_S), \\ \star \mathcal{W}_{NEQ}^S[(\mathbf{F}_{Se})_n] &= \mathcal{W}_{NEQ}^S[(\star \mathbf{F}_{Se})_n], \end{aligned} \quad (154)$$

where $(\star \cdot)$ indicates the quantities of the translated and/or rotated actual configuration. With the rigid-body rotations represented by arbitrary proper orthogonal tensors $\mathbf{Q}_S \in SO_3$, the covariant transformation mechanisms read

$$\begin{aligned} \star \mathbf{F}_S &= \star \mathbf{a}_k \otimes \mathbf{h}^k = (\mathbf{Q}_S \mathbf{a}_k) \otimes \mathbf{h}^k = \mathbf{Q}_S (\mathbf{a}_k \otimes \mathbf{h}^k) = \mathbf{Q}_S \mathbf{F}_S, \\ \star \mathbf{F}_{Se} &= \star \mathbf{a}_k \otimes \hat{\mathbf{z}}^k = (\mathbf{Q}_S \mathbf{a}_k) \otimes \hat{\mathbf{z}}^k = \mathbf{Q}_S (\mathbf{a}_k \otimes \hat{\mathbf{z}}^k) = \mathbf{Q}_S \mathbf{F}_{Se}, \end{aligned} \quad (155)$$

so that with the natural objectivity of scalar-valued quantities, $\star \Psi(\cdot) = \Psi(\cdot)$, it follows

$$\begin{aligned} \mathcal{W}_{EQ}^S(\mathbf{F}_S) &= \mathcal{W}_{EQ}^S(\mathbf{Q}_S \mathbf{F}_S), \\ \mathcal{W}_{NEQ}^S[(\mathbf{F}_{Se})_n] &= \mathcal{W}_{NEQ}^S[(\mathbf{Q}_S)_n (\mathbf{F}_{Se})_n]. \end{aligned} \quad (156)$$

Then, with the special choices $\mathbf{Q}_S = \mathbf{R}_S^T$ and $(\mathbf{Q}_S)_n = (\mathbf{R}_{Se}^T)_n$ and use of the right polar decompositions of \mathbf{F}_S (45)₁ and $(\mathbf{F}_{Se})_n$ (61)₁, respectively, one finds

$$\begin{aligned} \mathcal{W}_{EQ}^S(\mathbf{F}_S) &= \mathcal{W}_{EQ}^S(\mathbf{U}_S), \\ \mathcal{W}_{NEQ}^S[(\mathbf{F}_{Se})_n] &= \mathcal{W}_{NEQ}^S[(\hat{\mathbf{U}}_{Se})_n]. \end{aligned} \quad (157)$$

Following this, the solid strain energies depend only on the stretching parts of the deformation gradients, and hence, it is convenient to express \mathcal{W}_{EQ}^S and \mathcal{W}_{NEQ}^S in terms of the deformation tensors $\mathbf{C}_S = \mathbf{U}_S^2$ and $(\hat{\mathbf{C}}_{Se})_n = (\hat{\mathbf{U}}_{Se}^2)_n$ or the related strains (cf. (28)):

$$\begin{aligned} \mathcal{W}_{EQ}^S(\mathbf{F}_S) &= \mathcal{W}_{EQ}^S(\mathbf{C}_S) = \mathcal{W}_{EQ}^S(\mathbf{E}_S), \\ \mathcal{W}_{NEQ}^S[(\mathbf{F}_{Se})_n] &= \mathcal{W}_{NEQ}^S[(\hat{\mathbf{C}}_{Se})_n] = \mathcal{W}_{NEQ}^S[(\hat{\mathbf{E}}_{Se})_n]. \end{aligned} \quad (158)$$

Note that the representation by means of the right Cauchy-Green deformation or the Green-Lagrange strain tensors is a natural consequence as these are the basic deformation and strain measures of the reference and the intermediate configurations, and thus, are unaffected by changes to the actual configuration.

In addition to the above discussed conditions, which must be fulfilled independent of the considered material behavior, the present work proceeds from further additional assumptions. For obvious reasons, in the undeformed initial or natural state at time $t = t_0$ where $\mathbf{F}_S = (\mathbf{F}_{Se})_n = (\mathbf{F}_{Si})_n \equiv \mathbf{I}$, the solid strain energy is assumed to vanish which furthermore implies a stress-free reference configuration:

$$\mathcal{W}_{0S}^S(\mathbf{I}) = 0, \quad \mathbf{T}_{E0}^S(\mathcal{W}_{0S}^S) \equiv \mathbf{0}. \quad (159)$$

Following these *normalization* assumptions together with the polyconvexity and growth conditions, the strain energy has its global minimum in the undeformed reference state, i.e., $\mathcal{W}^S[\mathbf{F}_S, (\mathbf{F}_{Se})_n] \geq 0$ must hold for all conceivable processes. Moreover, the *downward compatibility* of the constitutive material equations to the Hooke-type formulations of the linear viscoelasticity theory is demanded at the transition to the small strain regime which yields further restrictions on the class of admissible constitutive functions. Beside these self-evident assumptions, the following considerations proceed from *isotropy*, i.e., the simplification to orientation-independent, uniform material properties. An isotropic material possesses complete material symmetry, i.e., has no preferred directions. Mathematically, this is guaranteed by the invariance of the constitutive energy functions

due to any rigid-body rotations of the reference and intermediate configurations, respectively, which implies that the whole set of proper orthogonal mappings (rotations) builds the group of symmetry-preserving transformations. Following this, with arguments similar to those used for the evaluation of the principle of frame indifference, the solid strain energies take the form

$$\begin{aligned}\mathcal{W}_{EQ}^S(\mathbf{F}_S) &= \mathcal{W}_{EQ}^S(\mathbf{V}_S) = \mathcal{W}_{EQ}^S(\mathbf{B}_S), \\ \mathcal{W}_{NEQ}^S[(\mathbf{F}_{Se})_n] &= \mathcal{W}_{NEQ}^S[(\mathbf{V}_{Se})_n] = \mathcal{W}_{NEQ}^S[(\mathbf{B}_{Se})_n].\end{aligned}\quad (160)$$

The formulation by means of the left Cauchy-Green deformation tensors is again a natural consequence as \mathbf{B}_S and $(\mathbf{B}_{Se})_n$ are tensor fields living on the current configuration, and thus, are invariant due to alterations of the reference and the intermediate configurations, respectively. In conclusion, together with the objectivity requirements (158), the dependency of the solid strain energies on \mathbf{F}_S and $(\mathbf{F}_{Se})_n$, respectively, must be equally expressible in both the corresponding right and left Cauchy-Green deformation tensors. This can be accomplished if \mathcal{W}_{EQ}^S and \mathcal{W}_{NEQ}^S take the form of isotropic tensor functions formulated in the principal invariants or the eigenvalues of the deformation tensors (cf. (70)):

$$\begin{aligned}\mathcal{W}_{EQ}^S(\mathbf{F}_S) &\longrightarrow \mathcal{W}_{EQ}^S(I_S, II_S, III_S) = \mathcal{W}_{EQ}^S(\lambda_{S(k)}), \\ \mathcal{W}_{NEQ}^S[(\mathbf{F}_{Se})_n] &\longrightarrow \mathcal{W}_{NEQ}^S[(I_{Se})_n, (II_{Se})_n, (III_{Se})_n] \\ &= \mathcal{W}_{NEQ}^S[(\lambda_{Se(k)})_n].\end{aligned}\quad (161)$$

Herein, $(I_{Se})_n$, $(II_{Se})_n$, and $(III_{Se})_n$ represent the elastic principal invariants of $(\hat{\mathbf{C}}_{Se})_n$ or $(\mathbf{B}_{Se})_n$, respectively, and are computed analogously to the principal invariants (51).

The next step before specifying the strain-energy functions and the inelastic evolution equations is the identification of the stress tensors of the finite theory. Proceeding from the objective form of the strain energy $\mathcal{W}^S[\mathbf{E}_S, (\hat{\mathbf{F}}_{Se})_n]$ given in (158), time derivation yields the effective solid stress power including the intrinsic dissipative contributions of φ^S :

$$(\mathcal{W}^S)'_S = \frac{\partial \mathcal{W}_{EQ}^S}{\partial \mathbf{E}_S} \cdot (\mathbf{E}_S)'_S + \sum_{n=1}^N \frac{\partial \mathcal{W}_{NEQ}^S}{\partial (\hat{\mathbf{F}}_{Se})_n} \cdot [(\hat{\mathbf{F}}_{Se})_n]'_S. \quad (162)$$

Then, by use of the upper inelastic Oldroyd derivative (42)₂, the elastic strain rate tensors of the $n = 1, \dots, N$ intermediate configurations can be rewritten as

$$(\hat{\mathbf{F}}_{Se})'_S = \mathbf{F}_{Si}^{T-1} (\mathbf{E}_S)'_S \mathbf{F}_{Si}^{-1} - \frac{1}{2} (\hat{\mathbf{L}}_{Si}^T \hat{\mathbf{C}}_{Se} + \hat{\mathbf{C}}_{Se} \hat{\mathbf{L}}_{Si}), \quad (163)$$

where, moreover, the transport property and the additive composition of the contravariant strain rates (Appendix A.3)

are exploited. Insertion into (162) yields

$$\begin{aligned}(\mathcal{W}^S)'_S &= \left[\frac{\partial \mathcal{W}_{EQ}^S}{\partial \mathbf{E}_S} + \sum_{n=1}^N (\mathbf{F}_{Si}^{-1})_n \frac{\partial \mathcal{W}_{NEQ}^S}{\partial (\hat{\mathbf{F}}_{Se})_n} (\mathbf{F}_{Si}^{T-1})_n \right] \cdot (\mathbf{E}_S)'_S \\ &\quad - \sum_{n=1}^N \frac{\partial \mathcal{W}_{NEQ}^S}{\partial (\hat{\mathbf{F}}_{Se})_n} \cdot [(\hat{\mathbf{C}}_{Se})_n (\hat{\mathbf{L}}_{Si})_n].\end{aligned}\quad (164)$$

Herein, the second term has been simplified utilizing the symmetry properties of $\hat{\mathbf{C}}_{Se}$ and $\partial \mathcal{W}_{NEQ}^S / \partial \hat{\mathbf{F}}_{Se}$. Next, recalling the evaluation procedure of the Clausius-Planck inequality of Sect. 3.1.4 together with $(\mathcal{W}^S)'_S$ of (164), the expression for the determination of the solid extra stress tensor in terms of the reference configuration is given by

$$\begin{aligned}\left[\underbrace{\mathbf{S}_E^S - \frac{\partial \mathcal{W}_{EQ}^S}{\partial \mathbf{E}_S}}_{\mathbf{S}_{EQ}^S} - \underbrace{\sum_{n=1}^N \overbrace{(\mathbf{F}_{Si}^{-1})_n \frac{\partial \mathcal{W}_{NEQ}^S}{\partial (\hat{\mathbf{F}}_{Se})_n} (\mathbf{F}_{Si}^{T-1})_n}^{\mathbf{S}_n^S}}_{\mathbf{S}_{NEQ}^S} \right] \cdot (\mathbf{E}_S)'_S \geq 0 \\ \forall (\mathbf{E}_S)'_S.\end{aligned}\quad (165)$$

In regard of the additive stress composition associated with the parallel rheological structure of the generalized Maxwell model and the fact that the above expression sufficiently fulfills the dissipation inequality for arbitrary values of the free variable $(\mathbf{E}_S)'_S$ if the term in brackets vanishes, the following relations are postulated:

$$\begin{aligned}\mathbf{S}_E^S &:= \mathbf{S}_{EQ}^S + \mathbf{S}_{NEQ}^S \quad \text{with } \mathbf{S}_{EQ}^S := \frac{\partial \mathcal{W}_{EQ}^S}{\partial \mathbf{E}_S}, \\ \mathbf{S}_{NEQ}^S &:= \sum_{n=1}^N \mathbf{S}_n^S = \sum_{n=1}^N \frac{\partial \mathcal{W}_{NEQ}^S}{\partial (\mathbf{E}_{Se})_n}.\end{aligned}\quad (166)$$

Moreover, following Sect. 2.3.1, in particular (81) and the concept of dual variables (82), the intermediate and Kirchhoff solid extra stress tensors are found as

$$\begin{aligned}(\hat{\boldsymbol{\tau}}_{EQ}^S)_n &:= \frac{\partial \mathcal{W}_{EQ}^S}{\partial (\hat{\mathbf{F}}_S)_n}, \quad (\hat{\boldsymbol{\tau}}_{NEQ}^S)_n := \hat{\boldsymbol{\tau}}_n^S := \frac{\partial \mathcal{W}_{NEQ}^S}{\partial (\hat{\mathbf{F}}_{Se})_n}, \\ \boldsymbol{\tau}_E^S &:= \boldsymbol{\tau}_{EQ}^S + \boldsymbol{\tau}_{NEQ}^S \quad \text{with } \boldsymbol{\tau}_{EQ}^S := \frac{\partial \mathcal{W}_{EQ}^S}{\partial \mathbf{A}_S}, \\ \boldsymbol{\tau}_{NEQ}^S &:= \sum_{n=1}^N \boldsymbol{\tau}_n^S = \sum_{n=1}^N \frac{\partial \mathcal{W}_{NEQ}^S}{\partial (\mathbf{A}_{Se})_n}.\end{aligned}\quad (167)$$

Note that in the general case of multiple Maxwell elements ($N > 1$), the individual intermediate stress tensors cannot be added to a total solid extra stress tensor $\hat{\boldsymbol{\tau}}_E^S$ as they are not referring to one and the same configuration.

To continue, the second term of (164) inserted into the Clausius-Planck inequality represents the intrinsic dissipative solid part remaining in the residual inequality. To make

this point clearer, one can alternatively proceed from the first term of the basic residual inequality (129). Following this, with $\mathbf{Q}_n^S = (\mathbf{F}_{Si})_n$ and multiplied by $J_S > n_{0S}^S > 0$, the original dissipative solid term becomes

$$\begin{aligned} -\rho^S \sum_{n=1}^N \frac{\partial \psi^S}{\partial \mathbf{Q}_n^S} \cdot (\mathbf{Q}_n^S)'_S &\geq 0 \\ \longrightarrow -\rho_{0S}^S \sum_{n=1}^N \frac{\partial \psi^S}{\partial (\mathbf{F}_{Si})_n} \cdot [(\mathbf{F}_{Si})_n]'_S &\geq 0. \end{aligned} \quad (168)$$

Then, utilizing the objective non-equilibrium strain energy (158)₂ and the definition of the non-equilibrium intermediate stresses (167)₁ which are conjugate to $(\hat{\mathbf{F}}_{Se})_n$ yields

$$\begin{aligned} -\sum_{n=1}^N \frac{\partial \mathcal{W}_{NEQ}^S[(\hat{\mathbf{F}}_{Se})_n]}{\partial (\mathbf{F}_{Si})_n} \cdot [(\mathbf{F}_{Si})_n]'_S \\ = -\sum_{n=1}^N \left[\frac{\partial (\hat{\mathbf{F}}_{Se})_n}{\partial (\mathbf{F}_{Si})_n} \right]^T \frac{\partial \mathcal{W}_{NEQ}^S}{\partial [(\hat{\mathbf{F}}_{Se})_n]} \cdot [(\mathbf{F}_{Si})_n]'_S \\ = -\sum_{n=1}^N \hat{\mathbf{T}}_n^S \cdot \frac{\partial (\hat{\mathbf{F}}_{Se})_n}{\partial (\mathbf{F}_{Si})_n} [(\hat{\mathbf{L}}_{Si})_n (\mathbf{F}_{Si})_n] \geq 0. \end{aligned} \quad (169)$$

The right hand side of the scalar product is then rewritten using the derivative

$$\begin{aligned} \frac{\partial \hat{\mathbf{F}}_{Se}}{\partial \mathbf{F}_{Si}} &= \frac{1}{2} \frac{\partial \hat{\mathbf{C}}_{Se}}{\partial \mathbf{F}_{Si}} = \frac{1}{2} \frac{\partial (\mathbf{F}_{Si}^{T-1} \mathbf{C}_S \mathbf{F}_{Si}^{-1})}{\partial \mathbf{F}_{Si}} \\ &= -\frac{1}{2} [(\mathbf{F}_{Si}^{T-1} \otimes \hat{\mathbf{C}}_{Se})^{24} + (\hat{\mathbf{C}}_{Se} \otimes \mathbf{F}_{Si}^{T-1})^{23}] \end{aligned} \quad (170)$$

which, multiplied by the inelastic solid material velocity gradient $(\mathbf{F}_{Si})'_S = \hat{\mathbf{L}}_{Si} \mathbf{F}_{Si}$ (cf. (32)), results in

$$\begin{aligned} -\frac{1}{2} [(\mathbf{F}_{Si}^{T-1} \otimes \hat{\mathbf{C}}_{Se})^{24} + (\hat{\mathbf{C}}_{Se} \otimes \mathbf{F}_{Si}^{T-1})^{23}] (\hat{\mathbf{L}}_{Si} \mathbf{F}_{Si}) \\ = -\frac{1}{2} (\hat{\mathbf{L}}_{Si}^T \hat{\mathbf{C}}_{Se} + \hat{\mathbf{C}}_{Se} \hat{\mathbf{L}}_{Si}). \end{aligned} \quad (171)$$

By insertion into (169) and use of the symmetry of the non-equilibrium intermediate stresses, $\hat{\mathbf{T}}_n^S = (\hat{\mathbf{T}}_n^S)^T$, one likewise recovers the residual solid term as if (164) is inserted into the dissipation inequality, viz.,

$$\sum_{n=1}^N \hat{\mathbf{T}}_n^S \cdot [(\hat{\mathbf{C}}_{Se})_n (\hat{\mathbf{L}}_{Si})_n] = \sum_{n=1}^N [(\hat{\mathbf{C}}_{Se})_n \hat{\mathbf{T}}_n^S] \cdot (\hat{\mathbf{L}}_{Si})_n \geq 0. \quad (172)$$

For the considered special case of isotropic skeleton properties, $(\hat{\mathbf{C}}_{Se})_n$ and $\hat{\mathbf{T}}_n^S$ commute yielding the symmetry of the Mandel stress tensors $(\hat{\mathbf{C}}_{Se})_n \hat{\mathbf{T}}_n^S$. Consequently, only

the symmetric part of the inelastic spatial velocity gradients $(\hat{\mathbf{D}}_{Si})_n = \frac{1}{2} [(\hat{\mathbf{L}}_{Si})_n + (\hat{\mathbf{L}}_{Si}^T)_n]$ complies, and thus, the isotropic representation of the solid residual inequality becomes

$$\begin{aligned} \sum_{n=1}^N \hat{\mathbf{T}}_n^S \cdot [(\hat{\mathbf{C}}_{Se})_n (\hat{\mathbf{D}}_{Si})_n] \\ = \sum_{n=1}^N \hat{\mathbf{T}}_n^S \cdot \{(\hat{\mathbf{C}}_{Se})_n [(\hat{\mathbf{F}}_{Si})_n^{\Delta}]_S\} \geq 0. \end{aligned} \quad (173)$$

By use of the respective transport mechanisms, the corresponding relations of the reference and the intermediate configurations are then found as

$$\begin{aligned} \sum_{n=1}^N \mathbf{S}_n^S \cdot \{\mathbf{C}_S (\mathbf{C}_{Si}^{-1})_n [(\mathbf{E}_{Si})_n]'_S\} &\geq 0, \\ \sum_{n=1}^N \mathbf{T}_n^S \cdot \{(\mathbf{B}_{Se})_n [(\mathbf{A}_{Si})_n]^{\Delta}_S\} &\geq 0. \end{aligned} \quad (174)$$

From the above inequalities, it is obvious that in the case of isotropy the inelastic deformation tensors $(\mathbf{C}_{Si})_n = (\mathbf{U}_{Si})_n^2$ take over the role of the strain-equivalent internal variables as they are invariant due to any rotations superimposed on the intermediate configurations. For the case of single-phasic materials comparable results can be found, e.g., in [73, 115, 116].

3.2.3 An Appropriate Porous Media Viscoelasticity Law

In the following, the nonlinear model of the viscoelastic porous solid matrix will be closed by specifying the solid strain-energy function \mathcal{W}^S and the evolution equations for the internal variables consistent with the conditions and assumptions discussed in the previous section. As large deformations of a porous solid matrix are accompanied by considerably larger distortions of the pore space, the macroscopic response of the entire material can be extremely nonlinear. These nonlinearities are particularly caused by deformation-induced instabilities and stiffening effects of the skeleton structure, such as buckling, alignment, or compaction of pore edges and walls, which can be very well observed in high-porosity foams. Thus, a suitable material formulation must be provided that can be successfully correlated with distinct nonlinear experimental observations. This draws the attention to an established class of constitutive models of finite isotropic elasticity, the so-called Ogden-type formulations, originally proposed by Ogden [101, 102] for the description of the nonlinear stress-strain response of rubber (cf. [134]).

For an isotropic hyperelastic solid skeleton, a general form of such an Ogden-type formulation which *a priori* sat-

ifies the normalization assumption (159)₁ is given by

$$\begin{aligned} \mathcal{W}^S(I_{\mathbf{F}_S}, II_{\mathbf{F}_S}, III_{\mathbf{F}_S}) \\ = \sum_{m=1}^{M_I} \frac{\bar{\mu}_m}{\alpha_m} (I_{\mathbf{F}_S}^{\alpha_m} - 3) + \sum_{m=1}^{M_{II}} \frac{\bar{\mu}_m}{\beta_m} (II_{\mathbf{F}_S}^{\beta_m} - 3) + \mathcal{U}^S(III_{\mathbf{F}_S}). \end{aligned} \quad (175)$$

Typically, the Ogden strain energy is expressed in terms of the principal invariants of the solid deformation gradient \mathbf{F}_S rather than of the deformation tensors \mathbf{C}_S or \mathbf{B}_S , namely

$$\begin{aligned} I_{\mathbf{F}_S} &= \text{tr } \mathbf{F}_S, & II_{\mathbf{F}_S} &= \text{tr}(\text{cof } \mathbf{F}_S), \\ III_{\mathbf{F}_S} &= J_S = \det \mathbf{F}_S \end{aligned} \quad (176)$$

which are of course identical to those of the right or left solid stretch tensors \mathbf{U}_S or \mathbf{V}_S , respectively (cf. Sect. 2.2.3). Moreover, in (175), $\bar{\mu}_m$, $\alpha_m \neq 0$ and $\bar{\mu}_m$, $\beta_m \neq 0$ are material constants, $M_I, M_{II} \in \mathbb{N}^+$ denote positive integers, and \mathcal{U}^S represents a convex volumetric response function describing the compressible material behavior where $\mathcal{U}^S(III_{\mathbf{F}_S} = 1) = 0$. As negative combinations of the Ogden parameters are generally valid, in order to have \mathcal{W}^S strictly positive, the following sufficient conditions are apparent [101]:

$$\bar{\mu}_m \alpha_m > 0, \quad \bar{\mu}_m \beta_m > 0. \quad (177)$$

However, in regard to the stability requirements, it is easily recognized that \mathcal{W}^S possesses a form similar to (145)₂, and hence, represents an additive polyconvex function provided that each term is convex in the associated variable. According to (147), this is guaranteed if the second derivatives are positive semidefinite, which finally yields the essential restrictions (cf. [103])

$$\begin{aligned} \bar{\mu}_m (\alpha_m - 1) \geq 0, \quad \bar{\mu}_m (\beta_m - 1) \geq 0 \\ \longrightarrow \begin{cases} \bar{\mu}_m > 0, \alpha_m \geq 1 \vee \bar{\mu}_m < 0, \alpha_m \leq 1 \wedge \alpha_m \neq 0, \\ m = 1, \dots, M_I, \\ \bar{\mu}_m > 0, \beta_m \geq 1 \vee \bar{\mu}_m < 0, \beta_m \leq 1 \wedge \beta_m \neq 0, \\ m = 1, \dots, M_{II}. \end{cases} \end{aligned} \quad (178)$$

Moreover, following Ciarlet [21], the strain energy (175) fulfills the growth conditions in form of the coerciveness inequality (149) if $\mathcal{U}^S(J_S \rightarrow n_{0S}^S) \rightarrow +\infty$ is satisfied. Further particulars on the general requirements of \mathcal{U}^S will be discussed later in this section.

Equally, the strain energy can be expressed by means of the principal stretches which, for convenience, are represented by the square roots of the eigenvalues $\lambda_{S(k)}$ of \mathbf{C}_S

or \mathbf{B}_S , respectively, yielding the more common representation

$$\begin{aligned} \mathcal{W}^S(\lambda_{S(k)}) &= \sum_{m=1}^{M_I} \sum_{k=1}^3 \frac{\bar{\mu}_m}{\alpha_m} (\lambda_{S(k)}^{\alpha_m/2} - 1) \\ &\quad + \frac{1}{2} \sum_{m=1}^{M_{II}} \sum_{\substack{k,l=1 \\ l \neq k}}^3 \frac{\bar{\mu}_m}{\beta_m} [(\lambda_{S(k)} \lambda_{S(l)})^{\beta_m/2} - 2] \\ &\quad + \mathcal{U}^S(J_S) \end{aligned} \quad (179)$$

with $J_S = \sqrt{\lambda_{S(1)} \lambda_{S(2)} \lambda_{S(3)}}$ according to (51)₃ and (52)₃. A simplified version of this strain energy which avoids products of eigenvalues is proved to be very successful in describing the nonlinear large strain response of rubber-like materials [104, 105]. Hence, we proceed from a reduced constitutive function of the form

$$\begin{aligned} \mathcal{W}^S(\lambda_{S(k)}) &= \mu^S \sum_{m=1}^{M_I} \left(\sum_{k=1}^3 \frac{\mu_m^*}{\alpha_m} (\lambda_{S(k)}^{\alpha_m/2} - 1) - \mu_m^* \ln J_S \right) \\ &\quad + \bar{\mathcal{U}}^S(J_S), \end{aligned} \quad (180)$$

where $\mu^S > 0$ is identified as the 1st Lamé constant, i.e., the conventional positive shear modulus of the linear theory, such that both $\mu_m^* = \bar{\mu}_m / \mu^S$ and α_m represent dimensionless, real-valued parameters. In this regard, by comparison with the geometrically linear theory, the downward compatibility to a linear Hookean-type elasticity formulation is satisfied if

$$\sum_{m=1}^{M_I} \mu_m^* \alpha_m = 2. \quad (181)$$

Moreover, in the strain-energy function (180), the additional logarithmic term is separated from \mathcal{U}^S in order to make the unstrained reference state stress-free, independent of the actual choice of the volumetric extension term $\bar{\mathcal{U}}^S(J_S)$, cf. [102]. Consequently, to further maintain polyconvexity, it must be additionally ensured that

$$\begin{aligned} \frac{\partial^2}{\partial J_S^2} \left(- \sum_m \mu_m^* \ln J_S \right) &= \sum_m \mu_m^* \frac{1}{J_S^2} \geq 0 \\ \longrightarrow \sum_{m=1}^{M_I} \mu_m^* &\geq 0. \end{aligned} \quad (182)$$

It should be noted that the single Ogden parameters generally cannot be associated with a distinct physical meaning as μ_m^* represent the coefficients of a trivariate polynomial in the variables $\lambda_{S(k)}$ ($k = 1, 2, 3$), whereas the powers α_m govern the actual nonlinearity.

In a next step, a volumetric extension term $\bar{\mathcal{U}}^S(J_S)$ must be derived, such that the requirements depicted in (184) are

met. Therein, in regard to the classical definition of a positive ground-state solid bulk modulus, one has

$$\kappa^S := \frac{\partial^2 \mathcal{W}^S}{\partial J_S^2} \bigg|_{\lambda_{S(k)}=1} = \frac{2}{3} \mu^S + \Lambda^S > 0 \quad (183)$$

for physical reasons. Thus, the second Lamé constant must satisfy $\Lambda^S > -\frac{2}{3} \mu^S$. Of course the convexity condition (184)₁ yielding the stronger restriction $\Lambda^S \geq 0$ together with the first classical inequality $\mu^S > 0$ renders the above inequality (183) redundant, and moreover, embraces the natural assumption of a positive Poisson's ratio.

Conditions for the volumetric extension term

$$\begin{aligned} \text{convexity condition:} \quad & \frac{\partial^2 \bar{\mathcal{U}}^S}{\partial J_S^2} \geq 0 \quad \forall J_S > n_{0S}^S > 0 \\ \text{growth conditions:} \quad & \bar{\mathcal{U}}^S \rightarrow +\infty, \quad \frac{\partial \bar{\mathcal{U}}^S}{\partial J_S} \rightarrow -\infty \text{ as } J_S \rightarrow n_{0S}^S \\ & \bar{\mathcal{U}}^S \rightarrow +\infty, \quad \frac{\partial \bar{\mathcal{U}}^S}{\partial J_S} \rightarrow +\infty \text{ as } J_S \rightarrow +\infty \\ \text{normalization assumption:} \quad & \bar{\mathcal{U}}^S = 0, \quad \frac{\partial \bar{\mathcal{U}}^S}{\partial J_S} = 0 \quad \text{as } J_S = 1 \\ \text{compatibility assumption:} \quad & \frac{\partial^2 \bar{\mathcal{U}}^S}{\partial J_S^2} \bigg|_{J_S=1} =: \Lambda^S \quad : \text{2nd Lamé constant} \end{aligned} \quad (184)$$

Following this, Eipper [51] extended the logarithmic volumetric strain energy proposed by Ogden [102] to porous media problems through incorporation of the compaction point accounting for all conditions given in (184) (see also [43]). However, applied to real porous materials, it turns out that the stress increase towards the point of compaction is not sufficiently fast. Therefore, the formulation is improved by

replacing the logarithmic term by an inverse power expression. Following this, the new volumetric response function and its derivatives take the form

$$\begin{aligned} \bar{\mathcal{U}}^S &= \frac{\Lambda^S}{\gamma^S (\gamma^S - 1 + \frac{\gamma^S + 1}{[1 - n_{0S}^S]^2})} \\ &\quad \times \left(J_S^{\gamma^S} - 2 + \left[\frac{1 - n_{0S}^S}{J_S - n_{0S}^S} \right] \gamma^S + \gamma^S n_{0S}^S \frac{J_S - 1}{1 - n_{0S}^S} \right), \\ \frac{\partial \bar{\mathcal{U}}^S}{\partial J_S} &= \frac{\Lambda^S}{\gamma^S - 1 + \frac{\gamma^S + 1}{[1 - n_{0S}^S]^2}} \\ &\quad \times \left(J_S^{\gamma^S - 1} - \frac{(1 - n_{0S}^S)^{\gamma^S}}{(J_S - n_{0S}^S)^{\gamma^S + 1}} + \frac{n_{0S}^S}{1 - n_{0S}^S} \right), \\ \frac{\partial^2 \bar{\mathcal{U}}^S}{\partial J_S^2} &= \frac{\Lambda^S}{\gamma^S - 1 + \frac{\gamma^S + 1}{[1 - n_{0S}^S]^2}} \\ &\quad \times \left((\gamma^S - 1) J_S^{\gamma^S - 2} + (\gamma^S + 1) \frac{(1 - n_{0S}^S)^{\gamma^S}}{(J_S - n_{0S}^S)^{\gamma^S + 2}} \right), \end{aligned} \quad (185)$$

where γ^S represents an additional dimensionless solid parameter to govern the compressive stiffening behavior of the skeleton. From the second derivative (185)₃, it is apparent that $\gamma^S \geq 1$ must hold to satisfy the convexity condition. Thus, proceeding from the Ogden strain-energy function (180) in combination with the volumetric extension term (185)₁, the equilibrium response of the solid skeleton is appropriately described by the formulation given in (186).

Equilibrium strain energy of the solid skeleton

$$\begin{aligned} \mathcal{W}_{EQ}^S(\mathbf{C}_S) &= \bar{\mathcal{W}}_{EQ}^S(\lambda_{S(k)}) + \bar{\mathcal{U}}_{EQ}^S(J_S) \quad \text{with} \\ \bar{\mathcal{W}}_{EQ}^S &= \mu_0^S \sum_{m=1}^{M_0} \left(\sum_{k=1}^3 \frac{\mu_{0(m)}^*}{\alpha_{0(m)}} (\lambda_{S(k)}^{\alpha_{0(m)}/2} - 1) - \mu_{0(m)}^* \ln J_S \right) \\ \bar{\mathcal{U}}_{EQ}^S &= \frac{\Lambda_0^S}{\gamma_0^S (\gamma_0^S - 1 + \frac{\gamma_0^S + 1}{[1 - n_{0S}^S]^2})} \left(J_S^{\gamma_0^S} - 2 + \left[\frac{1 - n_{0S}^S}{J_S - n_{0S}^S} \right] \gamma_0^S + \gamma_0^S n_{0S}^S \frac{J_S - 1}{1 - n_{0S}^S} \right) \end{aligned} \quad (186)$$

Therein, the additional subscript $(\cdot)_0$ indicates the belonging of the material parameters to the equilibrium branch associated with the single spring of the generalized Maxwell model. The hyperelastic equilibrium solid extra stress tensor of the reference configuration is then computed from

$$\mathbf{S}_{EQ}^S = \frac{\partial \mathcal{W}_{EQ}^S}{\partial \mathbf{E}_S} = 2 \frac{\partial \mathcal{W}_{EQ}^S}{\partial \mathbf{C}_S}$$

$$= 2 \left(\sum_{k=1}^3 \frac{\partial \bar{\mathcal{W}}_{EQ}^S}{\partial \lambda_{S(k)}} \frac{\partial \lambda_{S(k)}}{\partial \mathbf{C}_S} + \frac{\partial \bar{\mathcal{U}}_{EQ}^S}{\partial J_S} \frac{\partial J_S}{\partial \mathbf{C}_S} \right), \quad (187)$$

so that with the partial derivatives (65)₁, (185)₂, and

$$\frac{\partial \bar{\mathcal{W}}_{EQ}^S}{\partial \lambda_{S(k)}} = \mu_0^S \sum_{m=1}^{M_0} \frac{1}{2} \mu_{0(m)}^* \lambda_{S(k)}^{-1} (\lambda_{S(k)}^{\alpha_{0(m)}/2} - 1), \quad (188)$$

the equilibrium 2nd Piola-Kirchhoff stress finally becomes

$$\begin{aligned} \mathbf{S}_{EQ}^S = & \mu_0^S \sum_{m=1}^{M_0} \sum_{k=1}^3 \mu_{0(m)}^* \lambda_{S(k)}^{-1} (\lambda_{S(k)}^{\alpha_{0(m)}/2} - 1) \mathbf{M}_{S(k)} \\ & + \frac{\Lambda_0^S}{\gamma_0^S - 1 + \frac{\gamma_0^{S+1}}{[1-n_{0S}^S]^2}} \\ & \times \left(J_S^{\gamma_0^S} - \frac{J_S (1 - n_{0S}^S) \gamma_0^S}{(J_S - n_{0S}^S) \gamma_0^{S+1}} + \frac{J_S n_{0S}^S}{1 - n_{0S}^S} \right) \mathbf{C}_S^{-1}. \end{aligned} \quad (189)$$

The corresponding Kirchhoff stress tensor of the current frame results from a covariant push-forward of \mathbf{S}_{EQ}^S or from

the related derivatives (167)₂:

$$\begin{aligned} \boldsymbol{\tau}_{EQ}^S = & \mu_0^S \sum_{m=1}^{M_0} \sum_{k=1}^3 \mu_{0(m)}^* (\lambda_{S(k)}^{\alpha_{0(m)}/2} - 1) \mathbf{N}_{S(k)} \\ & + \frac{\Lambda_0^S}{\gamma_0^S - 1 + \frac{\gamma_0^{S+1}}{[1-n_{0S}^S]^2}} \\ & \times \left(J_S^{\gamma_0^S} - \frac{J_S (1 - n_{0S}^S) \gamma_0^S}{(J_S - n_{0S}^S) \gamma_0^{S+1}} + \frac{J_S n_{0S}^S}{1 - n_{0S}^S} \right) \mathbf{I}. \end{aligned} \quad (190)$$

Analogously, the stress tensors associated with the springs in the Maxwell elements are obtained from appropriate elastic potentials similar to (186).

Non-equilibrium strain energy of the solid skeleton

$$\begin{aligned} \mathcal{W}_{NEQ}^S[(\hat{\mathbf{C}}_{Se})_n] = & \overline{\mathcal{W}}_{NEQ}^S[\lambda_{Se(k)}] + \overline{\mathcal{U}}_{NEQ}^S[(J_{Se})_n] \quad \text{with} \\ \overline{\mathcal{W}}_{NEQ}^S = & \sum_{n=1}^N \mu_n^S \sum_{m=1}^{M_n} \left(\sum_{k=1}^3 \frac{\mu_{n(m)}^*}{\alpha_{n(m)}} [(\lambda_{Se(k)}^{\alpha_{n(m)}/2})_n - 1] - \mu_{n(m)}^* \ln(J_{Se})_n \right) \\ \overline{\mathcal{U}}_{NEQ}^S = & \sum_{n=1}^N \frac{\Lambda_n^S}{\gamma_n^S (\gamma_n^S - 1 + \frac{\gamma_n^{S+1}}{[1-(n_{Si}^S)_n]^2})} \\ & \left((J_{Se}^{\gamma_n^S})_n - 2 + \left[\frac{1 - (n_{Si}^S)_n}{(J_{Se})_n - (n_{Si}^S)_n} \right] \gamma_n^S + \gamma_n^S n_{0S}^S \frac{(J_{Se})_n - 1}{1 - (n_{Si}^S)_n} \right) \end{aligned} \quad (191)$$

Thus, proceeding from the non-equilibrium strain-energy function (191) where the inelastic solidities $(n_{Si}^S)_n$ serve as constant reference values for the elastic volume deformations, the individual intermediate and the total Kirchhoff non-equilibrium solid extra stress tensors take the form

$$\begin{aligned} \hat{\boldsymbol{\tau}}_n^S = & \mu_n^S \sum_{m=1}^{M_n} \sum_{k=1}^3 \mu_{n(m)}^* (\lambda_{Se(k)}^{-1})_n [(\lambda_{Se(k)}^{\alpha_{n(m)}/2})_n - 1] (\hat{\mathbf{M}}_{Se(k)})_n \\ & + \frac{\Lambda_n^S}{\gamma_n^S - 1 + \frac{\gamma_n^{S+1}}{[1-(n_{Si}^S)_n]^2}} \\ & \times \left((J_{Se}^{\gamma_n^S})_n - \frac{(J_{Se})_n [1 - (n_{Si}^S)_n] \gamma_n^S}{[(J_{Se})_n - (n_{Si}^S)_n] \gamma_n^{S+1}} \right. \\ & \left. + \frac{(J_{Se})_n (n_{Si}^S)_n}{1 - (n_{Si}^S)_n} \right) (\hat{\mathbf{C}}_{Se}^{-1})_n, \end{aligned} \quad (192)$$

$$\boldsymbol{\tau}_{NEQ}^S = \sum_{n=1}^N \left[\mu_n^S \sum_{m=1}^{M_n} \sum_{k=1}^3 \mu_{n(m)}^* [(\lambda_{Se(k)}^{\alpha_{0(m)}/2})_n - 1] (\mathbf{N}_{Se(k)})_n \right.$$

$$\begin{aligned} & + \frac{\Lambda_n^S}{\gamma_n^S - 1 + \frac{\gamma_n^{S+1}}{[1-(n_{Si}^S)_n]^2}} \\ & \times \left((J_{Se}^{\gamma_n^S})_n - \frac{(J_{Se})_n [1 - (n_{Si}^S)_n] \gamma_n^S}{[(J_{Se})_n - (n_{Si}^S)_n] \gamma_n^{S+1}} \right. \\ & \left. + \frac{(J_{Se})_n (n_{Si}^S)_n}{1 - (n_{Si}^S)_n} \right) \mathbf{I} \Big]. \end{aligned} \quad (193)$$

By use of the covariant transport properties of the stress tensors (81), the corresponding total overstress related to the reference configuration can be obtained from

$$\begin{aligned} \mathbf{S}_{NEQ}^S = & \sum_{n=1}^N \frac{\partial \mathcal{W}_{NEQ}^S}{\partial (\mathbf{E}_{Se})_n} = \sum_{n=1}^N (\mathbf{F}_{Si}^{-1})_n \hat{\boldsymbol{\tau}}_n^S (\mathbf{F}_{Si}^{T-1})_n \\ = & \mathbf{F}_S^{-1} \boldsymbol{\tau}_{NEQ}^S \mathbf{F}_S^{T-1}. \end{aligned} \quad (194)$$

Note that the formulation of an entire intermediate-state overstress tensor is not possible for $N > 1$ as the individual intermediate stresses $\hat{\boldsymbol{\tau}}_n^S$ operate on different configurations.

In addition to the conditional equations for the stresses, the efficient numerical treatment of the nonlinear problem by an iterative solution technique, such as the Newton-Raphson method, requires the linearization of the constitutive material equations. Therefore, the equilibrium and non-equilibrium *continuum tangents* or *material moduli* which relate the changes of the respective stresses to the changes of the conjugate strain variables must be provided. Accordingly, the equilibrium solid elasticity tensor of the reference configuration can be introduced by regarding the total differential of the equilibrium 2nd Piola-Kirchhoff extra stress:

$$\begin{aligned} d\mathbf{S}_{EQ}^S(\mathbf{E}_S) &= \frac{\partial \mathbf{S}_{EQ}^S}{\partial \mathbf{E}_S} d\mathbf{E}_S = \mathbf{B}_{EQ}^S d\mathbf{E}_S \\ \text{with } \mathbf{B}_{EQ}^S &:= \frac{\partial \mathbf{S}_{EQ}^S}{\partial \mathbf{E}_S}. \end{aligned} \quad (195)$$

Thus, following the concept of hyperelasticity, one finds

$$\begin{aligned} \mathbf{B}_{EQ}^S &= \frac{\partial^2 \mathcal{W}_{EQ}^S}{\partial \mathbf{E}_S \otimes \partial \mathbf{E}_S} = 4 \frac{\partial^2 \mathcal{W}_{EQ}^S}{\partial \mathbf{C}_S \otimes \partial \mathbf{C}_S} \\ &= 4 \left(\frac{\partial^2 \overline{\mathcal{W}}_{EQ}^S}{\partial \mathbf{C}_S \otimes \partial \mathbf{C}_S} + \frac{\partial^2 \overline{\mathcal{U}}_{EQ}^S}{\partial \mathbf{C}_S \otimes \partial \mathbf{C}_S} \right), \end{aligned} \quad (196)$$

where, in particular, according to the spectral representation (71)₂

$$\begin{aligned} \frac{\partial^2 \overline{\mathcal{W}}_{EQ}^S}{\partial \mathbf{C}_S \otimes \partial \mathbf{C}_S} &= \sum_{k,l=1}^3 \frac{\partial^2 \overline{\mathcal{W}}_{EQ}^S}{\partial \lambda_{S(k)} \partial \lambda_{S(l)}} \mathbf{M}_{S(k)} \otimes \mathbf{M}_{S(l)} \\ &+ \frac{1}{2} \sum_{\substack{k,l=1 \\ l \neq k}}^3 \frac{\frac{\partial \overline{\mathcal{W}}_{EQ}^S}{\partial \lambda_{S(k)}} - \frac{\partial \overline{\mathcal{W}}_{EQ}^S}{\partial \lambda_{S(l)}}}{\lambda_{S(k)} - \lambda_{S(l)}} 4 \mathbf{M}_{S[kl]} \end{aligned} \quad (197)$$

with $\partial \overline{\mathcal{W}}_{EQ}^S / \partial \lambda_{S(k)}$ from (188) and

$$\begin{aligned} \frac{\partial^2 \overline{\mathcal{W}}_{EQ}^S}{\partial \lambda_{S(k)} \partial \lambda_{S(l)}} &= \begin{cases} \mu_0^S \sum_{m=1}^{M_0} \frac{1}{4} \mu_{0(m)}^* \lambda_{S(k)}^{-2} [(\alpha_{0(m)} - 2) \lambda_{S(k)}^{\alpha_{0(m)}/2} + 2] \\ \text{if } l = k, \\ 0 \quad \text{if } l \neq k, \end{cases} \end{aligned} \quad (198)$$

as well as

$$\begin{aligned} \frac{\partial^2 \overline{\mathcal{U}}_{EQ}^S}{\partial \mathbf{C}_S \otimes \partial \mathbf{C}_S} &= \frac{1}{4} \left(J_S \frac{\partial \overline{\mathcal{U}}_{EQ}^S}{\partial J_S} + J_S^2 \frac{\partial^2 \overline{\mathcal{U}}_{EQ}^S}{\partial J_S^2} \right) \mathbf{C}_S^{-1} \otimes \mathbf{C}_S^{-1} \\ &- \frac{1}{2} J_S \frac{\partial \overline{\mathcal{U}}_{EQ}^S}{\partial J_S} (\mathbf{C}_S^{-1} \otimes \mathbf{C}_S^{-1})^T \end{aligned} \quad (199)$$

with the derivatives of $\overline{\mathcal{U}}_{EQ}^S$ in analogy to (185)_{2,3}. The corresponding elasticity tensor of the actual frame is then obtained from a covariant push-forward operation of $(\mathbf{B}_{EQ}^S)^4$ or from the related 2nd-order derivatives. Thus, one finally obtains

$$\begin{aligned} \mathbf{C}_{EQ}^S &= 4 \sum_{k,l=1}^3 \frac{\partial^2 \overline{\mathcal{W}}_{EQ}^S}{\partial \lambda_{S(k)} \partial \lambda_{S(l)}} \lambda_{S(k)} \lambda_{S(l)} \mathbf{N}_{S(k)} \otimes \mathbf{N}_{S(l)} \\ &+ 2 \sum_{\substack{k,l=1 \\ l \neq k}}^3 \frac{\frac{\partial \overline{\mathcal{W}}_{EQ}^S}{\partial \lambda_{S(k)}} - \frac{\partial \overline{\mathcal{W}}_{EQ}^S}{\partial \lambda_{S(l)}}}{\lambda_{S(k)} - \lambda_{S(l)}} \lambda_{S(k)} \lambda_{S(l)} 4 \mathbf{N}_{S[kl]} \\ &+ \left(J_S \frac{\partial \overline{\mathcal{U}}_{EQ}^S}{\partial J_S} + J_S^2 \frac{\partial^2 \overline{\mathcal{U}}_{EQ}^S}{\partial J_S^2} \right) (\mathbf{I} \otimes \mathbf{I}) \\ &- 2 J_S \frac{\partial \overline{\mathcal{U}}_{EQ}^S}{\partial J_S} (\mathbf{I} \otimes \mathbf{I})^T. \end{aligned} \quad (200)$$

Note that in the special cases of identical eigenvalues, in the tangent moduli (197) and (200) the rational expressions with $\lambda_{S(k)} - \lambda_{S(l)}$ in the denominator must be replaced by the limits (73) and (74), respectively. Moreover, it should be mentioned that the hyperelastic continuum tangents possess the minor and major symmetries. Thus, at each strain state they only have 21 instead of 36 independent coefficients which in the linearized isotropic case can be traced back to just two parameters, namely the Lamé constants μ_0^S and Λ_0^S .

Concerning the non-equilibrium part, the individual elasticity tensors of the intermediate configurations associated with the springs in the Maxwell elements can analogously be motivated from the total differential of the related stress tensors:

$$\begin{aligned} d\hat{\boldsymbol{\tau}}_n^S &= \hat{\mathbf{C}}_n^S d(\hat{\boldsymbol{\Gamma}}_{Se})_n \quad \text{with} \\ \hat{\mathbf{C}}_n^S &:= \frac{\partial \hat{\boldsymbol{\tau}}_n^S}{\partial (\hat{\boldsymbol{\Gamma}}_{Se})_n} = 4 \frac{\partial^2 \mathcal{W}_{NEQ}^S}{\partial (\hat{\mathbf{C}}_{Se})_n \otimes \partial (\hat{\mathbf{C}}_{Se})_n}. \end{aligned} \quad (201)$$

Thus, proceeding from the non-equilibrium strain-energy function (191), one finds

$$\begin{aligned} \hat{\mathbf{C}}_n^S &= 4 \sum_{k,l=1}^3 \frac{\partial^2 \overline{\mathcal{W}}_{NEQ}^S}{\partial (\lambda_{Se(k)})_n \partial (\lambda_{Se(l)})_n} (\mathbf{M}_{Se(k)})_n \otimes (\mathbf{M}_{Se(l)})_n \\ &+ 2 \sum_{\substack{k,l=1 \\ l \neq k}}^3 \frac{\frac{\partial \overline{\mathcal{W}}_{NEQ}^S}{\partial (\lambda_{Se(k)})_n} - \frac{\partial \overline{\mathcal{W}}_{NEQ}^S}{\partial (\lambda_{Se(l)})_n}}{(\lambda_{Se(k)})_n - (\lambda_{Se(l)})_n} 4 (\mathbf{M}_{Se[kl]})_n \\ &+ \left((J_{Se})_n \frac{\partial \overline{\mathcal{U}}_{NEQ}^S}{\partial (J_{Se})_n} + (J_{Se})_n^2 \frac{\partial^2 \overline{\mathcal{U}}_{NEQ}^S}{\partial (J_{Se})_n^2} \right) \end{aligned}$$

$$\begin{aligned} & \times (\widehat{\mathbf{C}}_{Se}^{-1})_n \otimes (\widehat{\mathbf{C}}_{Se}^{-1})_n \\ & - 2 (J_{Se})_n \frac{\partial \bar{\mathcal{U}}_{NEQ}^S}{\partial (J_{Se})_n} [(\widehat{\mathbf{C}}_{Se}^{-1})_n \otimes (\widehat{\mathbf{C}}_{Se}^{-1})_n]^{23} \end{aligned} \quad (202)$$

with the partial derivatives

$$\begin{aligned} \frac{\partial \bar{\mathcal{W}}_{NEQ}^S}{\partial (\lambda_{Se(k)})_n} &= \mu_n^S \sum_{m=1}^{M_n} \frac{1}{2} \mu_{n(m)}^* (\lambda_{Se(k)}^{-1})_n [(\lambda_{Se(k)}^{\alpha_{n(m)}/2})_n - 1], \\ \frac{\partial^2 \bar{\mathcal{W}}_{NEQ}^S}{\partial (\lambda_{Se(k)})_n \partial (\lambda_{Se(l)})_n} &= \begin{cases} \mu_n^S \sum_{m=1}^{M_n} \frac{1}{4} \mu_{n(m)}^* (\lambda_{Se(k)}^{-2})_n [(\alpha_{n(m)} - 2) (\lambda_{Se(k)}^{\alpha_{n(m)}/2})_n + 2] \\ \text{if } l = k, \\ 0 \quad \text{if } l \neq k. \end{cases} \end{aligned} \quad (203)$$

The individual tangent moduli of the current frame are found as

$$\begin{aligned} {}^4\mathbf{C}_n^S &= 4 \sum_{k,l=1}^3 \frac{\partial^2 \bar{\mathcal{W}}_{NEQ}^S}{\partial (\lambda_{Se(k)})_n \partial (\lambda_{Se(l)})_n} \\ & \times (\lambda_{Se(k)})_n (\lambda_{Se(l)})_n (\mathbf{N}_{Se(k)})_n \otimes (\mathbf{N}_{Se(l)})_n \\ & + 2 \sum_{\substack{k,l=1 \\ l \neq k}}^3 \frac{\frac{\partial \bar{\mathcal{W}}_{NEQ}^S}{\partial (\lambda_{Se(k)})_n} - \frac{\partial \bar{\mathcal{W}}_{NEQ}^S}{\partial (\lambda_{Se(l)})_n}}{(\lambda_{Se(k)})_n - (\lambda_{Se(l)})_n} \\ & \times (\lambda_{Se(k)})_n (\lambda_{Se(l)})_n (\mathbf{N}_{Se[kl]})_n^4 \\ & + \left((J_{Se})_n \frac{\partial \bar{\mathcal{U}}_{NEQ}^S}{\partial (J_{Se})_n} + (J_{Se}^2)_n \frac{\partial^2 \bar{\mathcal{U}}_{NEQ}^S}{\partial (J_{Se}^2)_n} \right) (\mathbf{I} \otimes \mathbf{I}) \\ & - 2 (J_{Se})_n \frac{\partial \bar{\mathcal{U}}_{NEQ}^S}{\partial (J_{Se})_n} (\mathbf{I} \otimes \mathbf{I})^{23} \end{aligned} \quad (204)$$

and those of the referential frame follow then from respective covariant pull-backs, viz.,

$$\begin{aligned} {}^4\mathbf{B}_n^S &= [(\mathbf{F}_{Si}^{-1})_n \otimes (\mathbf{F}_{Si}^{-1})_n]^{23} {}^4\widehat{\mathbf{C}}_n^S [(\mathbf{F}_{Si}^{T-1})_n \otimes (\mathbf{F}_{Si}^{T-1})_n]^{23} \\ &= (\mathbf{F}_S^{-1} \otimes \mathbf{F}_S^{-1})^{23} {}^4\mathbf{C}_n^S (\mathbf{F}_S^{T-1} \otimes \mathbf{F}_S^{T-1})^{23}. \end{aligned} \quad (205)$$

Note that similar to the total non-equilibrium stresses \mathbf{S}_{NEQ}^S and $\boldsymbol{\tau}_{NEQ}^S$, entire tangent moduli can be introduced as

$${}^4\mathbf{B}_{NEQ}^S = \sum_{n=1}^N {}^4\mathbf{B}_n^S, \quad {}^4\mathbf{C}_{NEQ}^S = \sum_{n=1}^N {}^4\mathbf{C}_n^S, \quad (206)$$

which, for obvious reasons, is not possible for the intermediate states. Similar to the equilibrium elasticity tensors,

the hyperelastic continuum tangents of the non-equilibrium parts exhibit the minor and major symmetries. However, also here, a special treatment of multiple eigenvalues $(\lambda_{Se(k)})_n$ is required according to (73) and (74), respectively.

The final task in order to complete the finite viscoelastic solid model is the specification of the inelastic evolution equations, i.e., the flow rules that govern the temporal development of the inelastic deformations. Proceeding from the solid residual inequality (173) and following the arguments of Sect. 3.1.4, the dissipation inequality is sufficiently satisfied if the individual terms of the residual inequality possess a positive quadratic form. Accordingly, in regard to the positive definiteness of $(\widehat{\mathbf{C}}_{Se})_n$, this can be accomplished by choosing the simple ansatz

$$(\widehat{\mathbf{D}}_{Si})_n \propto \widehat{\boldsymbol{\tau}}_n^S \longrightarrow (\widehat{\mathbf{D}}_{Si})_n = (\widehat{\mathbf{D}}_n^S)^{-1} \widehat{\boldsymbol{\tau}}_n^S, \quad (207)$$

where $(\widehat{\mathbf{D}}_n^S)^{-1}$ are positive definite, isotropic tensor functions of fourth order. Actually, they represent the viscous compliances associated with the dashpots of the underlying Maxwell elements and are chosen in such a way that their inverses are identical to the isotropic viscosity tensors of the linear theory presented in (134), viz.:

$$\begin{aligned} (\widehat{\mathbf{D}}_n^S)^{-1} &= \frac{1}{2\eta_n^S} (\mathbf{I} \otimes \mathbf{I})^{23} - \frac{\zeta_n^S}{2\eta_n^S (2\eta_n^S + 3\zeta_n^S)} (\mathbf{I} \otimes \mathbf{I}) \\ \Leftrightarrow \widehat{\mathbf{D}}_n^S &= 2\eta_n^S (\mathbf{I} \otimes \mathbf{I})^{23} + \zeta_n^S (\mathbf{I} \otimes \mathbf{I}). \end{aligned} \quad (208)$$

Therein, the viscosities possibly depend on the individual overstresses, which is appropriate if nonlinear rate-dependent behavior has to be modeled, cf. [70]. Moreover, it is apparent that they must satisfy

$$\begin{aligned} \eta_n^S &= \eta_n^S(\widehat{\boldsymbol{\tau}}_n^S) > 0, \quad \zeta_n^S = \zeta_n^S(\widehat{\boldsymbol{\tau}}_n^S) > -\frac{2}{3}\eta_n^S \\ \text{as } \xi_n^S &:= \frac{2}{3}\eta_n^S + \zeta_n^S > 0, \end{aligned} \quad (209)$$

where ξ_n^S denotes the macroscopic bulk viscosities of the skeleton. The inelastic evolution equations (207) describe the temporal changes of the strain-equivalent internal variables depending on their current values including the history information. Thus, it appears to be natural to formulate the evolution laws with respect to the intermediate configurations as they represent the actual frame for the inelastic deformation process. However, with regards to the numerical evaluation of the evolution equations, for the sake of convenience, the spatiotemporal discretization is usually carried out on the constant reference configuration. Therefore, the constitutive evolution laws (207) must be rephrased by means of referential quantities, which can be accomplished using the known transport mechanisms. Thus, the

conditional differential equations for the inelastic deformation tensors become

$$\begin{aligned} [(\mathbf{C}_{Si})_n]_S' &= \frac{1}{\eta_n^S} (\mathbf{C}_{Si})_n \mathbf{S}_n^S (\mathbf{C}_{Si})_n \\ &\quad - \frac{\zeta_n^S}{\eta_n^S (2\eta_n^S + 3\zeta_n^S)} [\mathbf{S}_n^S \cdot (\mathbf{C}_{Si})_n] (\mathbf{C}_{Si})_n, \\ \mathbf{h}^k \otimes \mathbf{h}^l : [(\hat{\mathbf{z}}_{kl})_n]_S' &= \frac{1}{\eta_n^S} (\hat{\mathbf{z}}_{kl})_n (\tau^{ij})_n (\hat{\mathbf{z}}_{jl})_n \\ &\quad - \frac{\zeta_n^S}{\eta_n^S (2\eta_n^S + 3\zeta_n^S)} [(\tau^{ij})_n (\hat{\mathbf{z}}_{ij})_n] (\hat{\mathbf{z}}_{kl})_n \end{aligned} \quad (210)$$

or, equivalently, in covariant representation

$$\begin{aligned} [(\mathbf{C}_{Si}^{-1})_n]_S' &= -\frac{1}{\eta_n^S} \mathbf{S}_n^S \\ &\quad + \frac{\zeta_n^S}{\eta_n^S (2\eta_n^S + 3\zeta_n^S)} [\mathbf{S}_n^S \cdot (\mathbf{C}_{Si})_n] (\mathbf{C}_{Si}^{-1})_n, \\ \mathbf{h}_k \otimes \mathbf{h}_l : [(\hat{\mathbf{z}}^{kl})_n]_S' &= -\frac{1}{\eta_n^S} (\tau^{kl})_n + \frac{\zeta_n^S}{\eta_n^S (2\eta_n^S + 3\zeta_n^S)} \\ &\quad \times [(\tau^{ij})_n (\hat{\mathbf{z}}_{ij})_n] (\hat{\mathbf{z}}^{kl})_n. \end{aligned} \quad (211)$$

The formulation in terms of the reference configuration is favorable as all dependencies on the internal variables are explicit, which is apparently not the case if the intermediate configurations are used. Moreover, from the natural basis representations (210)₂ and (211)₂, it is seen that the evolution laws actually determine the six independent intermediate metric coefficients $(\hat{\mathbf{z}}_{kl})_n$ or $(\hat{\mathbf{z}}^{kl})_n$, respectively. In this context, note that the choice of the preferred representation of the evolution equations is a computational rather than a physical question depending on the algorithmic implementation of the internal variable concept. A summary of the different representations of the evolution laws is provided in Appendix A.4.

Linearized Theories This paragraph is concerned with the downward compatibility of the presented finite solid viscoelasticity model to linear theories. The required linearization procedure can be carried out in two steps. In a first step, a linearization can be performed about the thermodynamic equilibrium state which can be regarded as a linearization about the intermediate configurations representing the reference states of the elastic deformation processes associated with totally relaxed springs in the Maxwell elements, i.e., $(\hat{\mathbf{F}}_{Se})_n = \mathbf{0}$ (cf. also (141)). The resulting semi-linear model is then said to belong to the theory of *finite linear viscoelasticity* which is restricted to slow deformation or fast relaxation processes that take place close to thermodynamic equilibrium but is still valid for large deformations. In a second step, the linearization procedure can be completed through linearization about the undeformed reference (natural) state

implying $\mathbf{E}_S = \mathbf{0}$ and $(\mathbf{E}_{Se})_n = \mathbf{0}$, finally yielding the linear viscoelasticity model of the infinitesimal theory. For the sake of clarity, in the sequel, $(\cdot)_{\text{lin}}$ is used to indicate linearizations about the intermediate configurations and $(\cdot)_{\text{lin}}$ denotes linearizations with respect to the natural state.

To begin with, the linearization of the intermediate over-stresses about the thermodynamic equilibrium state is carried out by a Taylor series expansion up to the first order

$$(\hat{\mathbf{T}}_n^S)_{\text{lin}} = \hat{\mathbf{T}}_n^S \Big|_{(\hat{\mathbf{F}}_{Se})_n = \mathbf{0}} + \frac{\partial \hat{\mathbf{T}}_n^S}{\partial (\hat{\mathbf{F}}_{Se})_n} \Big|_{(\hat{\mathbf{F}}_{Se})_n = \mathbf{0}} (\hat{\mathbf{F}}_{Se})_n, \quad (212)$$

where $(\hat{\mathbf{F}}_{Se})_n = \mathbf{0}$ implies

$$\begin{aligned} (\hat{\mathbf{C}}_{Se})_n = \mathbf{I} &\Leftrightarrow (\hat{\mathbf{F}}_{Se})_n = \mathbf{I} \\ &\Leftrightarrow (\lambda_{Se(k)})_n = 1, \quad (J_{Se})_n = 1. \end{aligned} \quad (213)$$

Thus, with

$$\begin{aligned} \hat{\mathbf{T}}_n^S[(\hat{\mathbf{F}}_{Se})_n = \mathbf{0}] &= \mathbf{0}, \\ \mathbf{E}_n^S &:= \frac{\partial \hat{\mathbf{T}}_n^S}{\partial (\hat{\mathbf{F}}_{Se})_n} \Big|_{(\hat{\mathbf{F}}_{Se})_n = \mathbf{0}} \\ &= \hat{\mathbf{C}}_n^S[(\hat{\mathbf{F}}_{Se})_n = \mathbf{0}] = 2\mu_n^S (\mathbf{I} \otimes \mathbf{I})^{23} + \Lambda_n^S (\mathbf{I} \otimes \mathbf{I}), \end{aligned} \quad (214)$$

one finds the linear relationship

$$(\hat{\mathbf{T}}_n^S)_{\text{lin}} = \mathbf{E}_n^S (\hat{\mathbf{F}}_{Se})_n = 2\mu_n^S (\hat{\mathbf{F}}_{Se})_n + \Lambda_n^S [(\hat{\mathbf{F}}_{Se})_n \cdot \mathbf{I}] \mathbf{I}. \quad (215)$$

Next, applying the linearization procedure to the evolution equations (207),

$$[(\hat{\mathbf{D}}_{Si})_n]_{\text{lin}} = (\hat{\mathbf{D}}_{Si})_n \Big|_{(\hat{\mathbf{F}}_{Se})_n = \mathbf{0}} + \frac{\partial (\hat{\mathbf{D}}_{Si})_n}{\partial (\hat{\mathbf{F}}_{Se})_n} \Big|_{(\hat{\mathbf{F}}_{Se})_n = \mathbf{0}} (\hat{\mathbf{F}}_{Se})_n, \quad (216)$$

together with the results (214) and

$$\begin{aligned} (\hat{\mathbf{D}}_n^S)^{-1} &:= (\hat{\mathbf{D}}_n^S)^{-1}[(\hat{\mathbf{F}}_{Se})_n = \mathbf{0}] \\ &= \frac{1}{2\eta_n^S} (\mathbf{I} \otimes \mathbf{I})^{23} - \frac{\zeta_n^S}{2\eta_n^S (2\eta_n^S + 3\zeta_n^S)} (\mathbf{I} \otimes \mathbf{I}), \end{aligned} \quad (217)$$

one obtains the linearized form

$$\begin{aligned} [(\hat{\mathbf{D}}_{Si})_n]_{\text{lin}} &= \{[(\hat{\mathbf{F}}_{Si})_n]_{\text{lin}}\}_{\text{lin}} = (\hat{\mathbf{D}}_n^S)^{-1} \mathbf{E}_n^S (\hat{\mathbf{F}}_{Se})_n \\ &= (\hat{\mathbf{T}}_n^S)^{-1} [\hat{\mathbf{T}}_S - (\hat{\mathbf{T}}_{Si})_n]. \end{aligned} \quad (218)$$

Alternatively, in terms of the reference and the actual configuration, they read

$$\begin{aligned} \{[(\mathbf{E}_{Si})_n]_S'\}_{\text{lin}} &= (\hat{\mathbf{T}}_n^S)^{-1} [\mathbf{E}_S - (\mathbf{E}_{Si})_n], \\ \{[(\mathbf{A}_{Si})_n]_S'\}_{\text{lin}} &= (\hat{\mathbf{T}}_n^S)^{-1} [\mathbf{A}_S - (\mathbf{A}_{Si})_n]. \end{aligned} \quad (219)$$

Therein, the positive definite, inverse 4th-order relaxation tensors $(\boldsymbol{\tau}_n^S)^{-1} = (\mathbf{D}_n^S)^{-1} \mathbf{E}_n^S$ are identical to those of the geometrically linear theory presented in (134). A meaningful representation of the individual relaxation tensors is, for instance, given by

$$(\boldsymbol{\tau}_n^S)^{-1} = \frac{1}{(\tau_{\text{dev}}^S)_n} \left[(\mathbf{I} \otimes \mathbf{I})^{\frac{23}{T}} - \frac{1}{3} (\mathbf{I} \otimes \mathbf{I}) \right] + \frac{1}{3(\tau_{\text{vol}}^S)_n} (\mathbf{I} \otimes \mathbf{I}) \quad (220)$$

with the deviatoric and volumetric relaxation time constants

$$(\tau_{\text{dev}}^S)_n = \frac{\eta_n^S}{\mu_n^S} > 0, \quad (\tau_{\text{vol}}^S)_n = \frac{\xi_n^S}{\kappa_n^S} = \frac{\frac{2}{3}\eta_n^S + \zeta_n^S}{\frac{2}{3}\mu_n^S + \Lambda_n^S} > 0. \quad (221)$$

In this context, some authors proceed from unique relaxation times, i.e., $\tau_n^S := (\tau_{\text{dev}}^S)_n = (\tau_{\text{vol}}^S)_n$, which, e.g., proceeding from (219)₁, yields exactly the simplified evolution equations proposed by Lubliner [88]:

$$\begin{aligned} (\boldsymbol{\tau}_n^S)^{-1} &= \frac{1}{\tau_n^S} (\mathbf{I} \otimes \mathbf{I})^{\frac{23}{T}} \\ &\rightarrow \{[(\mathbf{C}_{Si})_n]_S'\}_{\text{lin}} = \frac{1}{\tau_n^S} [\mathbf{C}_S - (\mathbf{C}_{Si})_n]. \end{aligned} \quad (222)$$

From the above equations, it is directly seen that the finite linear model proceeds from a linearization of the constitutive laws associated with the inelastic Maxwell branches. Accordingly, the semi-linear formulation in some respect represents the viscoelastic counterpart to the St. Venant-Kirchhoff elasticity law which is valid for large deformations but obeys a constant continuum tangent. Following this, finite linear viscoelasticity can only be expected to be useful in a narrow range of small perturbations away from thermodynamic equilibrium such that the intermediate configurations are adjacent to the current configuration, i.e., $(\mathbf{F}_{Si})_n \approx \mathbf{F}_S$ as $[(\mathbf{F}_{Se})_n]_{\text{lin}} \approx \mathbf{I}$. However, note that the equilibrium part is not affected by this first linearization step, and hence, still describes a spontaneous nonlinear elastic response. For further particulars including a comparative literature review of large deformation viscoelasticity models, see [115].

To continue, according to condition (181) and the proposed form of the volumetric extensions (185), the complete linearization about the unstrained reference state reveals the downward compatibility to the linear viscoelasticity model of the infinitesimal theory as depicted in (134). In detail, application of the linearization procedure yields

$$\begin{aligned} (\mathbf{S}_E^S)_{\text{lin}} \\ &= (\mathbf{S}_{EQ}^S)_{\text{lin}} \end{aligned}$$

$$+ \sum_{n=1}^N (\mathbf{S}_n^S)_{\text{lin}} \left\{ \begin{aligned} &(\mathbf{S}_{EQ}^S)_{\text{lin}} = \mathbf{S}_{EQ}^S \Big|_{(\mathbf{E}_{Se})_n=0}^{\mathbf{E}_S=0} \\ &\quad + \frac{\partial \mathbf{S}_{EQ}^S}{\partial \mathbf{E}_S} \Big|_{(\mathbf{E}_{Se})_n=0}^{\mathbf{E}_S=0} \mathbf{E}_S, \\ &(\mathbf{S}_n^S)_{\text{lin}} = \mathbf{S}_n^S \Big|_{(\mathbf{E}_{Se})_n=0}^{\mathbf{E}_S=0} \\ &\quad + \frac{\partial \mathbf{S}_n^S}{\partial (\mathbf{E}_{Se})_n} \Big|_{(\mathbf{E}_{Se})_n=0}^{\mathbf{E}_S=0} (\mathbf{E}_{Se})_n, \end{aligned} \right. \quad (223)$$

where, in particular,

$$\begin{aligned} \mathbf{S}_{EQ}^S(\mathbf{E}_S = \mathbf{0}) &= \mathbf{0}, \\ \mathbf{S}_n^S \Big|_{(\mathbf{E}_{Se})_n=0}^{\mathbf{E}_S=0} &= [(\mathbf{F}_{Si}^{-1})_n \hat{\boldsymbol{\tau}}_n^S (\mathbf{F}_{Si}^{T-1})_n] \Big|_{(\hat{\mathbf{F}}_{Se})_n=0}^{(\mathbf{E}_{Si})_n=0} = \mathbf{0}, \\ \mathbf{E}_0^S &:= \frac{\partial \mathbf{S}_{EQ}^S}{\partial \mathbf{E}_S} \Big|_{(\mathbf{E}_{Se})_n=0}^{\mathbf{E}_S=0} = \mathbf{E}_{EQ}^S(\mathbf{E}_S = \mathbf{0}) \\ &= 2\mu_0^S (\mathbf{I} \otimes \mathbf{I})^{\frac{23}{T}} + \Lambda_0^S (\mathbf{I} \otimes \mathbf{I}), \end{aligned} \quad (224)$$

$$\begin{aligned} \frac{\partial \mathbf{S}_n^S}{\partial (\mathbf{E}_{Se})_n} \Big|_{(\mathbf{E}_{Se})_n=0}^{\mathbf{E}_S=0} &= \left\{ [(\mathbf{F}_{Si}^{-1})_n \otimes (\mathbf{F}_{Si}^{-1})_n] \right\}^{\frac{23}{T}} \frac{\partial \hat{\boldsymbol{\tau}}_n^S}{\partial (\hat{\mathbf{F}}_{Se})_n} \\ &\quad \times [(\mathbf{F}_{Si}^{T-1})_n \otimes (\mathbf{F}_{Si}^{T-1})_n] \Big|_{(\hat{\mathbf{F}}_{Se})_n=0}^{(\mathbf{E}_{Si})_n=0} \\ &= \mathbf{E}_n^S. \end{aligned}$$

Note that a further linearization of the referential evolution equations (219)₁ is not necessary as they already possess a linear shape. However, in the context of a geometrical linearization procedure, one proceeds from small deformations which can be expressed by $\mathbf{u}_S = \epsilon \mathbf{u}_S$ where ϵ denotes a small positive infinitesimal quantity with the properties $\epsilon \ll 1$ and $\epsilon^{n+1} \ll \epsilon^n$. Following this, it is easily concluded that

$$\begin{aligned} (\mathbf{F}_S)_{\text{lin}} &= \mathbf{I} + \epsilon \text{Grad}_S \mathbf{u}_S \approx \mathbf{I}, \\ (\mathbf{E}_S)_{\text{lin}} &= \frac{1}{2} (\epsilon \text{Grad}_S \mathbf{u}_S + \epsilon \text{Grad}_S^T \mathbf{u}_S \\ &\quad + \epsilon^2 \text{Grad}_S^T \mathbf{u}_S \text{Grad}_S \mathbf{u}_S) \\ &\approx \frac{1}{2} (\text{Grad}_S \mathbf{u}_S + \text{Grad}_S^T \mathbf{u}_S), \end{aligned} \quad (225)$$

which likewise holds for the elastic and inelastic deformation measures. Thus, in a geometrical linear framework, the current as well as the intermediate configurations are close to the reference configuration, so that a distinction between

configurations is no longer necessary. Thus, one commonly defines

$$\begin{aligned}\boldsymbol{\varepsilon}_S &:= (\mathbf{E}_S)_{\text{lin}} \approx [(\hat{\boldsymbol{\Gamma}}_S)_n]_{\text{lin}} \approx (\mathbf{A}_S)_{\text{lin}}, \\ \boldsymbol{\sigma}_E^S &:= (\mathbf{S}_E^S)_{\text{lin}} \approx [(\hat{\boldsymbol{\tau}}_E^S)_n]_{\text{lin}} \approx (\boldsymbol{\tau}_E^S)_{\text{lin}},\end{aligned}\quad (226)$$

which transferred to the equilibrium and non-equilibrium contributions and inserted into the linearized expressions (219)₁ and (223) precisely recovers the linear viscoelasticity formulation of the small strain regime given in (134).

3.3 Viscous Pore-Fluid Constituent

3.3.1 Compressible Fluid Behavior

In the case of compressible fluid behavior, a further constitutive law is necessary which uniquely assigns the effective fluid density to the present pressure state or *vice versa*. Proceeding from isothermal conditions $\Theta^\alpha \equiv \Theta = \text{const.}$, according to (128), the free energy $\psi^F = \psi^F(\rho^{FR})$ must be specified in order to find functions $p = p(\rho^{FR})$ or $\rho^{FR} = \rho^{FR}(p)$ describing *barotropic* fluid behavior. For the purpose of this work, the compressible pore gas air is of particular interest. Thus, excluding extremal values of p and Θ , it is convenient to proceed from the ideal gas law (Boyle-Mariotte's law)

$$\begin{aligned}\psi^F(\rho^{FR}, \Theta) &= \frac{R\Theta}{M_m^F} \ln \rho^{FR} + g(\Theta) \\ \longrightarrow p(\rho^{FR}) &= (\rho^{FR})^2 \frac{\partial \psi^F}{\partial \rho^{FR}} = \frac{R\Theta}{M_m^F} \rho^{FR},\end{aligned}\quad (227)$$

where R is the universal gas constant, M_m^F is the molar mass of the considered gas, and $g(\Theta)$ is a temperature-dependent function. In this context, recall that for the case of an incompressible pore liquid, no constitutive equation is necessary as p simply acts as a Lagrangean multiplier which has to be determined from the boundary conditions.

3.3.2 Darcy and Non-Darcy Filter Laws

The simplest model for the description of 1-d incompressible pore-fluid flow through a homogeneous, saturated porous medium is a linear transport equation commonly referred to as Darcy's law [28]. However, empirical evidence revealed that the linearity between superficial velocity and hydraulic gradient breaks down for large enough flow speeds [57] which restricts the applicability of Darcy's law to lingering flows governed by small permeabilities or driven by slight pressure gradients. In other words, Darcy flows proceed from a regular, smooth pore-fluid motion (laminar flow) in the limit of a vanishingly small Reynolds number associated with negligible inertia forces.

From a physical perspective, the percolation process is mainly governed by the solid-fluid interaction mechanisms taking place at the walls of the pore channels as the common interface for momentum exchange between solid and fluid on the microscopic level [83]. These dissipative mechanisms depend on the properties of the permeating fluid as well as the morphology (structure and connectivity) of the pore space. The general capability of a porous material to transmit fluid is known as permeability, whereas the ease of the pore-fluid flow is usually subsumed by the term tortuosity which can be thought of as a measure of the irregularity of the pore-channels cross-sections. Particularly the expansion and contraction losses during the flow through microscopically disordered porous media strongly depend on the flow speed and are assumed to be responsible for the deviations from the narrow range where linear conditions are valid. The loss of linearity is also brought into connection with the onset of turbulence in the seepage flow which is believed to be enhanced by the tortuosity of the pore structure [8].

Here, proceeding from the macroscopic TPM approach, singlephasic pore-fluid flow is governed by the local interaction force per unit volume of fluid $\hat{\mathbf{p}}_E^F$ which must constitutively account for the relevant mechanisms of momentum transfer between the deforming skeleton and the permeating fluid. Following this, according to the sufficient condition (130)₃, it is convenient to proceed from the ansatz

$$\begin{aligned}\hat{\mathbf{p}}_E^F &\propto -\mathbf{w}_{FR} \\ \longrightarrow \hat{\mathbf{p}}_E^F &= -(n^F)^2 (\mathbf{K}^F)^{-1} \mathbf{w}_{FR} \\ &= -n^F (\mathbf{K}^F)^{-1} \mathbf{w}_F\end{aligned}\quad (228)$$

with $(\mathbf{K}^F)^{-1}$ representing a positive definite hydraulic resistivity or inverse permeability tensor which apparently depends on the deformable pore structure, the fluid properties, and also on the filter velocity $\mathbf{w}_F = n^F \mathbf{w}_{FR}$ consistent with the principle of equipresence. To continue, the quasi-static fluid momentum balance (104)₂ is rewritten by means of the extra quantities (113)_{2,3} yielding

$$\mathbf{0} = \text{div } \mathbf{T}_E^F + \hat{\mathbf{p}}_E^F - n^F \text{grad } p + \rho^F \mathbf{b}, \quad (229)$$

where, on the basis of a dimensional analysis, an admissible estimate of the volume-specific fluid friction force $\mathbf{t}_E^F := \text{div } \mathbf{T}_E^F$ is $|\mathbf{t}_E^F| \ll |\hat{\mathbf{p}}_E^F|$, thus assuming that dissipation only occurs in the wall boundary layers of the pore channels, whereas the fluid behaves more or less inviscid in the flow, i.e., $\mathbf{T}_E^F \approx \mathbf{0}$ [92]. Finally, by inserting the constitutive ansatz (228), one obtains a generalized 3-d filter law:

$$\begin{aligned}\mathbf{0} &= -n^F (\mathbf{K}^F)^{-1} \mathbf{w}_F - n^F \text{grad } p + \rho^F \mathbf{b} \\ \longrightarrow \mathbf{w}_F &= -\mathbf{K}^F (\text{grad } p - \rho^F \mathbf{b}).\end{aligned}\quad (230)$$

For the following considerations, the presentation is restricted to deformation-independent and isotropic permeability properties, so that the permeability tensor simplifies to

$$\mathbf{K}^F = K^F \mathbf{I} = \frac{k^F}{\gamma^{FR}} \mathbf{I} = \frac{K^S}{\mu^{FR}} \mathbf{I}. \quad (231)$$

Herein, K^F , k^F , and K^S represent the commonly used scalar-valued permeability parameters, viz., the specific permeability, the Darcy flow coefficient, and the intrinsic permeability, which, for the moment, depend only on the filter velocity \mathbf{w}_F . Moreover, $\gamma^{FR} = g \rho^{FR} > 0$ is the effective fluid weight with $g = |\mathbf{b}|$ as the scalar gravitational acceleration and $\mu^{FR} > 0$ is the effective fluid viscosity which for moderate levels of pressure can be regarded as constant. Thus, using the conventional permeability parameter k^F , one can rewrite the filter law (230)₂ in the well-known form

$$\mathbf{w}_F = k^F \mathbf{i} \quad \text{with } \mathbf{i} = -\frac{1}{\gamma^{FR}} (\text{grad } p - \rho^{FR} \mathbf{b}) \quad (232)$$

representing the dimensionless hydraulic gradient. To continue, in order to constitutively describe the nonlinear influence on the flow speed, it is convenient for most applications to proceed from the classical 1-d Forchheimer law [57]

$$-\frac{\partial p}{\partial x} = \frac{\mu^{FR}}{K^S} w_F + \frac{\rho^{FR}}{B^S} w_F^2, \quad (233)$$

where the increasing importance of inertia effects at larger filter velocities w_F is described proportional to the kinetic energy $\frac{1}{2} \rho^{FR} w_F^2$ per unit of fluid volume, cf. [69, 118]. Therein, the nonlinear velocity dependence is controlled by the tortuosity parameter B^S which describes the inherent irregularity of the pore channels. Note that the usage of the intrinsic measures K^S and B^S is preferred as they are independent of the properties of the permeating fluid [117]. Transferred to 3-D, the quadratic form is retained by use of the norm of the filter velocity yielding

$$\begin{aligned} -\text{grad } p &= \left(\frac{\mu^{FR}}{K^S} + \frac{\rho^{FR}}{B^S} |\mathbf{w}_F| \right) \mathbf{w}_F \\ \Leftrightarrow -\frac{1}{\gamma^{FR}} \text{grad } p &= \left(\frac{1}{k^F} + \frac{1}{b^S} |\mathbf{w}_F| \right) \mathbf{w}_F \end{aligned} \quad (234)$$

which precisely recovers the formulation obtained by Hasanizadeh and Gray [69] via volume averaging within the hybrid mixture theory, cf. [8]. In (234)₂, $b^S := g B^S$ is the non-Darcy flow coefficient. Following this, the included nonlinearity can be totally assigned to a velocity-dependent permeability parameter as desired, viz.,

$$\begin{aligned} \mathbf{w}_F &= -K_F^F \text{grad } p \\ \text{with } K_F^F(\mathbf{w}_F) &:= K^F \left(1 + \frac{\rho^{FR} K^S}{\mu^{FR} B^S} |\mathbf{w}_F| \right)^{-1}. \end{aligned} \quad (235)$$

Therein, the rational expression in parentheses represents a Reynolds-type dimensionless number which governs the relative importance of the tortuosity-induced inertia forces in the sense of the classical Forchheimer equation. However, for the further treatment, it is expedient to substitute the dependency on the filter velocity in (235)₂ with a pressure-gradient dependence by eliminating $|\mathbf{w}_F|$. This can be accomplished by taking the norm on both sides of (234)₁ and by solving the resulting quadratic equation for $|\mathbf{w}_F|$ yielding

$$|\mathbf{w}_F| = \frac{1}{2} \left(-\frac{\mu^{FR} B^S}{\rho^{FR} K^S} + \sqrt{\left(\frac{\mu^{FR} B^S}{\rho^{FR} K^S} \right)^2 + 4 \frac{B^S}{\rho^{FR}} |\text{grad } p|} \right), \quad (236)$$

where only the positive root is of interest as it satisfies the natural condition $|\mathbf{w}_F| = 0$ whenever $|\text{grad } p| = 0$. Then, by inserting $|\mathbf{w}_F|$ into (235)₂, one finally obtains

$$K_F^F(\text{grad } p) := K^F \left(\frac{1}{2} + \sqrt{\frac{1}{4} + \frac{\rho^{FR}}{B^S} \left(\frac{K^S}{\mu^{FR}} \right)^2 |\text{grad } p|} \right)^{-1}. \quad (237)$$

3.3.3 Deformation-Dependent Permeability Properties

The sensitivity of the permeability to the current size of the interconnected pore volume (effective porosity) is apparent. Thus, proceeding from a finite-deformation theory, it is inevitable to consider the flow controlling parameters as functions of the deformation state. For obvious reasons, the deformation dependency is best described if permeability changes are directly linked to porosity changes which becomes clear by investigating the corresponding extremal values. On the one hand, the permeability decreases to zero (impermeable state) whenever the volumetric compression increases until all pores are closed (compaction point). On the other hand, a finite dilatation of the pore space is associated with rather perfectly permeable conditions, i.e., an infinitely increasing permeability. Thus, proceeding from the initial values k_{0S}^F , K_{0S}^F , K_{0S}^S , b_{0S}^S , and B_{0S}^S of the flow-controlling parameters in the undeformed state, the following limits must be met:

$$\begin{aligned} \left\{ \begin{array}{l} k^F, K^F, K^S, \\ b^S, B^S \end{array} \right\} &\rightarrow \left\{ \begin{array}{l} 0 \\ \infty \end{array} \right\} \\ \text{if } \left\{ \begin{array}{l} n^F \rightarrow 0 \Leftrightarrow n^S \rightarrow 1 \Leftrightarrow J_S \rightarrow n_{0S}^S, \\ n^F \rightarrow 1 \Leftrightarrow n^S \rightarrow 0 \Leftrightarrow J_S \rightarrow \infty. \end{array} \right. & \end{aligned} \quad (238)$$

In this regard, several formulations of deformation-dependent permeability measures have been proposed ranging from power functions of the porosity [51] to exponential functions of the volumetric strain [79]. However, applied to highly

porous materials, such as soft polymeric foams, which allow complete compression and finite dilatation, it turns out that these formulations are unable to completely describe the nonlinear development of the permeability in the whole deformation range or even violate the limiting cases (238) [92]. Therefore, a new deformation-dependent permeability function is proposed which proceeds from a hyperbolic power function of the porosity and considers both physical limits consistent with (238). In particular, we define

$$\begin{aligned} K^S(n^F) &= K_{0S}^S \left(\frac{n^F}{1-n^F} \frac{1-n_{0S}^F}{n_{0S}^F} \right)^\kappa = K_{0S}^S \left(\frac{n^F}{n_{0S}^F} \frac{n_{0S}^S}{n^S} \right)^\kappa \\ &= K_{0S}^S \left(\frac{J_S - n_{0S}^S}{n_{0S}^S} \right)^\kappa \end{aligned} \quad (239)$$

with the exponent $\kappa \geq 0$ as an additional material parameter controlling the deformation dependency, where $\kappa = 0$ is associated with constant permeability properties depending on the initial value. Analogously, one proceeds from a porosity-dependent tortuosity parameter

$$B^S(n^F) = B_{0S}^S \left(\frac{n^F}{1-n^F} \frac{1-n_{0S}^F}{n_{0S}^F} \right)^\beta = B_{0S}^S \left(\frac{n^F}{n_{0S}^F} \frac{n_{0S}^S}{n^S} \right)^\beta \quad (240)$$

with the power $\beta \geq 0$ controlling the nonlinearity.

3.3.4 Anisotropic Permeability

Hitherto, the presentation was restricted to isotropic permeability properties. However, real foam materials, such as extruded strand foams, often show distinct orientation-dependent seepage flows, i.e., their interconnected pore space possesses preferred flow directions. Besides this natural hydraulic anisotropy, moreover preferred flow paths may develop during finite distortions of the solid skeleton. Following this, it is expedient to proceed from a permeability tensor of the form

$$\mathbf{K}^F := K^F \mathcal{H}^S \quad \text{with } \mathcal{H}^S := \mathcal{H}_{0S}^S \mathcal{K}^S \quad (241)$$

representing a dimensionless, symmetric, and positive definite hydraulic structural tensor which is composed of a constant part \mathcal{H}_{0S}^S and a deformation-dependent part $\mathcal{K}^S = \mathcal{K}^S(\mathbf{F}_S)$. In particular, \mathcal{H}_{0S}^S describes the natural hydraulic anisotropy of φ^S and can be associated with a hydraulic symmetry group $\mathcal{H}\mathcal{G}_3$ describing the inherent type of anisotropic permeability. Following this, the six independent components of $\mathcal{H}_{0S}^S = (\mathcal{H}_{0S}^S)^T$ must be determined from permeability experiments on undeformed but variously rotated samples of the considered porous material. Therefore, in order that \mathcal{H}_{0S}^S is dimensionless, the experimentally determined permeability tensor, say $\mathbf{K}_{0S}^{\text{exp}}$, must be normalized, for instance, with respect to its mean value or the

average value of its coefficients. Then, by interpreting the normalizing constant as the initial, scalar-valued permeability parameter, e.g., $K_{0S}^F = \frac{1}{3} \text{tr} \mathbf{K}_{0S}^{\text{exp}}$ or $K_{0S}^F = \frac{1}{9} \sum K_{0S(kl)}^{\text{exp}}$ ($k, l = 1, 2, 3$), one finally obtains $\mathcal{H}_{0S}^S = \mathbf{K}_{0S}^{\text{exp}} / K_{0S}^F$. Following this, in the case of isotropic permeability properties associated with $\mathbf{K}_{0S}^{\text{exp}} = K_{0S}^F \mathbf{I}$, it is easily concluded that $\mathcal{H}_{0S}^S = \mathbf{I}$, cf. [92].

To continue, the deformation-dependent part of the hydraulic structural tensor \mathcal{K}^S must be specified in order to describe the deformation-induced permeability changes with respect to an undeformed reference state where $\mathcal{K}_{0S}^S = \mathcal{K}^S(\mathbf{F}_S = \mathbf{I}) = \mathbf{I}$. The derivation of \mathcal{K}^S can be motivated with the help of capillary tube models which proceed from an idealization of the real pore channels by a bundle of parallel tubes embedded in a solid material (cf. [7, Sect. 5.10.1]). Assuming the tubes to be oriented along the orthogonal axes of a cube, confined uniaxial compression in the direction of one of the axes causes a decrease in the permeable cross-sections perpendicular to the loading direction, whereas the flow through the pipes in the loading direction is assumed to remain unchanged. Then, expressing the deformation dependency of \mathcal{K}^S by means of the eigenvalues of the deformation tensors, it is apparent that the diagonal elements take the form $\mathcal{K}_{kk}^S = \mathcal{K}_{kk}^S(\lambda_{S(l)}) \sum k \forall l \neq k$, so that

$$\begin{aligned} &\mathcal{K}^S(\lambda_{S(k)}) \\ &= \begin{bmatrix} \mathcal{K}_{11}^S(\lambda_{S(2)} \lambda_{S(3)}) & 0 & 0 \\ 0 & \mathcal{K}_{22}^S(\lambda_{S(3)} \lambda_{S(1)}) & 0 \\ 0 & 0 & \mathcal{K}_{33}^S(\lambda_{S(1)} \lambda_{S(2)}) \end{bmatrix} \\ &\quad \times \mathbf{e}_k \otimes \mathbf{e}_l. \end{aligned} \quad (242)$$

Following this, proceeding from \mathcal{K}^S as an isotropic tensor function of the current configuration which in contrast to \mathcal{H}_{0S}^S is invariant to changes of the reference configuration, formal generalization yields the following spectral representation (cf. Sect. 2.2.3):

$$\mathcal{K}^S(\lambda_{S(k)}) = \frac{1}{2} \sum_{\substack{k=1 \\ j \neq l \neq k \neq j}}^3 (\lambda_{S(j)} \lambda_{S(l)})^\vartheta \mathbf{N}_{S(k)} \equiv (\text{cof} \mathbf{B}_S)^\vartheta. \quad (243)$$

Herein, the real-valued power $\vartheta \geq 0$ is introduced to control the nonlinearity of the deformation-induced anisotropy where the deformation dependency is turned off if $\vartheta = 0$, i.e., $\mathcal{K}^S = \mathbf{I}$. Moreover, since $\lambda_{S(j)} \lambda_{S(l)}$ ($j \neq l$) represent the eigenvalues of the cofactors of the deformation tensors, the deformation-dependent hydraulic anisotropy tensor essentially represents a real-valued power of the cofactor of \mathbf{B}_S . Consequently, from a computational perspective, the calculation of \mathcal{K}_S does not cause additional expenses as the eigenvalues and eigentensors of \mathbf{B}_S are also required for

the equilibrium-stress computation based on the Ogden-type formulation presented in Sect. 3.2.3.

Finally, the constitutive filter law is summarized in (244) where the advantage of the proposed formulation is directly seen. Although all relevant nonlinearities are included, it still has the simple form of a Darcy-type equation as the

nonlinear dependencies are completely considered by the permeability tensor \mathbf{K}^F . Thus, the anisotropic, non-Darcy filter law is easy to implement and the idea of a velocity and deformation-dependent permeability can at least be adopted to extend existing linear formulations.

Complete 3-d nonlinear filter law

$$\begin{aligned}
 \text{basic filter law:} \quad & \mathbf{w}_F = n^F \mathbf{w}_{FR} = -\mathbf{K}^F (\text{grad } p - \rho^{FR} \mathbf{b}) \\
 \text{permeability tensor:} \quad & \mathbf{K}^F = K_F^F \mathcal{H}^S = K_F^F \mathcal{H}_{0S}^S (\text{cof } \mathbf{B}_S)^\vartheta, \quad \vartheta \geq 0 \\
 \text{nonlinear permeability:} \quad & K_F^F = \frac{K^S}{\mu^{FR}} \left(\frac{1}{2} + \sqrt{\frac{1}{4} + \frac{\rho^{FR}}{B^S} \left(\frac{K^S}{\mu^{FR}} \right)^2 |\text{grad } p|} \right)^{-1} \\
 \text{intrinsic permeability:} \quad & K^S = K_{0S}^S \left(\frac{n^F}{n_{0S}^F} \frac{n_{0S}^S}{n^S} \right)^\kappa, \quad \kappa \geq 0 \\
 \text{tortuosity parameter:} \quad & B^S = B_{0S}^S \left(\frac{n^F}{n_{0S}^F} \frac{n_{0S}^S}{n^S} \right)^\beta, \quad \beta \geq 0
 \end{aligned} \tag{244}$$

4 Numerical Treatment

4.1 Weak Formulation

The Finite Element Method (FEM) has been proven to provide a suitable formalism for generating a discrete algorithm to approximate the solution of the descriptive set of coupled partial differential equations. In this regard, the quasi-static biphasic model under consideration incorporates three independent fields, namely the solid displacement \mathbf{u}_S , the seepage velocity \mathbf{w}_{FR} , and the effective pore-fluid pressure p , which basically demands three corresponding equations for the solution. However, proceeding from quasi-static conditions, the seepage velocity can be substituted by the constitutive filter law (244), which is actually a function of \mathbf{u}_S and p . Consequently, \mathbf{w}_{FR} loses the nature of an independent field variable, and thus, can be calculated in a post processing step, so that the number of unknowns of the process as well as the number of required conditional equations reduces to two. In particular, the governing partial differential equations are the fluid mass balance (103) with \mathbf{w}_{FR} eliminated by use of the filter law (244) and the time derivatives rewritten with respect to the solid motion

$$\begin{aligned}
 & n^F (\rho^{FR})'_S + \rho^{FR} \text{div} (\mathbf{u}_S)'_S \\
 & - \text{div} [\rho^{FR} \mathbf{K}^F (\text{grad } p - \rho^{FR} \mathbf{b})] = 0,
 \end{aligned} \tag{245}$$

and the momentum balance of the mixture obtained as the sum of the partial momentum balances (104) by taking into account that $\hat{\mathbf{p}}^S + \hat{\mathbf{p}}^F = \mathbf{0}$ yielding

$$\text{div} (\mathbf{T}_E^S - p \mathbf{I}) + (n^S \rho^{SR} + n^F \rho^{FR}) \mathbf{b} = \mathbf{0}. \tag{246}$$

Now, following the idea of the FEM, the above field equations must be transferred to weak formulations. Therefore, the balance relations are weighted by independent test functions and integrated over the spatial domain Ω occupied by the mixture body \mathcal{B} . As usual, the surface $\Gamma = \partial \Omega$ is split into a Dirichlet (essential) and a Neumann (natural) boundary yielding $\Gamma = \Gamma_p \cup \Gamma_q$ for the fluid mass balance and $\Gamma = \Gamma_{\mathbf{u}_S} \cup \Gamma_{\mathbf{t}}$ for the mixture momentum balance. Then, applying the product rule and the Gaußian integral theorem, one obtains the weak formulation of the fluid balance of mass as

$$\begin{aligned}
 & \mathcal{G}_p(\delta p, \mathbf{u}_S, p) \\
 & \equiv \int_{\Omega} \delta p [n^F (\rho^{FR})'_S + \rho^{FR} \text{div} (\mathbf{u}_S)'_S] dv \\
 & + \int_{\Omega} \text{grad } \delta p \cdot [\rho^{FR} \mathbf{K}^F (\text{grad } p - \rho^{FR} \mathbf{b})] dv \\
 & + \int_{\Gamma_q} \delta p \bar{q} da = 0,
 \end{aligned} \tag{247}$$

and the weak formulation of the mixture momentum balance becomes

$$\begin{aligned} \mathcal{G}_{\mathbf{u}_S}(\delta \mathbf{u}_S, \mathbf{u}_S, p) & \equiv \int_{\Omega} \operatorname{grad} \delta \mathbf{u}_S \cdot (\mathbf{T}_E^S - p \mathbf{I}) \, dv \\ & - \int_{\Omega} \delta \mathbf{u}_S \cdot (n^S \rho^{SR} + n^F \rho^{FR}) \mathbf{b} \, dv \\ & - \int_{\Gamma_t} \delta \mathbf{u}_S \cdot \bar{\mathbf{t}} \, da = 0. \end{aligned} \quad (248)$$

Herein, $\delta \mathbf{u}_S$ and δp are the test functions, which can be interpreted as virtual fields corresponding to the solid displacement \mathbf{u}_S and the pore-fluid pressure p . In this context, note that $\mathbf{u}_S = \bar{\mathbf{u}}_S$ on $\Gamma_{\mathbf{u}_S}$ and $p = \bar{p}$ on Γ_p exactly fulfill the Dirichlet boundary conditions, whereas the test functions $\delta \mathbf{u}_S$ and δp identically vanish on Dirichlet boundaries. Moreover, $\bar{\mathbf{t}} = (\mathbf{T}_E^S - p \mathbf{I}) \mathbf{n}$ is the external load vector acting on the Neumann boundary Γ_t with the outward oriented unit surface normal \mathbf{n} and $\bar{q} = n^F \rho^{FR} \mathbf{w}_{FR} \cdot \mathbf{n}$ denotes the filter mass flow rate of the fluid draining through the Neumann boundary Γ_q . Note that the surface traction $\bar{\mathbf{t}} = \bar{\mathbf{t}}^S + \bar{\mathbf{t}}^F$ acts on both the solid and the fluid phase. This is essential for the formulation of boundary-value problems as no separation of the boundary conditions into actions on the different phases is needed, and thus, physically meaningful boundary conditions can be applied.

For the special case of a materially incompressible pore liquid ($\rho^{FR} = \text{const.}$), the weak form of the fluid mass balance (247) naturally reduces to a volume balance

$$\begin{aligned} \mathcal{G}_p(\delta p, \mathbf{u}_S, p) & \equiv \int_{\Omega} \delta p \operatorname{div} (\mathbf{u}_S)'_S \, dv \\ & + \int_{\Omega} \operatorname{grad} \delta p \cdot [\mathbf{K}^F (\operatorname{grad} p - \rho^{FR} \mathbf{b})] \, dv \\ & + \int_{\Gamma_q} \delta p \bar{v} \, da = 0 \end{aligned} \quad (249)$$

with $\bar{v} = n^F \mathbf{w}_{FR} \cdot \mathbf{n}$ denoting the volume efflux of φ^F through the boundary Γ_q . However, both weak formulations (247) and (249) essentially determine p such that the saturation condition is preserved, which becomes clear from the fact that both relations can be attributed to the constraint $(n^S + n^F)'_S = 0$ (cf. (110) and (111)).

4.2 Linearization

The two-field variational formulation given by (247) and (248) possesses geometrical as well as material nonlinearities. Therefore, in preparation for an efficient numerical treatment by an iterative solution technique, such as the Newton-Raphson method, the linearization of the weak forms is required. In this context, a so-called *consistent* linearization must be carried out which proceeds from a complete (consistent) equal-order linearization with respect

to all occurring unknowns of the process, namely the solid displacement \mathbf{u}_S and the effective pore-fluid pressure p . The keystone of the linearization procedure is the directional or Gâteaux derivative [74, 142]

$$\begin{aligned} \mathcal{D}_{\Delta \mathbf{u}} \mathcal{F}(\mathbf{u}) & := \lim_{\epsilon \rightarrow 0} \frac{\mathcal{F}(\mathbf{u} + \epsilon \Delta \mathbf{u}) - \mathcal{F}(\mathbf{u})}{\epsilon} = \frac{d}{d\epsilon} \mathcal{F}(\mathbf{u} + \epsilon \Delta \mathbf{u}) \Big|_{\epsilon=0} \end{aligned} \quad (250)$$

assuming that a linear Gâteaux differential (weak differential) $\mathcal{D}_{\Delta \mathbf{u}} \mathcal{F}(\mathbf{u})$ exists, which describes the change of the function \mathcal{F} at \mathbf{u} in the direction of $\Delta \mathbf{u}$. Thus, the linearization of a nonlinear function \mathcal{F} about $\tilde{\mathbf{u}}$ results from a first-order Taylor series expansion

$$\begin{aligned} \mathcal{F}(\mathbf{u}) & = \mathcal{F}(\tilde{\mathbf{u}}) + \mathcal{D}_{\Delta \mathbf{u}} \mathcal{F}(\tilde{\mathbf{u}}) + \mathcal{R}(\Delta \mathbf{u}) \\ \longrightarrow \quad \mathcal{F}_{\text{lin}}(\mathbf{u}) & = \mathcal{F}(\tilde{\mathbf{u}}) + \mathcal{D}_{\Delta \mathbf{u}} \mathcal{F}(\tilde{\mathbf{u}}) \end{aligned} \quad (251)$$

under the assumption that the remainder term $\mathcal{R}(\Delta \mathbf{u})$ is negligibly small.

To begin with, for the sake of a clear and compact representation, the weak forms $\mathcal{G}_{\mathbf{u}_S}$ and \mathcal{G}_p are collected in a function vector $\mathcal{G}_{\mathbf{u}}$ and the primary unknown field variables \mathbf{u}_S and p are summarized in a vector of unknowns \mathbf{u} :

$$\begin{aligned} \mathcal{G}_{\mathbf{u}} & = \begin{bmatrix} \mathcal{G}_{\mathbf{u}_S} \\ \mathcal{G}_p \end{bmatrix}, \quad \mathbf{u} = \begin{bmatrix} \mathbf{u}_S \\ p \end{bmatrix}, \quad \delta \mathbf{u} = \begin{bmatrix} \delta \mathbf{u}_S \\ \delta p \end{bmatrix}, \\ (\mathbf{u})'_S & = \begin{bmatrix} (\mathbf{u}_S)'_S \\ (p)'_S \end{bmatrix}, \quad \Delta \mathbf{u} = \begin{bmatrix} \Delta \mathbf{u}_S \\ \Delta p \end{bmatrix}. \end{aligned} \quad (252)$$

In this connection, one additionally introduces the corresponding vector of test functions $\delta \mathbf{u}$, the solid time derivative of the vector of unknowns $(\mathbf{u})'_S$ which will be discretized by an appropriate time integration scheme, and the incremental vector $\Delta \mathbf{u}$ which can be viewed as the increment of an iterative solution procedure at a fixed time. Note that $(\mathbf{u}_S)'_S$ and $(p)'_S$ are not additional degrees of freedom (DOF) in the sense of a weak formulation. They merely serve to transform the global set of equations into a system of first-order differential equations in time. Following this, the linearization of the two-field variational formulation which is still continuous in the space and the time domain takes the form

$$\begin{aligned} (\mathcal{G}_{\mathbf{u}})_{\text{lin}}[\delta \mathbf{u}, \mathbf{u}, (\mathbf{u})'_S] & = \tilde{\mathcal{G}}_{\mathbf{u}} + \mathcal{D}_{\Delta \mathbf{u}} \tilde{\mathcal{G}}_{\mathbf{u}} + \mathcal{D}_{\Delta(\mathbf{u})'_S} \tilde{\mathcal{G}}_{\mathbf{u}} \\ & \text{with } \tilde{\mathcal{G}}_{\mathbf{u}} = \mathcal{G}_{\mathbf{u}}[\delta \mathbf{u}, \tilde{\mathbf{u}}, (\tilde{\mathbf{u}})'_S], \end{aligned} \quad (253)$$

where $\tilde{\mathbf{u}}$ indicates the expansion point of the current configuration. In this representation, the Gâteaux differentials can be expressed in concise matrix form, viz.

$$\begin{aligned}\mathcal{D}_{\Delta u} \tilde{\mathbf{G}}_u &= \begin{bmatrix} \mathcal{D}_{\Delta \mathbf{u}_S} \tilde{\mathbf{G}}_{\mathbf{u}_S} & \mathcal{D}_{\Delta p} \tilde{\mathbf{G}}_{\mathbf{u}_S} \\ \mathcal{D}_{\Delta \mathbf{u}_S} \tilde{\mathbf{G}}_p & \mathcal{D}_{\Delta p} \tilde{\mathbf{G}}_p \end{bmatrix}, \\ \mathcal{D}_{\Delta(u)_S'} \tilde{\mathbf{G}}_u &= \begin{bmatrix} \mathcal{D}_{\Delta(\mathbf{u}_S)'} \tilde{\mathbf{G}}_{\mathbf{u}_S} & \mathcal{D}_{\Delta(p)'} \tilde{\mathbf{G}}_{\mathbf{u}_S} \\ \mathcal{D}_{\Delta(\mathbf{u}_S)'} \tilde{\mathbf{G}}_p & \mathcal{D}_{\Delta(p)'} \tilde{\mathbf{G}}_p \end{bmatrix}.\end{aligned}\quad (254)$$

Since the directional derivative (250) represents a linear operator, the common rules of differential calculus can be applied. Following this, together with the transport properties of the gradient operator (25), the required basic linearizations can be straightforwardly computed and are summarized in (255).

Collection of basic linearizations

$$\begin{aligned}\mathcal{D}_{\Delta \mathbf{u}_S} \mathbf{F}_S &= \frac{d}{d\epsilon} \text{Grad}_S(\mathbf{x} + \epsilon \Delta \mathbf{u}_S) \Big|_{\epsilon=0} = \text{Grad}_S \Delta \mathbf{u}_S \\ \mathcal{D}_{\Delta \mathbf{u}_S} \mathbf{F}_S^{-1} &= -\mathbf{F}_S^{-1} (\mathcal{D}_{\Delta \mathbf{u}_S} \mathbf{F}_S) \mathbf{F}_S^{-1} = -\mathbf{F}_S^{-1} \text{grad} \Delta \mathbf{u}_S \\ \mathcal{D}_{\Delta \mathbf{u}_S} \text{grad} \Psi &= (\text{Grad}_S \Psi) \mathcal{D}_{\Delta \mathbf{u}_S} \mathbf{F}_S^{-1} = -(\text{grad} \Psi) \text{grad} \Delta \mathbf{u}_S \\ \mathcal{D}_{\Delta \mathbf{u}_S} \text{grad} \Psi &= (\mathcal{D}_{\Delta \mathbf{u}_S} \mathbf{F}_S^{T-1}) \text{Grad}_S \Psi = -(\text{grad}^T \Delta \mathbf{u}_S) \text{grad} \Psi \\ \mathcal{D}_{\Delta \mathbf{u}_S} J_S &= \frac{\partial J_S}{\partial \mathbf{F}_S} \cdot \mathcal{D}_{\Delta \mathbf{u}_S} \mathbf{F}_S = J_S \mathbf{F}_S^{T-1} \cdot \text{Grad}_S \Delta \mathbf{u}_S = J_S \text{div} \Delta \mathbf{u}_S \\ \mathcal{D}_{\Delta \mathbf{u}_S} \left[\int_{\Omega} (\cdot) dv \right] &= \int_{\Omega_0} \mathcal{D}_{\Delta \mathbf{u}_S} [(\cdot) J_S] dV_S = \int_{\Omega} [\mathcal{D}_{\Delta \mathbf{u}_S} (\cdot) + (\cdot) \text{div} \Delta \mathbf{u}_S] dv \\ \mathcal{D}_{\Delta(\mathbf{u}_S)'} \text{div} (\mathbf{u}_S)'_S &= \frac{d}{d\epsilon} \text{div} [(\mathbf{u}_S)'_S + \epsilon \Delta(\mathbf{u}_S)'_S] \Big|_{\epsilon=0} = \text{div} \Delta(\mathbf{u}_S)'_S \\ \mathcal{D}_{\Delta p} \text{grad} p &= \frac{d}{d\epsilon} \text{grad} (p + \epsilon \Delta p) \Big|_{\epsilon=0} = \text{grad} \Delta p\end{aligned}\quad (255)$$

For convenience, in the following considerations, the boundary terms $\bar{\mathbf{t}}$ and \bar{q} , and thus, the surface integrals are assumed to be independent of the deformation, i.e., they do not contribute to the linearization. Moreover, the uniform mass-specific external body force \mathbf{b} is identified with the gravitational acceleration and regarded as constant. Therefore, for the determination of the individual elements of $\mathcal{D}_{\Delta u} \tilde{\mathbf{G}}_u$ and $\mathcal{D}_{\Delta(u)_S'} \tilde{\mathbf{G}}_u$, besides the basic linearizations in (255), it remains to take into account the functional dependencies of the solid extra stress tensor, the effective fluid density, and the permeability tensor on the set of primary unknowns \mathbf{u} according to the underlying constitutive equations. In particular, with the inelastic deformation tensors summarized in a vector of internal (history) variables $\mathbf{q} = [(\mathbf{C}_{Si})_1, \dots, (\mathbf{C}_{Si})_N]^T$, it holds

$$\begin{aligned}\mathbf{T}_E^S &= J_S^{-1} \mathbf{F}_S \mathbf{S}_E^S \mathbf{F}_S^T \quad \text{with } \mathbf{S}_E^S = \mathbf{S}_E^S[\mathbf{u}_S, \mathbf{q}(\mathbf{u}_S)], \\ \rho^{FR} &= \rho^{FR}(p) \\ \longrightarrow \quad (\rho^{FR})'_S &= \frac{\partial \rho^{FR}}{\partial p} (p)'_S, \quad \mathbf{K}^F = \mathbf{K}^F(\mathbf{u}_S, p).\end{aligned}\quad (256)$$

Beginning with the weak formulation of the mixture momentum balance (248), linearization of the individual terms

yields the following partial results:

$$\begin{aligned}\mathcal{D}_{\Delta \mathbf{u}_S} \left[\int_{\Omega} \text{grad} \delta \mathbf{u}_S \cdot \mathbf{T}_E^S dv \right] &= \int_{\Omega} \text{grad} \delta \mathbf{u}_S \cdot [J_S^{-1} \mathbf{F}_S (\mathcal{D}_{\Delta \mathbf{u}_S} \mathbf{S}_E^S) \mathbf{F}_S^T \\ &\quad + (\text{grad} \Delta \mathbf{u}_S) \mathbf{T}_E^S] dv,\end{aligned}\quad (257)$$

$$\begin{aligned}\mathcal{D}_{\Delta \mathbf{u}_S} \left[\int_{\Omega} -\text{grad} \delta \mathbf{u}_S \cdot p \mathbf{I} dv \right] &= \int_{\Omega} \text{grad} \delta \mathbf{u}_S \cdot p [\text{grad}^T \Delta \mathbf{u}_S - (\text{div} \Delta \mathbf{u}_S) \mathbf{I}] dv,\end{aligned}\quad (258)$$

$$\begin{aligned}\mathcal{D}_{\Delta \mathbf{u}_S} \left[\int_{\Omega} \delta \mathbf{u}_S \cdot (n^S \rho^{SR} + n^F \rho^{FR}) \mathbf{b} dv \right] &= \int_{\Omega} \delta \mathbf{u}_S \cdot (\text{div} \Delta \mathbf{u}_S) \rho^{FR} \mathbf{b} dv,\end{aligned}\quad (259)$$

$$\begin{aligned}\mathcal{D}_{\Delta p} \left[\int_{\Omega} -\text{grad} \delta \mathbf{u}_S \cdot p \mathbf{I} dv \right] &= \int_{\Omega} -\text{grad} \delta \mathbf{u}_S \cdot \Delta p \mathbf{I} dv,\end{aligned}\quad (260)$$

$$\begin{aligned} \mathcal{D}_{\Delta p} \left[\int_{\Omega} \delta \mathbf{u}_S \cdot (n^S \rho^{SR} + n^F \rho^{FR}) \mathbf{b} \, dv \right] \\ = \int_{\Omega} -\delta \mathbf{u}_S \cdot n^F \frac{\partial \rho^{FR}}{\partial p} \Delta p \mathbf{b} \, dv. \end{aligned} \quad (261)$$

Therein, in (257), the covariant push-forward of the directional derivative of the referential solid extra stress tensor is obtained as

$$\begin{aligned} \mathbf{F}_S (\mathcal{D}_{\Delta \mathbf{u}_S} \mathbf{S}_E^S) \mathbf{F}_S^T \\ = (\mathbf{F}_S \otimes \mathbf{F}_S)^T \mathcal{B}^S (\mathbf{F}_S^T \otimes \mathbf{F}_S^T)^{23} \\ \times \frac{1}{2} [\text{grad } \Delta \mathbf{u}_S + \text{grad}^T \Delta \mathbf{u}_S] \\ = \mathcal{C}^S \frac{1}{2} [\text{grad } \Delta \mathbf{u}_S + \text{grad}^T \Delta \mathbf{u}_S], \end{aligned} \quad (262)$$

where

$$\mathcal{B}^S := \frac{d\mathbf{S}_E^S}{d\mathbf{E}_S} \quad \text{and} \quad \mathcal{C}^S := (\mathbf{F}_S \otimes \mathbf{F}_S)^T \mathcal{B}^S (\mathbf{F}_S^T \otimes \mathbf{F}_S^T)^{23} \quad (263)$$

represent the consistent tangent moduli of the finite solid viscoelasticity formulation related to the reference and the actual configuration.

Consistent Viscoelastic Tangent Operator In the course of the subsequent discretization procedure, the viscoelastic solid stress tangent $(\mathcal{C}^S)^4$ must be replaced with its discrete counterpart. In order to improve the convergence characteristic of the global iterative solution algorithm in expectation of a quadratic rate of asymptotic convergence of the overall nonlinear biphase problem, the consistency of the inelastic stiffness tensor is essential (cf. [129]). Particularly the included transient non-equilibrium stiffness contributions associated with the Maxwell elements must be carefully handled taking into account the algorithmic treatment of the viscous evolution equations. This becomes clear by looking closer at the *algorithmically consistent* tangent operator of the reference configuration. In analogy to the continuum tangent, it can be split into an equilibrium and a non-equilibrium part:

$$\begin{aligned} \mathcal{B}^S = \frac{d\mathbf{S}_E^S}{d\mathbf{E}_S} = \mathcal{B}_{EQ}^S + \mathcal{B}_{NEQ}^S, \\ \text{where} \quad \begin{cases} \mathcal{B}_{EQ}^S = \frac{d\mathbf{S}_{EQ}^S}{d\mathbf{E}_S} \equiv \mathcal{B}_{EQ}^S, \\ \mathcal{B}_{NEQ}^S = \frac{d\mathbf{S}_{NEQ}^S}{d\mathbf{E}_S} \neq \mathcal{B}_{NEQ}^S. \end{cases} \end{aligned} \quad (264)$$

It is apparent that the non-equilibrium parts of the consistent and the continuum tangents are different which calls for

a detailed examination. In anticipation of the numerical solution strategy, the consistent non-equilibrium tangent is derived as follows:

$$\begin{aligned} \mathcal{B}_{NEQ}^S &= \frac{d\mathbf{S}_{NEQ}^S}{d\mathbf{E}_S} \\ &= \underbrace{\sum_{n=1}^N \frac{\partial \mathbf{S}_n^S}{\partial (\mathbf{E}_{Se})_n} \frac{d(\mathbf{E}_{Se})_n}{d\mathbf{E}_S}}_{\mathcal{B}_{NEQ}^S} + \underbrace{\sum_{n=1}^N \frac{\partial \mathbf{S}_n^S}{\partial (\mathbf{E}_{Si})_n} \frac{d(\mathbf{E}_{Si})_n}{d\mathbf{E}_S}}_{\mathcal{B}_q^S}. \end{aligned} \quad (265)$$

Herein, besides the non-equilibrium continuum tangent known from (204)–(206), a new 4th-order tensor $(\mathcal{B}_q^S)^4$ can be identified which involves contributions related to the internal inelastic strain variables. Thus, as a matter of fact, the consistent non-equilibrium tangent depends on the implemented solution algorithm. Here, following the common practice in computational plasticity (cf. [128]), a two-stage iterative solution strategy is applied. First, the internal variables \mathbf{q} are determined locally at the integration points of the numerical quadrature for fixed global variables \mathbf{u} , i.e., the actual configuration is regarded as fixed implying $\mathbf{F}_S(\mathbf{u}_S) = \text{const.}$ for the iterative solution of the time discrete viscous evolution equations. Thereafter, in the global iteration step, the inelastic deformation tensors $(\mathbf{C}_{Si})_n$ are regarded as constant given history variables associated with fixed intermediate configurations $(\mathbf{F}_{Si})_n = \text{const.}$ However, the internal variables are iterated depending on the current values of the external variables, and thus, indirectly contribute as an explicit function of \mathbf{u}_S to the Jacobian matrix of the discrete nonlinear global system. For further particulars on the solution algorithm, see Sect. 4.3.2.

For the sake of completeness, supposing $\mathbf{F}_S = \text{const.}$, the first term of $(\mathcal{B}_q^S)^4$ is given as

$$\begin{aligned} \frac{\partial \mathbf{S}_n^S}{\partial (\mathbf{E}_{Si})_n} &= 2 \frac{\partial \mathbf{S}_n^S}{\partial (\mathbf{C}_{Si})_n} \\ &= 2 (\mathbf{F}_S^{-1} \otimes \mathbf{F}_S^{-1})^T \frac{\partial \boldsymbol{\tau}_n^S}{\partial (\mathbf{B}_{Se})_n} \frac{\partial (\mathbf{B}_{Se})_n}{\partial (\mathbf{C}_{Si})_n} \end{aligned} \quad (266)$$

with the derivative of the solid Kirchhoff overstress tensor

$$\begin{aligned} \frac{\partial \boldsymbol{\tau}_n^S}{\partial (\mathbf{B}_{Se})_n} &= \sum_{k=1}^3 \left(\underbrace{\frac{\partial \boldsymbol{\tau}_n^S}{\partial (\lambda_{Se(k)})_n}}_{(a)} \otimes \underbrace{(\mathbf{N}_{Se(k)})_n}_{(67)_1} \right. \\ &\quad \left. + \underbrace{\frac{\partial \boldsymbol{\tau}_n^S}{\partial (\mathbf{N}_{Se(k)})_n}}_{(b)} \underbrace{(\mathbf{N}_{Se(k)})_n}_{(67)_3} \right) \end{aligned} \quad (267)$$

where in detail

$$(a) = 2 \sum_{l=1}^3 \left(\frac{\partial^2 \mathcal{W}_{NEQ}^S}{\partial (\lambda_{Se(k)})_n \partial (\lambda_{Se(l)})_n} (\lambda_{Se(l)})_n (\mathbf{N}_{Se(l)})_n \right) + 2 \frac{\partial \mathcal{W}_{NEQ}^S}{\partial (\lambda_{Se(k)})_n} (\mathbf{N}_{Se(k)})_n, \quad (268)$$

$$(b) = 2 \frac{\partial \mathcal{W}_{NEQ}^S}{\partial (\lambda_{Se(k)})_n} (\lambda_{Se(k)})_n (\mathbf{I} \otimes \mathbf{I})^{\frac{23}{T}}.$$

Moreover, the second partial derivative in (266) takes the form

$$\frac{\partial (\mathbf{B}_{Se})_n}{\partial (\mathbf{C}_{Si})_n} = (\mathbf{F}_S \otimes \mathbf{F}_S)^T \frac{\partial (\mathbf{C}_{Si}^{-1})_n}{\partial (\mathbf{C}_{Si})_n} = -[\mathbf{F}_S (\mathbf{C}_{Si}^{-1})_n \otimes \mathbf{F}_S (\mathbf{C}_{Si}^{-1})_n]^{\frac{23}{T}}. \quad (269)$$

Note that the determination of the total derivative $d(\mathbf{E}_{Si})_n/d\mathbf{E}_S = d(\mathbf{C}_{Si})_n/d\mathbf{C}_S$ in $(\mathbf{B}_q^S)^4$ depends on the time discretization method used for the evolution equations and is therefore discussed later in Sect. 4.4.

To continue, linearization of the weak form of the fluid mass balance equation yields:

$$\mathcal{D}_{\Delta \mathbf{u}_S} \left[\int_{\Omega} \delta p n^F \frac{\partial \rho^{FR}}{\partial p} (p)'_S dv \right] = \int_{\Omega} \delta p (\operatorname{div} \Delta \mathbf{u}_S) \frac{\partial \rho^{FR}}{\partial p} (p)'_S dv, \quad (270)$$

$$\mathcal{D}_{\Delta \mathbf{u}_S} \left[\int_{\Omega} \delta p \rho^{FR} \operatorname{div}(\mathbf{u}_S)'_S dv \right] = \int_{\Omega} \delta p \rho^{FR} [\operatorname{div}(\mathbf{u}_S)'_S \operatorname{div} \Delta \mathbf{u}_S - \operatorname{grad}(\mathbf{u}_S)'_S \cdot \operatorname{grad}^T \Delta \mathbf{u}_S] dv, \quad (271)$$

$$\begin{aligned} \mathcal{D}_{\Delta \mathbf{u}_S} \left[\int_{\Omega} \operatorname{grad} \delta p \cdot \rho^{FR} \mathbf{K}^F (\operatorname{grad} p - \rho^{FR} \mathbf{b}) dv \right] &= \int_{\Omega} \operatorname{grad} \delta p \cdot \rho^{FR} \left\{ [(\operatorname{div} \Delta \mathbf{u}_S) \mathbf{K}^F + \mathcal{D}_{\Delta \mathbf{u}_S} \mathbf{K}^F \right. \\ &\quad \left. - (\operatorname{grad} \Delta \mathbf{u}_S) \mathbf{K}^F] \right. \\ &\quad \times (\operatorname{grad} p - \rho^{FR} \mathbf{b}) \\ &\quad \left. - \mathbf{K}^F (\operatorname{grad}^T \Delta \mathbf{u}_S) \operatorname{grad} p \right\} dv, \end{aligned} \quad (272)$$

$$\begin{aligned} \mathcal{D}_{\Delta p} \left[\int_{\Omega} \delta p \rho^{FR} \operatorname{div}(\mathbf{u}_S)'_S dv \right] &= \int_{\Omega} \delta p \frac{\partial \rho^{FR}}{\partial p} \Delta p \operatorname{div}(\mathbf{u}_S)'_S dv, \end{aligned} \quad (273)$$

$$\begin{aligned} \mathcal{D}_{\Delta p} \left[\int_{\Omega} \operatorname{grad} \delta p \cdot \rho^{FR} \mathbf{K}^F (\operatorname{grad} p - \rho^{FR} \mathbf{b}) dv \right] &= \int_{\Omega} \operatorname{grad} \delta p \cdot \left[\left(\frac{\partial \rho^{FR}}{\partial p} \Delta p \mathbf{K}^F + \rho^{FR} \mathcal{D}_{\Delta p} \mathbf{K}^F \right) \right. \\ &\quad \times (\operatorname{grad} p - \rho^{FR} \mathbf{b}) \\ &\quad \left. + \rho^{FR} \mathbf{K}^F \left(\operatorname{grad} \Delta p - \frac{\partial \rho^{FR}}{\partial p} \Delta p \mathbf{b} \right) \right] dv, \end{aligned} \quad (274)$$

$$\begin{aligned} \mathcal{D}_{\Delta p} \left[\int_{\Omega} \delta p n^F \frac{\partial \rho^{FR}}{\partial p} (p)'_S dv \right] &= \int_{\Omega} \delta p n^F \frac{\partial^2 \rho^{FR}}{\partial p^2} \Delta p (p)'_S dv, \end{aligned} \quad (275)$$

$$\begin{aligned} \mathcal{D}_{\Delta(\mathbf{u}_S)'_S} \left[\int_{\Omega} \delta p \rho^{FR} \operatorname{div}(\mathbf{u}_S)'_S dv \right] &= \int_{\Omega} \delta p \rho^{FR} \operatorname{div} \Delta(\mathbf{u}_S)'_S dv, \end{aligned} \quad (276)$$

$$\begin{aligned} \mathcal{D}_{\Delta(p)'_S} \left[\int_{\Omega} \delta p n^F \frac{\partial \rho^{FR}}{\partial p} (p)'_S dv \right] &= \int_{\Omega} \delta p n^F \frac{\partial \rho^{FR}}{\partial p} \Delta(p)'_S dv. \end{aligned} \quad (277)$$

Herein, in (272) and (274), the corresponding Gâteaux differentials of the permeability tensor are obtained by use of the chain rule, viz.

$$\begin{aligned} \mathcal{D}_{\Delta \mathbf{u}_S} \mathbf{K}^F &= \frac{\partial \mathbf{K}^F}{\partial K_F^F} \left(\frac{\partial K_F^F}{\partial J_S} J_S \operatorname{div} \Delta \mathbf{u}_S \right. \\ &\quad \left. + \frac{\partial K_F^F}{\partial |\operatorname{grad} p|} |(\operatorname{grad}^T \Delta \mathbf{u}_S) \operatorname{grad} p| \right) \\ &\quad + \frac{\partial \mathbf{K}^F}{\partial \operatorname{cof} \mathbf{B}_S} \frac{\partial \operatorname{cof} \mathbf{B}_S}{\partial \mathbf{B}_S} [(\operatorname{grad} \Delta \mathbf{u}_S) \mathbf{B}_S \\ &\quad + \mathbf{B}_S \operatorname{grad}^T \Delta \mathbf{u}_S], \end{aligned} \quad (278)$$

$$\mathcal{D}_{\Delta p} \mathbf{K}^F = \frac{\partial \mathbf{K}^F}{\partial K_F^F} \frac{\partial K_F^F}{\partial |\operatorname{grad} p|} |\operatorname{grad} \Delta p|.$$

Thus, with the above linearizations, the Gâteaux differentials (254) are assembled as

$$\begin{aligned} \mathcal{D}_{\Delta \mathbf{u}} \tilde{\mathbf{g}}_{\mathbf{u}} &= \left[\begin{array}{c|c} (257) + (258) + (259) & (260) + (261) \\ \hline (270) + (271) + (272) & (273) + (274) + (275) \end{array} \right], \\ \mathcal{D}_{\Delta(\mathbf{u}_S)'_S} \tilde{\mathbf{g}}_{\mathbf{u}} &= \left[\begin{array}{c|c} 0 & 0 \\ \hline (276) & (277) \end{array} \right]. \end{aligned} \quad (279)$$

Note that the linearized expression (275) actually yields zero as this work proceeds from the ideal gas law (227) for the description of a compressible pore gas, such that the second derivative of the fluid density with respect to the effective pore-fluid pressure vanishes identically, i.e., $\partial^2 \rho^{FR} / \partial p^2 \equiv 0$. Moreover, note that in the special case of a materially incompressible pore liquid, relation (277) also becomes zero as no evolution equation for $\rho^{FR}(p)$ or $p(\rho^{FR})$, respectively, exists and p degenerates to an unspec-

ified Lagrangean multiplier which must be determined from the boundary conditions as already mentioned.

4.3 Discretization

4.3.1 Spatial Semi-discretization

Proceeding from the weak formulations (247) and (248) together with the introduced abbreviations, the two-field variational problem can be rewritten in abstract form as [45]:

$$\text{Find } \mathbf{u} \in \mathcal{S}_u(t) \text{ such that } \mathcal{G}_u(\delta \mathbf{u}, \mathbf{u}; \mathbf{q}) = \mathbf{0} \quad \forall \delta \mathbf{u} \in \mathcal{T}_u, t \in [t_0, T]. \quad (280)$$

Herein, $\mathcal{S}_u(t)$ is the trial space for the external variables \mathbf{u} , \mathcal{T}_u is the test space for the corresponding test functions $\delta \mathbf{u}$, and $[t_0, T]$ is the considered time interval. Without going into mathematical details, the function spaces \mathcal{S}_u and \mathcal{T}_u must be chosen in such a way that the integrals involved in the definition of \mathcal{G}_u “make sense”. Moreover, the dependence on the internal variables \mathbf{q} is noted after a semicolon as they enter the weak form only indirectly via the solid extra stress tensor. Now, for the solution of the variational problem (280), the Finite Element Method (FEM) is applied. Therefore, the spatial domain occupied by the mixture body \mathcal{B} is subdivided into N_e finite elements yielding an approximation of the continuous domain Ω by the discrete domain Ω^h . This spatial semi-discretization yields a finite element mesh with N_x nodes for the geometry approximation, on which the following discrete trial and test functions are defined:

$$\begin{aligned} \mathbf{u}^h(\mathbf{x}, t) &= \bar{\mathbf{u}}^h(\mathbf{x}, t) + \sum_{i=1}^{N_u} N_{u(i)}(\mathbf{x}) \mathbf{u}_{(i)}(t) \in \mathcal{S}_u^h(t), \\ \delta \mathbf{u}^h(\mathbf{x}) &= \sum_{i=1}^{M_u} M_{u(i)}(\mathbf{x}) \delta \mathbf{u}_{(i)} \in \mathcal{T}_u^h. \end{aligned} \quad (281)$$

Therein, $\bar{\mathbf{u}}^h = [\bar{\mathbf{u}}_S^h, \bar{p}^h]^T$ represents the approximated Dirichlet boundary conditions of the considered problem, N_u denotes the number of FE nodes used for the approximation of \mathbf{u}_S and p , respectively, and $N_{u(i)}$ represents the global basis functions at node i which depend only on the spatial position \mathbf{x} , while the degrees of freedom (DOF) $\mathbf{u}_{(i)}$

are the time-dependent nodal coefficients. Moreover, M_u is the number of FE nodes used for the test functions $\delta \mathbf{u}_S$ and δp , respectively, $M_{u(i)}$ denotes the global basis functions, and $\delta \mathbf{u}_{(i)}$ represents the corresponding nodal values of the test functions. Furthermore, $\mathcal{S}_u^h(t)$ and \mathcal{T}_u^h are the discrete, finite-dimensional trial and test spaces.

Remark Without entering into particulars of the FE implementation, note that the shape functions are defined on the element level using local coordinates ξ . The corresponding global basis functions $N_{u(i)}$ and $M_{u(i)}$ are then obtained from a transformation to global coordinates \mathbf{x} . In this context, the present work proceeds from an isoparametric representation of finite elements where geometry and displacements are described by the same set of shape functions involving all nodes of the FE mesh, i.e., $N_{u_S} \equiv N_x$. Moreover, the Bubnov-Galerkin procedure is applied using the same basis functions $N_{u(i)} \equiv M_{u(i)}$ for the approximation of \mathbf{u} and $\delta \mathbf{u}$, which implies that the trial and test spaces coincide except for the shift through the Dirichlet boundary conditions $\mathcal{S}_u^h(t) = \bar{\mathbf{u}}^h + \mathcal{T}_u^h$. However, the individual approximation spaces of \mathbf{u}_S and p usually differ in the sense of a *mixed method* meaning that N_{u_S} and $N_{u_S(i)}$ in general do not coincide with N_p and $N_{p(i)}$, respectively.

Next, in the course of the FE discretization, one additionally introduces a space-discrete set of internal variables $\mathbf{q}^h = \mathbf{q}^h(\mathbf{x}_j, t) =: \mathbf{q}_{(j)}(t)$ at the $j = 1, \dots, N_q$ integration points of the FE mesh with global coordinates \mathbf{x}_j . Following this, the semi-discrete FE-Galerkin formulation of the variational problem (280) reads:

$$\text{Find } \mathbf{u}^h \in \mathcal{S}_u^h(t) \text{ such that } \mathcal{G}_u^h(\delta \mathbf{u}^h, \mathbf{u}^h; \mathbf{q}^h) = \mathbf{0} \quad \forall \delta \mathbf{u}^h \in \mathcal{T}_u^h, t \in [t_0, T]. \quad (282)$$

To complete the spatial discretization procedure, the discrete trial and test functions must be specified by choosing an appropriate mixed finite element formulation. A pragmatic way of finding potential interpolation functions is to look at the form in which the basis functions enter the variational problem. For instance, regarding the fluid mass balance (247), the gradient of the pressure field, and thus, the derivatives of $N_{p(i)}$ are required, which at least demands for a linear interpolation of p . Furthermore, in the mixture momentum balance (248), the pressure enters the stress term directly, whereas the gradient of \mathbf{u}_S , and thus, the derivatives of the basis functions $N_{\mathbf{u}_S(i)}$ come into play indirectly via the extra stress tensor. Thus, in regard to an equal-order representation of the total stress, it suggests itself to choose the displacement interpolation one order higher than the pressure interpolation yielding a quadratic ansatz for \mathbf{u}_S . This, at a first glance, fairly natural choice of a quadratic displacement-linear pressure mixed finite element formulation was already proposed by Sandhu and Wilson [119] in 1969. However, the suitable choice of mixed element formulations in regard to accuracy, stability, and computational costs is by no means natural and is therefore the subject of the next paragraph.

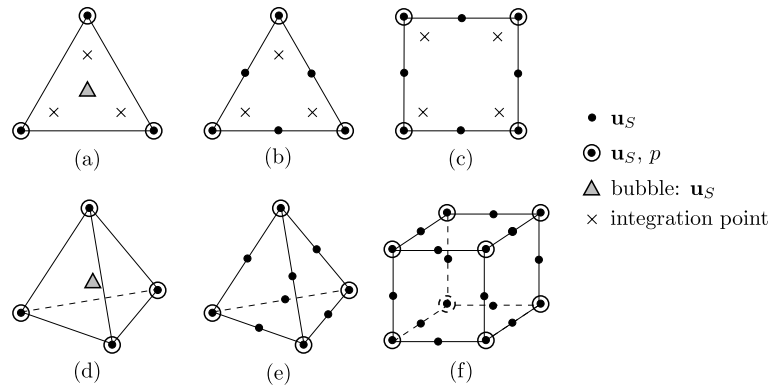
Mixed Element Formulations Since the considered solid-fluid problem belongs to the class of *strongly coupled* systems (cf. [84, 149]), the simultaneous approximation of the primary unknowns \mathbf{u}_S and p is required. Accordingly, this entails the usage of the mixed Finite Element Method with discrete approximation spaces for \mathbf{u}_S and p which is known to exhibit a great robustness with respect to the roughness of the coefficients of the equations. However, in analogy to the Stokes problem of viscous incompressible fluid flow, the considered two-field variational principle yields a saddle-point problem rather than an extremal problem, i.e., the solution corresponds simultaneously to a minimum with respect to the displacement \mathbf{u}_S and a maximum with respect to the pressure p . In general, minimization of an energy functional subject to a side condition, such as the continuity condition in the Stokes problem or the saturation constraint in the porous media problem, results in a saddle-point problem, i.e., the discrete system is indefinite so that a number of standard solution methods cannot be applied directly. Moreover, the problem occurs that not all choices of finite element spaces will lead to convergent approximations, i.e., the stability of mixed methods is by no means automatic [3]. Therefore, in mixed formulations, the *inf-sup condition* (Ladyshenskaya-Babuška-Brezzi (LBB) condition) is a crucial criterion for the stability of the numerical solution [18]. Without going into mathematical details, the inf-sup condition compares the size of the approximation spaces, e.g., here of $\mathcal{S}_{\mathbf{u}_S}^h$ and \mathcal{S}_p^h , and essentially serves as a compatibility

condition in the sense that it keeps the balance between consistency error and approximation quality, see [64] for references.

One possible choice of a stable discretization which fulfills the discrete version of the LBB condition is to use quadratic shape functions for the solid displacement \mathbf{u}_S and linear shape functions for the pressure p as proposed by [119] which is known as the Taylor-Hood element. However, using this element formulation the major disadvantage of the simultaneous approximation of \mathbf{u}_S and p emerges as the discrete system will typically involve many more degrees of freedom. In particular, in the three-dimensional case, the quadratic approximation of the displacements leads to an enormous number of mid nodes in finer meshes, which increases the computational costs rapidly. In order to overcome this problem, one has to reduce the order of the displacement interpolation, which leads to an equal-interpolation element with a linear approximation for both the solid displacement \mathbf{u}_S and the pore pressure p . In general, this mixed element can be used for the computation of coupled problems but users have to be aware that their results are strongly mesh dependent. More precisely, the element formulation is unstable in the sense of giving non-physical oscillations in the pore pressure caused by a very strange instability of the pressure approximation due to so-called *spurious pressure modes* [18]. This unpredictable behavior of equal-order interpolation methods led to the introduction of the more sophisticated Taylor-Hood elements as mentioned above.

However, to get a stable pressure-continuous element while keeping the linear approximation for \mathbf{u}_S , one has to add bubble functions to the displacement field. This results in the so-called MINI element of Arnold et al. [4] where the additional bubbles enrich the trial space for the displacements $\mathcal{S}_{\mathbf{u}_S}^h$, which guarantees stability, see also [16]. Since the bubble functions are restricted to a single finite element, the barycentric bubble nodes can be removed via static condensation. A further strategy of enrichment is to use a finer mesh for the displacement approximation than for the pressure. However, this involves at least as many DOFs as the Taylor-Hood element but has a lower accuracy as the quadratic interpolation of the Taylor-Hood element is replaced by a piecewise linear approximation, and therefore, the method is deemed inefficient for general porous media applications. Thus, for the numerical treatment of large coupled solid-fluid problems in the sense of the TPM approach, besides the established Taylor-Hood element, the MINI element is a compromise concerning accuracy and computational costs. Particularly for porous media problems with complex 3-d geometries which require a detailed spatial discretization, the tetrahedral MINI element may have tangible advantages. For illustration, the reasonable and employed 2-d and 3-d mixed element formulations are depicted in Fig. 6.

Fig. 6 Stable mixed finite elements: (a) 2-d MINI element (T3P3B), (b) triangular Taylor-Hood element (T6P3), (c) quadrilateral Taylor-Hood element (Q8P4), (d) 3-d MINI element (T4P4B), (e) tetrahedral Taylor-Hood element (T10P4), (f) hexahedral Taylor-Hood element (H20P8)



To continue, in preparation for the time discretization, the contravariant viscoelastic evolution equations (210) (alternatively (211)) are collected in a local residuum vector

$$\mathcal{L}_q \equiv \begin{bmatrix} [(\mathbf{C}_{Si})_1]_S' - \frac{1}{\eta_1^S} (\mathbf{C}_{Si})_1 \mathbf{S}_1^S (\mathbf{C}_{Si})_1 + \frac{\xi_1^S}{\eta_1^S (2\eta_1^S + 3\xi_1^S)} [\mathbf{S}_1^S \cdot (\mathbf{C}_{Si})_1] (\mathbf{C}_{Si})_1 \\ \dots & \dots & \dots \\ [(\mathbf{C}_{Si})_N]_S' - \frac{1}{\eta_N^S} (\mathbf{C}_{Si})_N \mathbf{S}_N^S (\mathbf{C}_{Si})_N + \frac{\xi_N^S}{\eta_N^S (2\eta_N^S + 3\xi_N^S)} [\mathbf{S}_N^S \cdot (\mathbf{C}_{Si})_N] (\mathbf{C}_{Si})_N \end{bmatrix} = \mathbf{0}. \quad (283)$$

After the finite element discretization, its semi-discrete counterpart \mathcal{L}_q^h contains the set of space-discrete evolution equations of all N_q integration points of the FE mesh for the computation of the inelastic solid deformation tensors in the sense of a collocation method.

4.3.2 Time Discretization

For the time discretization, let \mathbf{u} represent all nodal degrees of freedom $\mathbf{u}_{(i)}(t)$ of the FE mesh and \mathbf{q} all the internal variables $\mathbf{q}_{(j)}(t)$ at the integration points. Then, introducing an entire vector of unknowns $\mathbf{y} := [\mathbf{u}, \mathbf{q}]^T \in \mathbb{R}^m$ with $m = \dim(\mathbf{u}) + \dim(\mathbf{q})$ and taking all semi-discrete equations together, one obtains an initial-value problem of differential-algebraic equations (DAE) in time

$$\begin{aligned} \mathbf{F}[t, \mathbf{y}, (\mathbf{y})_S'] &\equiv \begin{bmatrix} \mathcal{G}_u^h[t, \mathbf{u}, (\mathbf{u})_S'; \mathbf{q}] \\ \mathcal{L}_q^h[t, \mathbf{q}, (\mathbf{q})_S'; \mathbf{u}] \end{bmatrix} \\ &\equiv \begin{bmatrix} \mathbf{M} (\mathbf{u})_S' + \mathbf{k}[\mathbf{u}; \mathbf{q}] - \mathbf{f} \\ \mathbf{A} (\mathbf{q})_S' - \mathbf{l}[\mathbf{q}; \mathbf{u}] \end{bmatrix} \stackrel{!}{=} \mathbf{0} \end{aligned} \quad (284)$$

with $\mathbf{y}(t_0) = \mathbf{y}_0$ and $t \in [t_0, T]$ (cf. [44]). Therein, the upper equation is an abstract representation of the semi-discrete balance equations at all FE nodes where \mathbf{M} denotes a generalized mass matrix, \mathbf{k} is a generalized stiffness vector, and \mathbf{f} is a generalized external force vector. The lower equation

represents the space-discrete evolution equations of all integration points of the FE mesh which essentially are ODEs with \mathbf{A} being simply the identity matrix and the vector \mathbf{l} containing the semi-discrete right-hand sides of the original evolution equations (210). In the case of a quasi-static and/or a materially incompressible description, the generalized mass matrix does not possess the full rank. In particular, the quasi-static formulation of the mixture balance of momentum (248) delivers no contribution to the generalized mass matrix that is related to $(\mathbf{u}_S)_S'$. Furthermore, concerning the materially incompressible model, no evolution equation for p exists and, as a consequence, \mathbf{M} has no entry corresponding to $(p)_S'$. Thus, (284) becomes an index 1 system of differential-algebraic equations (DAE) of first order in time [52] which must be handled by a suitable time integration method. Note that if the evaluation of the inelastic evolution equations is additionally subject to algebraic constraints, such as the yield condition in plasticity, $\mathcal{L}_q^h = \mathbf{0}$ also becomes a DAE system with singular matrix \mathbf{A} .

In order to integrate large DAE systems of index 1, one-step s -stage diagonally-implicit Runge-Kutta (DIRK) methods provide a suitable means at moderate storage and computational costs as they allow the solution of the stage equations in a decoupled fashion [35, 52]. In this connection, with regard to a proper treatment of the included algebraic equations, stiffly accurate methods are appropriate. Moreover, certain stability requirements must be fulfilled in order to enable large time steps and to guarantee the accurate time

integration of the overall dissipative physical problem. Following this, for the solution of the time-continuous initial-

value problem by use of a stiffly accurate s -stage DIRK,

$$\text{Find } \mathbf{y}(t) \in \mathbb{R}^m \text{ such that } \mathbf{F}[t, \mathbf{y}, (\mathbf{y})'_S] = \mathbf{0}, \quad \mathbf{y}(t_0) = \mathbf{y}_0 \quad \forall t \in [t_0, T] \quad (285)$$

the considered time interval is divided into a finite number of subintervals $[t_n, t_{n+1}]$ with time step size $\Delta t_n = t_{n+1} - t_n$

on which (285) is successively solved according to the time step algorithm given in (286).

Time step algorithm of a stiffly accurate s -stage DIRK method

Given: coefficients c_i, a_{ij} of a stiffly accurate s -stage DIRK method, approximate solution $\mathbf{y}_n \approx \mathbf{y}(t_n)$ at time t_n , time step size Δt_n

Find: approximate solution $\mathbf{y}_{n+1} \approx \mathbf{y}(t_{n+1})$ at time t_{n+1}

Step 1: for each Runge-Kutta stage $i = 1, \dots, s$

$$\begin{aligned} \text{(a)} \quad & \text{set stage time } T_{ni} := t_n + c_i \Delta t_n \text{ and} \\ & \text{accumulated stage derivative } \bar{\mathbf{Y}}_{ni} := \Delta t_n \sum_{j=1}^{i-1} a_{ij} \mathbf{Y}'_{nj} \end{aligned} \quad (286)$$

(b) solve nonlinear system for stage increments $\Delta \mathbf{Y}_{ni}$

$$\mathbf{R}_{ni}(\Delta \mathbf{Y}_{ni}) \equiv \mathbf{F}\left(T_{ni}, \mathbf{y}_n + \Delta \mathbf{Y}_{ni}, \frac{1}{\Delta t_n a_{ii}} [\Delta \mathbf{Y}_{ni} - \bar{\mathbf{Y}}_{ni}]\right) = \mathbf{0}$$

$$\text{(c) set stage derivative } \mathbf{Y}'_{ni} := \frac{1}{\Delta t_n a_{ii}} [\Delta \mathbf{Y}_{ni} - \bar{\mathbf{Y}}_{ni}]$$

Step 2: set $\mathbf{y}_{n+1} := \mathbf{Y}_{ns} = \mathbf{y}_n + \Delta \mathbf{Y}_{ns}$ and $t_{n+1} := T_{ns}$

Remark Regarding the time step algorithm (286) for a current time step n , it should be noted that instead of the stage solutions \mathbf{Y}_{ni} , the stage increments $\Delta \mathbf{Y}_{ni} := \mathbf{Y}_{ni} - \mathbf{y}_n$ are used as unknowns in order to reduce round-off errors during the solution of the time-discrete nonlinear system in step 1(b), see [66, IV.8]. In this context, the accumulated stage derivatives $\bar{\mathbf{Y}}_{ni}$ depend only on previously computed quantities, and thus, are constant for the current Runge-Kutta stage i .

For the special choice of coefficients $s = 1$ and $c_1 = a_{11} = 1$, one obtains the well-known implicit or backward Euler method and the nonlinear system simplifies to

$$\mathbf{R}_n(\Delta \mathbf{Y}_n) \equiv \mathbf{F}\left(\underbrace{t_n + \Delta t_n}_{t_{n+1}}, \underbrace{\mathbf{y}_n + \Delta \mathbf{Y}_n}_{\mathbf{y}_{n+1}}, \underbrace{\Delta \mathbf{Y}_n / \Delta t_n}_{\mathbf{y}'_{n+1}}\right) = \mathbf{0}. \quad (287)$$

Note that the implicit Euler scheme is in fact a one-stage singly diagonal-implicit Runge-Kutta (SDIRK) method. For mildly nonlinear systems, SDIRK methods are advantageous as they allow the reusability of previously factorized matrices, such as in the simplified Newton method, which may drastically reduce the required solution time.

Moreover, it is worth mentioning that so-called *embedded* Runge-Kutta methods allow for an efficient estimation of the time error. In particular, these methods compute, besides the approximate solution \mathbf{y}_{n+1} of order r , an additional approximate solution $\hat{\mathbf{y}}_{n+1}$ of lower order $\hat{r} < r$. As a result,

an embedded error estimation is given by the difference of these solutions through

$$ERR \approx \|\mathbf{y}_{n+1} - \hat{\mathbf{y}}_{n+1}\|. \quad (288)$$

Accordingly, as pointed out by Diebels et al. [35], this type of an error estimation is *cheap* as it does not require the additional solution of nonlinear systems but only a weighted sum of already computed quantities. Following this, Runge-Kutta methods with embedded error estimators are well suited for large nonlinear systems of equations.

The main computational effort in solving the initial-value problem (285) using a DIRK method is in the solution of the nonlinear system given in step 1(b) of the algorithm in (286). For its efficient solution with the Newton-Raphson method, the derivative of the nonlinear vector function $\mathbf{R}_{ni}(\Delta \mathbf{Y}_{ni})$ with respect to the stage increments $\Delta \mathbf{Y}_{ni}$ is required. The Jacobian matrix of the whole nonlinear system takes the form

$$\mathbf{J}_{ni} := \frac{d\mathbf{R}_{ni}}{d\Delta \mathbf{Y}_{ni}} = \frac{\partial \mathbf{F}}{\partial \mathbf{y}} \Big|_{\mathbf{z}} + \frac{1}{\Delta t_n a_{ii}} \frac{\partial \mathbf{F}}{\partial (\mathbf{y})'_S} \Big|_{\mathbf{z}}, \quad (289)$$

where $\mathbf{z} = \{T_{ni}, \mathbf{Y}_{ni}, \mathbf{Y}'_{ni}\}$ denotes the current set of arguments of \mathbf{F} in \mathbf{R}_{ni} . However, it would be disastrous to solve the linear system directly with \mathbf{J}_{ni} as the usual sparse structure of the linearized global FEM equations is completely

destroyed by the included linearizations of the time-discrete system of local evolution equations [45]. Therefore, it is better to take advantage of the special structure of the DAE system (284) and apply a suitable blockwise solution strategy which retains the sparse structure of the FEM system and treats the integration point equations in a decoupled fashion. Following this, proceeding from a consistent time integration by use of the same time-discretization method for both the global FEM system as well as the local viscoelastic rate equations, the discrete nonlinear system $\mathbf{R}_{ni}(\Delta \mathbf{Y}_{ni})$ reads

$$\begin{bmatrix} \mathbf{G}_{ni}(\Delta \mathbf{U}_{ni}; \Delta \mathbf{Q}_{ni}) \\ \mathbf{L}_{ni}(\Delta \mathbf{Q}_{ni}; \Delta \mathbf{U}_{ni}) \end{bmatrix} \equiv \begin{bmatrix} \frac{1}{\Delta t_n a_{ii}} \mathbf{M}[\Delta \mathbf{U}_{ni} - \bar{\mathbf{U}}_{ni}] + \mathbf{k}(\mathbf{u}_n + \Delta \mathbf{U}_{ni}; \mathbf{q}_n + \Delta \mathbf{Q}_{ni}) - \mathbf{f} \\ \frac{1}{\Delta t_n a_{ii}} \mathbf{A}[\Delta \mathbf{Q}_{ni} - \bar{\mathbf{Q}}_{ni}] - \mathbf{l}(\mathbf{q}_n + \Delta \mathbf{Q}_{ni}; \mathbf{u}_n + \Delta \mathbf{U}_{ni}) \end{bmatrix} = \mathbf{0}. \quad (290)$$

Herein, $\Delta \mathbf{U}_{ni}$, $\Delta \mathbf{Q}_{ni}$ are the unknown stage increments and $\bar{\mathbf{U}}_{ni}$, $\bar{\mathbf{Q}}_{ni}$ are the accumulated stage derivatives of the

global FEM variables \mathbf{u} and the local history variables \mathbf{q} , respectively. Then, exploiting the inherent dependence of the global equations \mathbf{G} on the local equations \mathbf{L} , the nonlinear DAE system (290) is efficiently iterated by a generalized Block Gauß Seidel Newton (BGSN) method in the sense of a two-stage Newton procedure. In particular, at first the evolution equations of the viscoelasticity model are solved by a local Newton iteration with fixed increments $\Delta \mathbf{U}_{ni}$ of the global variables resulting in local increments $\Delta \mathbf{Q}_{ni}(\Delta \mathbf{U}_{ni})$ depending on the fixed global increments. This actually corresponds to a local evaluation of the constitutive equations in each finite element. The second step of the procedure is the solution of the global sparse linear FEM system by taking into account the local algorithm during the consistent linearization. In summary, for each global Newton step k of the current Runge-Kutta stage i of the current time step n , the nonlinear system (290) is solved according to the algorithm given in (291). The procedure is repeated until a suitable convergence criterion, such as $\|\mathbf{G}_{ni}^k\| < \text{TOL}_G$ or $\|\Delta \mathbf{u}_{ni}^k\| < \text{TOL}_u$, is met.

2-stage solution algorithm for the nonlinear G-L system

Stage 1: solve nonlinear local integration point system with fixed $\Delta \mathbf{U}_{ni}^k$

$$\mathbf{L}_{ni}^k(\Delta \mathbf{Q}_{ni}^k; \Delta \mathbf{U}_{ni}^k) = \mathbf{0} \quad \longrightarrow \quad \Delta \mathbf{Q}_{ni}^k = \Delta \mathbf{Q}_{ni}^k(\Delta \mathbf{U}_{ni}^k)$$

Stage 2: solve nonlinear global FEM system

(a) compute consistent global Jacobian matrix

$$(\mathbf{J}_u)_{ni}^k = \frac{d\mathbf{G}_{ni}^k}{d\Delta \mathbf{U}_{ni}^k} = \frac{\partial \mathbf{G}_{ni}^k}{\partial \Delta \mathbf{U}_{ni}^k} + \frac{\partial \mathbf{G}_{ni}^k}{\partial \Delta \mathbf{Q}_{ni}^k} \frac{d\Delta \mathbf{Q}_{ni}^k}{d\Delta \mathbf{U}_{ni}^k} \quad (291)$$

(b) solve global sparse linear FEM system

$$(\mathbf{J}_u)_{ni}^k \Delta \mathbf{u}_{ni}^k = -\mathbf{G}_{ni}^k \quad \longrightarrow \quad \Delta \mathbf{u}_{ni}^k$$

(c) update vector of global variables (nodal DOFs)

$$\mathbf{u}_{ni}^{k+1} := \mathbf{u}_{ni}^k + \Delta \mathbf{u}_{ni}^k$$

4.4 Solid Stress Computation

The principle of the overall solution algorithm has been described in the previous section. However, in a finite element code, a stress computation algorithm is required that returns the solid stress tensor \mathbf{T}_E^S as well as the consistent tangent operator $(\mathcal{C}^S)^4$. This algorithm is applied for every integration point of the numerical quadrature, and thus, includes the solution of the local system (283) as well as the computation of the contribution to the global Jacobian matrix from the current integration point.

For the considered viscoelastic model, according to the additive split of the solid extra stress into an equilibrium and a non-equilibrium part,

$$\mathbf{T}_E^S = \mathbf{T}_{EQ}^S + \mathbf{T}_{NEQ}^S = J_S^{-1} (\boldsymbol{\tau}_{EQ}^S + \boldsymbol{\tau}_{NEQ}^S), \quad (292)$$

the stress computation is carried out in two steps. First, the purely elastic part $\boldsymbol{\tau}_{EQ}^S$ is computed using (190), which requires the preceding determination of the eigenvalues and tensors of the solid deformation tensor \mathbf{B}_S . In a second step, the total overstress $\boldsymbol{\tau}_{NEQ}^S = \sum_{n=1}^N \boldsymbol{\tau}_n^S$ is obtained by sequentially computing the individual non-equilibrium stresses $\boldsymbol{\tau}_n^S$ together with the time-discrete evolution of the internal variables $(\mathbf{C}_{Si})_n$ associated with the $n = 1, \dots, N$ Maxwell elements. The procedure is basically similar to the one known from elastoplasticity except for the fact that there is no yield criterion to be checked. Following this, for each Maxwell branch an independent elastic trial state is computed via

$$(\mathbf{B}_{Se})_n^{\text{trial}} = (\mathbf{F}_S)^{\text{act}} (\mathbf{C}_{Si}^{-1})_n^{\text{last}} (\mathbf{F}_S^T)^{\text{act}} \quad (293)$$

with the actual solid deformation gradient $(\mathbf{F}_S)^{\text{act}}$ but with the history variables $(\mathbf{C}_{Si})_n^{\text{last}}$ taken from the last time step or Runge-Kutta stage. Then, the corresponding elastic eigenvalues and tensors are calculated, e.g., by an efficient Householder- QL algorithm (cf. [114]), followed by the computation of the individual trial stress $(\boldsymbol{\tau}_n^S)^{\text{trial}}$ using (193). Next, for the treatment of the viscoelastic evolution laws, the resulting stress is pulled back to the reference frame, $(\mathbf{S}_n^S)^{\text{trial}} = (\mathbf{F}_S^{-1})^{\text{act}} (\boldsymbol{\tau}_n^S)^{\text{trial}} (\mathbf{F}_S^{T-1})^{\text{act}}$. Then, the time-discrete viscoelastic ODE system corresponding to the n th Maxwell element of the considered integration point which is included in the local equation vector \mathbf{L} is solved by Newton's method. After the iteration, the final $\boldsymbol{\tau}_n^S$ is accumulated in $\boldsymbol{\tau}_{NEQ}^S$ and the history variable is updated.

If, in addition, the global Jacobian \mathbf{J}_u is to be computed in stage 2(a) of the solution algorithm given in (291), the consistent solid stress tangent of the actual configuration is required. From (263) and (264), it is apparent that

$$\begin{aligned} \mathcal{C}^S &= \mathcal{C}_{EQ}^S + \mathcal{C}_{NEQ}^S \\ &= \mathcal{C}_{EQ}^S + (\mathbf{F}_S \otimes \mathbf{F}_S)^T \mathcal{B}_{NEQ}^S (\mathbf{F}_S^T \otimes \mathbf{F}_S^T)^T. \end{aligned} \quad (294)$$

Therein, the purely elastic part $(\mathcal{C}_{EQ}^S)^4$ is directly computed from (200), whereas the non-equilibrium tangent, as a matter of fact, depends on the solution of the local system. In particular, according to (265), the consistent tangent modulus of the reference configuration is determined from

$$\mathcal{B}_{NEQ}^S = \sum_{n=1}^N \left(\mathcal{B}_n^S + 2 \frac{\partial \mathbf{S}_n^S}{\partial (\mathbf{C}_{Si})_n} \frac{d(\mathbf{C}_{Si})_n}{d\mathbf{C}_S} \right), \quad (295)$$

where, after the iteration of the viscoelastic evolution equations, only the total derivative on the right is still unknown. However, assuming the local system to be solved exactly for the increment $\Delta(\mathbf{C}_{Si})_n$ for any given $\Delta\mathbf{C}_S$ on each Runge-Kutta stage,

$$\begin{aligned} \mathbf{L}[\Delta(\mathbf{C}_{Si})_n; \Delta\mathbf{C}_S] &= \mathbf{0} \\ \rightarrow \Delta(\mathbf{C}_{Si})_n &= \Delta(\mathbf{C}_{Si})_n[\Delta\mathbf{C}_S], \end{aligned} \quad (296)$$

the total derivative of \mathbf{L} with respect to $\Delta\mathbf{C}_S$ also vanishes identically. Thus, the unknown derivative is obtained as follows (cf. [45, 52]):

$$\begin{aligned} \frac{d\mathbf{L}}{d\Delta\mathbf{C}_S} &= \frac{\partial \mathbf{L}}{\partial \Delta\mathbf{C}_S} + \frac{\partial \mathbf{L}}{\partial \Delta(\mathbf{C}_{Si})_n} \frac{d\Delta(\mathbf{C}_{Si})_n}{d\Delta\mathbf{C}_S} = \mathbf{0} \\ \rightarrow \frac{d\Delta(\mathbf{C}_{Si})_n}{d\Delta\mathbf{C}_S} &= - \left[\frac{\partial \mathbf{L}}{\partial \Delta(\mathbf{C}_{Si})_n} \right]^{-1} \frac{\partial \mathbf{L}}{\partial \Delta\mathbf{C}_S}. \end{aligned} \quad (297)$$

Finally, the global Jacobian matrix \mathbf{J}_u is obtained by the usual summation over all integration points together with the FE assembly of all element contributions.

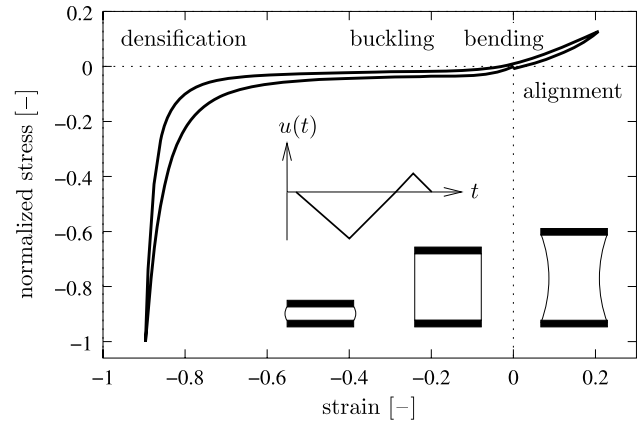


Fig. 7 Typical uniaxial stress-strain response of an open-celled polyurethane foam. Here, results of a displacement-driven uniaxial hysteresis experiment performed in our laboratory on a cubic PUR foam specimen (size $70 \times 70 \times 70 \text{ mm}^3$, bulk density 48 kg/m^3 , deformation rate 7.7 mm/s)

5 Application

5.1 Mechanical Behavior of Soft Polymeric Foams

Viscoelastic polymer foams and synthetic sponges are exploited in a wide range of engineering applications. The cellular microstructure as a result of the foaming process gives these porous materials their outstanding mechanical characteristics. Particularly the recovery and energy absorbing capabilities of soft polymer foams under large compressive deformations or during impacts predestines their usage for bumper systems, packaging, or cushioning. Basically, low-density polymer foams consist of a biphasic microstructure built by an interconnected network of air-filled polyhedral cells with slender strut edges where the cell faces can be open, partly closed, or closed depending on the chemical constitution of the ground substance. Under external loads, this cellular microstructure undergoes complex deformation mechanisms resulting in the characteristic highly nonlinear stress-strain behavior of the macroscopic foam.

Here, the focus is on soft polyurethane (PUR) foams which exhibit a permeable cellular structure with open cell faces. During a complete uniaxial loading and unloading cycle, soft PUR foams are capable of absorbing a large amount of energy due to their highly hysteretic nature. This strain-rate-dependent behavior is due to the intrinsic viscoelasticity of the polymer matrix and the deformation-dependent viscous fluid flow through the open-celled structure. In principle, the typical stress-strain curve from a cyclic uniaxial experiment can be separated into four distinct regions which are governed by the deformation mechanisms on the cell level (Fig. 7). In particular, small macroscopic deformations are associated with bending of the beam-like cell edges resulting in a linearly increasing stress response. Moderate

to large compressions of the foam are governed by buckling of the slender struts, which macroscopically results in a low-level stress plateau. Under very large compressions where the cells are almost collapsed and the cell edges are folded on each other, a stiffening of the foam can be observed due to the densification of the polymeric skeleton. It is worth mentioning that high-porosity foams show almost no lateral deformation or bulging under finite uniaxial compression. Conversely, large tension causes the cell edges to rotate towards the loading direction accompanied by a contraction of the foam perpendicular to the tensile axis. This alignment of the struts results in a stiffening of the structure with the stress response reflecting the tensile properties of solid polyurethane. In this context, note that soft PUR foams on the one hand are non-crushable under compression, i.e., they recover (sometimes with low recovery rate) from complete compression without showing remarkable permanent deformations but, on the other hand, they only sustain moderate tensile strains before certain struts begin to rupture. However, the tensile properties are important as they also dominate the shear response and allow the development of high gas pressures inside the foam, which is essential for the pneumatic damping behavior during impacts.

Next, in order to illustrate the above mentioned structural properties of open-cell foams, discrete simulations are carried out on an idealized beam structure using LS-DYNA. For convenience, proceeding from a 3-d periodic cellular network, a cubic lattice composed of volume-filling dodecahedral cells is generated. Each cell edge is discretized using eight beam elements where the initial orientation of the beam cross sections are randomly chosen. The principal axes of inertia are set based on the assumption of ellipsoidal cross sections and the ratio of strut thickness to cell radius is reasonably chosen as 1/20. Additionally, in order to avoid unwanted symmetry effects, the vertex coordinates of the initially regular lattice are randomly perturbed and an imperfection is included on each cell edge. For computational efficiency, the Belytschko-Schwer resultant beam formulation (ELFORM = 2) with a 2×2 Gauß quadratic integration is used. Since at this point only the deformation mechanism is of interest, the matrix material is modeled as linear elastic (*MAT_ELASTIC) using the density and the Young's modulus of flexible solid polyurethane according to Gibson and Ashby [60, Table 3.1]. The contact is modeled setting the keyword option *CONTACT_AUTOMATIC_SINGLE_SURFACE (cf. LS-DYNA keyword manual). Following this, a cubic geometry containing 365 dodecahedral cells discretized by a total of 31 168 beam elements is generated to simulate uniaxial compression, tension, and shear. In particular, for the compression simulation, the geometry is placed between a fixed and a moving rigid wall, whereas for the tension and shear simulations an adhesive bonding is modeled by defining single point constraints on the lower

boundary and by prescribing a uniform displacement on the nodes of the upper boundary. The resulting deformed configurations are depicted in Fig. 8. It is directly seen that the compression of the discrete beam structure almost shows no lateral deformation or bulging, whereas tension is accompanied by a distinct contraction. Moreover, regarding the shear simulation, the cell edge alignment along the diagonal tension field reveals the tension dominated response. This becomes clearer by looking at the computed stress-strain curves in Fig. 8 which show that the result from the tensile simulation is almost identical to the computed shear response. For further particulars on the behavior of cellular solids in general and foamed plastics in particular, see the quotations given in the introduction.

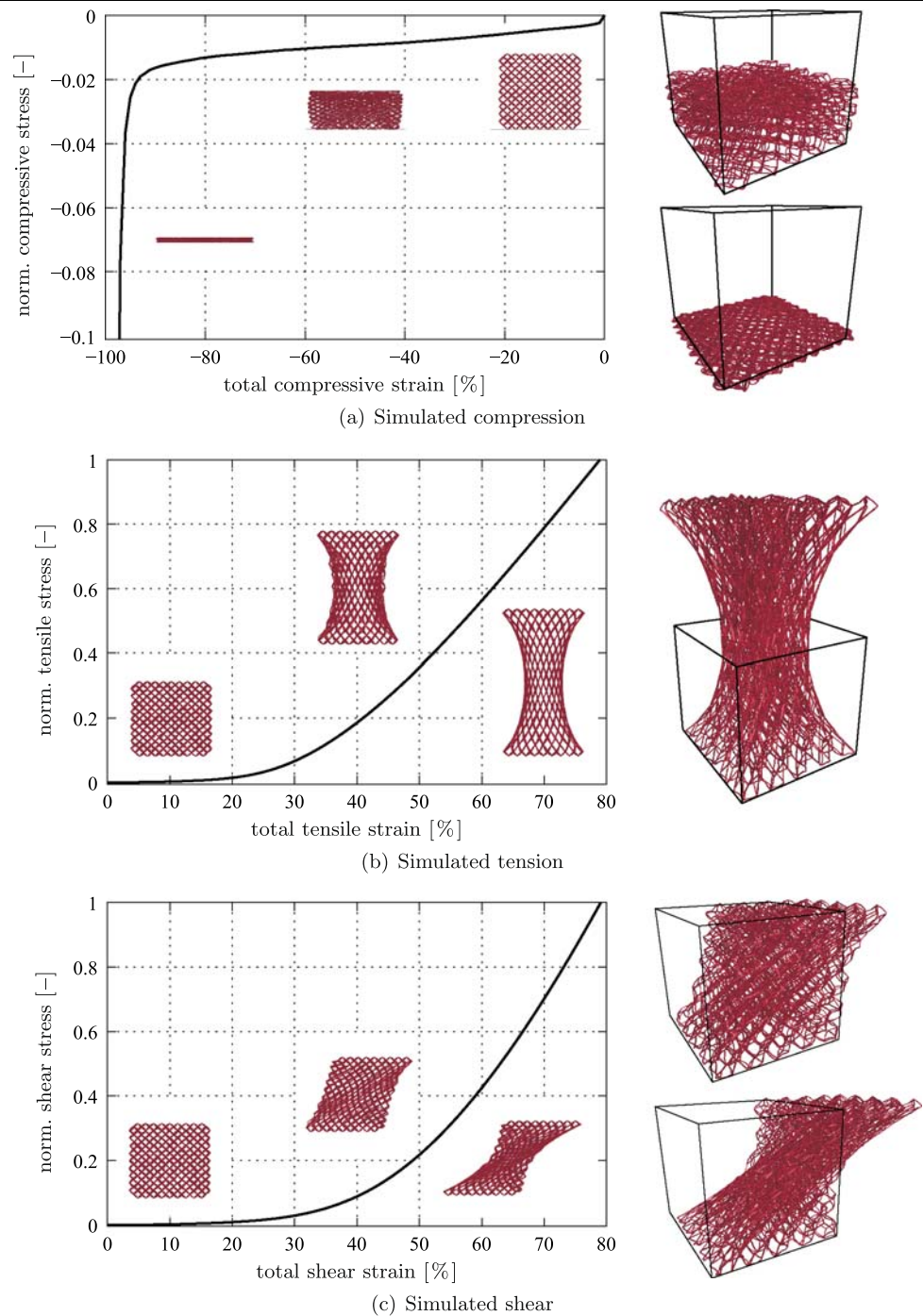
5.2 Model Adaption

5.2.1 Parameter Identification

To set an example, the biphase viscoelastic model is adapted for the description of a highly porous soft polyurethane (PUR) foam with a bulk density of 48 kg/m^3 which finds its main application as cushioning material in seating systems. Therefore, the material-specific and unknown parameters which are theoretically introduced in the constitutive equations (186), (191), and (244) must be identified. The adaption process essentially proceeds from well-defined experiments which are suitable to determine all relevant physical properties of the considered material. The identification is then carried out by comparing the experimental observations with the results of numerical simulations based on the chosen material model. A common procedure for this purpose is to strategically vary the searched material parameters until the numerical simulation is satisfactorily correlated with the experimental data. Usually, this strategy leads to a nonlinear optimization problem which implies the minimization of a least-squares functional representing the deviation between simulation and experiment. More precisely, this least-squares functional (*objective function*) has to be minimized in consideration of certain equality and inequality constraints which represent the restrictions on the unknown set of material parameters, such as the stability and compatibility conditions (178), (181), and (182). In principle, the constraints simply restrict the search space for the parameters to some feasible set yielding a constrained optimization problem seeking for the minimizing feasible vector of constitutive parameters. The major task is now the solution of this constrained nonlinear optimization (CNLO) problem by use of an appropriate numerical optimization strategy. Here, for convenience, we focus on derivative-free methods.

The main advantage of direct search or derivative-free methods is that they only require function values but no

Fig. 8 Computed stress-strain curves and deformed configurations



derivatives with respect to the unknown parameters. Thus, they can be applied without any modifications to the existing FE implementation of the considered material model. In general, most of the derivative-free methods are applicable to non-smooth and noisy objective functions where the comprehensible and self-contained algorithms usually allow the straightforward application of available codes and libraries, see [114]. However, due to the lack of gradient and curvature information, derivative-free methods unfortunately re-

quire a larger number of function evaluations compared to gradient-based methods, which makes them only expedient for problems whose computational burden is small. At first glance, this sounds like an exclusion criterion for optimization problems that involve time-consuming FE simulations. To ease this disadvantage, the adaption process is carried out in a hierarchical fashion. Therefore, the optimization process is started using a coarse FE approximation for the simulation in order to find a trend in the parameters and to

create a good initial parameter set. Then, the parameter vector is improved by the successive restart of the optimization procedure using refined FE meshes for the simulations with the previously found parameters as starting values. This essentially guarantees the cheap computation of the objective function at the beginning of the optimization process where the parameters are worse and many function evaluations are required. In the course of approaching the minimizing feasible vector of parameters, the accuracy of the FE approximation, and thus, the computing time is stepwise increased, whereas, conversely, the number of function evaluations decreases.

In general, depending on the underlying search strategy, a diversity of direct search or derivative-free optimization methods can be distinguished, see, e.g., [17, 56, 100]. For the purpose of this work, Powell's [111–113] *constraint optimization by linear approximation* (COBYLA) algorithm is the method of choice. COBYLA is a sequential trust region method for constrained nonlinear optimization which iteratively makes use of linear programming (LP) problems in the sense of a sequential linear programming (SLP) algorithm. There are no smoothness assumptions to the objective function, but only inequality constraints are considered, which, however, does not affect the applicability of COBYLA for the parameter optimization. The main advantage of COBYLA lies in the individual treatment of the inequality constraints during the iterative optimization procedure instead of lumping all constraints into a single penalty function. However, it should be noted that linear approximations can be highly inefficient, so that the number of variables should be kept small.

Following the above, in order to get interpretable and sound solutions, the possibility of reducing the number of variables is decisive for the convergence property and the efficiency of the numerical optimization process. In general, the material parameters of the viscoelastic porous media model can be divided into three classes, viz., the parameters that govern (i) the porous characteristics and fluid properties, (ii) the basic solid elasticity, and (iii) the intrinsic solid viscoelasticity. However, to realize this separation, experiments are needed that allow the unique assignment of the material response either to the flow-dependent mechanisms or to the equilibrium and non-equilibrium properties of the solid skeleton, respectively. Here, applying the viscoelastic TPM model to a high-porosity PUR foam, one can take advantage of the highly permeable microstructure of cellular polyurethane, which allows the successive determination of the three parameter classes. Therefore, at first, the porous and flow-dependent properties are obtained from appropriate permeability experiments. Then, displacement-driven uniaxial compression-tension tests with incorporated relaxation periods are performed for the identification of the macroscopic equilibrium response of the skeleton. Finally,

after the adjustment of the basic elasticity model, the parameters of the rate-dependent solid overstress formulation are determined from respective hysteresis experiments.

5.2.2 Porous Characteristics and Fluid Properties

Following the previous paragraph, the first class of parameters to be determined governs the porous and flow-dependent properties of the viscoelastic TPM model. In this parameter set, the cellular polyurethane structure, its permeability properties, and the percolating pore fluid (here: pore gas air) are characterized. To begin, at first, the initial solidity is determined from the definition of the mixture density (4)₃. Accordingly, proceeding from a homogeneous foam material, it is easily concluded that

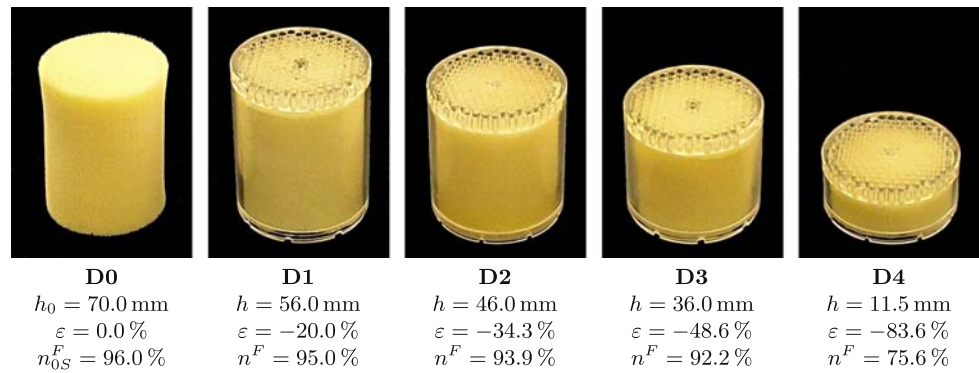
$$\rho_0 = \sum_{\alpha} n_{0S}^{\alpha} \rho_{0S}^{\alpha R}$$

$$\rightarrow n_{0S}^S = \frac{\rho_0 - \rho_{0S}^{FR}}{\rho_{0S}^{SR} - \rho_{0S}^{FR}} \approx \frac{\rho_0}{\rho_{0S}^{SR}} \quad (298)$$

where the ground-state bulk density of the considered PUR foam is about $\rho_0 = 48 \text{ kg/m}^3$ and the effective density of flexible solid polyurethane is $\rho_{0S}^{SR} = 1200 \text{ kg/m}^3$ [60, Table 3.1] which is regarded as constant assuming a materially incompressible skeleton. Since the effective density of air at standard conditions is comparatively low, viz., $\rho_{0S}^{FR} = 1.2 \text{ kg/m}^3$ at 20°C at an ambient pressure of $p_0 = 1.013 \cdot 10^5 \text{ N/m}^2$, the initial solid volume fraction can be approximately determined assuming an empty solid skeleton. Following this, the initial solidity of the PUR foam is about $n_{0S}^S = 0.04$.

Next, to obtain information about the nonlinear permeability properties, respective percolation experiments must be performed. For this purpose, we constructed two experimental devices which allow permeability measurements on cylindrical foam specimens at different deformation states [92]. In particular, for low filter velocities, the first testing device is used with degassed water as the permeating fluid where the ingoing pressure is measured for varying prescribed fluid volume fluxes (30–420 l/h in steps of 30 l/h ± 2 l/h) against a constant outgoing pressure of 2 m water head. Following this, a filter velocity range from 3.6 mm/s up to 5.2 cm/s could be realized. However, the problem occurs that high water flow velocities enlarge the apertures between the ribs outlining the individual cells of the soft foam, which causes an overestimation of the permeability. Therefore, for higher filter velocities, the second testing device is used with compressed air as percolate, where, for varying ingoing pressures (maximum $8 \cdot 10^5 \text{ N/m}^2$), the pressure drop over the sample and the velocity profile based on six measuring points in the half of the cylindrical cross section on the outflow side are measured with a differential pressure

Fig. 9 Cylindrical PUR foam specimens for the permeability experiments (radius $r = 27$ mm) pasted into acrylic glass tubes of different length



transducer (measured range $0.125 \cdot 10^5$ – $0.825 \cdot 10^5$ N/m² in steps of 0.0625 N/m²) and a standard Prandtl tube. With this setup mean flow velocities from 0.7 m/s up to 8.6 m/s were possible.

For both experimental devices, cylindrical foam specimens are prepared (initial height $h_0 = 70$ mm, radius $r = 27$ mm) which are compressed along the cylinder axis and pasted into acrylic glass tubes of different length to verify the deformation dependency of the permeability (Fig. 9). Therefore, the glass cylinders are closed by coarse filter platens which have a magnitudes higher permeability compared to the considered foam. Then, the tubes are integrated into the testing devices and the specimens are streamed parallel to their compression direction. In the case of the water experiments, in order to ensure a complete liquid saturation, the foam samples are initially flooded with carbon dioxide (CO₂) to displace the air inside the pores as CO₂ dissolves better in the permeating water which is taken from a large volume vacuum degasser. Moreover, in order to prove whether the considered PUR foam exhibits anisotropic permeability properties, additional percolation experiments are carried out, where, in contrast to the previously mentioned setups, rectangular specimens are tested which are deformed perpendicular to the flow direction. However, neither initial nor deformation-induced anisotropic permeability properties could be observed, so that, for the following considerations, it is convenient to proceed from an isotropic permeability associated with $\mathcal{H}^S \equiv \mathbf{I}$ (cf. Sect. 3.3.4). In this regard, it should be noted that this might be totally different for other types of foams, especially, when they have a higher density, i.e., a lower porosity, or exhibit a distinct inherent anisotropy due to the manufacturing process, e.g., when the cells (and thus the pores) are elongated in the foam rise direction [144] or the foam has a strand-like mesostructure (strand foam).

Then, based on the data obtained from the 1-d percolation experiments, the constitutive filter law (244) has to be adapted. Therefore, the basic flow equation in the form of the 1-d Forchheimer law (233) is correlated with the experimental data by optimizing the intrinsic permeability K^S

and the tortuosity parameter B^S independently for each of the compression states D1–D4. Since in addition to incompressible water compressible air is also used as a permeating fluid, the variability of the fluid density along the flow path must be conveniently taken into account. This can be accomplished by a suitable redefinition of the dependent and independent variables in the Forchheimer equation through multiplication by the factor $\rho^{FR}/(\mu^{FR})^2$ yielding (cf. [98, Chap. II])

$$-\underbrace{\frac{\rho^{FR}}{(\mu^{FR})^2} \frac{\partial p}{\partial x}}_{\partial \tilde{p}/\partial x} = \frac{1}{K^S} \underbrace{\left(\frac{\rho^{FR}}{\mu^{FR}} w_F \right)}_{\tilde{q}} + \frac{1}{B^S} \underbrace{\left(\frac{\rho^{FR}}{\mu^{FR}} w_F \right)^2}_{\tilde{q}^2}$$

$$\rightarrow -\frac{\partial \tilde{p}}{\partial x} = \frac{1}{K^S} \tilde{q} + \frac{1}{B^S} \tilde{q}^2. \quad (299)$$

Therein,

$$\frac{\partial \tilde{p}}{\partial x} := \frac{\rho^{FR}(p)}{(\mu^{FR})^2} \frac{\partial p}{\partial x} = \frac{M_m^F}{R \Theta (\mu^{FR})^2} \frac{\partial p^2}{\partial x} \quad (300)$$

$$\text{and } \tilde{q} := \frac{\rho^{FR}(p)}{\mu^{FR}} w_F = \frac{1}{\mu^{FR}} q$$

define the new dependent and independent variables, where the ideal gas law (227) and the specific filter mass flux $q := \rho^{FR} w_F$ have been used. The results of the permeability experiments and the corresponding curves of the fitted flow equation (299) are depicted in Fig. 10, where the double-logarithmic representation shows the very good accordance for all compression states within the considered range of the flow velocity.

Subsequently, the previously found parameter pairs $\{K_{D1}^S, B_{D1}^S\}, \dots, \{K_{D4}^S, B_{D4}^S\}$ are used as optimization points for the fit of the porosity-dependent permeability and tortuosity functions (239) and (240). From the corresponding graphs depicted in Fig. 11, it is directly seen that the proposed power law can be brought into satisfactory accordance with the four discrete values of K^S and B^S associated with the deformation states D1–D4. The optimized parameters yielding the best approximation based on a least-squares fit of the

respective functions and the other parameters governing the porous characteristics and fluid properties are listed below.

<i>Porous characteristics and fluid properties</i>			
$n_{0S}^S = 0.04$	$[-]$	$g = 9.81$	$[m/s^2]$
$\rho^{SR} = 1200.0$	$[kg/m^3]$	$p_0 = 1.013 \cdot 10^5$	$[N/m^2]$
$K_{0S}^S = 1.695 \cdot 10^{-9}$	$[m^2]$	$R = 8.3144$	$[J/(K \text{ mol})]$
$\kappa = 2.65$	$[-]$	$\Theta = 293.15$	$[K]$
$B_{0S}^S = 4.77 \cdot 10^{-5}$	$[m]$	$M_m^F = 2.897 \cdot 10^{-2}$	$[kg/mol]$
$\beta = 2.34$	$[-]$	$\mu^{FR} = 1.82 \cdot 10^{-5}$	$[Ns/m^2]$

(301)

5.2.3 Basic Solid Elasticity

After the definition of the porous characteristics and the fluid properties, the basic solid elasticity model (186) has to be adjusted. Therefore, proceeding from viscoelastic skeleton properties, the equilibrium response of the cellular polyurethane matrix must be separated from the rate-dependent contributions. As usual, this is accomplished by displacement-driven experiments with incorporated holding times which allow the relaxation of the non-equilibrium stresses at distinct deformation states finally yielding a set of discrete optimization points representing the purely elastic response. In particular, unconfined uniaxial compression-tension experiments on cubic PUR foam specimens of size $70 \times 70 \times 70 \text{ mm}^3$ (Fig. 12) are performed in our laboratory and at the Institute for Polymer Testing and Polymer Science (IKP) of the Universität Stuttgart. During the experiments, the specimens are subjected to complete deformation cycles at a constant deformation rate of 0.077 mm/s which are interspersed with several holding times of 60 minutes, while the responding force is continuously recorded. Therefore, the foam specimens are bonded to aluminum platens at two opposite sides using a quick-setting adhesive, where,

during the tests, one platen is used to prescribe the deformation, whereas the other one is fixed. In particular, a maximal compression of 90% and a maximal tension of 20% of the initial edge length is imposed, where the prescribed tensile deformation is kept comparatively small in order to limit damage effects and to avoid the rupture of the adhesive bonds. The obtained experimental results are depicted in the stress-strain diagram in Fig. 13. Since the overstresses are not completely relaxed, it is apparent that the chosen holding times of 60 minutes are too short. However, assuming the PUR matrix to behave purely viscoelastic, thereby excluding a plastic equilibrium hysteresis, the midpoints between the relaxed stress tips of the two branches of the stress-strain loops can be taken as input values for the numerical optimization procedure. In fact, for the considered PUR foam this is not an arbitrary assumption as the complete stress relaxation onto a non-hysteretic equilibrium curve can be verified by long term experiments with holding times above 20 hours [76]. Thus, proceeding from the midpoints as optimization points, the actual adaption of the extended Ogden formulation (186) is carried out numerically using the previously described COBYLA algorithm. In this regard, following the arguments of Sect. 3.2.3, the involved material parameters are subject to the inequality constraints

$$\mu_0^S > 0, \quad \Lambda_0^S \geq 0, \quad \gamma_0^S \geq 1, \quad (302)$$

$$\sum_{m=1}^{M_0} \mu_{0(m)}^* \geq 0, \quad \mu_{0(m)}^* (\alpha_{0(m)} - 1) \geq 0.$$

Moreover, the compatibility condition (181) as an equality constraint is considered by expressing one of the unknown Ogden parameters dependent on the others, viz.,

$$\sum_{m=1}^{M_0} \mu_{0(m)}^* \alpha_{0(m)} = 2$$

$$\rightarrow \mu_{0(1)}^* = \frac{1}{\alpha_{0(1)}} \left(2 - \sum_{m=2}^{M_0} \mu_{0(m)}^* \alpha_{0(m)} \right), \quad (303)$$

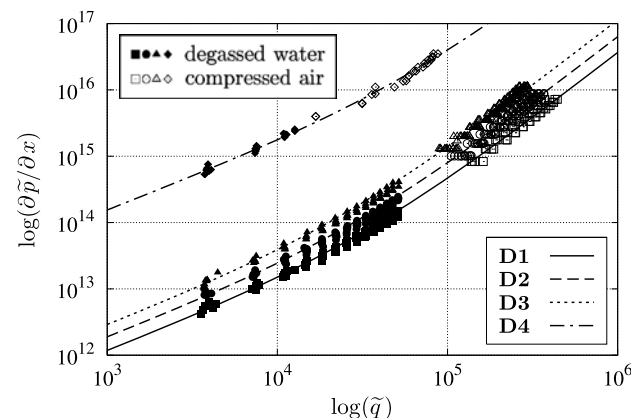


Fig. 10 Experimental data of percolation experiments and curves of the fitted Forchheimer equation (299) plotted using a double-logarithmic scale

Fig. 11 Best approximations by least-squares fits of the proposed functions (239) and (240) describing the deformation-dependent flow properties

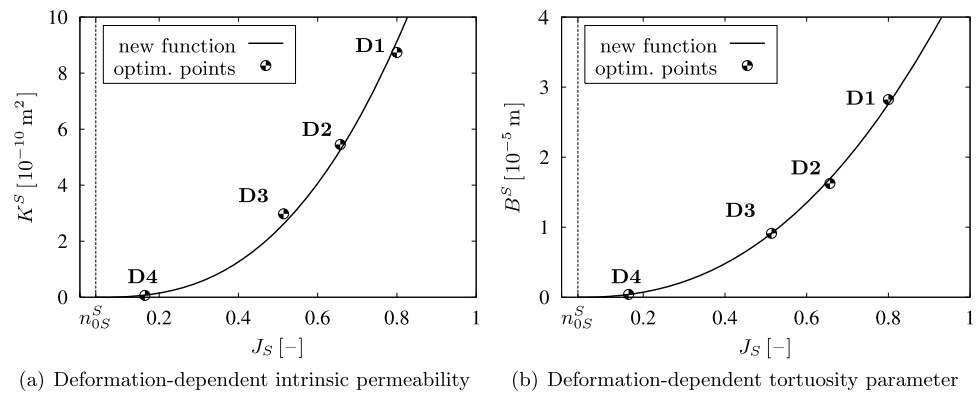
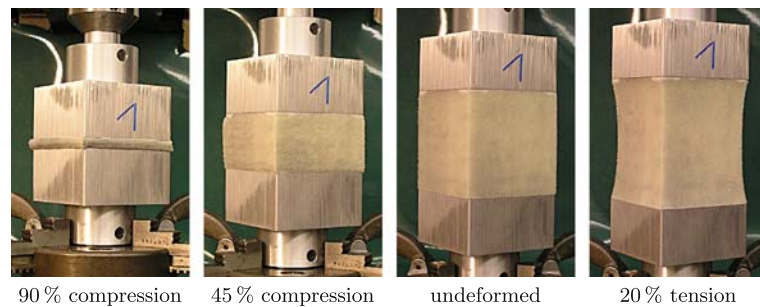


Fig. 12 Deformed PUR foam specimen during a compression-tension test



thereby reducing the number of variables of the optimization process. According to the general optimization procedure, the evaluation of the least-squares functional furthermore demands appropriate FE simulations of the uniaxial compression-tension experiments, where, at first, only the computed elastic response is considered. Therefore, proceeding from the numerical treatment described in Sect. 4, the presented material model is implemented in the FE package PANDAS (www.get-pandas.com), an adaptive finite element tool for multi-phase problems, and respective boundary-value problems describing the experiments are defined. In this context, note that all simulations re-

quired for the optimization are carried out fully 3-d since the displacement-boundary constraints representing the adhesive bonds and the possibility of a developing pore pressure may generally lead to inhomogeneous stress states. Following this, pursuing a hierarchical adaption strategy, the successive restart of the optimization procedure using refined FE meshes for the simulations with the previously found parameters as starting values, already yields an acceptable fit of the basic elasticity model to the experimental data for $M_0 = 2$ Ogden terms (Fig. 13). The final set of material parameters resulting from the optimization procedure with COBYLA reads:

Basic solid elasticity (equilibrium part)

$$\begin{aligned}
 \mu_0^S &= 2.5743 \cdot 10^4 \quad [\text{N/m}^2] & \mu_{0(1)}^* &= 2.0098 \cdot 10^{-1} \quad [-] \\
 \Lambda_0^S &= 6.879 \cdot 10^2 \quad [\text{N/m}^2] & \alpha_{0(1)} &= 1.0951 \cdot 10^1 \quad [-] \\
 \gamma_0^S &= 1.836 \quad [-] & \mu_{0(2)}^* &= -2.0098 \cdot 10^{-1} \quad [-] \\
 M_0 &= 2 \quad [-] & \alpha_{0(2)} &= 1.0 \quad [-]
 \end{aligned} \tag{304}$$

5.2.4 Intrinsic Solid Viscoelasticity

After the adjustment of the basic elasticity model, the parameters of the non-equilibrium material formulation (191) and the viscous evolution equations (210) must be identified.

Therefore, proceeding from the previously described experimental setups, additional displacement-driven hysteresis tests without holding times are performed at varying deformation velocities to capture the rate-dependent properties of the skeleton. In particular, cyclic compression-tension ex-

periments are carried out at deformation rates of 7.7, 0.77, 0.077, and 0.0077 mm/s, where the maximum speed is limited by the available spindle-driven testing device. The obtained stress-strain curves are plotted in Fig. 14 where it can be seen that the hysteresis loops exhibit a distinct sensitivity to the strain rate within the considered four decades of the velocity range. In this context, the necessity of the preceding identification of the permeability properties emerges since otherwise the intrinsic dissipative contributions of the PUR skeleton to the transient response of the foam could not be separated from the flow-dependent ones. In other words, due to the overlay of the dissipative solid and fluid properties, the rate-dependent behavior could be neither clearly assigned to the viscoelastic polymer matrix nor to the viscous percolation process, which would make a unique parameter identification almost impossible.

To continue, based on the above hysteresis data and the relaxation data from the previously described holding-time experiments, the parameter optimization is again carried out numerically using the COBYLA method where the required FE computations are performed with PANDAS. Therefore,

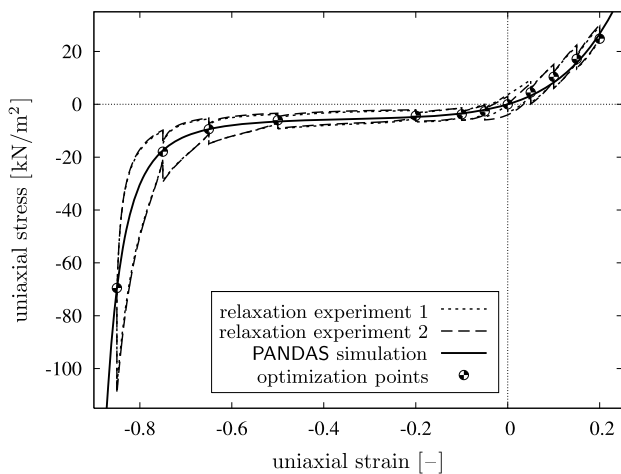
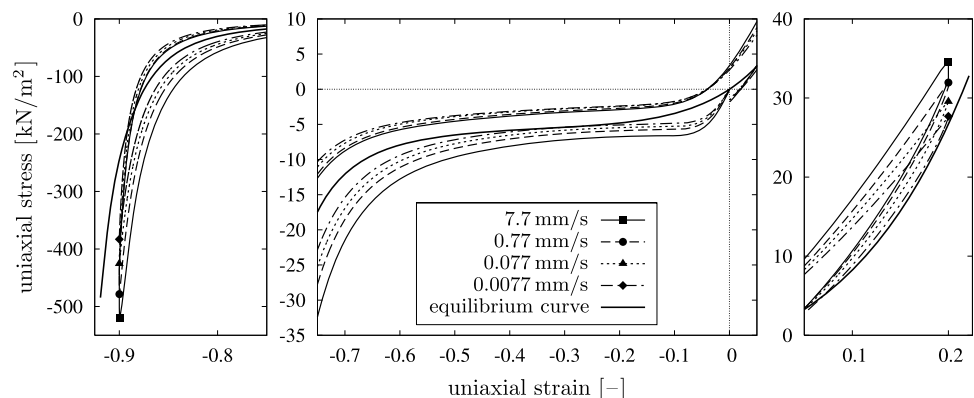


Fig. 13 Stress-strain diagram of uniaxial holding-time experiments and the basic elasticity response computed with PANDAS using (304)

Fig. 14 Stress-strain diagram of uniaxial hysteresis experiments in comparison with computed elastic response using the optimized parameters (304)

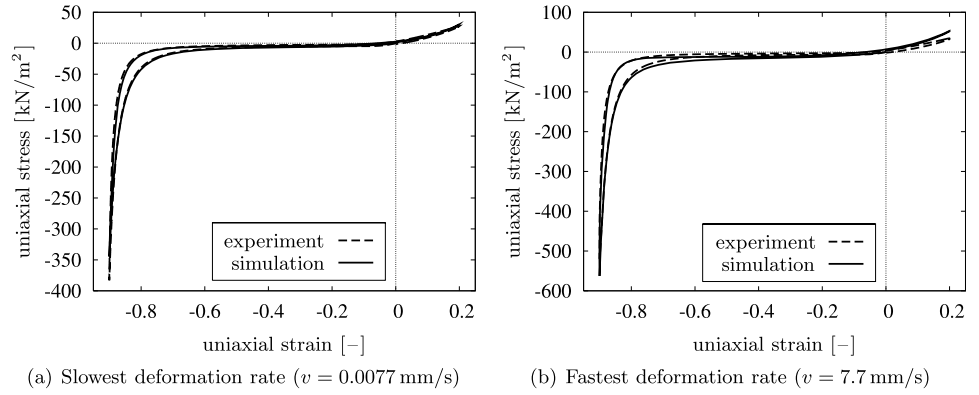


in analogy to the material parameter constraints (302) and (303) of the basic elasticity model, respective conditions must also be taken into account for each Maxwell element during the adaption of the non-equilibrium elasticity formulation (191). Moreover, according to (209), the viscosity parameters associated with the rheological dashpot elements must satisfy $\eta_n^S > 0$ and $\frac{2}{3}\eta_n^S + \zeta_n^S > 0$. In this connection, a shortcoming of the discrete spectrum algorithm becomes apparent as the satisfactory description of the nonlinear relaxation behavior of the PUR skeleton requires the consideration of an adequate number of Maxwell elements. Accompanied with each additional Maxwell element is a total of $4 + 2M_n$ unknown material parameters depending on the individual number M_n of Ogden terms where compatibility conditions analogous to (303) are already taken into account. Therefore, in order to keep the optimization effort under an acceptable limit, besides a hierarchical adaption strategy, we proceed from the simplifying assumption that the individual deviatoric and volumetric relaxation times coincide (cf. page 52):

$$\begin{aligned} \tau_n^S := (\tau_{\text{dev}}^S)_n = (\tau_{\text{vol}}^S)_n &\longrightarrow \frac{\eta_n^S}{\mu_n^S} = \frac{\frac{2}{3}\eta_n^S + \zeta_n^S}{\frac{2}{3}\mu_n^S + \Lambda_n^S} \\ &\longrightarrow \zeta_n^S = \frac{\eta_n^S \Lambda_n^S}{\mu_n^S}. \end{aligned} \quad (305)$$

Hence, the second viscosity parameters ζ_n^S can be removed from the list of unknowns. Moreover, the maximum number of Maxwell elements is restricted to $N = 3$, where the individual non-equilibrium elasticity laws are *a priori* equipped with $M_n = 2$ Ogden terms. Following this, for the adaption of the rate-dependent part of the solid model, one seeks for an optimal feasible set of $N_{\text{mat}} = 21$ material parameters in comparison to $N_{\text{mat}} = 6$ for the basic elasticity model. Accordingly, it is even more important to start the optimization with a good initial guess of the parameters in the right order of magnitude as the COBYLA algorithm may become very inefficient due to the sometimes fast decrease of the trust region radius resulting in only small changes to the variables.

Fig. 15 Stress-strain diagrams of uniaxial hysteresis experiments in comparison with the PANDAS simulations using the optimized parameters (306)



The model adaption is additionally aggravated by the fact that the optimization is only based on uniaxial experimental data. In general, it would be necessary to gain more information about the material behavior by further experimental investigations as, for instance, volumetric compression or shear tests which particularly address specific subsets of the parameters, and thus, allow for a stepwise fitting procedure with a reduced number of variables. Furthermore,

it seems promising to additionally incorporate information about the local material response into the least-squares functional, e.g., by applying optical methods in combination with point tracking algorithms which are able to capture local deformations on the skin of the test specimens. Nevertheless, Fig. 15 shows that the restricted model can already be brought into good accordance with the available hysteresis data yielding the optimized set of parameters:

Intrinsic solid viscoelasticity (non-equilibrium part) ($N = 3$)

..... 1st Maxwell element		
$\mu_1^S = 2.0025 \cdot 10^4$ [N/m ²]	$M_1 = 2$	[-]
$\Lambda_1^S = 2.5969 \cdot 10^{-2}$ [N/m ²]	$\mu_{1(1)}^* = 4.2065 \cdot 10^{-1}$	[-]
$\eta_1^S = 1.603 \cdot 10^6$ [N s/m ²]	$\alpha_{1(1)} = 5.7545$	[-]
$\zeta_1^S = 2.0788 \cdot 10^5$ [N s/m ²]	$\mu_{1(2)}^* = -4.2065 \cdot 10^{-1}$	[-]
$\tau_1^S = 8.005 \cdot 10^1$ [s]	$\alpha_{1(2)} = 1.0$	[-]
$\gamma_1^S = 1.0307$ [-]		
..... 2nd Maxwell element		
$\mu_2^S = 3.7342 \cdot 10^4$ [N/m ²]	$M_2 = 2$	[-]
$\Lambda_2^S = 1.1117 \cdot 10^2$ [N/m ²]	$\mu_{2(1)}^* = 3.0835$	[-]
$\eta_2^S = 3.3296 \cdot 10^3$ [N s/m ²]	$\alpha_{2(1)} = 1.0951$	[-]
$\zeta_2^S = 9.9121$ [N s/m ²]	$\mu_{2(2)}^* = -1.3918$	[-]
$\tau_2^S = 8.9165 \cdot 10^{-2}$ [s]	$\alpha_{2(2)} = 9.8913 \cdot 10^{-1}$	[-]
$\gamma_2^S = 7.7397$ [-]		
..... 3rd Maxwell element		
$\mu_3^S = 9.8088 \cdot 10^1$ [N/m ²]	$M_3 = 2$	[-]
$\Lambda_3^S = 4.1837 \cdot 10^1$ [N/m ²]	$\mu_{3(1)}^* = 4.924 \cdot 10^{-1}$	[-]
$\eta_3^S = 1.5259 \cdot 10^7$ [N s/m ²]	$\alpha_{3(1)} = 4.061$	[-]
$\zeta_3^S = 6.5085 \cdot 10^6$ [N s/m ²]	$\mu_{3(2)}^* = -2.018 \cdot 10^{-2}$	[-]
$\tau_3^S = 1.5556 \cdot 10^5$ [s]	$\alpha_{3(2)} = -1.8122 \cdot 10^{-2}$	[-]
$\gamma_3^S = 2.9212$ [-]		

(306)

5.3 Numerical Examples

5.3.1 Impact of a Foam Cushion

As previously mentioned, the considered PUR foam is primarily used as cushioning material for automotive seating systems. In regard to the increasing requirements for passenger safety during crash situations, the further development of seating systems is an important issue. The proper design demands a detailed understanding of the mechanical behavior of the cushioning material under impact loading. Therefore, by order of the German Association for Research in Automotive Technology FAT, working party AK 27, subgroup *Foam in Crash Simulation*, the Fraunhofer Institute for High-Speed Dynamics, Ernst Mach Institute (EMI) in Freiburg investigated the influence of the cushion size on the transient compressive response of soft PUR foam during impact experiments. In particular, PUR foam cushions with an original size of $400 \times 400 \times 100 \text{ mm}^3$ were impacted by a pneumatically driven impactor with a mass of 150 kg at an impact velocity of about 5 m/s and the responding force and the resulting deformation were recorded. For these experiments, some of the original foam cushions were cut into equal-sized pieces, e.g., four pieces of size $200 \times 200 \times 100 \text{ mm}^3$ or sixteen pieces of size $100 \times 100 \times 100 \text{ mm}^3$, and tested together with a small space in between the pieces to allow their unconfined deformation. It was found that an increasing fragmentation of the cushion is accompanied by a decrease in the transient stiffness that can only be explained by the outstreaming pore air through the permeable cut surfaces. More precisely, by increasing the fragmentation, the drained surface is enlarged, thereby concurrently reducing the flow path length of the air to that surface. Therefore, the consolidation process is much faster causing a lower pore-pressure development and, as a consequence, results in a softer material response.

Now, this flow-dependent size effect is simulated with PANDAS applying the previously adapted biphasic viscoelastic material model. For convenience, the impact of the different PUR foam cushions is simulated by a displacement-driven computation at a constant deformation rate of 5 m/s which is equal to the average impact velocity of the crash experiments. Note in passing that the prescription of a high but constant deformation velocity in combination with a low fluid density is consistent with the quasi-static model as we have $\rho^S \ddot{\mathbf{x}}_S = \mathbf{0}$ and $\rho \ddot{\mathbf{x}} \approx \mathbf{0}$. Concerning the drainage conditions, the original PUR foam cushions have a closed skin due to the manufacturing process which is regarded as impermeable for the computations, whereas the cut surfaces are modeled as fully drained boundaries. As can be seen from the simulation results depicted in Fig. 16, the phenomenon that under high-speed compression an undivided cushion of the considered foam is much

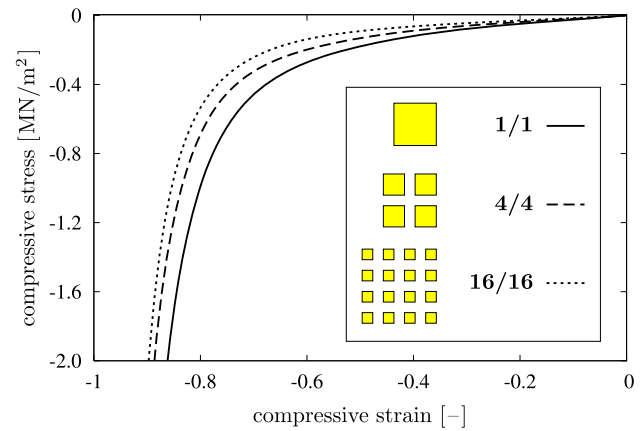


Fig. 16 Computed stress-strain curves of the simulated impact experiments of variously fragmented PUR foam cushions using the adapted model

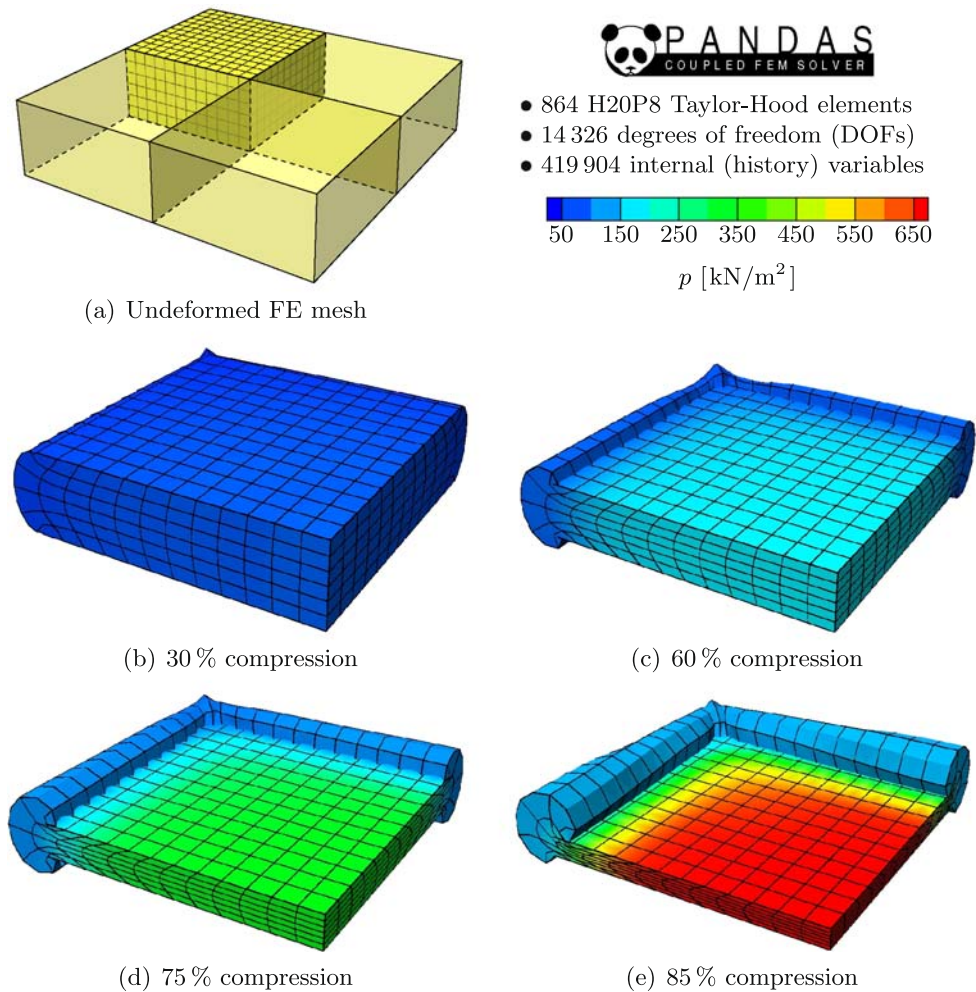
stiffer than a fragmented cushion of the same size is perfectly described.

Next, in order to gain insight into the development of the pore-fluid pressure, the pressure distribution at different deformation states for a non-fragmented cushion is given in Fig. 17. It can be observed that the pressure develops significantly primarily beyond 60% compression due to the large compressibility of the pore air as well as the deformation-dependent permeability and tortuosity properties of the PUR skeleton. The dynamic compression is accompanied by an immense bulging of the cushion as the air cannot escape through the assumed impermeable skin. Moreover, it is remarkable that at 85% compression, the developed internal gas pressure contributes to more than one third of the computed macroscopic stress response. In this context, it should be mentioned that in some of the impact experiments, the occurrence of high pore pressures actually caused the non-fragmented foam cushions to burst. Particularly the above described pneumatic damping behavior gives open-celled polymer foams their outstanding mechanical characteristics under dynamical loading and makes these types of materials favorable for cushioning or packaging applications. Consequently, only a multiphase model that accounts for the nonlinear and deformation-dependent percolation process as well as the complex deformation habits of the cellular polymer skeleton is appropriate for the realistic description.

5.3.2 Simulation of a Real Car Seat Cushion

In order to demonstrate the overall applicability of the presented model and the efficiency of its numerical implementation within the mixed Finite Element Method, the dynamic loading of the cushioning of a real car seat is simulated. Therefore, the geometry of a whole car seat cushion is reconstructed in a slightly simplified form using the

Fig. 17 Undeformed FE mesh and computed pore-pressure distributions during the dynamic compression of a non-fragmented PUR foam cushion. Note that due to double symmetry only a quarter of the cushion is computed



Rhinoceros NURBS (non-uniform rational B-splines) modeling software. The reconstructed geometry model of the cushioning is then spatially discretized by the different 3-d mixed finite elements shown in Fig. 6, where several meshes with variable degrees of refinement are generated using the CUBIT mesh generation toolkit. A photo of the original car seat, the reconstructed geometry model of the cushion, and a selection of the generated FE meshes are depicted in Fig. 18. As an illustrative example, an initial boundary-value problem is defined which qualitatively simulates an impact of the seat cushion, e.g., by a passenger or a crash-test dummy. For convenience, the abrupt loading is idealized by a distributed force on the mid parts of the cushion (Fig. 18(b) left) which is applied within 0.2 s, where the magnitude is reasonably chosen in order to yield realistic deformations. Against the background of the low density of the considered foam and the moderate acceleration during loading, it is assumed that inertial effects are negligibly small in comparison to the occurring rate-dependent phenomena, such that the quasi-static approximation is still valid. For the compu-

tations, the bottom of the seat and the rear of the back are regarded as spatially fixed (cf. Fig. 19). Moreover, the dense textile cover of the cushioning is assumed to be impermeable under transient conditions, and therefore, all surfaces are modeled as undrained boundaries. Note that due to the symmetry properties only half of the seat cushion must be computed taking into account appropriate symmetry boundary conditions.

For comparison of the different element types and discretizations, all computations are carried out with the sequential 64 bit version of PANDAS on the Beowulf Linux Cluster in our institute which is based on dual and quad AMD Opteron compute nodes equipped with 2.2 GHz CPUs and a maximum of 6 GB memory available for single processor jobs. Due to the large sparse linear systems of equations that arise from the finer FE discretizations, the application of Krylov-subspace iterative solvers is expedient. Following this, based on a compact sparse row (CSR) storage format, the generalized minimal residual (GMRES) method is used in conjunction with an ILUK preconditioner

Fig. 18 Photo of the original car seat, reconstructed geometry model of the seat cushion, and selection of tetra- and hexahedral FE discretizations

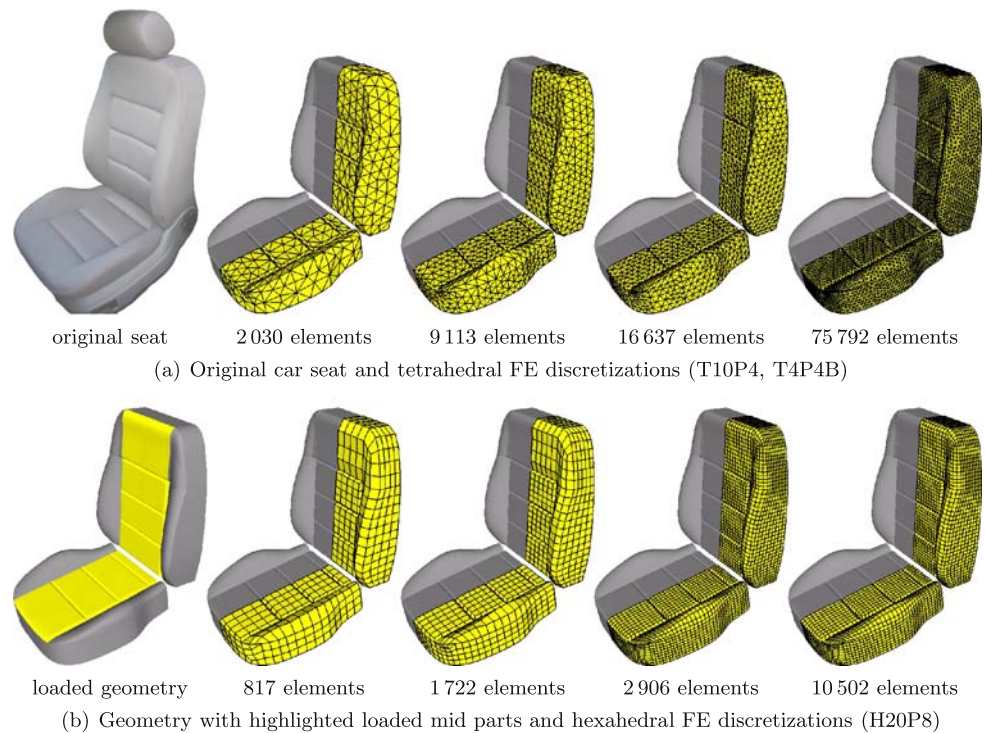
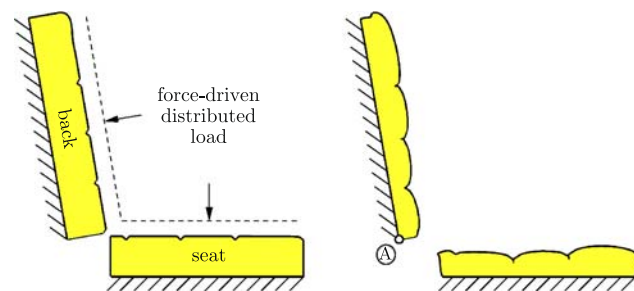


Fig. 19 Undeformed and deformed geometry in the symmetry plane of the seat



which in sequential computations yields a good performance and a stable convergence for the considered class of problems and fairly holds the balance between computational effort and required storage. For the global as well as the local time discretization, the implicit Euler scheme is used, where the time step size is adaptively controlled depending on the number of required Newton iterations as an objective indicator of the actual convergence behavior. The numerical quadrature proceeds from 27 integration points in the case of the hexahedral H20P8 Taylor-Hood elements and 15 Gauß points for both types of the mixed tetrahedral elements T10P4 and T4P4B, respectively. Following this, proceeding from the adapted solid viscoelasticity model with $N = 3$ Maxwell elements, a total number of $3 \times 6 = 18$ internal (history) variables must be treated and stored at each integration point of the FE mesh (recall (283)). Moreover, concerning the implementation of the T4P4B MINI element,

it should be noted that for the present investigations, the barycentric bubble nodes are not condensed on the element level, i.e., the associated three solid displacements per element enter the global equation system as additional unknowns.

Following the above, altogether 19 computations have been carried out of which 18 converged successfully comprising six different refinement levels of the spatial discretization for all three types of the considered mixed finite elements. The corresponding statistical information of the generated FE meshes including the total numbers of elements, degrees of freedom (DOFs), and internal variables, as well as the required storage (RAM in MB) and computing times (CPU time in hh:mm:ss) with the number of accepted versus rejected time steps and whether the end time is reached is provided in the following table:

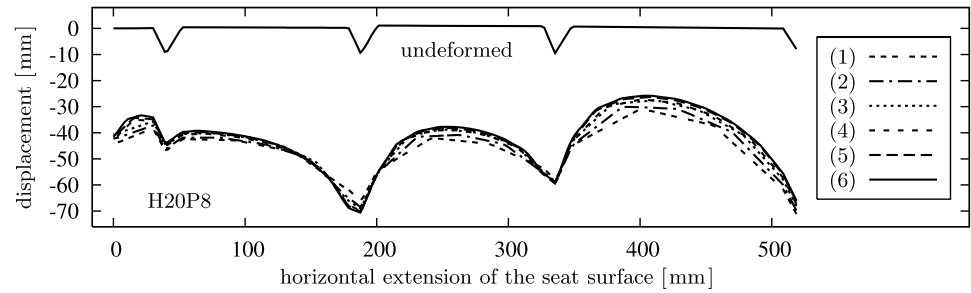
	# elems.	# DOFs	# int. vars.	RAM	CPU time (steps)	end
H20P8 (1)	344	7 061	167 184		00:07:14 (9/2)	yes
(2)	817	15 051	397 062		00:30:51 (11/4)	yes
(3)	1 722	29 227	836 892		01:00:31 (10/2)	yes
(4)	2 906	47 587	1 412 316		02:13:33 (11/2)	yes
(5)	5 030	80 793	2 444 580	1 582	07:30:43 (15/5)	yes
(6)	7 120	109 948	3 460 320	2 343	17:30:06 (20/10)	yes
(7)	10 502	159 707	5 103 972	4 360	57:31:28 (27/30)	no
T10P4 (1)	673	4 576	181 710		00:04:20 (7/0)	yes
(2)	2 030	11 817	548 100		00:17:23 (8/1)	yes
(3)	9 113	45 779	2 460 510		02:14:04 (11/2)	yes
(4)	16 637	81 029	4 491 990	878	05:31:16 (14/3)	yes
(5)	33 340	157 047	9 001 800	1 505	16:55:01 (14/4)	yes
(6)	47 256	219 447	12 759 120	4 880	53:14:06 (24/17)	yes
T4P4B (1)	673	3 079	181 710		00:06:10 (7/0)	yes
(MINI) (2)	2 030	8 562	548 100		00:17:36 (7/0)	yes
(3)	9 113	35 915	2 460 510		01:29:34 (7/0)	yes
(4)	16 637	64 703	4 491 990	439	02:42:56 (7/0)	yes
(5)	33 340	127 908	9 001 800	1 259	10:36:35 (14/0)	yes
(6)	75 792	287 400	20 463 840	2 204	39:26:37 (22/1)	yes

(307)

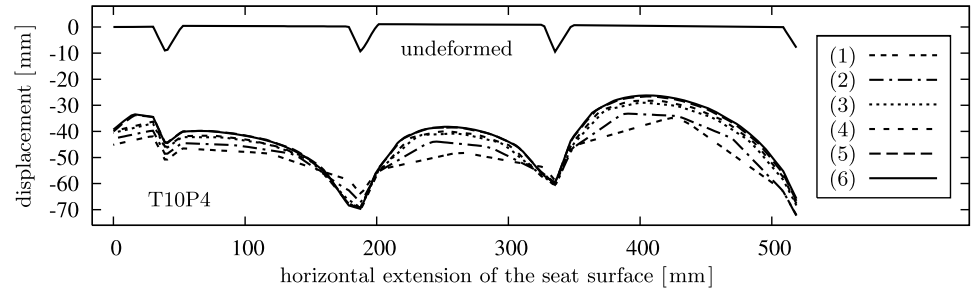
Now, based on the obtained simulation results, the comparison is carried out in two ways. At first, the computed deformations of the seat surface in the symmetry plane (cf. Fig. 19) are compared by plotting the final vertical displacements of the surface relative to its undeformed reference position for all discretizations (see Fig. 20). As can be observed in subfigures 20(a)–(c), by increasing the refinement of the spatial discretization the convergence property of the FEM is clearly verified for each element formulation. In this regard, coarse discretizations usually yield stiffer solutions than finer meshes which, following the basic idea of the Finite Element Method, are closer to the real solution. However, comparison of the finest discretizations of all element types in subfigure 20(d) reveals the inferior approximation of the seat surface deformation by the MINI elements as expected. It is a well-known fact that 1st-order tetrahedral elements are stiffer than 2nd-order tetrahedrons, which is also the major drawback of the T4P4B element followed by its undoubtful lower accuracy which may falsify the results especially in areas around stress concentrations. Nevertheless, the disadvantages of the MINI element can be put into perspective by looking at the computational effort and the

required storage in comparison to the H20P8 or T10P4 Taylor-Hood elements, respectively. Due to the additional mid nodes needed for the quadratic interpolation of \mathbf{u}_S which, in contrast to the barycentric bubble nodes, are shared with adjacent elements, besides the larger number of unknowns also the bandwidth of the global system matrix is generally larger causing a higher memory load and an increase of the total solution time. Moreover, for the problem under study where all simulations proceed from the same settings (tolerances, stopping criteria, etc.), the computations with the Taylor-Hood elements show a more cumbersome convergence behavior. It is apparent from table (307) that the number of rejected time steps, i.e., the computed time steps where finally no convergence is found in the global Newton iteration, is considerably larger for the discretizations based on the Taylor-Hood elements than on the MINI element. For the finest hexahedral mesh H20P8 (7), the force-driven analysis is interrupted when 95.8 % of the final load is applied as the chosen minimal time step size of 10^{-10} s is reached and still no convergence is found. This might be explained by the general observation that in large deformation problems the finer discretizations by 20-noded brick el-

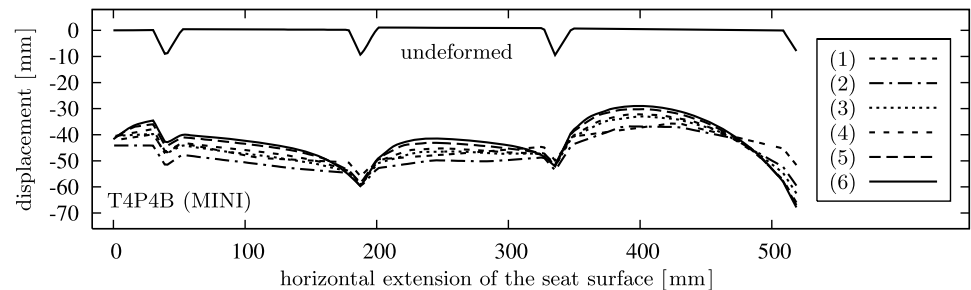
Fig. 20 Comparison of computed vertical displacements of the seat surface in the symmetry plane for the different mixed FE meshes listed in (307)



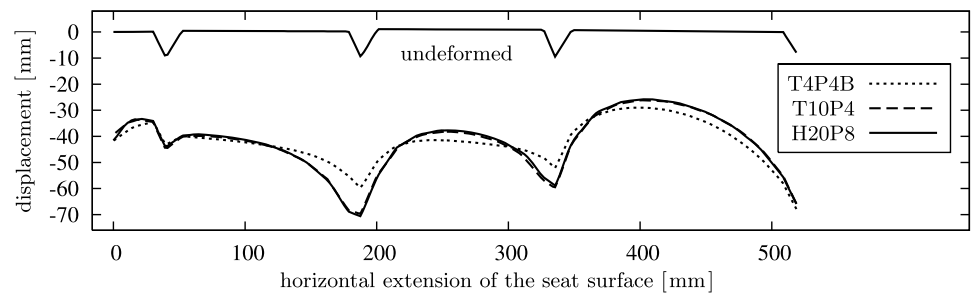
(a) Hexahedral discretizations with H20P8 Taylor-Hood elements



(b) Tetrahedral discretizations with T10P4 Taylor-Hood elements



(c) Tetrahedral discretizations with T4P4B (MINI) elements



(d) Comparison of the finest (refinement level (6)) mixed FE discretizations

elements are more vulnerable to critical aspect ratios and interior angles than tetrahedral meshes.

As a next step, the quality of the pore-pressure approximations is compared. Therefore, the computed maximum pore-gas pressure occurring in the lower part of the back of the seat cushion in the symmetry plane at point A marked in Fig. 19 is plotted for all element types over the six refinement levels of the respective discretization (see Fig. 21). Surprisingly, despite the underestimated solid displacements, the pressure approximations based on the MINI

element are close to those of the H20P8 brick elements which are known to yield good interpolations of the pressure field, whereas the tetrahedral Taylor-Hood elements underestimate the maximal pressure of about 6%. Finally, in order to get an impression of the overall development of the pore-gas pressure and the 3-d deformation behavior of the seat cushion, a sequence of deformed configurations at different loading states with the pore-pressure distribution displayed as isosurfaces is depicted in Fig. 22.

In conclusion, the above example convincingly shows that the presented biphasic viscoelastic model together with its numerical treatment by the mixed Finite Element Method is well suited for application to real engineering problems. Concerning the choice of the mixed element type, one has to balance between computational costs and accuracy. On the one hand, for 3-d porous media problems with moderate solid stresses and small skeleton deformations or generally lower accuracy requirements, such as for testing purposes or qualitative simulations, the T4P4B element seems to be

the economic choice. Another potential application of the MINI element might be its use in commercial FE packages where sophisticated TPM models can be incorporated via the user material interface as higher-order mixed element formulations are usually not or only partly available. On the other hand, whenever high accuracy is required, the H20P8 or T10P4 Taylor-Hood elements are the convenient choice. However, if the complexity of the geometry or the used material model demands a fine-resolution mesh, the large equation system that arises can only be efficiently handled by recourse to domain decomposition methods which enable a distributed parallel treatment of the strongly coupled problem.

6 Conclusions

6.1 Summary

The goal of this contribution was to present a consistent biphasic continuum model for viscoelastic high-porosity foams that accounts for the essential nonlinearities and the rate-dependent solid and fluid properties within the realm of a finite deformation theory. Therefore, on the basis of the established Theory of Porous Media (TPM), a general biphasic solid-fluid model was modularly extended by incorporating a sophisticated solid viscoelasticity formulation and a 3-d deformation-dependent non-Darcy filter law. The efficient

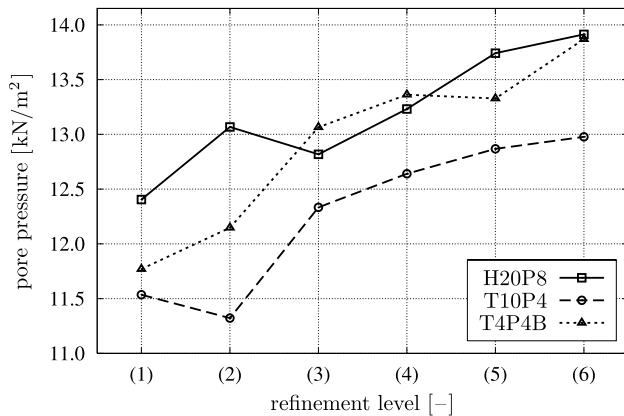
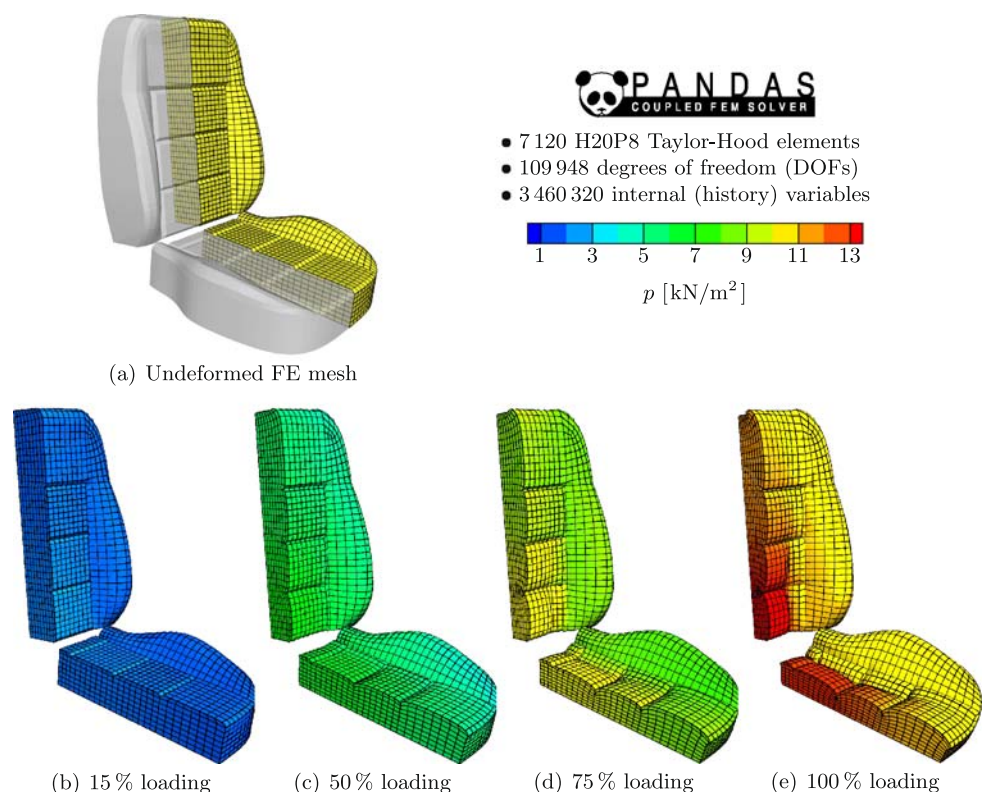


Fig. 21 Computed maximal pore-gas pressures in the back of the seat cushion (point A) depending on the element type and the refinement level according to table (307)

Fig. 22 Computed deformations and pore-pressure distributions during the force-driven simulation of an impact of a car seat cushion using the H20P8 (6) discretization



numerical treatment of the strongly coupled inelastic problem was carried out by the mixed Finite Element Method (FEM), where the overall solution procedure and the algorithmic implementation were described. In order to show its practical applicability, the proposed model was adapted to real experimental data of a soft open-celled polyurethane (PUR) foam by use of a numerical optimization strategy. Finally, two illustrative boundary-value problems were computed to show the capabilities of the macroscopic formulation and its numerical implementation, and the overall applicability of the model to real engineering problems.

6.2 Conclusion and Discussion

Proceeding from a comprehensible introduction of finite deformation measures by means of natural curvilinear coordinates, it could be shown that the multiplicative geometric concept associated with stress-free intermediate configurations represents a convenient constitutive basis in finite solid inelasticity. For the considered case of a viscoelastic solid skeleton, from a modeling as well as a computational perspective, the rheological structure of the generalized Maxwell model turned out to be well suited to serve as a constitutive phenomenological framework. In particular, the differential representation of viscoelasticity with a discrete relaxation spectrum in combination with strain-equivalent internal variables, such as the inelastic deformation tensors, allows the application of an efficient iterative solution algorithm based on a two-stage Newton procedure. In conjunction with sophisticated Runge-Kutta time integration schemes this enables the economic computation of large coupled viscoelastic DAE systems.

The proposed isotropic strain-energy function for the description of the macroscopically compressible viscoelastic skeleton could be very well correlated with the highly nonlinear stress-strain data of a low-density polyurethane foam. This was only possible through the polynomial structure of the strain energy which basically proceeds from Ogden-type formulations for the equilibrium and non-equilibrium parts extended by appropriate volumetric response functions. In this context, the developing non-equilibrium contributions are governed by adequate rate equations formulated on the intermediate configurations, such that the model remains its validity even for finite viscoelastic processes which are far away from thermodynamic equilibrium.

Concerning the description of the nonlinear percolation process, it could be shown that the proposed non-Darcy filter law is very successful in describing real liquid and gas flows through variously compressed samples of the considered PUR foam. Since for this foam no distinct anisotropic effects were observed in the pore-fluid flow, it remains to be shown that the presented ansatz of a deformation-induced anisotropic permeability can be experimentally verified for other permeable porous materials.

The general adjustment of the biphase viscoelastic model for the description of an open-celled polyurethane foam was successfully carried out by use of a gradient-free, sequential, trust region optimization algorithm. In this regard, the used hierarchical simulation strategy kept the computational overhead under an acceptable limit and somehow weakens the conventional wisdom by which function-value only methods should be avoided unless there is no other choice. However, in order to fit the constitutive model more accurately and possibly expose its weak points, further experimental evidence is necessary to precisely capture the properties of the considered foam material under general loading conditions. This will additionally guide further improvements of the biphase model.

The two final numerical examples convincingly showed that the presented biphase viscoelastic model together with its numerical treatment by the mixed FEM is well suited for practical applications. From the impact simulations, it became apparent that only a multiphase model that accounts for the essential nonlinearities and rate-dependent solid and fluid properties is appropriate for the realistic description of soft polymeric foams. Concerning the choice of the mixed element type, a convergence study showed that all discussed element formulations yield a stable solution and an increasing accuracy in finer meshes. However, in comparison to the computationally more expensive H20P8 and T10P4 Taylor-Hood elements, one has to be aware of the generally stiffer solution and lower accuracy if the T4P4B MINI element is used for the spatial discretization.

In conclusion, the present work delivers several new aspects to porous media theories concerning consistent modeling, efficient numerical treatment, and model adaption, where the overall combination defines the new state of the art in porous media viscoelasticity with special focus on cellular polymers.

6.3 Future Work

Due to the manifold further improvements of the presented viscoelastic porous media model, only a selective choice of conceivable extensions is presented. Two obvious improvements could be the generalization to overall anisotropic skeleton properties and the consideration of damage and aging effects. In this connection, quite a lot of work exists in the related literature of singlephase materials where the basic concepts can be straightforwardly adopted and integrated into the existing model. Further interesting possibilities are provided by an extension of the biphase model with an additional fluid constituent and the consideration of individual constituent temperatures, which allows the description of partially saturated conditions and heat transfer processes. Moreover, the presented approach offers future potentials when applied in the aspiring field of biomechanics, e.g.,

for the description of soft biological tissues, such as articular cartilage. Particularly hydrated biological tissues are believed to exhibit intrinsic rate-dependent properties besides the dissipative interstitial flow and diffusion phenomena, which may be explained by their proteinic microstructure that is somehow comparable to a viscoelastic network of polymer chains. Furthermore, as the modular structure of the constitutive equations is not only restricted to binary solid-fluid mixtures, they may be exploited in all kinds of

multiphasic TPM models, and thus, can find their application in various engineering disciplines.

Appendix

A.1 General Transport Mechanisms

Co- and contravariant transport mechanisms

1st-order tensors (vectors):

$$\begin{array}{ccc} \mathbf{h}_k & \xrightarrow[\mathbf{F}_{Si}^{-1}]{\mathbf{F}_{Si}} \hat{\mathbf{z}}_k & \xrightarrow[\mathbf{F}_{Se}^{-1}]{\mathbf{F}_{Se}} \mathbf{a}_k \\ & \nwarrow \mathbf{F}_S^{-1} & \nwarrow \mathbf{F}_S^T \\ \mathbf{h}^k & \xrightarrow[\mathbf{F}_{Si}^T]{\mathbf{F}_{Si}^{T-1}} \hat{\mathbf{z}}^k & \xrightarrow[\mathbf{F}_{Se}^T]{\mathbf{F}_{Se}^{T-1}} \mathbf{a}^k \\ & \nwarrow \mathbf{F}_S^T & \nwarrow \mathbf{F}_S^{T-1} \end{array}$$

2nd-order tensors:

$$\begin{array}{ccc} \mathbf{h}_k \otimes \mathbf{h}_l & \xrightarrow[\mathbf{F}_{Si}^{-1}(\hat{\cdot}) \mathbf{F}_{Si}^{T-1}]{\mathbf{F}_{Si}(\cdot) \mathbf{F}_{Si}^T} \hat{\mathbf{z}}_k \otimes \hat{\mathbf{z}}_l & \xrightarrow[\mathbf{F}_{Se}^{-1}(\cdot) \mathbf{F}_{Se}^{T-1}]{\mathbf{F}_{Se}(\hat{\cdot}) \mathbf{F}_{Se}^T} \mathbf{a}_k \otimes \mathbf{a}_l \\ & \nwarrow \mathbf{F}_S^{-1}(\cdot) \mathbf{F}_S^{T-1} & \nwarrow \mathbf{F}_S^{T-1}(\cdot) \mathbf{F}_S^{-1} \\ \mathbf{h}^k \otimes \mathbf{h}^l & \xrightarrow[\mathbf{F}_{Si}^T(\hat{\cdot}) \mathbf{F}_{Si}]{\mathbf{F}_{Si}^{T-1}(\cdot) \mathbf{F}_{Si}^{-1}} \hat{\mathbf{z}}^k \otimes \hat{\mathbf{z}}^l & \xrightarrow[\mathbf{F}_{Se}^T(\cdot) \mathbf{F}_{Se}]{\mathbf{F}_{Se}^{T-1}(\hat{\cdot}) \mathbf{F}_{Se}^{-1}} \mathbf{a}^k \otimes \mathbf{a}^l \\ & \nwarrow \mathbf{F}_S^T(\cdot) \mathbf{F}_S & \nwarrow \mathbf{F}_S^T(\cdot) \mathbf{F}_S \end{array}$$

(308)

4th-order tensors:

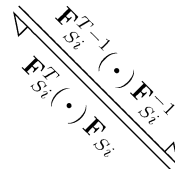
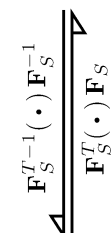
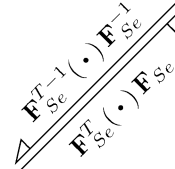
$$\begin{array}{ccc} \mathbf{H}^{\sharp} & \xrightarrow[\mathbf{F}_{Si}^{-1} \otimes \mathbf{F}_{Si}^{-1}]{(\mathbf{F}_{Si} \otimes \mathbf{F}_{Si})^T(\cdot) (\mathbf{F}_{Si}^T \otimes \mathbf{F}_{Si}^T)^T} \hat{\mathbf{Z}}^{\sharp} & \xrightarrow[\mathbf{F}_{Se}^{-1} \otimes \mathbf{F}_{Se}^{-1}]{(\mathbf{F}_{Se} \otimes \mathbf{F}_{Se})^T(\hat{\cdot}) (\mathbf{F}_{Se}^T \otimes \mathbf{F}_{Se}^T)^T} \mathbf{A}^{\sharp} \\ & \nwarrow (\mathbf{F}_S^{-1} \otimes \mathbf{F}_S^{-1})^T(\cdot) (\mathbf{F}_S^{T-1} \otimes \mathbf{F}_S^{T-1})^T & \nwarrow (\mathbf{F}_S^{T-1} \otimes \mathbf{F}_S^{T-1})^T(\cdot) (\mathbf{F}_S^{-1} \otimes \mathbf{F}_S^{-1})^T \\ \mathbf{H}^{\flat} & \xrightarrow[\mathbf{F}_{Si}^T \otimes \mathbf{F}_{Si}^T]{(\mathbf{F}_{Si}^{T-1} \otimes \mathbf{F}_{Si}^{T-1})^T(\cdot) (\mathbf{F}_{Si}^{-1} \otimes \mathbf{F}_{Si}^{-1})^T} \hat{\mathbf{Z}}^{\flat} & \xrightarrow[\mathbf{F}_{Se}^T \otimes \mathbf{F}_{Se}^T]{(\mathbf{F}_{Se}^{T-1} \otimes \mathbf{F}_{Se}^{T-1})^T(\hat{\cdot}) (\mathbf{F}_{Se}^{-1} \otimes \mathbf{F}_{Se}^{-1})^T} \mathbf{A}^{\flat} \\ & \nwarrow (\mathbf{F}_S^T \otimes \mathbf{F}_S^T)^T(\cdot) (\mathbf{F}_S \otimes \mathbf{F}_S)^T & \nwarrow (\mathbf{F}_S^T \otimes \mathbf{F}_S^T)^T(\cdot) (\mathbf{F}_S \otimes \mathbf{F}_S)^T \end{array}$$

$$\text{where } \left\{ \begin{array}{l} \mathbf{H}^{\sharp} = \mathbf{h}_k \otimes \mathbf{h}_l \otimes \mathbf{h}_m \otimes \mathbf{h}_n \\ \hat{\mathbf{Z}}^{\sharp} = \hat{\mathbf{z}}_k \otimes \hat{\mathbf{z}}_l \otimes \hat{\mathbf{z}}_m \otimes \hat{\mathbf{z}}_n \\ \mathbf{A}^{\sharp} = \mathbf{a}_k \otimes \mathbf{a}_l \otimes \mathbf{a}_m \otimes \mathbf{a}_n \end{array} \right\} \text{ and } \left\{ \begin{array}{l} \mathbf{H}^{\flat} = \mathbf{h}^k \otimes \mathbf{h}^l \otimes \mathbf{h}^m \otimes \mathbf{h}^n \\ \hat{\mathbf{Z}}^{\flat} = \hat{\mathbf{z}}^k \otimes \hat{\mathbf{z}}^l \otimes \hat{\mathbf{z}}^m \otimes \hat{\mathbf{z}}^n \\ \mathbf{A}^{\flat} = \mathbf{a}^k \otimes \mathbf{a}^l \otimes \mathbf{a}^m \otimes \mathbf{a}^n \end{array} \right\}^a$$

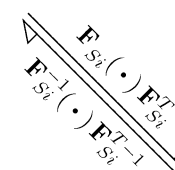
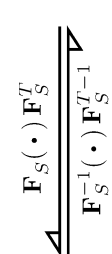

^aHere, the identifiers $(\cdot)^{\sharp}$ and $(\cdot)^{\flat}$ are used to distinguish co- and contravariant tensors.

A.2 Transport Properties of Strain Tensors

Transport properties of contravariant solid strain tensors ($N = 1$)

<p style="text-align: center;"><i>reference configuration</i></p> <hr/> $\mathbf{E}_S = \frac{1}{2}(\mathbf{C}_S - \mathbf{I}) = \frac{1}{2}(a_{kl} - h_{kl})\mathbf{h}^k \otimes \mathbf{h}^l$ $\mathbf{E}_{Se} = \frac{1}{2}(\mathbf{C}_S - \mathbf{C}_{Si}) = \frac{1}{2}(a_{kl} - \hat{z}_{kl})\mathbf{h}^k \otimes \mathbf{h}^l$ $\mathbf{E}_{Si} = \frac{1}{2}(\mathbf{C}_{Si} - \mathbf{I}) = \frac{1}{2}(\hat{z}_{kl} - h_{kl})\mathbf{h}^k \otimes \mathbf{h}^l$ <hr/> $\mathbf{E}_S = \mathbf{E}_{Se} + \mathbf{E}_{Si}$	
	<p style="text-align: center;"><i>intermediate configuration</i></p> <hr/> $\hat{\mathbf{\Gamma}}_S = \frac{1}{2}(\hat{\mathbf{C}}_{Se} - \hat{\mathbf{B}}_{Si}^{-1}) = \frac{1}{2}(a_{kl} - h_{kl})\hat{\mathbf{z}}^k \otimes \hat{\mathbf{z}}^l$ $\hat{\mathbf{\Gamma}}_{Se} = \frac{1}{2}(\hat{\mathbf{C}}_{Se} - \mathbf{I}) = \frac{1}{2}(a_{kl} - \hat{z}_{kl})\hat{\mathbf{z}}^k \otimes \hat{\mathbf{z}}^l$ $\hat{\mathbf{\Gamma}}_{Si} = \frac{1}{2}(\mathbf{I} - \hat{\mathbf{B}}_{Si}^{-1}) = \frac{1}{2}(\hat{z}_{kl} - h_{kl})\hat{\mathbf{z}}^k \otimes \hat{\mathbf{z}}^l$ <hr/> $\hat{\mathbf{\Gamma}}_S = \hat{\mathbf{\Gamma}}_{Se} + \hat{\mathbf{\Gamma}}_{Si}$
<p style="text-align: center;"><i>actual configuration</i></p> <hr/> $\mathbf{A}_S = \frac{1}{2}(\mathbf{I} - \mathbf{B}_S^{-1}) = \frac{1}{2}(a_{kl} - h_{kl})\mathbf{a}^k \otimes \mathbf{a}^l$ $\mathbf{A}_{Se} = \frac{1}{2}(\mathbf{I} - \mathbf{B}_{Se}^{-1}) = \frac{1}{2}(a_{kl} - \hat{z}_{kl})\mathbf{a}^k \otimes \mathbf{a}^l$ $\mathbf{A}_{Si} = \frac{1}{2}(\mathbf{B}_{Se}^{-1} - \mathbf{B}_S^{-1}) = \frac{1}{2}(\hat{z}_{kl} - h_{kl})\mathbf{a}^k \otimes \mathbf{a}^l$ <hr/> $\mathbf{A}_S = \mathbf{A}_{Se} + \mathbf{A}_{Si}$	

Transport properties of covariant solid strain tensors ($N = 1$)

<p style="text-align: center;"><i>reference configuration</i></p> <hr/> $\mathbf{K}_S^R = \frac{1}{2}(\mathbf{I} - \mathbf{C}_S^{-1}) = \frac{1}{2}(h^{kl} - a^{kl})\mathbf{h}_k \otimes \mathbf{h}_l$ $\mathbf{K}_{Se}^R = \frac{1}{2}(\mathbf{C}_{Si}^{-1} - \mathbf{C}_S^{-1}) = \frac{1}{2}(\hat{z}^{kl} - a^{kl})\mathbf{h}_k \otimes \mathbf{h}_l$ $\mathbf{K}_{Si}^R = \frac{1}{2}(\mathbf{I} - \mathbf{C}_{Si}^{-1}) = \frac{1}{2}(h^{kl} - \hat{z}^{kl})\mathbf{h}_k \otimes \mathbf{h}_l$ <hr/> $\mathbf{K}_S^R = \mathbf{K}_{Se}^R + \mathbf{K}_{Si}^R$	
	<p style="text-align: center;"><i>intermediate configuration</i></p> <hr/> $\hat{\mathbf{K}}_S = \frac{1}{2}(\hat{\mathbf{B}}_{Si} - \hat{\mathbf{C}}_{Se}^{-1}) = \frac{1}{2}(h^{kl} - a^{kl})\hat{\mathbf{z}}_k \otimes \hat{\mathbf{z}}_l$ $\hat{\mathbf{K}}_{Se} = \frac{1}{2}(\mathbf{I} - \hat{\mathbf{C}}_{Se}^{-1}) = \frac{1}{2}(\hat{z}^{kl} - a^{kl})\hat{\mathbf{z}}_k \otimes \hat{\mathbf{z}}_l$ $\hat{\mathbf{K}}_{Si} = \frac{1}{2}(\hat{\mathbf{B}}_{Si} - \mathbf{I}) = \frac{1}{2}(h^{kl} - \hat{z}^{kl})\hat{\mathbf{z}}_k \otimes \hat{\mathbf{z}}_l$ <hr/> $\hat{\mathbf{K}}_S = \hat{\mathbf{K}}_{Se} + \hat{\mathbf{K}}_{Si}$
<p style="text-align: center;"><i>actual configuration</i></p> <hr/> $\mathbf{K}_S = \frac{1}{2}(\mathbf{B}_S - \mathbf{I}) = \frac{1}{2}(h^{kl} - a^{kl})\mathbf{a}_k \otimes \mathbf{a}_l$ $\mathbf{K}_{Se} = \frac{1}{2}(\mathbf{B}_{Se} - \mathbf{I}) = \frac{1}{2}(\hat{z}^{kl} - a^{kl})\mathbf{a}_k \otimes \mathbf{a}_l$ $\mathbf{K}_{Si} = \frac{1}{2}(\mathbf{B}_S - \mathbf{B}_{Se}) = \frac{1}{2}(h^{kl} - \hat{z}^{kl})\mathbf{a}_k \otimes \mathbf{a}_l$ <hr/> $\mathbf{K}_S = \mathbf{K}_{Se} + \mathbf{K}_{Si}$	

A.3 Transport Properties of Strain Rate Tensors

Transport properties of contravariant solid strain rates ($N = 1$)

<div style="border: 1px solid black; padding: 10px; margin-bottom: 10px;"> <p style="text-align: center; margin: 0;"><i>reference configuration</i></p> <hr style="margin: 5px 0;"/> $\begin{aligned} (\mathbf{E}_S)'_S &= \frac{1}{2} (\mathbf{C}_S)'_S = \frac{1}{2} (a_{kl})'_S \mathbf{h}^k \otimes \mathbf{h}^l \\ (\mathbf{E}_{Se})'_S &= \frac{1}{2} (\mathbf{C}_S - \mathbf{C}_{Si})'_S = \frac{1}{2} (a_{kl} - \hat{z}_{kl})'_S \mathbf{h}^k \otimes \mathbf{h}^l \\ (\mathbf{E}_{Si})'_S &= \frac{1}{2} (\mathbf{C}_{Si})'_S = \frac{1}{2} (\hat{z}_{kl})'_S \mathbf{h}^k \otimes \mathbf{h}^l \end{aligned}$ <hr style="margin: 5px 0;"/> $(\mathbf{E}_S)'_S = (\mathbf{E}_{Se})'_S + (\mathbf{E}_{Si})'_S$ </div> <div style="border: 1px solid black; padding: 10px; margin-bottom: 10px;"> <p style="text-align: center; margin: 0;"><i>intermediate configuration</i></p> <hr style="margin: 5px 0;"/> $\begin{aligned} (\hat{\Gamma}_S)_{Si}^\Delta &= \frac{1}{2} (\hat{\mathbf{C}}_{Se})_{Si}^\Delta = \frac{1}{2} (a_{kl})'_S \hat{\mathbf{z}}^k \otimes \hat{\mathbf{z}}^l \\ (\hat{\Gamma}_{Se})_{Si}^\Delta &= \frac{1}{2} (\hat{\mathbf{C}}_{Se} - \mathbf{I})_{Si}^\Delta = \frac{1}{2} (a_{kl} - \hat{z}_{kl})'_S \hat{\mathbf{z}}^k \otimes \hat{\mathbf{z}}^l \\ (\hat{\Gamma}_{Si})_{Si}^\Delta &= \hat{\mathbf{D}}_{Si} = \frac{1}{2} (\hat{z}_{kl})'_S \hat{\mathbf{z}}^k \otimes \hat{\mathbf{z}}^l \end{aligned}$ <hr style="margin: 5px 0;"/> $(\hat{\Gamma}_S)_{Si}^\Delta = (\hat{\Gamma}_{Se})_{Si}^\Delta + (\hat{\Gamma}_{Si})_{Si}^\Delta$ </div> <div style="border: 1px solid black; padding: 10px;"> <p style="text-align: center; margin: 0;"><i>actual configuration</i></p> <hr style="margin: 5px 0;"/> $\begin{aligned} (\mathbf{A}_S)^\Delta_S &= \mathbf{D}_S = \frac{1}{2} (a_{kl})'_S \mathbf{a}^k \otimes \mathbf{a}^l \\ (\mathbf{A}_{Se})^\Delta_S &= \frac{1}{2} (\mathbf{I} - \mathbf{B}_{Se}^{-1})^\Delta_S = \frac{1}{2} (a_{kl} - \hat{z}_{kl})'_S \mathbf{a}^k \otimes \mathbf{a}^l \\ (\mathbf{A}_{Si})^\Delta_S &= \frac{1}{2} (\mathbf{B}_{Se}^{-1})^\Delta_S = \frac{1}{2} (\hat{z}_{kl})'_S \mathbf{a}^k \otimes \mathbf{a}^l \end{aligned}$ <hr style="margin: 5px 0;"/> $(\mathbf{A}_S)^\Delta_S = (\mathbf{A}_{Se})^\Delta_S + (\mathbf{A}_{Si})^\Delta_S$ </div>	<div style="text-align: center; margin-bottom: 20px;"> </div> <div style="text-align: center;"> </div>
---	--

(311)

with the lower (contravariant) Lie or Oldroyd derivatives of φ^S

$$\begin{aligned}
 (\cdot)_S^\Delta &:= (\cdot)'_S + \mathbf{L}_S^T(\cdot) + (\cdot)\mathbf{L}_S, \\
 (\hat{\cdot})_{Si}^\Delta &:= (\hat{\cdot})'_{Si} + \hat{\mathbf{L}}_{Si}^T(\hat{\cdot}) + (\hat{\cdot})\hat{\mathbf{L}}_{Si}
 \end{aligned}$$

and the contravariant identities

$$\begin{aligned}
 \mathbf{D}_S &= \frac{1}{2} (\mathbf{L}_S + \mathbf{L}_S^T) = (\mathbf{A}_S)^\Delta_S, \quad \hat{\mathbf{D}}_{Si} = \frac{1}{2} (\hat{\mathbf{L}}_{Si} + \hat{\mathbf{L}}_{Si}^T) = (\hat{\Gamma}_{Si})_{Si}^\Delta, \\
 (\mathbf{B}_S^{-1})^\Delta_S &= (h_{kl} \mathbf{a}^k \otimes \mathbf{a}^l)_S^\Delta = \mathbf{0}, \quad (\hat{\mathbf{B}}_{Si}^{-1})_{Si}^\Delta = (h_{kl} \hat{\mathbf{z}}^k \otimes \hat{\mathbf{z}}^l)_{Si}^\Delta = \mathbf{0}.
 \end{aligned}$$

Transport properties of covariant solid strain rates ($N = 1$)

<div style="border: 1px solid black; padding: 10px; margin-bottom: 10px;"> <p style="text-align: center; margin: 0;"><i>reference configuration</i></p> <hr style="margin: 5px 0;"/> $\begin{aligned} {}^R(\mathbf{K}_S)'_S &= \frac{1}{2} (\mathbf{C}_S^{-1})'_S = \frac{1}{2} (a^{kl})'_S \mathbf{h}_k \otimes \mathbf{h}_l \\ ({}^R\mathbf{K}_{Se})'_S &= \frac{1}{2} (\mathbf{C}_{Si}^{-1} - \mathbf{C}_S^{-1})'_S = \frac{1}{2} (\hat{z}^{kl} - a^{kl})'_S \mathbf{h}_k \otimes \mathbf{h}_l \\ ({}^R\mathbf{K}_{Si})'_S &= -\frac{1}{2} (\mathbf{C}_{Si}^{-1})'_S = -\frac{1}{2} (\hat{z}^{kl})'_S \mathbf{h}_k \otimes \mathbf{h}_l \end{aligned}$ <hr style="margin: 5px 0;"/> $\mathbf{K}_S = {}^R\mathbf{K}_{Se} + {}^R\mathbf{K}_{Si}$ </div> <div style="text-align: center; margin: 10px 0;"> $\begin{array}{c} \uparrow \\ \mathbf{F}_S(\cdot) \mathbf{F}_S^T \\ \downarrow \\ \mathbf{F}_S^{-1}(\cdot) \mathbf{F}_S^{T-1} \end{array}$ </div> <div style="border: 1px solid black; padding: 10px; margin-bottom: 10px;"> <p style="text-align: center; margin: 0;"><i>intermediate configuration</i></p> <hr style="margin: 5px 0;"/> $\begin{aligned} (\hat{\mathbf{K}}_S)_{Si}^\nabla &= -\frac{1}{2} (\hat{\mathbf{C}}_{Se}^{-1})_{Si}^\nabla = \frac{1}{2} (a^{kl})'_S \hat{\mathbf{z}}_k \otimes \hat{\mathbf{z}}_l \\ (\hat{\mathbf{K}}_{Se})_{Si}^\nabla &= \frac{1}{2} (\mathbf{I} - \hat{\mathbf{C}}_{Se}^{-1})_{Si}^\nabla = \frac{1}{2} (\hat{z}^{kl} - a^{kl})'_S \hat{\mathbf{z}}_k \otimes \hat{\mathbf{z}}_l \\ (\hat{\mathbf{K}}_{Si})_{Si}^\nabla &= \hat{\mathbf{D}}_{Si} = -\frac{1}{2} (\hat{z}^{kl})'_S \hat{\mathbf{z}}_k \otimes \hat{\mathbf{z}}_l \end{aligned}$ <hr style="margin: 5px 0;"/> $(\hat{\mathbf{K}}_S)_{Si}^\nabla = (\hat{\mathbf{K}}_{Se})_{Si}^\nabla + (\hat{\mathbf{K}}_{Si})_{Si}^\nabla$ </div> <div style="text-align: center; margin: 10px 0;"> $\begin{array}{c} \uparrow \\ \mathbf{F}_{Se}(\cdot) \mathbf{F}_{Se}^T \\ \downarrow \\ \mathbf{F}_{Se}^{-1}(\cdot) \mathbf{F}_{Se}^{T-1} \end{array}$ </div> <div style="border: 1px solid black; padding: 10px;"> <p style="text-align: center; margin: 0;"><i>actual configuration</i></p> <hr style="margin: 5px 0;"/> $\begin{aligned} (\mathbf{K}_S)^\nabla_S &= \mathbf{D}_S = \frac{1}{2} (a^{kl})'_S \mathbf{a}_k \otimes \mathbf{a}_l \\ (\mathbf{K}_{Se})^\nabla_S &= \frac{1}{2} (\mathbf{B}_{Se} - \mathbf{I})^\nabla_S = \frac{1}{2} (\hat{z}^{kl} - a^{kl})'_S \mathbf{a}_k \otimes \mathbf{a}_l \\ (\mathbf{K}_{Si})^\nabla_S &= -\frac{1}{2} (\mathbf{B}_{Se})^\nabla_S = -\frac{1}{2} (\hat{z}^{kl})'_S \mathbf{a}_k \otimes \mathbf{a}_l \end{aligned}$ <hr style="margin: 5px 0;"/> $(\mathbf{K}_S)^\nabla_S = (\mathbf{K}_{Se})^\nabla_S + (\mathbf{K}_{Si})^\nabla_S$ </div>	<div style="text-align: center;"> $\begin{array}{c} \nearrow \\ \mathbf{F}_{Si}(\cdot) \mathbf{F}_{Si}^T \\ \searrow \\ \mathbf{F}_{Si}^{-1}(\cdot) \mathbf{F}_{Si}^{T-1} \end{array}$ </div> <div style="text-align: center; margin-top: 20px;"> (312) </div>
--	--

with the lower (covariant) Lie or Oldroyd derivatives of φ^S

$$\begin{aligned} (\cdot)_S^\nabla &:= (\cdot)'_S - \mathbf{L}_S(\cdot) - (\cdot) \mathbf{L}_S^T, \\ (\hat{\cdot})_{Si}^\nabla &:= (\hat{\cdot})'_{Si} - \hat{\mathbf{L}}_{Si}(\hat{\cdot}) - (\hat{\cdot}) \hat{\mathbf{L}}_{Si}^T \end{aligned}$$

and the covariant identities

$$\begin{aligned} \mathbf{D}_S &= -\frac{1}{2} (\mathbf{L}_S^{-1} + \mathbf{L}_S^{T-1}) = (\mathbf{K}_S)^\nabla_S, \quad \hat{\mathbf{D}}_{Si} = -\frac{1}{2} (\hat{\mathbf{L}}_{Si}^{-1} + \hat{\mathbf{L}}_{Si}^{T-1}) = (\hat{\mathbf{K}}_{Si})_{Si}^\nabla, \\ (\mathbf{B}_S)^\nabla_S &= (h^{kl} \mathbf{a}_k \otimes \mathbf{a}_l)^\nabla_S = \mathbf{0}, \quad (\hat{\mathbf{B}}_{Si})_{Si}^\nabla = (h^{kl} \hat{\mathbf{z}}_k \otimes \hat{\mathbf{z}}_l)_{Si}^\nabla = \mathbf{0}. \end{aligned}$$

A.4 Evolution Equations

Contravariant inelastic evolution equations ($N = 1$)

<div style="border: 1px solid black; padding: 10px; margin-bottom: 10px;"> <p style="text-align: center; margin: 0;"><i>reference configuration</i></p> <hr style="width: 80%; margin: 5px auto;"/> $(\mathbf{E}_{Si})'_S = \frac{1}{2} (\mathbf{C}_{Si})'_S = (\overset{4}{\mathbf{D}}^S)^{-1} \mathbf{S}_{NEQ}^S$ $(\overset{4}{\mathbf{D}}^S)^{-1} = \alpha (\mathbf{C}_{Si} \otimes \mathbf{C}_{Si})^{23T} - \beta (\mathbf{C}_{Si} \otimes \mathbf{C}_{Si})^a$ $(\mathbf{E}_{Si})'_S = \alpha \mathbf{C}_{Si} \mathbf{S}_{NEQ}^S \mathbf{C}_{Si} - \beta (\mathbf{S}_{NEQ}^S \cdot \mathbf{C}_{Si}) \mathbf{C}_{Si}$ </div> <div style="border: 1px solid black; padding: 10px; margin-bottom: 10px;"> <p style="text-align: center; margin: 0;"><i>intermediate configuration</i></p> <hr style="width: 80%; margin: 5px auto;"/> $(\hat{\mathbf{T}}_{Si})_{Si}^\Delta = \hat{\mathbf{D}}_{Si} = (\overset{4}{\mathbf{D}}^S)^{-1} \hat{\boldsymbol{\tau}}_{NEQ}^S$ $(\hat{\overset{4}{\mathbf{D}}}^S)^{-1} = \alpha (\mathbf{I} \otimes \mathbf{I})^{23} - \beta (\mathbf{I} \otimes \mathbf{I})^a$ $(\hat{\mathbf{T}}_{Si})_{Si}^\Delta = \alpha \hat{\boldsymbol{\tau}}_{NEQ}^S - \beta (\hat{\boldsymbol{\tau}}_{NEQ}^S \cdot \mathbf{I}) \mathbf{I}$ </div>	$\begin{array}{c} \nearrow \mathbf{F}_{Si}^{T-1}(\cdot) \mathbf{F}_{Si}^{-1} \\ \mathbf{F}_{Si}^T(\cdot) \mathbf{F}_{Si} \end{array}$	<div style="border: 1px solid black; padding: 10px; margin-bottom: 10px;"> <p style="text-align: center; margin: 0;"><i>actual configuration</i></p> <hr style="width: 80%; margin: 5px auto;"/> $(\mathbf{A}_{Si})_S^\Delta = \frac{1}{2} (\mathbf{B}_{Se}^{-1})_S^\Delta = (\overset{4}{\mathbf{D}}^S)^{-1} \boldsymbol{\tau}_{NEQ}^S$ $(\overset{4}{\mathbf{D}}^S)^{-1} = \alpha (\mathbf{B}_{Se}^{-1} \otimes \mathbf{B}_{Se}^{-1})^{23T} - \beta (\mathbf{B}_{Se}^{-1} \otimes \mathbf{B}_{Se}^{-1})^a$ $(\mathbf{A}_{Si})_S^\Delta = \alpha \mathbf{B}_{Se}^{-1} \boldsymbol{\tau}_{NEQ}^S \mathbf{B}_{Se}^{-1} - \beta (\boldsymbol{\tau}_{NEQ}^S \cdot \mathbf{B}_{Se}^{-1}) \mathbf{B}_{Se}^{-1}$ </div> <div style="border: 1px solid black; padding: 10px; margin-bottom: 10px;"> <p style="text-align: center; margin: 0;"><i>reference configuration</i></p> <hr style="width: 80%; margin: 5px auto;"/> $(\mathbf{E}_{Si})'_S = \frac{1}{2} (\mathbf{C}_{Si})'_S = (\overset{4}{\mathbf{D}}^S)^{-1} \mathbf{S}_{NEQ}^S$ $(\overset{4}{\mathbf{D}}^S)^{-1} = \alpha (\mathbf{C}_{Si} \otimes \mathbf{C}_{Si})^{23T} - \beta (\mathbf{C}_{Si} \otimes \mathbf{C}_{Si})^a$ $(\mathbf{E}_{Si})'_S = \alpha \mathbf{C}_{Si} \mathbf{S}_{NEQ}^S \mathbf{C}_{Si} - \beta (\mathbf{S}_{NEQ}^S \cdot \mathbf{C}_{Si}) \mathbf{C}_{Si}$ </div>	$\begin{array}{c} \nearrow \mathbf{F}_{Se}^{T-1}(\cdot) \mathbf{F}_{Se}^{-1} \\ \mathbf{F}_{Se}^T(\cdot) \mathbf{F}_{Se} \end{array}$
---	---	--	---

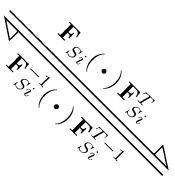
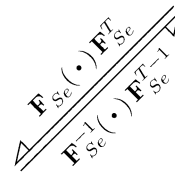
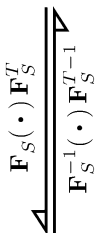
(313)

with the abbreviations

$$\alpha = \frac{1}{2\eta^S}, \quad \beta = \frac{\zeta^S}{2\eta^S (2\eta^S + 3\zeta^S)}, \quad \text{where} \quad \begin{cases} \eta^S > 0, \\ \frac{2}{3}\eta^S + \zeta^S > 0. \end{cases}$$

^aFor the transport mechanism of 4th-order tensors, see (308).

Covariant inelastic evolution equations ($N = 1$)

<p style="text-align: center; margin: 0;"><i>reference configuration</i></p> <hr style="margin: 5px 0;"/> $ \begin{aligned} (\mathbf{K}_{Si})'_S &= -\frac{1}{2} (\mathbf{C}_{Si}^{-1})'_S = (\hat{\mathbf{D}}^S)^{-1} \mathbf{S}_{NEQ}^S \\ (\hat{\mathbf{D}}^S)^{-1} &= \alpha (\mathbf{I} \otimes \mathbf{I})^{23} - \beta (\mathbf{C}_{Si}^{-1} \otimes \mathbf{C}_{Si})^b \\ (\mathbf{K}_{Si})'_S &= \alpha \mathbf{S}_{NEQ}^S - \beta (\mathbf{S}_{NEQ}^S \cdot \mathbf{C}_{Si}) \mathbf{C}_{Si}^{-1} \end{aligned} $		(314)
<p style="text-align: center; margin: 0;"><i>intermediate configuration</i></p> <hr style="margin: 5px 0;"/> $ \begin{aligned} (\hat{\mathbf{K}}_{Si})_{Si}^\nabla &= \hat{\mathbf{D}}_{Si} = (\hat{\mathbf{D}}^S)^{-1} \hat{\boldsymbol{\tau}}_{NEQ}^S \\ (\hat{\mathbf{D}}^S)^{-1} &= \alpha (\mathbf{I} \otimes \mathbf{I})^{23} - \beta (\mathbf{I} \otimes \mathbf{I})^b \\ (\hat{\mathbf{K}}_{Si})_{Si}^\nabla &= \alpha \hat{\boldsymbol{\tau}}_{NEQ}^S - \beta (\hat{\boldsymbol{\tau}}_{NEQ}^S \cdot \mathbf{I}) \mathbf{I} \end{aligned} $		
<p style="text-align: center; margin: 0;"><i>actual configuration</i></p> <hr style="margin: 5px 0;"/> $ \begin{aligned} (\mathbf{K}_{Si})_S^\nabla &= -\frac{1}{2} (\mathbf{B}_{Se})_S^\nabla = (\hat{\mathbf{D}}^S)^{-1} \boldsymbol{\tau}_{NEQ}^S \\ (\hat{\mathbf{D}}^S)^{-1} &= \alpha (\mathbf{I} \otimes \mathbf{I})^{23} - \beta (\mathbf{B}_{Se} \otimes \mathbf{B}_{Se}^{-1})^b \\ (\mathbf{K}_{Si})_S^\nabla &= \alpha \boldsymbol{\tau}_{NEQ}^S - \beta (\boldsymbol{\tau}_{NEQ}^S \cdot \mathbf{B}_{Se}^{-1}) \mathbf{B}_{Se} \end{aligned} $		

with the abbreviations

$$\alpha = \frac{1}{2\eta^S}, \quad \beta = \frac{\zeta^S}{2\eta^S(2\eta^S + 3\zeta^S)}, \quad \text{where} \quad \begin{cases} \eta^S > 0, \\ \frac{2}{3}\eta^S + \zeta^S > 0. \end{cases}$$

^bFor the transport mechanism of 4th-order tensors, see (308).

References

1. Andrade JS, Costa UMS, Almeida MP, Makse HA, Stanley HE (1999) Inertial effects on fluid flow through disordered porous media. *Phys Rev Lett* 82:5249–5252
2. Antman SS (1970) Existence of solutions of the equilibrium equations for nonlinearly elastic rings and arches. *Indiana Univ Math J* 20:281–302
3. Arnold DN (1990) Mixed finite element methods for elliptic problems. *Comput Methods Appl Mech Eng* 82:281–300
4. Arnold DN, Brezzi F, Fortin M (1984) A stable finite element for the Stokes equations. *Calcolo* 21:337–344
5. Baker M, Ericksen JL (1954) Inequalities restricting the form of the stress deformation relations for isotropic elastic solids and Reiner-Rivlin fluids. *J Wash Acad Sci* 44:33–35
6. Ball JM (1977) Convexity conditions and existence theorems in non-linear elasticity. *Arch Ration Mech Anal* 63:337–403
7. Bear J (1988) Dynamics of fluids in porous media. Dover, Mineola. Reprint of American Elsevier Publishing Company, New York, 1972
8. Bennethum LS, Giorgi T (1997) Generalized Forchheimer equation for two-phase flow based on hybrid mixture theory. *Transp Porous Media* 26:261–275
9. Biot MA (1956) Theory of deformation of a porous viscoelastic anisotropic solid. *J Appl Phys* 5:459–467
10. Bischoff JR, Catsiff E, Tobolsky AV (1952) Elastoviscous properties of amorphous polymers in the transition region—I. *J Am Chem Soc* 74:3378–3381
11. Bitzenbauer J, Schweizerhof K (2003) Mehrgitterberechnungen von nichtlinearen Hohlstrukturen. *Proc Appl Math Mech* 3:252–253
12. Blatz PJ, Ko WL (1962) Application of finite elasticity theory to the deformation of rubbery materials. *Trans Soc Rheol* 6:223–251
13. Bowen RM (1976) Theory of mixtures. In: Eringen AC (ed) *Continuum physics*, vol III. Academic, New York, pp 1–127
14. Bowen RM (1980) Incompressible porous media models by use of the theory of mixtures. *Int J Eng Sci* 18:1129–1148
15. Bowen RM (1982) Compressible porous media models by use of the theory of mixtures. *Int J Eng Sci* 20:697–735
16. Braess D (1997) *Finite elemente*. Springer, Berlin
17. Brent RP (1973) *Algorithms for minimization without derivatives*. Prentice-Hall, Englewood Cliffs
18. Brezzi F, Fortin M (1991) *Mixed and hybrid finite element methods*. Springer, New York
19. Brydon AD, Bardenhagen SG, Miller EA, Seidler GT (2005) Simulation of the densification of real open-celled foam microstructures. *J Mech Phys Solids* 53:2638–2660
20. Christensen RM (1971) *Theory of viscoelasticity: an introduction*. Academic, New York
21. Ciarlet PG (1988) *Mathematical elasticity: three dimensional elasticity*, vol 1. North-Holland, Amsterdam
22. Coleman BD (1964) Thermodynamics of materials with memory. *Arch Ration Mech Anal* 17:1–46
23. Coleman BD, Gurtin ME (1967) Thermodynamics with internal state variables. *J Chem Phys* 47:597–613

24. Coleman BD, Noll W (1960) An approximation theorem for functionals, with applications in continuum mechanics. *Arch Ration Mech Anal* 6:356–370
25. Coleman BD, Noll W (1963) The thermodynamics of elastic materials with heat conduction and viscosity. *Arch Ration Mech Anal* 13:167–178
26. Crochet MJ, Naghdi PM (1966) On constitutive equations for flow of fluid through an elastic solid. *Int J Eng Sci* 4:383–401
27. Dacorogna B (1989) *Direct methods in the calculus of variations*. Springer, Berlin
28. Darcy H (1856) *Les fontaines publiques de la ville de Dijon*. Dalmont, Paris
29. de Boer R (1982) *Vektor- und Tensorrechnung für Ingenieure*. Springer, Berlin
30. de Boer R (1996) Highlights in the historical development of porous media theory: toward a consistent macroscopic theory. *Appl Mech Rev* 49:201–262
31. de Boer R (2000) *Theory of porous media*. Springer, Berlin
32. de Boer R, Ehlers W (1990) The development of the concept of effective stresses. *Acta Mech* 83:77–92
33. Diebels S (2000) Mikropolare Zweiphasenmodelle: Formulierung auf der Basis der Theorie Poröser Medien. Habilitation, Bericht Nr II-4 aus dem Institut für Mechanik (Bauwesen), Universität Stuttgart
34. Diebels S, Ehlers W (1996) On fundamental concepts of multiphase micropolar materials. *Tech Mech* 16:77–88
35. Diebels S, Ellsiepen P, Ehlers W (1999) Error-controlled Runge-Kutta time integration of a viscoplastic hybrid two-phase model. *Tech Mech* 19:19–27
36. Droste A (2002) Beschreibung und Anwendung eines elastisch-plastischen Materialmodells mit Schädigung für hochporöse Metallschäume. Dissertation, Bericht Nr II-9 aus dem Institut für Mechanik (Bauwesen), Universität Stuttgart
37. Dullien FAL (1992) *Porous media—fluid transport and pore structure*, 2nd edn. Academic, San Diego
38. Ehlers W (1989) Poröse Medien—ein kontinuumsmechanisches Modell auf der Basis der Mischungstheorie. Forschungsberichte aus dem Fachbereich Bauwesen, Heft 47, Universität-GH-Essen
39. Ehlers W (1993) Constitutive equations for granular materials in geomechanical context. In: Hutter K (ed) *Continuum mechanics in environmental sciences and geophysics*. CISM courses and lectures, No 337. Springer, Wien, pp 313–402
40. Ehlers W (1995) A single-surface yield function for geomaterials. *Arch Appl Mech* 65:246–259
41. Ehlers W (1996) Grundlegende Konzepte in der Theorie Poröser Medien. *Techn Mech* 16:63–76
42. Ehlers W (1996) 2002, Foundations of multiphase and porous materials. In: Ehlers W, Bluhm J (eds) *Porous media: theory, experiments and numerical applications*. Springer, Berlin, pp 3–86
43. Ehlers W, Eipper G (1999) Finite elastic deformations in liquid-saturated and empty porous solids. *Transp Porous Media* 34:179–191
44. Ehlers W, Ellsiepen P (1997) Zeitschrittgesteuerte Verfahren bei stark gekoppelten Festkörper-Fluid-Problemen. *ZAMM* 77:S81–S82
45. Ehlers W, Ellsiepen P (2001) Theoretical and numerical methods in environmental continuum mechanics based on the theory of porous media. In: Schrefler BA (ed) *Environmental geomechanics*. CISM courses and lectures, No 417. Springer, Wien, pp 1–81
46. Ehlers W, Markert B (2000) On the viscoelastic behaviour of fluid-saturated materials. *Granul Matter* 2:153–161
47. Ehlers W, Markert B (2001) A linear viscoelastic biphasic model for soft tissues based on the theory of porous media. *ASME J Biomech Eng* 123:418–424
48. Ehlers W, Markert B (2001) Viscoelastic polyurethane foams at finite deformations. In: Wall WA, Bletzinger K-U, Schweizerhof K (eds) *Trends in computational structural mechanics*. CIMNE, Barcelona, pp 89–98
49. Ehlers W, Markert B (2003) A macroscopic finite strain model for cellular polymers. *Int J Plast* 19:961–976
50. Ehlers W, Müllerschön H (1998) Stress-strain behaviour of cohesionless soils: experiments, theory and numerical computations. In: Cividini A (ed) *Application of numerical methods to geotechnical problems*. CISM courses and lectures, vol 397. Springer, Wien, pp 675–684
51. Eipper G (1998) *Theorie und Numerik finiter elastischer Deformationen in fluidgesättigten porösen Medien*. Dissertation, Bericht Nr II-1 aus dem Institut für Mechanik (Bauwesen), Universität Stuttgart
52. Ellsiepen P (1999) *Zeit- und ortsadaptive Verfahren angewandt auf Mehrphasenprobleme poröser Medien*. Dissertation, Bericht Nr. II-3 aus dem Institut für Mechanik (Bauwesen), Universität Stuttgart
53. Elmoutaouakki A, Fuchs G, Bergounhon P, Péres R (2003) Three-dimensional quantitative analysis of polymer foams from synchrotron radiation x-ray microtomography. *J Phys D: Appl Phys* 36:A37–A43
54. Ericksen JL (1960) Tensor fields. In: Flügge S (ed) *Handbuch der Physik*, vol III/1. Springer, Berlin, pp 794–858
55. Findley WN, Lai JS, Onaran K (1976) *Creep and relaxation of nonlinear viscoelastic materials: with an introduction to linear viscoelasticity*. North-Holland, Amsterdam
56. Fletcher R (1987) *Practical methods of optimization*. Wiley, Chichester
57. Forchheimer P (1901) Wasserbewegung durch Boden. *Z Ver Deutsch Ing* 50:1781–1788
58. Fung YC (1972) Stress-strain-history relations of soft tissues in simple elongation. In: Fung YC, Perrone N, Anliker M (eds) *Biomechanics: its foundations and objectives*. Prentice-Hall, Englewood Cliffs, pp 181–208
59. Fung YC (1981) *Bio-viscoelastic solids*. In: *Biomechanics: mechanical properties of living tissues*. Springer, New York, pp 106–260
60. Gibson LJ, Ashby F (1997) *Cellular solids: structure and properties*, 2nd edn. Cambridge University Press, Cambridge
61. Gibson RE, England GL, Hussey MJL (1967) The theory of one-dimensional consolidation of saturated clays. *Géotechnique* 17:261–273
62. Gong L, Kyriakides S, Jang W-Y (2005) Compressive response of open-cell foams. Part I: Morphology and elastic properties. *Int J Solids Struct* 42:1355–1379
63. Green AE, Zerna W (1968) *Theoretical elasticity*, 2nd edn. Oxford University Press, Oxford
64. Gresho PM, Sani RL (2000) *Incompressible flow and the finite element method*, vol 2. Wiley, Chichester. Second corrected reprint of 1998
65. Gurtin ME, Sternberg E (1962) On the linear theory of viscoelasticity. *Arch Ration Mech Anal* 11:291–356
66. Hairer E, Wanner G (1991) *Solving ordinary differential equations*, vol 2: stiff and differential-algebraic problems. Springer, Berlin
67. Hartmann S (2002) Computation in finite strain viscoelasticity: finite elements based on the interpretation as differential-algebraic equations. *Comput Methods Appl Mech Eng* 191:1439–1470
68. Hassanizadeh SM, Gray WG (1979) General conservation equations for multi-phase-systems: 2. mass, momenta, energy and entropy equations. *Adv Water Resour* 2:191–203
69. Hassanizadeh SM, Gray WG (1987) High velocity flow in porous media. *Trans Porous Media* 2:521–531

70. Haupt P (2000) Continuum mechanics and theory of materials. Springer, Berlin
71. Hilyard NC (1971) Observations on the impact behaviour of polyurethane foams; II. The effect of fluid flow. *J Cell Plast* 7:84–90
72. Holzapfel GA (1996) On large strain viscoelasticity: continuum formulation and finite element applications to elastomeric structures. *Int J Numer Methods Eng* 39:3903–3926
73. Huber N, Tsakmakis C (2000) Finite deformation viscoelasticity laws. *Mech Mater* 32:1–18
74. Hughes TJR, Pister KS (1978) Consistent linearization in mechanics of solids and structures. *Comput Struct* 8:391–397
75. Kaliske M, Rothert H (1997) Formulation and implementation of three-dimensional viscoelasticity at small and finite strains. *Comput Mech* 19:228–239
76. Klar O, Ehlers W (2005) Experimental investigations on polymeric foams. *PAMM* 4:402–403
77. Kleiber M (1975) Kinematics of deformation processes in materials subjected to finite elastic-plastic strains. *Int J Eng Sci* 13:513–525
78. Kraynik AM (2003) Foam structure: From soap froth to solid foams. *MRS Bull* 28:275–278
79. Lai WM, Mow VC (1980) Drag-induced compression of articular cartilage during a permeation experiment. *Biorheology* 17:111–123
80. Laroussi M, Sab K, Alaoui A (2002) Foam mechanics: nonlinear response of an elastic 3d-periodic microstructure. *Int J Solids Struct* 39:3599–3623
81. le Tallec P, Rahier C, Kaiss A (1993) Three-dimensional incompressible viscoelasticity in large strains: formulation and numerical approximation. *Comput Methods Appl Mech Eng* 109:133–258
82. Lee EH (1969) Elastic-plastic deformation at finite strains. *J Appl Mech* 1–6
83. Levy A, Levi-Hevroni D, Sorek S, Ben-Dor G (1999) Derivation of Forchheimer terms and their verification by application to waves propagation in porous media. *Int J Multiphase Flow* 25:683–704
84. Lewis RW, Schrefler BA (1998) The finite element method in the static and dynamic deformation and consolidation of porous media, 2nd edn. Wiley, Chichester
85. Lion A (1997) A physically based method to represent the thermomechanical behaviour of elastomers. *Acta Mech* 123:1–25
86. Lion A (1998) Thixotropic behaviour of rubber under dynamic loading histories: experiments and theory. *J Mech Phys Solids* 46:895–930
87. Lubliner J (1973) On the structure of the rate equations of materials with internal variables. *Acta Mech* 17:109–119
88. Lubliner J (1985) A model of rubber viscoelasticity. *Mech Res Commun* 12:93–99
89. Mahnkopf D (2000) Lokalisierung fluidgesättigter poröser Festkörper bei finiten elastoplastischen Deformationen. Dissertation, Bericht Nr II-5 aus dem Institut für Mechanik (Bauwesen), Universität Stuttgart
90. Mak AF (1986) The apparent viscoelastic behaviour of articular cartilage—the contributions from the intrinsic matrix viscoelasticity and interstitial fluid flows. *ASME J Biomech Eng* 108:123–130
91. Markert B (2005) Porous media viscoelasticity with application to polymeric foams. Dissertation, Report No II-12 of the Institute of Applied Mechanics (CE), Universität Stuttgart, Germany
92. Markert B (2007) A constitutive approach to 3-d nonlinear fluid flow through finite deformable porous continua. *Trans Porous Media*. Available online, DOI [10.1007/s11242-007-9107-6](https://doi.org/10.1007/s11242-007-9107-6)
93. Marsden JE, Hughes TJR (1994) Mathematical foundations of elasticity. Dover, New York. Reprint of Prentice-Hall, 1983
94. Meguid SA, Cheon SS, El-Abbasi N (2002) Fe modelling of deformation localization in metallic foams. *Finite Elem Anal Des* 38:631–643
95. Mills NJ (2005) The wet Kelvin model for air flow through open-cell polyurethane foams. *J Mater Sci* 40:5845–5851
96. Morrey CB (1952) Quasi-convexity and the lower semicontinuity of multiple integrals. *Pac J Math* 2:25–53
97. Mow VC, Lai WM, Holmes MH (1982) Advanced theoretical and experimental techniques in cartilage research. In: Huijskes R, van Campen D, de Wijn J (eds) *Biomechanics: principles and applications*. Martinus Nijhoff, The Hague, pp 47–74
98. Muskat M (1937) The flow of homogeneous fluids through porous media. McGraw-Hill, New York
99. Nikolaevskiy VN (1990) Mechanics of porous and fractured media. World Scientific, Singapore
100. Nocedal J, Wright SJ (1999) Numerical optimization. Springer, Wien
101. Ogden RW (1972) Large deformation isotropic elasticity—on the correlation of theory and experiment for incompressible rubberlike solids. *Proc R Soc Lond A* 326:565–584
102. Ogden RW (1972) Large deformation isotropic elasticity—on the correlation of theory and experiment for compressible rubberlike solids. *Proc R Soc Lond A* 328:323–338
103. Ogden RW (1977) Inequalities associated with the inversion of elastic stress-deformation relations and their implications. *Math Proc Camb Philos Soc* 81:313–324
104. Ogden RW (1982) Elastic deformations of rubberlike solids. In: Hopkins HG, Sewell MJ (eds) *Mechanics of solids*. Pergamon, Oxford, pp 499–537. The Rodney Hill 60th anniversary volume
105. Ogden RW (1984) Nonlinear elastic deformations. Ellis Harwood Ltd, Chichester
106. Oldroyd JG (1950) On the formulation of rheological equations of state. *Proc R Soc Lond A* 200:523–541
107. Pan C, Hilpert M, Miller CT (2001) Pore-scale modeling of saturated permeabilities in random sphere packings. *Phys Rev E* 64:066702
108. Papastavridis JG (1999) Tensor calculus and analytical dynamics. CRC Press LLC, Boca Raton
109. Pastor M, Li T, Liu X, Zienkiewicz OC, Quecedo M (2000) A fractional step algorithm allowing equal order of interpolation for coupled analysis of saturated soil problems. *Mech Cohes-Frict Mater* 5:511–534
110. Perrot C, Panneton R, Olry X (2007) Periodic unit cell reconstruction of porous media: application to open-cell aluminum foams. *J Appl Phys* 101:113538
111. Powell MJD (1994) A direct search optimization method that models the objective and constraint functions by linear interpolation. In: Gomez S, Hennart JP (eds) *Advances in optimization and numerical analysis*. Kluwer Academic, Dordrecht, pp 51–67
112. Powell MJD (1998) Direct search algorithms for optimization calculations. *Acta Numer* 7:287–336
113. Powell MJD (2003) On trust region methods for unconstrained minimization without derivatives. *Math Program* 97:605–623
114. Press WH, Teukolsky SA, Vetterling WT, Flannery BP (1999) Numerical recipes in C, 2nd edn. Cambridge University Press, Cambridge. Corrected reprint of 1992
115. Reese S (2001) Thermomechanische Modellierung gummiartiger Polymerstrukturen. Habilitation, Bericht Nr F01/4 aus dem Institut für Baumechanik und Numerische Mechanik, Universität Hannover
116. Reese S, Govindjee S (1998) A theory of finite viscoelasticity and numerical aspects. *Int J Solids Struct* 35:3455–3482
117. Rusch KC (1965) Dynamic behaviour of flexible open-cell foams. PhD thesis, Engineering, general, University of Akron
118. Ruth DW, Ma H (1992) On the derivation of the Forchheimer equation by means of the averaging theorem. *Transp Porous Media* 5:97–102

119. Sandhu RS, Wilson EL (1969) Finite-element analysis of seepage in elastic media. *J Eng Mech Div ASCE* 95:641–652
120. Schraad MW, Harlow FH (2006) A multi-field approach to modeling the dynamic response of cellular materials. *Int J Mech Sci* 48:85–106
121. Schröder J (2000) Homogenisierungsmethoden der nichtlinearen Kontinuumsmechanik unter Beachtung von Stabilitätsproblemen. Habilitation, Bericht Nr I-7 aus dem Institut für Mechanik (Bauwesen), Universität Stuttgart
122. Setton LA, Zhu W, Mow VC (1993) The biphasic poroviscoelastic behavior of articular cartilage: role of the surface zone in governing the compressive behavior. *J Biomech* 26:581–592
123. Shulmeister V, van der Burg MWD, van der Giessen E, Marissen R (1998) A numerical study of large deformations of low-density elastomeric open-cell foams. *Mech Mater* 30:125–140
124. Sidoroff F (1973) The geometrical concept of intermediate configuration and elastic-plastic finite strain. *Arch Mech* 25:299–308
125. Sidoroff F (1974) Un modèle viscoélastique non linéaire avec configuration intermédiaire. *J Méc* 13:679–713
126. Šilhavý M (1997) The mechanics and thermodynamics of continuous media. Springer, Berlin
127. Simo JC (1987) On a fully three-dimensional finite-strain viscoelastic damage model: formulation and computational aspects. *Comput Methods Appl Mech Eng* 99:153–173
128. Simo JC, Hughes TJR (1998) Computational inelasticity. Springer, New York
129. Simo JC, Taylor RL (1985) Consistent tangent operators for rate-independent elastoplasticity. *Comput Methods Appl Mech Eng* 48:101–118
130. Suh J-K, Bai S (1998) Finite element formulation of biphasic poroviscoelastic model of articular cartilage. *ASME J Biomech Eng* 120:195–201
131. Taylor RL, Pister KS, Goudreau GL (1970) Thermomechanical analysis of viscoelastic solids. *Int J Numer Methods Eng* 2:45–59
132. Terzaghi K, Jelinek R (1954) Theoretische Bodenmechanik. Springer, Berlin
133. Thomson (Lord Kelvin) S (1887) On the division of space with minimum partitional area. *Acta Math* 11:121–134
134. Treloar LRG (1975) The physics of rubber elasticity, 3rd edn. Clarendon, Oxford
135. Truesdell C (1984) Thermodynamics of diffusion. In: Truesdell C (ed) Rational thermodynamics, 2nd edn. Springer, New York, pp 219–236
136. Tschoegl NW (1989) The phenomenological theory of linear viscoelastic behavior: an introduction. Springer, New York
137. Valanis KC (1971) Internal variable theory. In: Valanis KC (ed) Irreversible thermodynamics of continuous media. CISM courses and lectures, No 77. Springer, Wien
138. van Genabeek O, Rothman DH (1996) Macroscopic manifestations of microscopic flows through porous media: phenomenology from simulation. *Annu Rev Earth Planet Sci* 24:63–87
139. Wang Y, Cuitiño A (2000) The deformation habits of compressed open-cell solid foams. *ASME J Eng Mat Tech* 122:376–378
140. Weaire D, Hutzler S (1999) The physics of foams. Clarendon, Oxford
141. Williams G, Watts DC (1970) Non-symmetrical dielectric relaxation behavior arising from a simple empirical decay function. *Trans Faraday Soc* 66:80–85
142. Wriggers P (1988) Konsistente Linearisierung in der Kontinuumsmechanik und ihre Anwendung auf die Finite-Elemente-Methode. Technischer Bericht Nr F88/4, Forschungs- und Seminarberichte aus dem Bereich der Mechanik der Universität Hannover
143. Youseff S, Maire E, Gaertner R (2005) Finite element modelling of the actual structure of cellular materials determined by x-ray tomography. *Acta Mater* 53:719–730
144. Zhu HX, Mills NJ, Knott JF (1997) Analysis of high strain compression of open-cell foams having tetrakaidecahedral cells. *J Mech Phys Solids* 45:1875–1904
145. Zhu HX, Windle AH (2002) Effects of cell irregularity on the high strain compression of open-cell foams. *Acta Mater* 50:1041–1052
146. Zienkiewicz OC, Chan AHC, Pastor M, Schrefler BA, Shiomi T (1999) Computational geomechanics with special reference to earthquake engineering. Wiley, Chichester
147. Zienkiewicz OC, Codina R (1995) A general algorithm for compressible and incompressible flow—Part I. The split, characteristic-based scheme. *Int J Numer Methods Fluids* 20:869–885
148. Zienkiewicz OC, Rojek J, Taylor RL, Pastor M (1998) Triangles and tetrahedra in explicit dynamic codes for solids. *Int J Numer Methods Eng* 43:565–583
149. Zienkiewicz OC, Taylor RL (2000) The finite element method. The basis, vol 1, 5th edn. Butterworth Heinemann, Oxford